



International Journal of Fracture Fatigue & Wear

Volume 1, 2013

ISSN 2294-7868

Editor: Professor Magd Abdel Wahab

© Labo Soete, Universiteit Gent



International Journal of Fracture Fatigue and Wear:

A Conference Series proceedings

Volume 1, 2013

Proceedings of the 2nd International Symposium
on Engineering Mechanics and its Applications,
Kitakyushu, Japan, 30 – 31 August 2013

Published by
Laboratory Soete – Ghent University
Technologiepark Zwijnaarde 903
B-9052 Zwijnaarde, Belgium
<http://www.soetelaboratory.ugent.be/>
Edited by: Professor Magd Abdel Wahab
ISSN: 2294-7868

2nd International Symposium on Engineering Mechanics and its Applications, Kitakyushu, Japan, 30 – 31 August 2013

Chairman

Professor NODA Nao-Aki

Department of Mechanical and Control Engineering

Kyushu Institute of Technology

International Scientific Committee

Prof. ABDEL WAHAB Magd, Ghent University

Prof. CHEN JT, National Taiwan Ocean University

Prof. CHIU Tz-Cheng, National Cheng Kung University

Prof. CHUE Ching Hwei, National Cheng Kung University

Prof. CHUNG Tae Jin, Kunsan National University

Prof. CUI Xin-zhuang, Shandong University

Prof. FENG Weiming, Shandong University

Prof. JIN Qing, Shandong University

Prof. LIANG Bin, Henan University of Science and Technology

Associate Prof. MIYAZAKI Tatsujirou, Ryukyus University

Prof. NODA Nao-Aki, Kyushu Institute of Technology

Prof. ODA Kazuhiro, Oita University

Dr. TAKASE Yasushi, Kyushu Institute of Technology

Prof. WANG Guangyue, Shandong University

Prof. WANG Lei, Shandong University

Prof. WU Chengwei, Dalian University of Technology

Prof. XU Hongyu, Henan University of Science and Technology

Editorial

The first volume of the International Journal of Fracture Fatigue and Wear contains the proceedings of the 2nd International Symposium on Engineering Mechanics and its Applications (EMA), which was held in Kitakyushu, Japan during the period 30-31 August 2013. The symposium was attended by several international participants from different countries including Japan, China, Taiwan, South Korea and Belgium. It covers different topics on Engineering Mechanics and its Applications and serves as a forum to exchange ideas on these topics between the participants.

Each paper presented in this volume has been sent to two reviewers, who are members of the International Scientific Committee of EMA 2013. The decision for publishing a paper in the conference proceedings was based on the recommendation of the reviewers. The Editor would like to thank all members of Scientific Committee for their valuable contribution in evaluating the papers.

The meeting was very successful and the participants have enjoyed the technical presentations, as well as the wonderful social program organised by Kyushu Institute of Technology (Kyutech). The Editor would like to thank the EMA 2013 organizer, Prof Nao-Aki Noda, and the EMA 2013 secretary Dr Yasushi Takase, for organizing the symposium and the social program.

Finally, thanks to all authors who have contributed to this volume and presented their research work at Kyutech.



The 2nd International Symposium on Engineering Mechanics and its Applications,
Kitakyushu, Japan, 30 – 31 August 2013

The Editor
Prof. Magd Abdel Wahab

Table of Contents

EMA 1: The energy conservation analysis and numerical simulation of in-plane and out-plane nonlinear vibrations of cable-stayed beams, F. Weiming and S. Yixia Sun	1-9
EMA 2: Stability and reinforcement of guardrail post in central separate belt of expressways based on MCPT, Q. Jin, X. Z. Cui, Y. X. Zhou, W. Sui and Z. J. Gao	10-16
EMA 3: Thermal analysis of two-dimensional temperature-dependent functionally graded open cylindrical shells, B. Sobhani Aragh and M. Abdel Wahab	17-23
EMA 4: Study on vibration and stability of functionally graded cylindrical shells subjected to hydrostatic pressure, B. Liang, R. Li, N.A. Noda and H.Y. Xu	24-30
EMA 5: Effects of rainfall infiltration on stability of geocell reinforced slope, Wang Guangyue and Zhang Janpeng	31-36
EMA 6: Propagation characteristics of coupled wave through micropolar elastic solid interlayer in micropolar fluid, Xu Hongyu, Dang Songyang, Sun Qingyong and Liang Bin	37-41
EMA 7: Growth behavior of small surface-cracks of ultrafine grained copper at high and low cyclic-stresses, K. Yamauchi, M. Goto, Sz. Han, K. Euh and T. Yakushiji	42-47
EMA 8: Investigation on dynamics and fatigue prevention of steel catenary riser, L. Guo, M.L. Duan, M. Ye and G.M. Cheng	48-54
EMA 9: Numerical modeling of axially loaded suction pile, G.M. Cheng, M.L. Duan, L. Guo, F. Wang	55-60
EMA 10: Solutions for s-lay vessels to install subsea production systems, Mao Ye, Menglan Duan, Mingjie Li, Chenbo Zhao, Wei Li, Guangluan Li, Zhenguo Hu	61-72
EMA 11: Effect of indenter shape on vickers hardness by finite element analysis, K. Morita, K. Oda and N. Tsutsumi	73-76
EMA 12: Review of the dual BEM and recent development of null-field integral equation approach in Taiwan, J. T. Chen, J. W. Lee	77-83
EMA 13: Simulation of interface delamination growth in microelectronic interconnect structures, T.-C. Chiu, Y.-S. Lai and C.-H. Chen	84-90
EMA 14: Accurate determination of stress intensity factors for interface crack problem under thermal stress by crack tip stress method, K. Oda, Y. Abe, T. Shinmoto and N. Tsutsumi	91-95
EMA 15: Topological optimization for machine structure design, Tae-Jin Chung, Henry Panganiban and Won-Cheol Kim	96-100
EMA 16: Estimation of the knee joint force during deep knee flexion, M. Fukunaga, K. Koguchi and S. Hirokawa	101-104
EMA 17: Debonding criterion based on the intensity of singular stress, Tatsujiro Miyazaki, Nao-Aki Noda, Long Li, Takumi Uchikoban and Yoshikazu Sano	105-111
EMA 18: Stability of flexural members on bi-moduli elastic foundation, L. Wang and Z.H. Lui	112-117
EMA 19: Effect of hydrogen on tensile properties of carbon steels, N. Tsutsumi and K. Oda	118-122

- EMA 20: Proposal of Practicing Education for Engineering Ethics using a Safety Activity, Genji Hotta
123-128
- EMA 21: The structure and mechanical property of turtle shell, C. W. Wu, w. Zhang, C. Z. Zhang and z. Chen
129-131
- EMA 22: Finite element analysis of fretting fatigue, M. Abdel Wahab and R. Hojjati-Talemi 132-137

THE ENERGY CONSERVATION ANALYSIS AND NUMERICAL SIMULATION OF IN-PLANE AND OUT-PLANE NONLINEAR VIBRATIONS OF CABLE-STAYED BEAMS

F. Weiming¹ and S. Yixia²

¹ Department of Engineering Mechanics, Shandong University, Jinan 250062

² School of Aerospace Engineering and Applied Mechanics, Tongji University, Shanghai 200092

Abstract: In the present work, the three-dimensional nonlinear vibration of a cable-stayed beam is investigated. A set of nonlinear partial differential equations describing the vibration of this coupling system is derived by Hamilton's principle. The Galerkin and multi-scale methods are employed to solve the nonlinear partial differential equations, which govern vibrations of the cable-stayed beam system. It is theoretically proved that the parametric resonances of in-plane and out-of-plane vibrations of the non-damped coupling structure satisfy the principle of conservation of energy. Finally, the nonlinear vibration of the cable-stayed beam is simulated by the Runge-Kutta method. It is found that the parametric resonances occur when the frequency ratio of the cable in-plane, out-plane vibration and beam vibration is equal to 1:0.9993:2. The vibration amplitude of the coupling structure demonstrates the periodic shift among the three types of vibrations, which is consistent with the result that is obtained by theoretical analysis.

Keywords: Non-Linear Vibration, Coupling Of Cable-Stayed Beam, Galerkin's Method, Multi-Scale Method, Parametric Excitation

1. INTRODUCTION

The cable-beam coupling structures are widely applied in the engineering area, such as the high voltage overhead power transmission lines and tower frame, cable crane, tethered satellite in aerospace technology and the cable-stayed bridges in bridge engineering. In modern engineering, the cable is becoming longer and longer, thus the large deform problem of cables is of great concern. Furthermore, vibrations of the cable-beam coupling structures are also greatly influenced by the interaction of the bending moment of beam along with the axial force of cable and other influential factors. The nonlinear parametric vibrations are easily induced in these coupling systems under the action of the wind, earthquake and traffic loads. Therefore, nonlinear vibrations of the cable-beam coupling structures are concerned by more and more experts. The modal coupling between the in-plane and out-plane vibrations of cable was investigated in discrete method by Bebetti et al. and Luongo et al. [1-2], who found that the energy was transferred between the two modes in the form of "beat". The parametric vibration of cables was studied by Lilien and Pinto da Costa [3], who found that the large amplitude vibration might occur under the low-frequency excitation. For the cable-beam coupling structures, Kang and Zhong reduced it to a kind of two-freedom nonlinear vibration system in which the bridge was modeled as a kind of mass-spring structure [4]. The nonlinear differential equations, which describe the in-plane vibration of the cable-beam coupling structure based on the Hamilton's principle was derived by Gattulli and Lepidi, who found that when the vibration frequency of beam is twice that of cable, the subharmonic resonance may occur [5]. For the cable-tower-beam coupling system, Guo et al. investigated the influence of the obliquity, initial perturbation and damping on the cable vibration [6]. For the cable-beam coupling system under the parametric excitation, Feng and Sun studied its nonlinear dynamic phenomena [7].

In the present work, we attempt to derive the three-dimensional governing equation of the cable-beam structure and quantitatively analyze the vibration of this system by using the Galerkin method and multiscale method. The "beat" phenomena (also called the energy conservation relation) found in Refs. [5-7] for the two-freedom systems will be proved theoretically for the three-freedom system describing the vibration of the cable-beam coupling structure. Finally, the Runge-Kutta method is employed to obtain the variations of displacements of the cable and beam with respect to the time. We believe that this work will provide theoretical basis for designs of cable-beam coupling structures.

¹ Corresponding author.
E-mail: fwm@sdu.edu.cn

2. ANALYSIS

2.1 Three-dimensional dynamic equations for cable-beam coupling system

For the cable-stayed beam illustrated in Fig.1, we use the Bernoulli-Euler beam theory to describe the beam vibration and take into account not only the in-plane but also the out-of-plane vibrations of the cable. As shown in Fig.1, a cantilever beam is subjected to a tension force exerted by the cable at right end of the beam, the cable

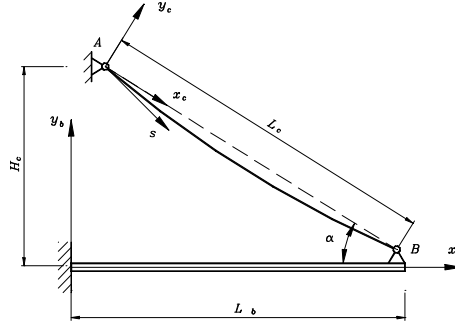


Fig.1 The cable-stayed beam configuration

vibrates in the three dimensional space- $Ox_c y_c z_c$, the beam vibrates in the plane- $Ox_b y_b$. For the cable, we assume that the bending stiffness, shear stiffness and torsional stiffness are neglected; the inclined cable is subjected to the action of pulling force; the deformation constitutive relationship satisfies Hook's law and the cable is uniformly forced; the static curve under self-weight of cable is approximately a parabola; the axial strain of the cable is sufficiently small.

According to the Hamilton principle, the nonlinear equations describing vibrations of the cable-beam coupling structure is expressed as follows:

$$\left. \begin{aligned} \frac{\partial}{\partial x_c} \left\{ T \frac{\partial v_c}{\partial x_c} + p \frac{dy_c}{dx_c} + p \frac{\partial v_c}{\partial x_c} \right\} &= m_c \frac{\partial^2 v_c}{\partial t^2} + c_c \frac{\partial v_c}{\partial t} \\ \frac{\partial}{\partial x_c} \left\{ T \frac{\partial w_c}{\partial x_c} + p \frac{\partial w_c}{\partial x_c} \right\} &= m_c \frac{\partial^2 w_c}{\partial t^2} + c'_c \frac{\partial w_c}{\partial t} \\ EI \frac{\partial^4 v_b}{\partial x_b^4} + F_N \frac{\partial^2 v_b}{\partial x_b^2} + m_b \frac{\partial^2 v_b}{\partial t^2} + c_b \frac{\partial v_b}{\partial t} + \delta(x_b - L_b) p \sin \theta &= 0 \end{aligned} \right\} \quad (1)$$

where L_b is the length of the beam, $\delta(x_b - L_b)$ is the Delta function and defined

as $\delta(x_b - L_b) = \begin{cases} \infty, & x_b = L_b \\ 0, & x_b \neq L_b \end{cases}$, T is the initial axial tension of the inclined cable, p is the additional axial

dynamic tension, v_c and w_c are respectively the in-plane and out-of-plane vibration displacements of the cable, v_b is the transverse vibration displacement of the beam, c_c and c'_c are respectively the in-plane and out-of-plane damping coefficients of the cable, c_b is the damping coefficient of the beam, $E_b I_b$ is the beam flexible bending stiffness, $E_c A_c$ is the cable tensile stiffness, m_c and m_b are respectively the masses of

the beam and cable per unit length, F_N is the axial tension of the beam, $y(x) = \frac{m_c g L \cos \theta}{2H} \left(x - \frac{x^2}{L} \right)$

describes the static curve under self-weight of the cable [7], θ is the dip angle of the inclined cable, L is length of the cable, and H is the static tension of the cable. In deriving Eq. (1), the three dimensional vibration equation of the cable has been reduced to the two dimensional one, the details of the reduction process can be referred to Ref. [7] where the two-dimensional vibration has been simplified into the one-dimensional one. The additional axial dynamic tension of the cable is expressed as:

$$p = \frac{E_c A_c}{L} \int_0^L \left[\frac{dy_c}{dx_c} \cdot \frac{\partial v_c}{\partial x_c} + \frac{1}{2} \left(\frac{\partial v_c}{\partial x_c} \right)^2 + \frac{1}{2} \left(\frac{\partial w_c}{\partial x_c} \right)^2 \right] dx_c + \frac{E_c A_c}{L} v_b(l, t) \sin \theta \quad (2)$$

The axial tension of the beam is written as:

$$F_N \approx (T + p) \cos \theta \quad (3)$$

The displacement compatibility condition for the cable-beam coupling structure reads:

$$\begin{aligned} v_c(0, t) &= v_b(0, t) = 0 \\ v_c(L, t) &= v_b(l, t) \cos \theta \end{aligned}$$

2.2 Quantitative analysis of the cable-beam coupling structure vibration

2.2. 1 Galerkin method

Now the Galerkin method is applied to get ordinary differential equations which approximates Eq.(1). The approximate displacements of the beam and cable are set as:

$$\left. \begin{aligned} v_c(x_c, t) &= \sum_{r=1}^n \phi_{cr}(x_c) q_{cr}(t) + \frac{x_c}{L} v_b(l, t) \cos \theta \\ w_c(x_c, t) &= \sum_{r=1}^n \phi'_{cr}(x_c) q'_{cr}(t) \\ v_b(x_b, t) &= \sum_{r=1}^n \phi_{br}(x_b) q_{br}(t) \end{aligned} \right\} \quad (4)$$

By experiment, Tagata found that for the tightening string excited at ends, the first mode dominates its vibration [9]. Therefore, when applying the Galerkin method, we only consider the first vibration mode. Eq. (2) representing the additional dynamic tension of the cable can be reduced to:

$$p = A_1 q_c + A_2 q_c^2 + A_3 q_b + A_4 q_b^2 + A_5 q_c'^2 \quad (5)$$

By substituting Eq. (3) and Eq. (5) into Eq. (1) and applying the Galerkin method with the first-order truncation, the ordinary differential equations approximately describing the vibration of the cable-beam coupling structure can be obtained as follows:

$$\left. \begin{aligned} C_1 \ddot{q}_c + C_2 \dot{q}_c + C_3 q_c q_b + C_4 \dot{q}_c + C_5 q_c^2 + C_6 q_c^3 + C_7 q_c q_b^2 + C_8 q_b + C_9 q_b^2 + C_{10} \ddot{q}_b + C_{11} \dot{q}_b \\ + C_{12} q_c'^2 + C_{13} q_c'^2 q_c = 0 \\ C_1' \ddot{q}_c + C_2' q_c + C_3' q_c' q_c + C_4' \dot{q}_c + C_5' q_c' q_c^2 + C_6' q_c' q_b + C_7' q_c' q_b^2 + C_8' q_c'^3 = 0 \\ B_1 \ddot{q}_b + B_2 q_b + B_3 q_b q_c + B_4 \dot{q}_b + B_5 q_b^2 + B_6 q_b^3 + B_7 q_b q_c^2 + B_8 q_c + B_9 q_c^2 + B_{10} q_c'^2 q_b \\ + B_{11} q_c'^2 = 0 \end{aligned} \right\} \quad (7)$$

where the expressions of $B_i (i = 1, 2, \dots, 11)$, $C_i (i = 1, 2, \dots, 13)$ and $C_i' (i = 1, 2, \dots, 8)$ are documented in Appendix.

By defining $\omega_c^2 = \frac{C_2}{C_1}$, $\omega_c'^2 = \frac{C_2'}{C_1'}$, $\omega_b^2 = \frac{B_2}{B_1}$, here ω_c and ω_c' are respectively the in-plane and

out-of-plane vibration frequencies of the cable and ω_b represents the beam vibration frequency. Then the following notations are introduced:

$$\hat{\alpha}_i = \frac{C_{i+2}}{C_1} (i = 1, 2, \dots, 11), \quad \hat{\alpha}'_i = \frac{C'_{i+2}}{C'_1} (i = 1, 2, \dots, 6), \quad \hat{\beta}_i = \frac{B_{i+2}}{B_1} (i = 1, 2, \dots, 9)$$

Therefore, Eq. (7) becomes

$$\left. \begin{aligned}
& \ddot{q}_c + \omega_c^2 q_c + \hat{\alpha}_1 q_c q_b + \hat{\alpha}_2 \dot{q}_c + \hat{\alpha}_3 q_c^2 + \hat{\alpha}_4 q_c^3 + \hat{\alpha}_5 q_c q_b^2 + \hat{\alpha}_6 q_b + \hat{\alpha}_7 q_b^2 \\
& + \hat{\alpha}_8 \ddot{q}_b + \hat{\alpha}_9 \dot{q}_b + \hat{\alpha}_{10} q_c'^2 + \hat{\alpha}_{11} q_c'^2 q_c = 0 \\
& \ddot{q}_c' + \omega_c'^2 q_c' + \hat{\alpha}_1' q_c' q_c + \hat{\alpha}_2' \dot{q}_c' + \hat{\alpha}_3' q_c' q_c^2 + \hat{\alpha}_4' q_c' q_b + \hat{\alpha}_5' q_c' q_b^2 + \hat{\alpha}_6' q_c'^3 = 0 \\
& \ddot{q}_b + \omega_b^2 q_b + \hat{\beta}_1 q_b q_c + \hat{\beta}_2 \dot{q}_b + \hat{\beta}_3 q_b^2 + \hat{\beta}_4 q_b^3 + \hat{\beta}_5 q_b q_c^2 + \hat{\beta}_6 q_c + \hat{\beta}_7 q_c^2 \\
& + \hat{\beta}_8 q_c'^2 q_b + \hat{\beta}_9 q_c'^2 = 0
\end{aligned} \right\} \quad (8)$$

2.2.2 The approximate solution by multiscale method

Setting $\tau = \omega_c t$ and introducing the frequency perturbation parameter $k' = \omega_b / \omega_c = k + \varepsilon \sigma$ ($0 < \varepsilon \ll 1$) with the σ as the detuning parameter, we get $k'^2 \approx k^2 + 2\varepsilon \sigma k$. In addition, we define the following quantities:

$$\varepsilon \alpha_i = \hat{\alpha}_i / \omega_c^2 \quad (i=1,3,4,5,6,7,10,11), \quad \varepsilon \alpha_2 = \hat{\alpha}_2 / \omega_c$$

$$\varepsilon \alpha_8 = \hat{\alpha}_8, \quad \varepsilon \alpha_9 = \hat{\alpha}_9 / \omega_c$$

$$\varepsilon \alpha_i' = \hat{\alpha}_i' / \omega_c^2 \quad (i=1,3,4,5,6), \quad \varepsilon \alpha_2' = \hat{\alpha}_2' / \omega_c$$

$$\varepsilon \beta_i = \hat{\beta}_i / \omega_c^2 \quad (i=1,3,4,5,6,7,8,9), \quad \varepsilon \beta_2 = \hat{\beta}_2 / \omega_c$$

Substituting the above expressions into Eq. (8) and rearranging the resulted equations yields:

$$\left. \begin{aligned}
& \ddot{q}_c + q_c + \varepsilon \alpha_1 q_c q_b + \varepsilon \alpha_2 \dot{q}_c + \varepsilon \alpha_3 q_c^2 + \varepsilon \alpha_4 q_c^3 + \varepsilon \alpha_5 q_c q_b^2 + \varepsilon \alpha_6 q_b + \varepsilon \alpha_7 q_b^2 \\
& + \varepsilon \alpha_8 \ddot{q}_b + \varepsilon \alpha_9 \dot{q}_b + \varepsilon \alpha_{10} q_c'^2 + \varepsilon \alpha_{11} q_c'^2 q_c = 0 \\
& \ddot{q}_c' + \left(\frac{\omega_c'}{\omega_c} \right)^2 q_c' + \varepsilon \alpha_1' q_c' q_c + \varepsilon \alpha_2' \dot{q}_c' + \varepsilon \alpha_3' q_c' q_c^2 + \varepsilon \alpha_4' q_c' q_b + \varepsilon \alpha_5' q_c' q_b^2 + \varepsilon \alpha_6' q_c'^3 = 0 \\
& \ddot{q}_b + \left(\frac{\omega_b}{\omega_c} \right)^2 q_b + \varepsilon \beta_1 q_b q_c + \varepsilon \beta_2 \dot{q}_b + \varepsilon \beta_3 q_b^2 + \varepsilon \beta_4 q_b^3 + \varepsilon \beta_5 q_b q_c^2 + \varepsilon \beta_6 q_c \\
& + \varepsilon \beta_7 q_c^2 + \varepsilon \beta_8 q_c'^2 q_b + \varepsilon \beta_9 q_c'^2 = 0
\end{aligned} \right\} \quad (9)$$

Note that quadratic and cubic terms are involved in Eq. (9). In order to solve Eq. (9), by the multiscale method, we introduce two temporal scales: $T_0 = \tau$ and $T_1 = \varepsilon \tau$ [10]. They represent the fast and slow time scales respectively. Assume the solution of Eq. (9) is:

$$\left\{ \begin{aligned}
q_c(t) &= q_{c1}(T_1, T_2) + \varepsilon q_{c2}(T_1, T_2) \\
q_c'(t) &= q_{c1}'(T_1, T_2) + \varepsilon q_{c2}'(T_1, T_2) \\
q_b(t) &= q_{b1}(T_1, T_2) + \varepsilon q_{b2}(T_1, T_2)
\end{aligned} \right. \quad (10)$$

Substituting Eq. (10) into Eq. (9), the equation of the order of magnitude ε , we can yield the following equations:

$$\left. \begin{aligned}
D_1^2(q_{c1}) + q_{c1} &= 0 \\
D_1^2(q_{c1}') + k_1^2 q_{c1}' &= 0 \\
D_1^2(q_{b1}) + k^2 q_{b1} &= 0
\end{aligned} \right\} \quad (11)$$

$$\left. \begin{aligned}
D_1^2(q_{c2}) + q_{c2} &= -2D_1 D_2(q_{c1}) - \alpha_4 q_{c1}^3 - \alpha_8 D_1^2(q_{b1}) - \alpha_3 q_{c1}^2 - \alpha_1 q_{c1} q_{b1} - \alpha_5 q_{c1} q_{b1}^2 \\
& - \alpha_9 D_1(q_{b1}) - \alpha_2 D_1(q_{c1}) - \alpha_6 q_{b1} - \alpha_7 q_{b1}^2 - \alpha_{10} q_{c1}'^2 - \alpha_{11} q_{c1}'^2 q_{c1} \\
D_1^2(q_{c2}') + k_1^2 q_{c2}' &= -2D_1 D_2(q_{c1}') - \alpha_2' D_1(q_{c1}') - \alpha_1' q_{c1}' q_{c1} - \alpha_3' q_{c1}' q_{c1}^2 - 2\sigma_1 k_1 q_{c1}' \\
& - \alpha_6' q_{c1}'^3 - \alpha_5' q_{c1}' q_{b1}^2 - \alpha_4' q_{c1}' q_{b1} \\
D_1^2(q_{b2}) + k^2 q_{b2} &= -2D_1 D_2(q_{b1}) - \beta_2 D_1(q_{b1}) - \beta_4 q_{b1}^3 - \beta_3 q_{b1}^2 - 2k\sigma q_{b1} - \beta_1 q_{b1} q_{c1} \\
& - \beta_5 q_{b1} q_{c1}^2 - \beta_7 q_{c1}^2 - \beta_6 q_{c1} - \beta_8 q_{c1}'^2 q_{b1} - \beta_9 q_{c1}'^2
\end{aligned} \right\} \quad (12)$$

Solving Eq. (11) gives

$$\left. \begin{aligned} q_{c1} &= A(T_2)e^{iT_1} + cc \\ q'_{c1} &= A'(T_2)e^{ik_1T_1} + cc \\ q_{b1} &= B(T_2)e^{ik_1T_1} + cc \end{aligned} \right\} \quad (13)$$

where “cc” represents the conjugate terms of the preceding terms. Substituting Eq. (13) into Eq. (12) and rearranging the resulted equation, yields:

$$\left. \begin{aligned} D_1^2(q_{c2}) + q_{c2} &= \left(-2i \frac{\partial A(T_2)}{\partial T_2} - 3\alpha_4 A^2 \bar{A} - 2\alpha_5 AB \bar{B} - \alpha_2 iA - 2\alpha_{11} A' \bar{A}' A \right) e^{iT_1} - \alpha_4 A^3 e^{3iT_1} + (k^2 \alpha_8 B - \alpha_9 ikB - \alpha_6 B) e^{ikT_1} \\ &\quad - \alpha_3 A^2 e^{2iT_1} - \alpha_1 AB e^{i(k+1)T_1} - \alpha_1 \bar{A} B e^{i(k-1)T_1} - \alpha_5 A B^2 e^{i(1+2k)T_1} - \alpha_5 \bar{A} B^2 e^{i(1-2k)T_1} - \alpha_7 B^2 e^{2ikT_1} - \alpha_3 A \bar{A} \\ &\quad - \alpha_7 B \bar{B} - \alpha_{10} A' \bar{A}' - \alpha_{10} A'^2 e^{2ik_1T_1} - \alpha_{11} A'^2 A e^{(2k_1+1)T_1} - \alpha_{11} A'^2 \bar{A} e^{(2k_1-1)T_1} + cc \\ D_1^2(q'_{c2}) + k_1^2 q'_{c2} &= \left(-2ik_1 \frac{\partial A'(T_2)}{\partial T_2} - \alpha'_2 ik_1 A' - 2\sigma_1 k_1 A' - 2\alpha'_3 A \bar{A} A' - 3\alpha'_6 A'^2 \bar{A}' - 2\alpha'_5 A' B \bar{B} \right) e^{ik_1T_1} - \alpha'_1 A' A e^{i(k_1+1)T_1} \\ &\quad - \alpha'_1 \bar{A}' A e^{i(1-k_1)T_1} - \alpha'_3 A' A^2 e^{(2+k_1)T_1} - \alpha'_3 \bar{A}' A^2 e^{(2-k_1)T_1} - \alpha'_6 A'^3 e^{3ik_1T_1} - \alpha'_5 A' B^2 e^{i(2k+k_1)T_1} - \alpha'_5 \bar{A}' B^2 e^{i(2k-k_1)T_1} \\ &\quad - \alpha'_4 A' B e^{i(k+k_1)T_1} - \alpha'_4 \bar{A}' B e^{i(k-k_1)T_1} + cc \\ D_1^2(q_{b2}) + k^2 q_{b2} &= \left(-2ik \frac{\partial B(T_2)}{\partial T_2} - \beta_2 ikB - 3\beta_4 B^2 \bar{B} - 2k\sigma B - 2\beta_5 A \bar{A} B - 2\beta_8 A' \bar{A}' B \right) e^{ikT_1} - \beta_4 B^3 e^{3ikT_1} - \beta_3 B^2 e^{2ikT_1} \\ &\quad - \beta_1 AB e^{i(k+1)T_1} - \beta_1 \bar{A} B e^{i(1-k)T_1} - \beta_5 A^2 B e^{i(2+k)T_1} - \beta_5 \bar{A}^2 B e^{i(k-2)T_1} - \beta_7 A^2 e^{2iT_1} - \beta_6 A e^{iT_1} - \beta_3 B \bar{B} \\ &\quad - \beta_7 A \bar{A} - \beta_8 A'^2 B e^{i(2k_1+k)T_1} - \beta_8 A'^2 \bar{B} e^{i(2k_1-k)T_1} - \beta_9 A'^2 e^{2ik_1T_1} - A \bar{A}' + cc \end{aligned} \right\} \quad (14)$$

2.2.3. Nonsteady solution and energy conservation relation

Noting that Eq. (14) involves many internal resonances, now we only consider the one: $k = 2$ and $k_1 = 1$. Eliminate the secular terms and express the solution as follows:

$$\left. \begin{aligned} A &= a e^{i\varphi_1} / 2 \\ A' &= a' e^{i\varphi'_1} / 2 \\ B &= b e^{i\varphi_2} / 2 \end{aligned} \right\} \quad (15)$$

Substituting Eq. (15) into Eq. (14) and separating the real and imaginary parts, we obtain the following average equations:

$$\left. \begin{aligned} \frac{\partial a}{\partial T_2} &= -\frac{1}{2} \alpha_2 a - \frac{1}{4} \alpha_1 ab \sin(\varphi_2 - 2\varphi_1) - \frac{1}{8} \alpha_{11} a'^2 a \sin(2\varphi'_1 - 2\varphi_1) \\ a \frac{\partial \varphi_1}{\partial T_2} &= \frac{3}{8} \alpha_4 a^3 + \frac{1}{4} \alpha_5 ab^2 + \frac{1}{4} \alpha_1 ab \cos(\varphi_2 - 2\varphi_1) + \frac{1}{8} \alpha_{11} a'^2 a \cos(2\varphi'_1 - 2\varphi_1) \\ \frac{\partial a'}{\partial T_2} &= -\frac{1}{2} \alpha'_2 a' - \frac{1}{8} \alpha'_3 a' a^2 \sin(2\varphi_1 - 2\varphi'_1) - \frac{1}{4} \alpha'_4 a' b \sin(\varphi_2 - 2\varphi'_1) \\ a' \frac{\partial \varphi'_1}{\partial T_2} &= \sigma_1 a' + \frac{1}{4} \alpha'_3 a'^2 a' + \frac{3}{8} \alpha'_6 a'^3 + \frac{1}{4} \alpha'_5 b^2 a' + \frac{1}{8} \alpha'_3 a'^2 a' \cos(2\varphi_1 - 2\varphi'_1) + \frac{1}{4} \alpha'_4 b a' \cos(\varphi_2 - 2\varphi'_1) \\ \frac{\partial b}{\partial T_2} &= -\frac{1}{2} \beta_2 b + \frac{1}{8} \beta_7 a^2 \sin(\varphi_2 - 2\varphi_1) + \frac{1}{8} \beta_9 a'^2 \sin(\varphi_2 - 2\varphi'_1) \\ b \frac{\partial \varphi_2}{\partial T_2} &= \frac{3}{16} \beta_4 b^3 + \frac{1}{8} \beta_5 a^2 b + \frac{1}{8} \beta_7 a^2 \cos(\varphi_2 - 2\varphi_1) + \sigma b + \frac{1}{8} \beta_8 a'^2 b + \frac{1}{8} \beta_9 a'^2 \cos(\varphi_2 - 2\varphi'_1) \end{aligned} \right\} \quad (16)$$

By introducing the new phase variables $\psi = \varphi_2 - 2\varphi_1$ and $\psi_1 = \varphi_2 - 2\varphi'_1$, we have

$$2\varphi_1 - 2\varphi'_1 = \psi_1 - \psi \quad (17)$$

If the damping effect is neglected, by setting $\alpha_2 = \alpha'_2 = \beta_2 = 0$, multiplying $\frac{\beta_7}{2\alpha_1} a$, $\frac{\beta_9}{2\alpha'_1} a'$ and b on both sides of the first, third and fifth equation respectively in Eq. (16) and adding them together, yields:

$$\frac{\beta_7}{2\alpha_1} a \frac{\partial a}{\partial T_2} + \frac{\beta_9}{2\alpha'_4} a' \frac{\partial a'}{\partial T_2} + b \frac{\partial b}{\partial T_2} = \frac{1}{16} \left(\frac{\beta_9}{\alpha'_4} \alpha'_3 - \frac{\beta_7}{\alpha_1} \alpha_{11} \right) a'^2 a^2 \sin(\psi - \psi_1) \quad (18)$$

The analysis of the coefficients β_9 、 α'_4 、 α'_3 、 β_7 、 α_1 、 α_{11} in the above equation gives

$$\frac{\beta_9}{\alpha'_4} \alpha'_3 - \frac{\beta_7}{\alpha_1} \alpha_{11} = 0$$

Therefore

$$\frac{\beta_7}{2\alpha_1} a \frac{\partial a}{\partial T_2} + \frac{\beta_9}{2\alpha'_4} a' \frac{\partial a'}{\partial T_2} + b \frac{\partial b}{\partial T_2} = 0$$

Integrating the above equation leads to the following energy conservation relation:

$$\frac{\beta_7}{2\alpha_1} a^2 + \frac{\beta_9}{2\alpha'_4} a'^2 + b^2 = E = \text{const} \quad (19)$$

From Eq. (19), it is obviously that:

- (1) when $\frac{\beta_7}{\alpha_1} > 0$ and $\frac{\beta_9}{\alpha'_4} > 0$, the energy level set is a elliptic surface in the space (a, a', b) .
- (2) when $\frac{\beta_7}{\alpha_1} < 0$ and $\frac{\beta_9}{\alpha'_4} < 0$, the energy level set is a hyperboloid of one sheet in the space (a, a', b) .
- (3) when $\frac{\beta_7}{\alpha_1} < 0$ and $\frac{\beta_9}{\alpha'_4} < 0$, the energy level set is a hyperboloid of two sheet in the space (a, a', b) .

2. 3 Numerical simulation and analysis

The cable parameters presented in Ref. [3] is considered and documented in Table1. The beam parameters are listed in Table2.

Table1 The basic parameters of the inclined cable

Dip angle (deg)	Length (m)	Area (cm ²)	Initial tension (N)	Mass (Kg/m)	Elastic modulus (GPa)
60	110.5	82.6	4.9	64.8	210

Table 2 The basic parameters of the beam

Length (m)	Mass (Kg/m)	Elastic modulus (GPa)	Moment of inertia (m ⁴)
55.25	4×10 ⁴	200	2.4

Assume the modal function of the cable is $\varphi_c(x) = \varphi'_c(x) = \sin(\pi x/L)$. Adjust the beam stiffness, so that the frequency ratio of the cable in-plane, out-of-plane and beam vibrations satisfies $\omega_c : \omega'_c : \omega_b = 1 : 0.9993 : 2$. If neglecting the damping effect, the sub-harmonic resonance may occur in the cable-beam coupling system. Assuming that the cable has an initial in-plane perturbation $q_c(0) = 0.001m$, and there being no out-of-plane perturbation, the initial disturbance of the beam is $q_b(0) = 0.1m$. The Runge-Kutta method is employed to solve the governing equations of the cable-beam coupling system. The numerical results show that the cable has no out-of-plane vibrations. The time response curves for the vibration at the right end of the beam and the mid-point on the in-plane of the cable is illustrated in Fig. 2 and Fig. 3, respectively. If keeping the above initial perturbations and giving the cable an out-of-plane initial disturbance $q'_c(0) = 0.001m$, the numerical results show that a large out-of-plane vibration for the cable occurs. The time response curves for the vibration at the right end of the beam, the in-plane and out-of-plane vibrations of the cable are displayed in Figs. (4)-(6), respectively.

The analysis of the time response curves shows that the vibrations of the cable and beam demonstrate the beat vibration phenomenon, that is, the amplitude varies periodically with respect to the time and the peak values of the displacement go up and down alternatively. The comparison between Fig. 3, Fig. 5 and Fig. 6 shows that the cable has large in-plane and out-of-plane vibrations, and the maximum amplitude of these

vibrations is much larger than their initial perturbations. It is also found that when the out-of-plane vibration is greatly excited, the corresponding in-plane vibration declines, which shows that the energy transfers from the in-plane vibration to the out-of-plane one. In a word, the comparison among Fig. 4, Fig. 5 and Fig. 6 (or between Fig. 2 and Fig. 3) shows that the vibration energy transfers from one type of vibration to another in the three-freedom system (or two-freedom system). In fact the similar result has been reported in Refs.[4-7] for two-freedom systems, while our result is obtained for the three-freedom case. Since the damping has been neglected, the system energy is conservative. This result coincides with the theoretical result obtained in Section 2.3.

In addition, from the time response curves of the cable and beam, one can see that the vibration amplitude of the beam has no significant variations when the time elapses. While the amplitude of the cable vibration experiences large variation, the maximum amplitude can reach 1.8m. This is because the mass of the beam is far greater than that of the cable. From the energy conservation relation Eq. (19), it is not difficult to see that the maximum amplitude of the beam is far less than that of the cable. From the theoretical analysis and the numerical result, it is found that the in-plane vibration frequency of the cable is very close to the out-of-plane one. When the cable has a strong amplitude vibration, the in-plane and out-of-plane vibrations are intercoupling. Therefore, under appropriate nonlinear coupling conditions, the internal resonance may occur. Many cable systems in the practical engineering are difficult to avoid the internal resonance. Furthermore the dynamic equation of the cable involves the strong coupling parametric vibrations. In practice, the coupling motion of the in-plane and out-of-plane vibrations is also called “air ring motion” or “sand ring motion”.

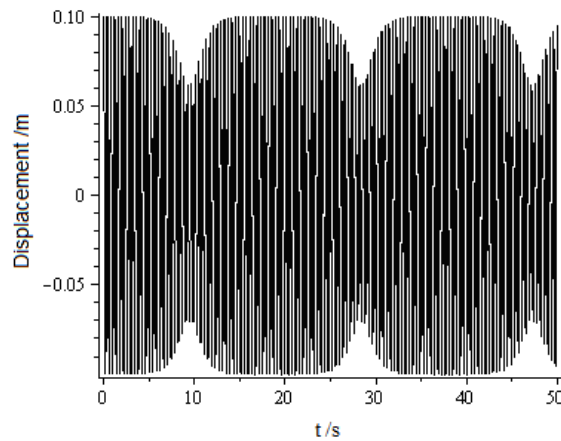


Fig.2 The time response curve for the parametric resonance at the right end of the beam

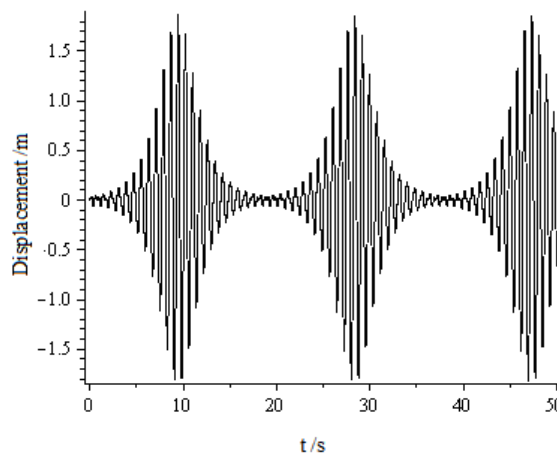


Fig. 3 The time response curve for the parametric resonance at the central-point of the in-plane of the cable

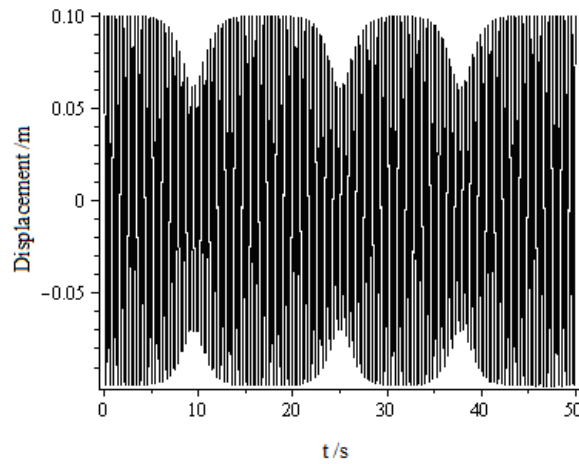


Fig. 4 The time response curve for the parametric resonance at the right end of the beam

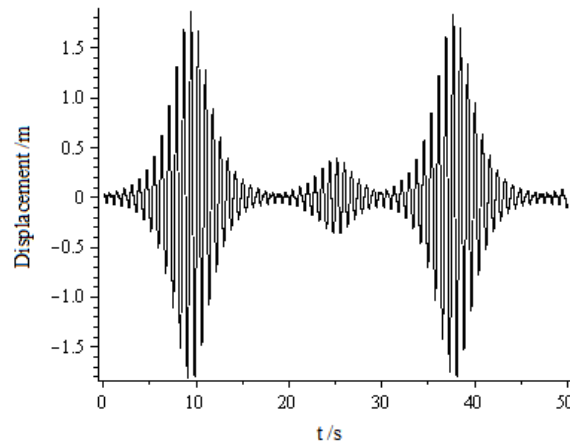


Fig. 5 The time response curve for the parametric resonance at the mid-point on the in-plane of the cable

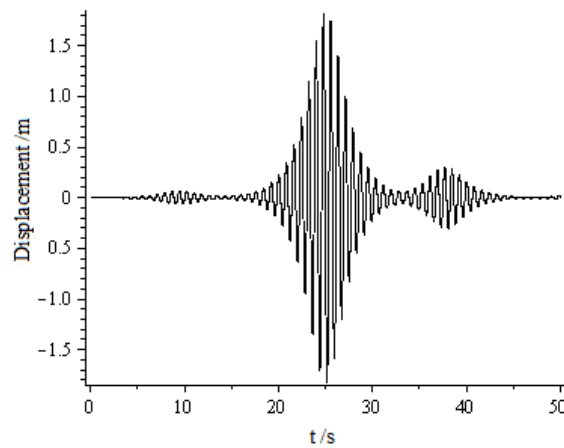


Fig. 6 The time response curve for the parametric resonance at the mid-point on the in-plane of the cable

3 CONCLUSIONS

By the theoretical analysis and numerical simulation of nonlinear parametric vibrations of the cable-beam coupling system, we conclude that:

1. The governing equation for the three dimensional nonlinear free vibration of the cable-beam coupling structure is established. The multi-scale method is employed to analytically search for the approximate solution. The average equations are obtained. And the energy conservative relation is proved theoretically.
2. The Runge-Kutta method is applied to simulate the differential equations describing the vibration of the coupling system. The numerical results show that when the ratio of the cable in-plane, out-of-plane and beam

vibration frequencies is equal to 1:0.9993:2, the parametric resonance may occur in the coupling system.

3. The vibration energy periodically transfers alternatively among different types of vibrations in the three dimensional space. When the damping is neglected, the vibration energy satisfies the conservative relation.

ACKNOWLEDGEMENTS

The support for our research by the National Natural Science Foundation of China (Grant No. 10372039) is greatly appreciated.

4 REFERENCES

- [1] F. Benedettini, G. Rega, F. Vestroni, Modal coupling in the free nonplanar finite motion of an elastic cable, *Meccanica* 21 (1986) 38-46.
- [2] A. Luongo, G. Rega, F. Vestroni, On large-amplitude vibrations of cable, *Journal of Sound and Vibration*, 116 (3) (1987) 573-575.
- [3] J.L.Lilien, A. Pinto Da Costa, Vibration amplitudes caused by parametric excitations of cable-stayed structures, *Journal of Sound and Vibration*, 174(2) (1994) 69-90.
- [4] Z.Kang, W. X. Zhong, Numerical study of parametric resonances of the stayed-bridge, *China Civil Engineering Journal* 31(4)(1998) 14-22. (In Chinese)
- [5] Vincenzo Gattulli, Marco Lepidi. Nonlinear interactions in the planar dynamics of cable-stayed beam [J]. *International Journal of Solids and Structures*, (40) (2003) 4729-4748.
- [6] C. C. Guo, B. Wang, H. B. Zhang, Parametric vibration of cable-tower-beam coupling structure, *Central South Highway Engineering* 35 (3) (2010)52-57. (In Chinese)
- [7] W. M. Feng, Y. X. Sun, The analysis of the nonlinear dynamic for cable-beam coupling system under the complete parametric excitation [J]. *Journal of Mechanical Engineering* (in China), 2009,45 (9): 19-23. (In Chinese)
- [8] H. M. Irvine, *Cable structures*, The Mit Press, London, 1981.
- [9] G. Tagata, Harmonically Forced, finite amplitude vibration of a string, *Journal of Sound and Vibration*, 51(4)(1977) 483-492.
- [10] H. Y. Hu, *Applying nonlinear dynamics*. Aeronautical Industry Press, Beijing, 2000. (In Chinese)

STABILITY AND REINFORCEMENT OF GUARDRAIL POST IN CENTRAL SEPARATE BELT OF EXPRESSWAYS BASED ON MCPT

Q. Jin, X. Z. Cui, Y. X. Zhou, W. Sui and Z. J. Gao

Shandong University, School of Civil Engineering, Jinan, China

Abstract: A series of laterally loading tests of guardrail posts of highway are carried out. The linear relation is found between the critical load representing lateral bearing capacity of posts and the limit cone tip resistance of the miniature penetrometer representing soil strength in the miniature cone penetration test (MCPT). Based on MCPT, a model of soil reaction distribution corresponding to the critical load is put forward and the unknown parameter in model is calculated inversely by test data. An effective method of using one steel plate to reinforce the post is presented and verified by tests.

Keywords: Stability, Guardrail Posts Of Highway, Bearing Capacity

1 INTRODUCTION

In China, with the rapid development of the expressway, traffic accidents happen frequently. However, many accidents can be avoided or mitigated with guardrails and other security facilities. However, there are no clear prescriptions to the compaction degree of subsoil around guardrail posts in the current expressway safety specification of China. Fig.1 shows the cross section diagram of the central separate belt of the expressway. The planting soil and the backfilled soil are too weak to meet the bearing capacity requirement of guardrail posts. Due to the low energy-dissipation capacity of guardrail posts, heavy vehicles out of control can penetrate or override the guardrail to the opposite lane, causing more traffic accidents, and the unbent guardrail posts may destroy communication lines. It is very necessary to analyze the stability of guardrail post under lateral load and put forward the reinforcement method.

The performance of guardrail is related closely to soil. Calcote and Kimball (1978) carried out pendulum tests on two guardrail posts installed in five different soil types and found that guardrail installations less than the recommended minimum length failed with severe impacts when installed in the poorer soils. Numerical methods are employed to study the interaction between the guardrail post and soil (Rohde et al. 1996; Plaxico et al. 1998; Wu and Thomson 2007). Rohde et al. (1996) demonstrated the differences in the failure mechanisms of post between stiff and soft cohesive soils and noncohesive soils by both stress distributions and total stresses measured with the pressure transducers.

In this paper, the miniature cone penetration test (MCPT) is used to characterize the post subsoil strength, and the experimental relation of the lateral bearing capacity of the guardrail post with the limit cone tip resistance of subsoil in MCPT is obtained. The model of soil reaction distribution on the post was presented and the reaction distribution coefficient in the model was obtained based on MCPT. According to the model, the reinforcement method of the post in weak subsoil was put forward.

2 MINIATURE CONE PENETRATION TESTS OF SUBSOIL

Subsoil for test was silty clay and was from the subgrade of the 4th Ring Road of Beijing. Water content of soil ranged from 9.85% to 13.85%. In order to obtain different strength of soil for tests, the compaction degrees were controlled from 79.1% to 97.7%. Before each loading test of post, MCPTs were performed to characterize the strength of soil. The Miniature cone penetrometer used is shown in Fig.2. Fig.3 shows the shape of the cone. In MCPTs, four kinds of cones were used. Though their maximum diameter were all 14mm, they had different cone angle, 19.85°, 22.62°, 26.03° and 31.28°, respectively. The diameter of the cone shaft was 7.3mm. Because cone shaft diameter is less than the diameter of cone, the frictional resistance of cone shaft was ignored and only the cone tip resistance was considered as the cone penetration resistance.

The cone tip resistance tends to be stable when attending to a critical depth, as shown in Fig.4. The stable cone tip resistance herein is called as limit cone tip resistance q_{cl} . It was also found that the cone tip resistance has no correlation with the cone angle. In test, the limit cone tip resistance q_{cl} is the average value

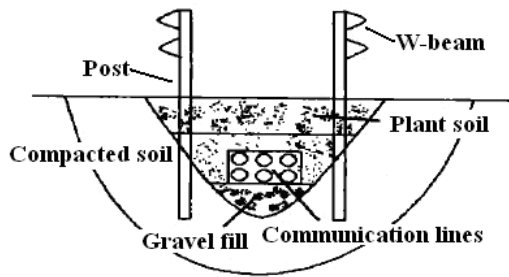


Fig.1. Diagram of central separate belt.



Fig. 2. Miniature cone penetrometer.

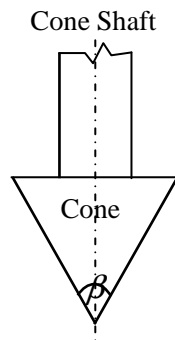


Fig. 3. Shape of the cone.

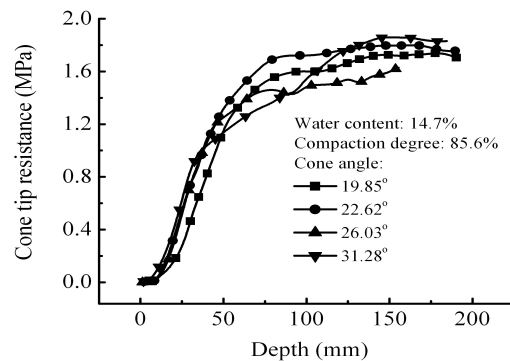


Fig. 4. Curves of penetration resistance vs. Depth.

3 LATERAL LOADING TESTS OF GUARDRAIL POSTS

In tests, the post was embedded in a test chamber. The chamber is 1.73 m in width, 1.86 m in length and 1.25 m in depth. The diameter of the post is 114mm and the wall thickness is 4mm, respectively. The embedding depth of the post is 1.2m. The height of loading point on post is 0.6m, the same as the height of W-beam shown in Fig.1. In each test, only one post was loaded, as shown in Fig.5.

Fig.6 shows the curves of the lateral load vs. the horizontal displacement of loading point. The limit cone tip resistances of subsoil corresponding to the curve No.1, No.2 and No.3 in Fig.6 were 1.17 MPa, 2.03 MPa and 2.27 MPa, respectively. The behavior of the post under lateral load depends on the strength of subsoil. When the soil is soft, the post is not bent and behaves as the rigid pile, as the curve No.1. When the soil is harder, the local buckling of the post happens and the lateral load descends sharply when the horizontal displacement attends a certain value. Under the impacting load of the vehicle out of control, the post is bent to absorb energy. The bent posts behave as curves No.2 and No.3. From curves No.2, No.3 and other curves of bent posts, some laws can be seen.

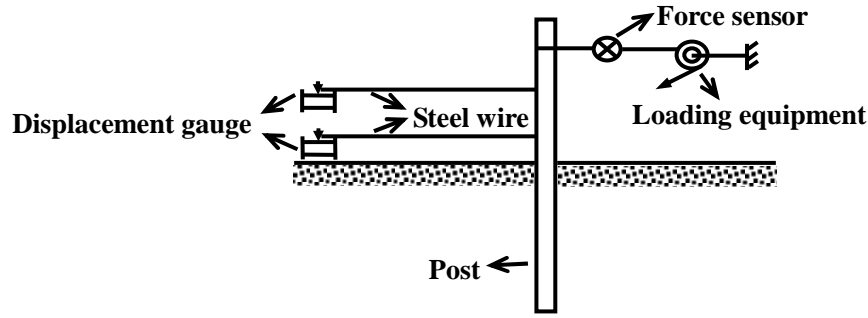


Fig. 5. Layout diagram of test equipments of post.

(1) The initial segment of the load-displacement curve is straight line. However, with the increase of the displacement, the lateral load increases nonlinearly, and then the second straight line segment appears on the curve. Once the local buckling happens, the lateral load will decrease sharply.

(2) The load at the intersection point of the extension lines of two straight line segments on the load-displacement curve is called as critical load P_{cr} . When the lateral load is less than P_{cr} , the subsoil around the post is linear elastic. The maximum load on the curve is called as buckling load P_b . P_{cr} and P_b both increase with the increase of the strength of soil. After carrying out a series of loading tests of posts, the following equations were obtained:

$$P_{cr} = 0.0038 q_{cl} . \quad (1)$$

$$P_b = 0.0092 q_{cl} . \quad (2)$$

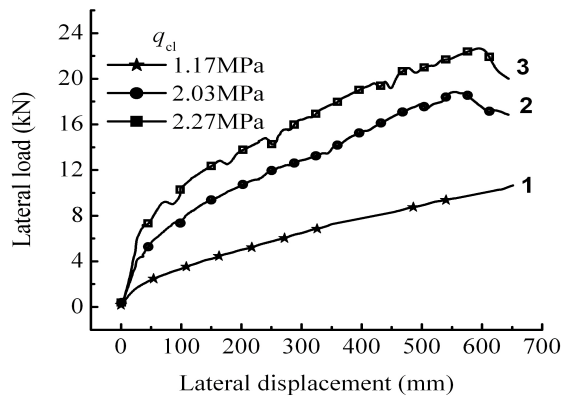


Fig. 6. Curve of load vs. displacement of loading point.

4 MODEL OF SOIL REACTION DISTRIBUTION ON POST

In order to guarantee the safety margin of the post, the critical load P_{cr} is taken as the allowable load. From Eq. 1 and Eq. 2, it can be seen that P_b is 2.42 times of P_{cr} , so the safety factor of post is 2.42.

Based on the MCPTs, assuming the soil reaction on post is in direct proportion to the limit cone tip resistance, a model of soil reaction distribution is presented corresponding to P_{cr} , as shown in Fig. 7. In Fig. 7, B and l are the diameter and the embedding depth of post, respectively; h is the height of the loading point on the post; f is the depth of the maximum moment point on the post; H is the distance of rotation center from the bottom of the post; α is the coefficient of the soil reaction and dimensionless. Before the buckling failure of post, the post rotates around the rotation center point that moves along the post with the increase of the loading. In Fig. 7, above the rotation center point, the right side and left side of post are subject to the passive and active soil pressure, respectively. However, this is contrary under the rotation center point. Herein assume that the total soil pressure at any point of post is not related to the depth. According to loading tests of posts, the coefficient of the soil reaction α was obtained by back calculation.

(1) At the maximum bending moment point on the post, the shear force is zero, so

$$-p_{cr} + \alpha q_{cl} B f = 0. \quad (3)$$

$$f = \frac{p_{cr}}{\alpha q_{cl} B}. \quad (4)$$

(2) According to the equilibrium of the lateral forces on the post, the following equations can be obtained:

$$P_{cr} - \alpha q_{cl} B l + 2 \alpha B H q_{cl} = 0. \quad (5)$$

$$H = \frac{\alpha q_{cl} B l - P_{cr}}{2 \alpha B q_{cl}} = \frac{1}{2} (l - f). \quad (6)$$

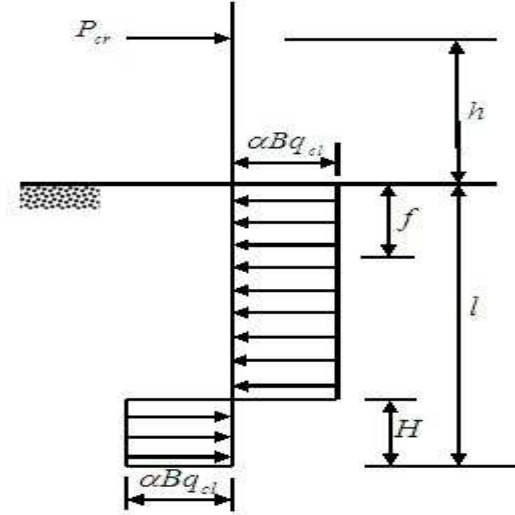


Fig. 7. Model of soil reaction distribution on post.

(3) According to the equilibrium of the force moment, the following equations can be obtained:

$$p_{cr} (l + h) - \frac{\alpha q_{cl} B l^2}{2} + \alpha q_{cl} B H^2 = 0. \quad (7)$$

From Eq.4, Eq.6 and Eq.7, we can obtain

$$p_{cr} = \alpha B^2 q_{cl} \left\{ \sqrt{\left[\left(\frac{l}{B} \right) + 2 \left(\frac{h}{B} \right) \right]^2 + \left(\frac{l}{B} \right)^2} - \left[\left(\frac{l}{B} \right) + 2 \left(\frac{h}{B} \right) \right] \right\}. \quad (8)$$

For the post, $l = 1.2\text{m}$, $h = 0.6\text{m}$, $B = 0.114\text{m}$,

$$p_{cr} = 0.0323 \alpha q_{cl}. \quad (9)$$

From Eq.1 and Eq.9, we can obtain $\alpha = 0.118$. According to Eq. 4 and Eq. 6, $f = 0.283\text{m}$, $H = 0.458\text{m}$. By comparison, it is found that the difference of the measured and calculated results is less than 5% for f and 1% for H .

5 REINFORCEMENT METHOD OF POST

In order to reinforce the post, a rectangular steel plate was vertically inserted to subsoil, touching closely with the post side opposite to the lane. The plate has an included angle of 15° with the lane direction, as shown in Fig.8. The thickness of the plate is 10mm and the height t is taken as 0.618 times of the width b according to

golden section rule. The anticorrosion requirement of the plate is the same as the post.

In the central separate belt of the expressway, the subsoil is different. The upper is the plant soil and the lower is the compacted soil, as shown in Fig.1. The limit cone tip resistances of the upper and the lower subsoil are expressed with q_{cl1} and q_{cl2} , respectively. Similar with the model shown in Fig.7, the soil reaction is assumed to be in direct proportion to the limit cone tip resistance and the effective width of post. In the range of the plate height under ground, the effective width of the post is the width of the plate, however, elsewhere is the diameter of the post. The proportional coefficient of soil reaction α is invariable and equal to 0.118. The model of soil reaction distribution on the reinforced post is as shown in Fig.9.

For compacted soil in the roadbed, the design compaction degree is 96% and the moisture content is optimum in China. For the silty clay used in tests, the limit cone tip resistance of the compacted silty clay is 2.27MPa and the corresponding critical load of post embedding totally in the compacted soil is 8656.2N according to Eq. 1. So in the Fig.9, $q_{cl2} = 2.27\text{MPa}$ and the object of reinforcement of the post embedding partly in the plant soil is that the critical load attends to 8656.2N and is equivalent to the case of $q_{cl1} = q_{cl2} = 2.27\text{MPa}$.

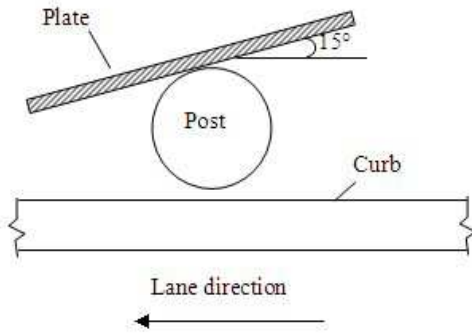


Fig. 8. Planeform of reinforced post.

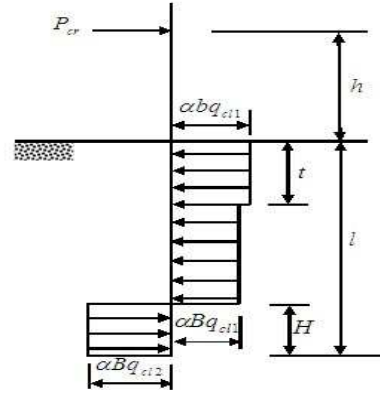


Fig. 9. Soil reaction distribution model of reinforced post.

According to the model shown in Fig.9, the dimension of steel plate corresponding to different strength of plant soil can be determined.

(1) According to the equilibrium of the lateral forces on the post, we obtain

$$P_{cr} - \alpha q_{cl1} B l + \alpha B H (q_{cl1} + q_{cl2}) - \alpha q_{cl1} (b - B) t = 0. \quad (10)$$

$$H = \frac{\alpha q_{cl1} B l + \alpha q_{cl1} (b - B) t - P_{cr}}{\alpha B (q_{cl1} + q_{cl2})}. \quad (11)$$

(2) According to the equilibrium of the force moment, the following equations can be obtained:

$$P_{cr} (l + h) - \frac{\alpha q_{cl1} B l^2}{2} + \frac{\alpha B (q_{cl1} + q_{cl2}) H^2}{2} - \frac{\alpha q_{cl1} (b - B) (2l - t) t}{2} = 0. \quad (12)$$

From Eq.11 and Eq.12, the relation between q_{cl1} and the dimension of the plate is obtained

$$q_{cl1} = \frac{-\Delta_2 - \sqrt{\Delta_2^2 - 4\Delta_1\Delta_3}}{2\Delta_1}. \quad (13)$$

Where: $\Delta_1 = \alpha^2 b (b - B) t^2$; $\Delta_2 = 2\alpha B h p_{cr} - (\alpha B l)^2 q_{cl2} - 2\alpha (b - B) t p_{cr} - \alpha^2 B (b - B) (2l - t) t q_{cl2}$;

and $\Delta_3 = 2\alpha B (l + h) p_{cr} q_{cl2} + p_{cr}^2$.

In Eq.13, $t = 0.618b$, $\alpha = 0.118$, $q_{cl2} = 2.27 \text{ MPa}$, $p_{cr} = 8656.2 \text{ N}$, $B = 0.114 \text{ m}$, $h = 0.6 \text{ m}$,

$l = 1.2$ m. The relation of the width of the plate with the limit cone tip resistance of the plant soil is shown in Fig.10.

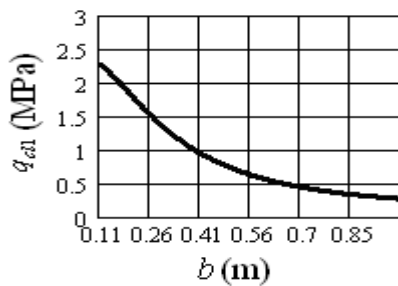


Fig. 10. Curve of q_{cl1} with b .

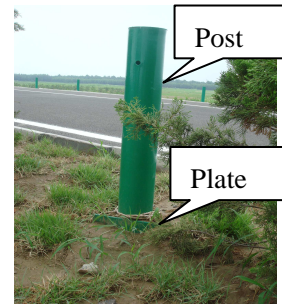


Fig. 11. Picture of reinforced post.

6 VERIFICATION OF REINFORCEMENT METHOD OF POST

In order to verify the reinforcement method, a laterally loading test of post was carried out. In test, the upper subsoil is the plant soil, with the thickness of 0.75m and $q_{cl1} = 1.3$ MPa. The lower subsoil is the compacted soil, with the thickness of 0.45m and $q_{cl2} = 2.24$ MPa ≈ 2.27 MPa. The dimension of the plate is from Fig.10, $b=310$ mm and $t=192$ mm. In verification test, the critical load of 9500N was obtained, more than the design load of 8656.2N. It is implied that the reinforcement method can satisfy the engineering requirement.

Now this reinforcement method has been applied to guardrail posts of some expressways of China, e.g., Rongwu expressway, as shown in Fig.11.

7 CONCLUSIONS

Laterally loading tests of the guardrail post in the central separate belt of the expressway were carried out. The subsoil around the post is silty clay. In order to reflect the strength of subsoil, the parallel MCPTs were performed. In MCPT, when the penetration depth of cone attends a critical depth, the cone tip resistance tends to a limit resistance. For the post embedding totally in the compacted soil, there are two characteristic loads – the critical load and the buckling load. The critical load reflects the elastic or plastic state of soil and the buckling load reflects the anti-buckling capacity of the post. The critical load and buckling load are all related directly to the cone limit penetration resistance. Based on the limit cone tip resistance, a model of soil reaction distribution on the post embedding totally in the compacted soil was presented. The coefficient of the soil reaction was obtained by back calculation.

A steel-plate reinforcement method of the post embedding partly in plant soil was put forward. Based on the model of soil reaction distribution, the dimension of the reinforcing plate was determined. The reinforcement method was verified and found to satisfy the requirement of bearing capacity of the post.

8 ACKNOWLEDGMENTS

This work was supported by the Chinese Natural Science Foundations (Nos.51078222, 50708056 and 50978207), Shandong Province Reward Foundation for Excellent Young and Middle-aged Scientists(No.2008BS09015) and Independent Innovation Foundation of Shandong University, IIFSDU(No.2010JQ001).

9 REFERENCES

- [1] L. R. Calcote, C. E. Kimball, Properties of guardrail posts for various soil types, Transportation Research Record, 679, 22-25, 1978.
- [2] C. A. Plaxico, G. S. Patzner, M. H. Ray, Finite-element modeling of guardrail timber posts and the post-soil interaction, 1647, 139-146, 1998.
- [3] J. R. Rohde, B. T. Rosson, R. Smith, Instrumentation for determination of guardrail-soil interaction, Transportation Research Record, 1528, 109-115, 1996.
- [4] W. J. Wu, R. Thomson, Finite-element modeling of guardrail timber posts and the post-soil interaction. International Journal of Impact Engineering, 34(5), 883-898, 2007.
- [5] A. E. Wright, M. H. Ray, Characterizing guardrail steel for LS-DYNA3D simulations, Transportation Research Record, 1528, 138-145, 1996.

THERMAL ANALYSIS OF TWO-DIMENSIONAL TEMPERATURE-DEPENDENT FUNCTIONALLY GRADED OPEN CYLINDRICAL SHELLS

B. Sobhani Aragh¹ and M. Abdel wahab²

¹Mechanical Engineering Department, Razi University, 67346-67149, Kermanshah, Iran

² Department of Mechanical Construction and Production, Faculty of Engineering, Ghent University, B-9000 Gent, Belgium

Abstract: Based on third-order shear deformation plate theory, this paper presents thermo-elastic response of a 2-D Functionally Graded Open Cylindrical Shell (2-D FGM OCS) with temperature-dependent material properties. The material properties of 2-D FGM OCS are assumed to be graded in radial and axial directions simultaneously according to a brand-new 2-D power-law distribution. Using this power-law distribution, it is possible to consider various kinds of two directional volume fraction profiles including sigmoidal radial variation as well as symmetrical or classical variation in axial direction. The nonlinear steady-state heat conduction equation is solved using an iterative solution procedure along with Generalized Differential Quadrature Method (GDQM). It is found that calculations and design based on temperature-independent properties yield conservative predictions.

Keywords: 2-D Functionally Graded Materials; Temperature-Dependent; Sigmoidal Radial Variation; 2-D Power-Law Distribution; Third-Order Shear Deformation Plate Theory.

1. INTRODUCTION

Functionally Graded Materials (FGMs) are advanced multiphase composites, engineered to have a smooth spatial variation of material constituents and have attracted considerable attention in recent years [1]. In most recent literature regarding FGM structures [2-3], the material properties are assumed having a smooth variation usually in one direction. A conventional FGM may also not be so effective in the design of the advanced machine elements, whose all one surface will have the same composition distribution. This is because temperature distribution in such advanced machine elements that are used in several applications such as space shuttles, nuclear reactors, aircrafts, ovens, combustion chambers, etc., changes in two or three directions. Therefore, if the FGM has two-dimensional dependent material properties, more effective high-temperature resistant material can be obtained. Nemat-Alla [4] introduced the concept of adding a third material constituent to the conventional FGM to withstand the induced severe thermal stresses. The rules of mixture for the introduced 2-D FGM were used to calculate the effective material properties of SiC/Al1100/Ti-6Al-4V 2-D FGM plate, with temperature-independent material properties. They found that it is possible to reduce the magnitude of thermal stresses by a proper management of the material properties in two directions. Asgari and Akhlaghi [5] investigated the transient thermal stresses in a 2-D FGM thick hollow cylinder with finite length based on the classical thermoelasticity theory. The proposed 2-D FGM model was made of four distinct materials consisting of two distinct ceramics on the inner surface and two metals on the outer surface. This work proposes a new 2-D power-law distribution for volume fractions of 2-D FGM that gives designers a powerful tool for flexible design of structures under multi-functional requirements. Various material profiles in two radial and axial directions can be illustrated using the 2-D power-law distribution. In fact, using the 2-D power-law distribution, it is possible to study the impact of the various kinds of two directional material profiles including sigmoidal radial variation as well as symmetrical or classical variation in axial direction on the temperature field and thermal stresses of OCS. Furthermore, distribution and magnitude of thermal stresses can be modified and reduced to a required level by selecting appropriate different parameters of power-law distribution and volume fractions profiles in two directions. In addition, this model allows ceramic volume fraction of conventional 1-D FGM to have a sigmoidal radial variation, as a special case of 2-D power-law distribution. The volume fraction of the ceramic phase approaches a discretely laminated composite with a sharp transition in contained quantity of ceramic at the mid-surface by increasing sigmoid exponent. In contrast to models introduced in [4-6], this novel model is capable of being employed in the different prediction methods of effective material properties. In this paper, Mori-Tanaka [7] scheme as an accurate micromechanics model is used for estimating the homogenized material properties of metal-ceramic composite materials.

2. THEORETICAL FORMULATION

2.1 2-D FGM constitute law

Let us consider a 2-D FGM OCS of length L , mean radius Z_m , uniform thickness h , as shown in Fig. 1. An orthogonal cylindrical coordinate system (x, θ, z) is used to label the material point of the shell in the unstressed reference configuration. In 2-D FGMs, the material properties are continuous functions of the coordinates and the volume fractions of the constituents vary in a predetermined composition profile. Now consider a two-phase graded material with a power-law variation of the volume fraction of the constituents through the radial and axial directions, it is proposed that the volume fraction of the ceramic phase follows 2-D power-law distribution:

$$V_c = \left((V_b - V_a) \left(\frac{e^{s((z/h)+0.5)} - 1}{(e^{s/2} - 1)(e^{s(z/h)} + 1)} \right) - V_a \right)^{\gamma_z} \left(1 - \frac{x}{L} + \alpha_x \left(\frac{x}{L} \right)^{\beta_x} \right)^{\gamma_x} \quad (1)$$

where the sigmoid exponent s , radial volume fraction index γ_z , the parameters α_x , β_x and axial volume fraction index γ_x govern the material variation profile through the radial and axial directions, respectively. The volume fractions V_a and V_b , which have values that range from 0 to 1, denote the ceramic volume fractions of the two different isotropic material. For example, with assumption $V_b = 1$ and $V_a = 0.3$, some material profiles through the radial ($\eta_z = z/h$) and axial ($\eta_x = x/L$) directions are illustrated in Fig. 2.

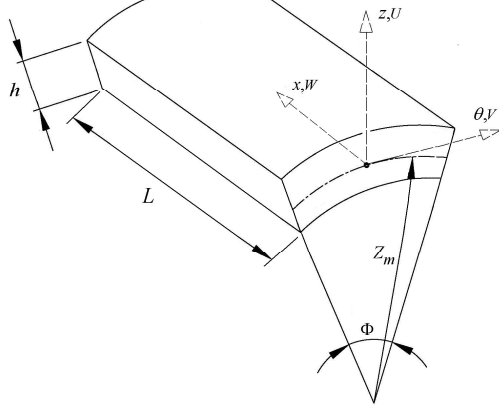


Fig. 1. Geometry of 2-D FGM OCS.

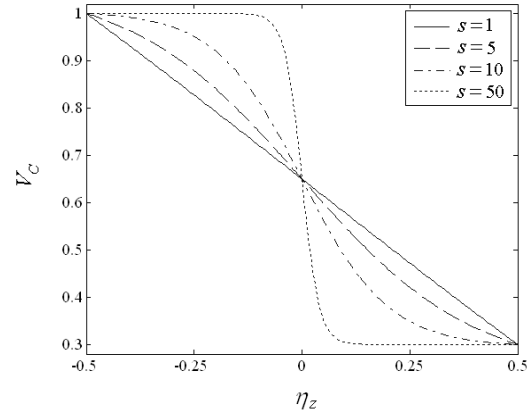


Fig. 2. Sigmoidal radial variation of ceramic volume fraction for 1-D FGM corresponding to different sigmoid exponents ($\gamma_z = 1$, $\gamma_x = 0$)

2.2 Temperature-dependent material properties

A typical temperature-dependent material property P , such as the modulus of elasticity E , the thermal conductivity k and the coefficient of thermal expansion α can be expressed as non-linear functions of temperature T (K) as [8],

$$P = P_0 (P_{-1} T^{-1} + 1 + P_1 T + P_2 T^2 + P_3 T^3) \quad (2)$$

where P_0 , P_{-1} , P_1 , P_2 and P_3 are constants in the cubic fit of the material property. The material properties are expressed in this way so that the higher order effects of the temperature on material properties can be readily discernible. The values of each coefficient appearing in the preceding equation

are listed in Table 1 for titanium (Ti-6Al-4V) and zirconium oxide (ZrO_2). Due to very small variation in Poisson's ratios of materials, they are assumed to be constant through the OCS.

2.3 The basic formulations

According to the Reddy's third-order shear deformation theory [9], straight lines normal to midsurface before deformation will no longer remain straight. Satisfying zero shear stress boundary conditions at the top and bottom of the shell, the displacement components of an arbitrary point within the shell domain, designated by U , V and W , are expressed as:

Table1. Material properties of titanium and zirconium oxide.

Materials		P_0	P_{-1}	P_1	P_2	P_3
titanium	E (Pa)	1.22.56e+9	0	-4.586e-4	0	0
	α (1/K)	7.5788e-6	0	6.638e-4	-3.147e-6	0
	k (W/mK)	1	0	1.704e-2	0	0
	ν	0.3				
zirconium oxide	E (Pa)	244.27e9	0	-1.371e-3	1.214e-6	-3.681e-10
	α (1/K)	12.766e-6	0	-1.491e-3	1.006e-5	-6.778e-11
	k (W/mK)	1.7	0	1.276e-4	6.648e-8	0
	ν	0.3	0	0	0	0

$$\begin{aligned}
 U &= u(x, \theta) + z\psi_1(x, \theta) - nz^3(\psi_1 + \frac{\partial w}{\partial x}) \\
 V &= v(x, \theta) + z\psi_2(x, \theta) + nz^3(\frac{v}{Z_m} - \psi_2 - \frac{\partial w}{Z_m \partial \theta}) \\
 W &= w(x, \theta)
 \end{aligned} \tag{3}$$

where $n = 4/3h^2$.

Using Hamilton principle, the governing equations of the third order shear deformation theory of 2-D FGM OCSs can be obtained as:

$$\begin{aligned}
 \frac{Z_m \partial N_{xx}}{\partial x} - \frac{\partial N_{x\theta}}{\partial \theta} &= 0 \\
 \frac{\partial N_{\theta\theta}}{\partial \theta} + \frac{Z_m \partial N_{x\theta}}{\partial x} + Q_{\theta z} + \frac{n}{Z_m} \frac{\partial P_{\theta\theta}}{\partial \theta} + n \frac{\partial P_{x\theta}}{\partial x} - 3nR_{\theta z} + \frac{n}{Z_m} P_{\theta z} &= 0 \\
 -nZ_m \frac{\partial^2 P_{xx}}{\partial x^2} + N_{\theta\theta} - \frac{n}{Z_m} \frac{\partial^2 P_{\theta\theta}}{\partial \theta^2} - n \frac{\partial^2 P_{x\theta}}{\partial x \partial \theta} - Z_m \frac{\partial Q_{xz}}{\partial x} + 3nZ_m \frac{\partial R_{xz}}{\partial x} - \frac{\partial Q_{\theta z}}{\partial \theta} + 3n \frac{\partial R_{\theta z}}{\partial \theta} - \frac{n}{Z_m} \frac{\partial P_{\theta z}}{\partial \theta} &= 0 \\
 \frac{Z_m \partial M_{xx}}{\partial x} - nZ_m \frac{\partial P_{xx}}{\partial x} + \frac{\partial M_{x\theta}}{\partial \theta} + n \frac{\partial P_{x\theta}}{\partial \theta} + 3nZ_m R_{xz} - RQ_{xz} &= 0 \\
 \frac{\partial M_{\theta\theta}}{\partial \theta} + n \frac{\partial P_{\theta\theta}}{\partial \theta} - nP_{xx} - Z_m \frac{\partial M_{x\theta}}{\partial x} + nZ_m \frac{\partial P_{x\theta}}{\partial x} - 3nR_{\theta z} + Z_m Q_{\theta z} + nP_{\theta z} &= 0
 \end{aligned} \tag{4}$$

Without the existence of heat sources, the equation of steady-state heat transfer is obtained as:

$$\frac{\partial k}{\partial z} \frac{\partial T}{\partial z} + k \frac{\partial^2 T}{\partial z^2} + \left(\frac{Z_m}{Z_m + z} \right)^2 k \frac{\partial T^2}{\partial \theta^2} + \frac{\partial k}{\partial x} \frac{\partial T}{\partial x} + k \frac{\partial^2 T}{\partial x^2} + \frac{1}{Z_m + z} k \frac{\partial T}{\partial z} = 0 \quad (5)$$

3. SOLUTION PROCEDURE

In order to evaluate the thermal displacements and stresses, the temperature distribution in the 2-D FGM OCS should be obtained. The 2-D FGM OCS is assumed to be exposed to ambient air T_∞ with a heat-transfer coefficient h_a at lower and upper edges. The inner surface of the OCS experiences a high heat flux while the outer surface is subjected to temperature load. The thermal boundary conditions are as follows:

$$\text{Heat flux at the inner radius } z = -h/2 : q = q_0 \quad (6)$$

$$\text{Heat convection at the lower edge } x = 0 : k \frac{\partial T}{\partial x} + h_a (T - T_\infty) = 0 \quad (7)$$

$$\text{Heat convection at the upper edge } x = L : k \frac{\partial T}{\partial x} + h_a (T - T_\infty) = 0 \quad (8)$$

$$\text{Temperature at the outer radius } z = h/2 : T = T_0 \quad (9)$$

At this stage, the GDQM [10] can be applied to discretize the equation of steady-state heat transfer (5) and the boundary conditions (6-9). After employing the aforementioned solution procedure, one obtains the discretized form of the equation of heat transfer and the related boundary conditions, which can be written in matrix form as,

$$\begin{bmatrix} [A_{bb}] & [A_{bd}] \\ [A_{db}] & [A_{dd}] \end{bmatrix} \begin{Bmatrix} \mathbf{T}_b \\ \mathbf{T}_d \end{Bmatrix} = \begin{Bmatrix} \{f_{conv}\} \\ \{0\} \end{Bmatrix} \quad (10)$$

where subscripts 'd' and 'b' refer to domain and boundary, respectively. $\{f_{conv}\}$ is a convection vector related to heat convection boundary conditions at upper and lower edges. Then temperature field is obtained from the following relations:

$$\mathbf{T}_d = [B]^{-1} [A_{db}] [A_{bb}]^{-1} \{f_{conv}\} \quad (11)$$

Where

$$[B] = [A_{db}] [A_{bb}]^{-1} [A_{bd}] - [A_{dd}] \quad (12)$$

Due to temperature-dependent thermal conductivity, a nonlinear ordinary differential equation (ODE) is obtained for the temperature field. Therefore, an iterative method should be used to solve the system of nonlinear equation. To start the iterations, the spatially varying thermal conductivity is evaluated at a constant reference temperature T_{ref} and the GDQM solution for the temperature field is obtained by solving a linear ODE with prescribed thermal conductivity. In the next iteration, the thermal conductivity is updated based on the temperature field from the previous iteration and the heat conduction problem is solved again to obtain an updated temperature field. This process is repeated until the change in peak temperature between two consecutive iterations falls below an absolute tolerance T_{tol} . In order to calculate the thermal displacements and stresses, the temperature field obtained from the thermal analysis is entered into the governing equations of the 2-D FGM OCS as a thermal loading and solved using GDQM.

4. RESULTS AND DISCUSSION

In this section, numerical computations have been carried out for 2-D FGM OCSs with temperature-dependent and independent material properties. We have compared various volume fraction profiles of conventional 1-D and 2-D FGMs with appropriate choice of the sigmoidal and axial parameters of the 2-D power-law distribution, as shown in Table 2. It should be noted that the notation *Sigmoidal-Symmetrical* indicates that the 2-D FGM OCS has sigmoidal and symmetrical volume fraction profiles in the radial and axial directions, respectively. The notation *Classical axially* indicates that 1-D FGM has only classical

volume fraction profile in axial direction. The influences of various volume fraction profiles on distribution of temperature field and circumferential stress of 2-D FGM OCS with C-C boundary conditions are examined in Fig. 3. As observed in Fig. 3a, the temperature in magnitude for *Sigmoidal-Classical* exhibits lower value than those of other types of volume fraction profiles. According to Fig. 3b, the magnitude of thermal stresses is been reduced by using *Sigmoidal-Classical* volume fraction profile. On the contrary, 1-D FGM OCS with sigmoidal radial variation has the maximum value of the thermal stresses. It is interesting to note that the variation of the thermal stresses through the thickness for *Sigmoidal-Classical* OCS is close to that of *Classical axially* one. Therefore, these observations imply that from design viewpoint it is important to note that the maximum magnitude of thermal stresses can be modified and reduced to a required manner by selecting suitable material distribution profiles in two directions. Another observation from Fig. 3 is that although the maximum values of the circumferential stress occur at an internal position, these positions are slightly shifted with varying volume fraction profiles. Moreover, the effect of varying volume fraction profiles on the circumferential stress is more pronounced for positions closer to the inner surface than those closer to the outer surface. In order to show the importance of considering the variation of material properties with temperature, distribution of temperature field and circumferential stress of 2-D FGM OCS with C-C boundary conditions through the thickness for the case of temperature-independent material properties are presented in Fig. 4 for various volume fraction profiles. The material properties for the case temperature-independent are calculated at the reference temperature, 300K. Comparing Figs. 3 and 4, it can be observed that the temperature field for the case of temperature-independent is found to be greater than that computed with temperature-dependent properties. The temperature-dependency of the material properties reduces peak of the non-dimensional axial and transverse shear stresses by 40% and 45 % for *Sigmoidal-Classical* profile. Thus calculations and design based on temperature-independent properties yield conservative estimates. It can also be inferred from Figs. 3 and 4 that the discrepancy between value of thermal stresses with different volume fractions for the case of temperature-dependent material properties is higher than those with temperature-independent properties.

Table 2. Different ceramic volume fraction profiles, different parameters and volume fraction indices of 2-D power-law distributions.

Volume fraction profile	Sigmoidal parameters	Axial volume fraction index and parameters
<i>Sigmoidal-Symmetrical</i>	$\gamma_z = 1$	$\alpha_x = 1, \beta_x = 2$
<i>Sigmoidal- Classical</i>	$\gamma_z = 1$	$\alpha_x = 0$
<i>Symmetrical axially</i>	$\gamma_z = 0$	$\alpha_x = 1, \beta_x = 2$
<i>Classical axially</i>	$\gamma_z = 0$	$\alpha_x = 0$
<i>Sigmoidal radially</i>	$\gamma_z = 1$	$\gamma_x = 0$

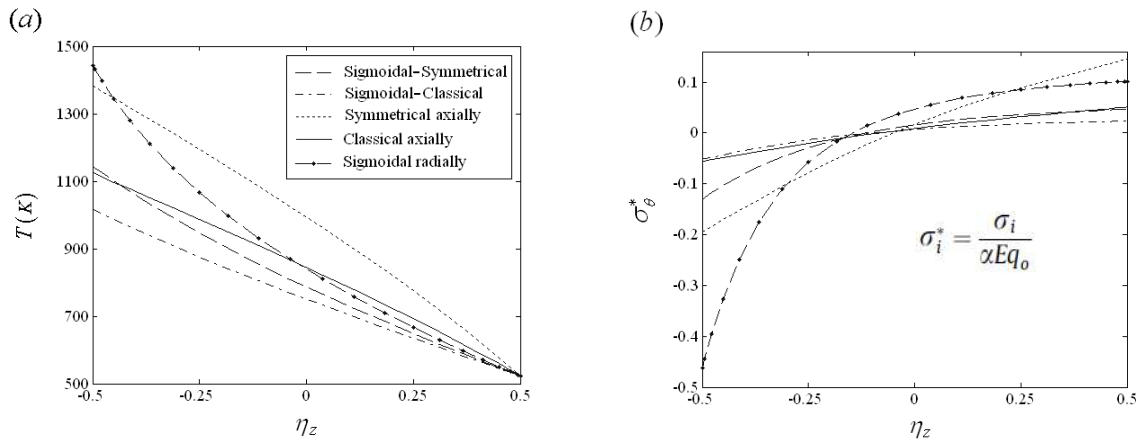


Fig. 3. Through-the-thickness variation of temperature field and hoop stress of 2-D FGM OCS with temperature-dependent materials for various volume fraction profiles ($Z_m/h = 10, \Theta = 3\pi/4, z = L/2, \theta = \pi/3, \gamma_x = 1$)

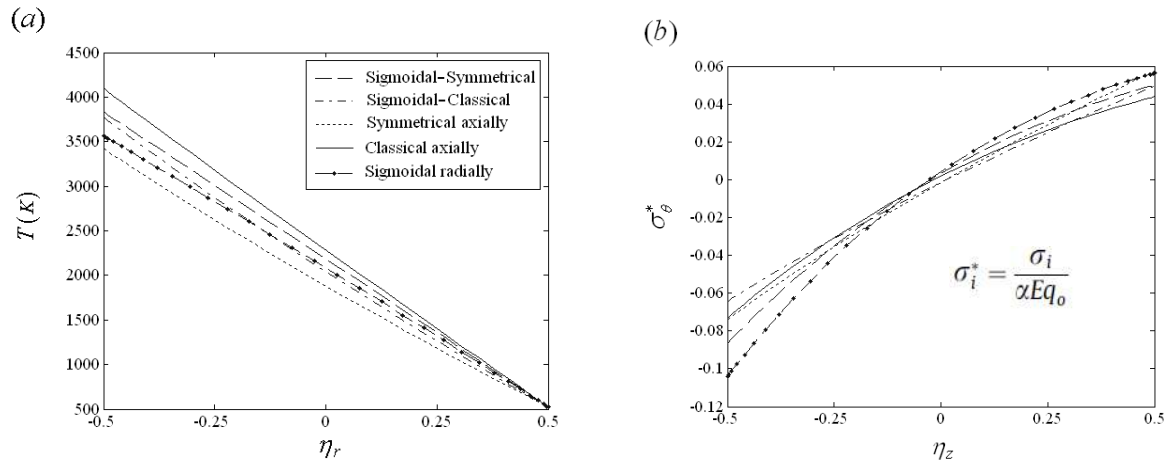


Fig. 4. Variation of temperature field and hoop stress of 2-D FGM OCS through the thickness various volume fraction profiles with temperature-independent materials

5. CONCLUSION

The thermo-elastic analysis of a 2-D FGM OCS has been investigated based on third-order shear deformation plate theory of Reddy in this article. The temperature-dependence of the elastic constants and thermal expansion coefficients are taken into consideration when solving the governing equations of 2-D FGM OCS. Various material profiles in two radial and axial directions can be illustrated using the 2-D power-law distribution. Mori-Tanaka scheme as an accurate micromechanics model is used to estimate the homogenized material properties of 2-D FGM. The nonlinear steady-state heat conduction equation is solved using an iterative solution procedure along with generalized differential quadrature method (GDQM). In the mechanical analysis, the temperature field obtained from the thermal analysis is entered into the governing equations of the 2-D FGM OCS as a thermal loading. The governing equations and associated boundary conditions are derived using the Hamilton's principle, and discretized by means of the GDQM to obtain the displacements and stresses. The present realistic investigation of the 2-D FGM OCS makes it a useful tool that will enable engineers to develop 2-D FGM OCSs with superior properties. It is found that calculations and design based on temperature-independent properties yield conservative estimates.

ACKNOWLEDGEMENTS

The authors wish to thank the Ghent University for the financial support received by the Special Funding of Ghent University (Bijzonder Onderzoeksfonds), BOF Scholarship 01DI3213.

REFERENCES

- [1] M. Koizumi, FGM activities in Japan. *Compos Part B-ENG* 28 (1997) 1–4.
- [2] D.P.H. Hasselman, G.E. Youngblood, Enhanced Thermal Stress Resistance of Structural Ceramics with Thermal Conductivity Gradient, *J. Am. Ceram. Soc.* 61(1978).
- [3] Z.S. Shao, T.L. Wang, Three-dimensional solutions for the stress fields in functionally graded cylindrical panel with finite length and subjected to thermal/mechanical loads, *Int. J. Solids Struct.* 43 (2006) 3856–3874.
- [4] M. Nemat-Alla, Reduction of thermal stresses by developing two dimensional functionally graded materials, *Int. J. Solids Struct.* 40 (2003) 7339–7356.
- [5] M. Asgari, M. Akhlaghi, Transient thermal stresses in two-dimensional functionally graded thick hollow cylinder with finite length, *Arch. Appl. Mech.* 80 (2010) 353–376.
- [6] M. Asgari, M. Akhlaghi, Transient heat conduction in two-dimensional functionally graded hollow cylinder with finite length, *Heat Mass Transfer.* 45(11) (2009) 1383–1392.
- [7] T. Mori, K. Tanaka, Average stress in matrix and average elastic energy of materials with misfitting Inclusions. *Acta Metall Mater.* 21 (1973) 571–574.

- [8] J.N. Reddy, C.D. Chin, Thermo-elastical analysis of functionally graded cylinders and plates, *J. Therm. Stresses*. 21 (1998) 593–626.
- [9] J. N, Reddy, A refined nonlinear theory of plates with transverse shear deformation, *Int. J. Solids Struct.* 20 (1984) 881–96.
- [10] C. Shu, B.E. Richards, Application of generalized differential quadrature to solve two-dimensional incompressible Navier Stockes equations, *Int. J. Numer. Method F.* 15 (1992), 791-798.

STUDY ON VIBRATION AND STABILITY OF FUNCTIONALLY GRADED CYLINDRICAL SHELLS SUBJECTED TO HYDROSTATIC PRESSURE

B. Liang¹, R. Li¹, N.A. Noda² and H.Y.Xu¹

¹ Henan University of Science and Technology, Luoyang, China

² Kyushu Institute of Technology, Kitakyushu, Japan

Abstract: Based on the Flügge's shell theory, the vibration characteristics and stability of submerged functionally graded (FG) cylindrical shell under hydrostatic pressure is examined. By means of conversion switch on axial wave number, the coupled frequency of submerged FG cylindrical shell with various boundary conditions is obtained, using wave propagation method and Newton method. Then the critical pressure of FG cylindrical shells is given by applying linear fitting method. Results are compared to known solutions, where these solutions exist. The natural frequency and critical pressure of FG cylindrical shell are illustrated. The effects of constituent materials, volume fraction, boundary condition and dimensions on the natural frequencies and critical pressures of submerged FG cylindrical shell are illustrated by examples.

Keywords: Natural Frequency; Critical Pressure; Functionally Graded Material; Cylindrical Shell; Hydrostatic Pressure

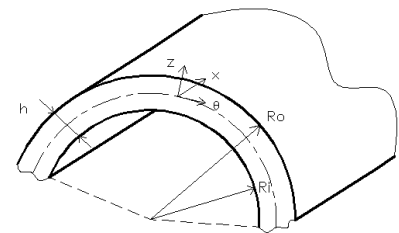
1 INTRODUCTION

Functionally graded materials, FGM for short, is a new kind of compound material structure with component and structure graded distribution along thickness. By using the new kind of functionally graded material, the requirements of special extreme environment such as ultra-temperature, larger temperature gradient and the strong thermal shock on FG cylindrical shell are satisfied. The liquid medium and the material properties of functionally graded material have significant impact on the vibration characteristics of cylindrical shell. And the structural analyses need to be carried out in the presence of critical pressure. Since the pioneer work of Junger [1] was published, a lot of theoretical investigations have appeared. Zhang et al. [2] used wave propagation method to consider the vibration characteristics of cylindrical shell with the impact of the fluid. Sheng and Wang [3] presented the report of an investigation into the vibration of FG cylindrical shells with flowing fluid by employing the first-order shear deformation theory. The input power flow for an infinite ring-stiffened cylindrical shell submerged in fluid was investigated by Liu et al. [4]. The hydrostatic buckling of shells with various boundary conditions is studied by Pinna and Ronalds [5].

Based on the Flügge shell theory, wave propagation method and Newton method, the coupled frequency of submerged FG cylindrical shell with various boundary conditions is derived. Then the critical pressure of FG cylindrical shells is given by applying linear fitting method. The effects of constituent materials, volume fraction, boundary condition and dimensions on the natural frequencies and critical pressures of submerged FG cylindrical shell are illustrated by examples. In numerical calculations, the functionally graded material has ceramic on its inner surface and has metal on its outer surface.

2 MECHANICAL MODEL

A FG cylindrical shell is considered, as shown in Fig.1. The shell is characterized by its inner radius R_i , outer radius R_o , represented radius R , length L and thickness h . The x , θ and z are the axial coordinates, circumferential coordinates and radial coordinates, respectively.



3 FUNCTIONALLY GRADED MATERIALS

Fig.1. Geometry of a FG cylindrical

The material property P of functionally graded material is the function of temperature and volume fraction, which is controlled by the volume fractions of material. The function can be defined as follows

$$P = P_0(P_{-1}T^{-1} + 1 + P_1T + P_2T^2 + P_3T^3) \quad (1)$$

where $P_0, P_{-1}, P_1, P_2, P_3$ are the coefficients of temperature T (K) and are unique to the constituent materials.

For cylindrical shell with thickness h , the volume percentages can be given as

$$V_o = \left[\frac{z + h/2}{R_0 - R_i} \right]^N = 1 - V_i \quad (2)$$

where V_i and V_o are the volume percentages of the internal and external surfaces of the functionally graded material, respectively. N is the power-law exponent ($0 \leq N \leq \infty$). So along the thickness of the shell, the Young's modulus E , Poisson ratio μ and the mass density ρ can be expressed as

$$\begin{cases} E = (E_o - E_i) \left[\frac{z + h/2}{R_0 - R_i} \right]^N + E_i \\ \mu = (\mu_o - \mu_i) \left[\frac{z + h/2}{R_0 - R_i} \right]^N + \mu_i \\ \rho = (\rho_o - \rho_i) \left[\frac{z + h/2}{R_0 - R_i} \right]^N + \rho_i \end{cases} \quad (3)$$

4 FORMULATION

By using Flügge's [6] theory, the equations of motion for a cylindrical shell subjected to hydrostatic pressure are obtained.

$$\begin{cases} u_{xx} + \frac{1-\mu}{2} u_{\theta\theta} + \frac{1+\mu}{2} v_{x\theta} + \mu w_x + K \left(\frac{1-\mu}{2} u_{\theta\theta} - w_{xxx} + \frac{1-\mu}{2} w_{x\theta\theta} \right) \\ + T_1 u_{xx} + T_2 (u_{\theta\theta} - w_x) - \frac{\rho R^2 (1-\mu^2)}{E} u_{tt} = 0 \\ \frac{1+\mu}{2} u_{x\theta} + \frac{1-\mu}{2} v_{xx} + v_{\theta\theta} + w_\theta + K \left(\frac{3(1-\mu)}{2} v_{xx} - \frac{3-\mu}{2} w_{xx\theta} \right) + T_1 v_{xx} \\ + T_2 (v_{\theta\theta} + w_\theta) - \frac{\rho R^2 (1-\mu^2)}{E} v_{tt} = 0 \\ \mu u_x - K u_{xxx} + K \frac{1-\mu}{2} u_{x\theta\theta} + v_\theta - K \frac{3-\mu}{2} v_{xx\theta} + (1+K)w + K w_{xxx} + 2K w_{xx\theta\theta} \\ + K w_{\theta\theta\theta} + 2K w_{\theta\theta} - T_1 w_{xx} - T_2 (u_x - v_\theta + w_{\theta\theta}) + \frac{\rho R^2 (1-\mu^2)}{E} w_{tt} = - \frac{R^2 (1-\mu^2)}{Eh} \psi \end{cases} \quad (4)$$

where $T_1 = \frac{R}{2Eh} (1-\mu^2) P_o$, $T_2 = \frac{R}{Eh} (1-\mu^2) P_o$, $\circ_x = R \frac{\partial(\circ)}{\partial x}$, $\circ_\theta = \frac{\partial(\circ)}{\partial \theta}$, $\circ_t = \frac{\partial(\circ)}{\partial t}$, $K = \frac{h^2}{12R^2}$, P_o is the hydrostatic pressure and ψ is the acoustic pressure.

The displacements of the cylindrical shell can be expressed in the form of wave propagation.

$$\begin{cases} u(x, \theta, t) = U_m \cos(n\theta) e^{(i\omega t - ik_m x)} \\ v(x, \theta, t) = V_m \sin(n\theta) e^{(i\omega t - ik_m x)} \\ w(x, \theta, t) = W_m \cos(n\theta) e^{(i\omega t - ik_m x)} \end{cases} \quad (5)$$

where U_m, V_m, W_m are the wave amplitudes in the x, θ and z directions, ω is the natural angular frequency. The fluid of the cylindrical shell is assumed non-viscous which satisfy the acoustic wave equation. The equation of motion of the fluid can be written in the cylindrical co-ordinate system (x, θ, r) as:

$$\frac{1}{r} \frac{\partial}{\partial r} \left(r \frac{\partial \psi}{\partial r} \right) + \frac{1}{r^2} \frac{\partial^2 \psi}{\partial \theta^2} + \frac{\partial^2 \psi}{\partial x^2} = \frac{1}{c^2} \frac{\partial^2 \psi}{\partial t^2} \quad (6)$$

where t is the time and c is the sound speed of the fluid. The associated form of the acoustic pressure field exterior of the shell, which satisfies the acoustic wave Eq.(6), is given as

$$\psi = \psi_m \cos(n\theta) H_n^{(2)}(k_r r) e^{(i\omega t - ik_m x)}, \quad \psi_m = \left[\omega^2 \rho_f / k_r H_n^{(2)'}(k_r R) \right] W_m \quad (7)$$

where $H_n^{(2)}()$ is the Hankel function of the second kind and order n , the prime on the $H_n^{(2)}()$ denotes differentiation with respect to the argument $k_r R$. The relationship between radial wave number k_r and axial wave number k_m is applied to $(k_r R)^2 = \Omega^2 (C_L / C_F)^2 - (k_m R)^2$.

In the function, Ω is the non-dimensional frequency, C_L and C_F are the sound speed of the shell and fluid respectively. The fluid radial displacement and shell radial displacement must be equal at the interface of the shell inner wall and the fluid.

Substituting Eq.(5) into Eq.(4), which consideration of acoustic pressure on the shell and coupling Eq.(7), the equations of motion of coupled system in matrix form can be obtained.

$$\begin{bmatrix} L_{11} & L_{12} & L_{13} \\ L_{12} & L_{22} & L_{23} \\ L_{31} & L_{32} & L_{33} + F_L \end{bmatrix} \begin{Bmatrix} U_m \\ V_m \\ W_m \end{Bmatrix} = \begin{Bmatrix} 0 \\ 0 \\ 0 \end{Bmatrix} \quad (8)$$

where $L_{ij}(i, j=1, 2, 3)$ are the parameters operated with the x and θ , F_L is the fluid loading term due to the presence of the fluid acoustic field.

$$F_L = \Omega^2 (\rho_f / \rho) (R / h) (k_r R)^{-1} \left[H_n^{(2)}(k_r R) / H_n^{(2)'}(k_r R) \right] \quad (9)$$

By substituting a boundary condition into k_r , the solution of Eq.(8) can be derived.

According to the classical theory, the function of elastic critical hydrostatic pressure is given in Шиманский [7]. However, the function can only analysis the elastic critical pressure of cylindrical shell for $m=1$ under simply supported (SS-SS) boundary condition. Because of linear relation between the frequency squared and hydrostatic pressure (Abramovich [8]), the critical hydrostatic pressure can be derived while the natural frequency is assumed to be zero. Therefore, the critical pressure can be obtained by using linear fitting method.

5 NUMERICAL RESULTS AND DISCUSSION

5.1 Vibration of FG cylindrical shell

In this paper, the metal materials are Stainless steel and Ti-6Al-4V, while the ceramic materials are Si_3N_4 and Zirconia. The material properties are taken into consideration the temperature dependency for the temperature of $T = 300\text{K}$ from Shariyat [9] and Kim [10].

The natural frequencies of FG cylindrical shell with simply supported ends are listed in Table 1. The functionally gradient material considered is composed of Stainless steel and nickel. The validity and feasibility of the study are verified by comparing results with those in Ref. [11]. The geometric parameters of the shell are defined as: $E_N = 2.05098 \times 10^{11} \text{N/m}^2$, $\mu_N = 0.31$, $\rho_N = 8900 \text{kg/m}^3$, $L/R = 20$, $h/R = 0.002$, $m = 1$.

Table 1. Comparison of natural frequencies of FG cylindrical shell

	$N \rightarrow 0$		$N=1$		$N \rightarrow \infty$	
n	Present	Loy	Present	Loy	Present	Loy
1	13.548	13.548	13.211	13.211	12.894	12.894
2	4.5916	4.5920	4.4768	4.480	4.3687	4.3690
3	4.2628	4.2633	4.1523	4.1569	4.0484	4.0489
4	7.2247	7.2250	7.0354	7.0384	6.8574	6.8577
5	11.542	11.542	11.239	11.241	10.954	10.955

As an example, critical pressures for a simply supported ends isotropic cylindrical shell are studies in Table 2. Because of linear relation between the natural frequency squared and hydrostatic pressure, the equations of cylindrical shells for different conditions can be obtained by using linear fitting method, and then the critical pressure can be derived. Compared with results from Eq.(15), the feasibility of the study is proved. Some parameters are selected as: $E = 2.1 \times 10^{11} \text{ N/m}^2$, $\mu = 0.3$, $\rho = 7850 \text{ kg/m}^3$, $h = 0.01 \text{ m}$, $L = 20 \text{ m}$, $R = 1 \text{ m}$, $m = 1$, $n = 2$.

Table 2. Comparison of critical pressures [MPa] of simply supported submerged isotropic cylindrical shell

h/R	L/R					
	2		5		10	
	Present	Eq(15)	Present	Eq(15)	Present	Eq(15)
0.005	36.448	36.115	2.6929	2.6586	0.2079	0.2072
0.01	73.049	72.333	5.4377	5.3692	0.4610	0.4599
0.02	147.10	145.48	11.287	11.154	1.2832	1.2831

Because of the structure will create instability when the hydrostatic pressure is larger than critical pressure, so in this paper, the hydrostatic pressures should aim for under critical pressures. The natural frequencies of FG cylindrical shells under hydrostatic pressure for different volume fractions, axial half wave numbers and boundary conditions are studied in this paper, see Fig.2-4. Results given in these figures are obtained by setting $L/R = 20$, $h/R = 0.01$, $R = 1 \text{ m}$, $N = 1$, $m = 1$, $n = 2$ and $z = 0$.

Fig.2 describes the variations of natural frequencies of clamped-free (C-F) FG cylindrical shells for some different values of volume fraction, and the functionally graded material is made up of Stainless steel and Si_3N_4 . It is shown in these figure that with the increasing of volume fraction, the natural frequency of FG cylindrical shell increases gradually. The effects of power-law exponent on natural frequencies are mainly reflected in the cases of low exponent.

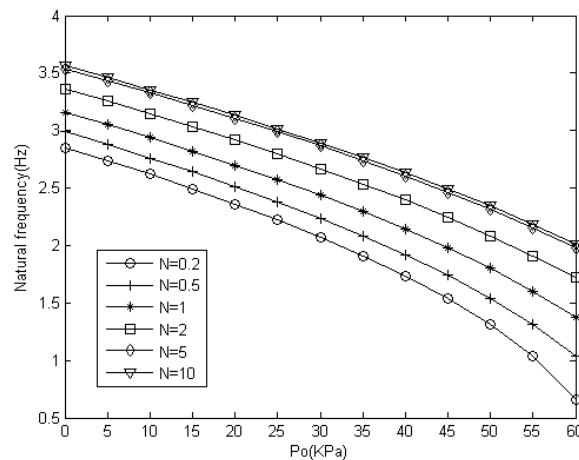


Fig.2. Variation of frequencies of submerged FG cylindrical shells for different values of volume fraction.

Fig.3 describes the change curves of natural frequencies of FG cylindrical shells for different support conditions. It is shown that the coupled frequencies for clamped-clamped (C-C) boundary condition are higher than those for other boundary conditions, the frequencies for free-sliding (F-S) boundary condition are lower than those for other boundary conditions. As the critical pressure approached, for clamped-free ends and free-sliding ends, the decline in natural frequency accelerated.

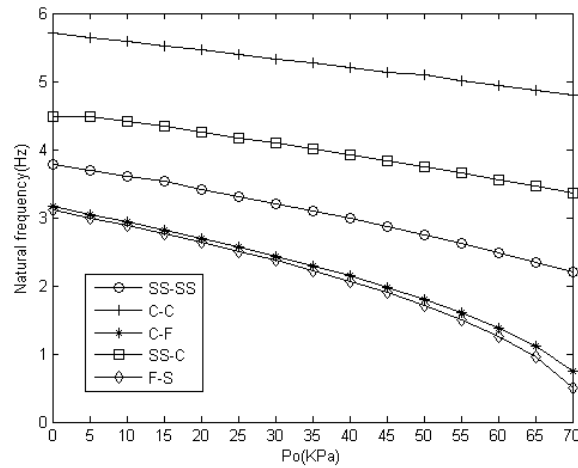


Fig.3. Variation of frequencies of submerged FG shells associated with various boundary conditions.

The variations of natural frequencies of clamped-free FG cylindrical shells for some different axial half wave numbers m under hydrostatic pressure are shown in Fig.4. It is shown that the natural frequency of FG cylindrical shell increased with the increasing of axial half wave number. With the increasing of axial half wave number, the range ability of the curves of natural frequency becomes smaller. Inferred by former results, with the increasing of axial half wave number, the critical pressure grows exponentially. When m comes to a certain degree, the change of the natural frequency is not significant.

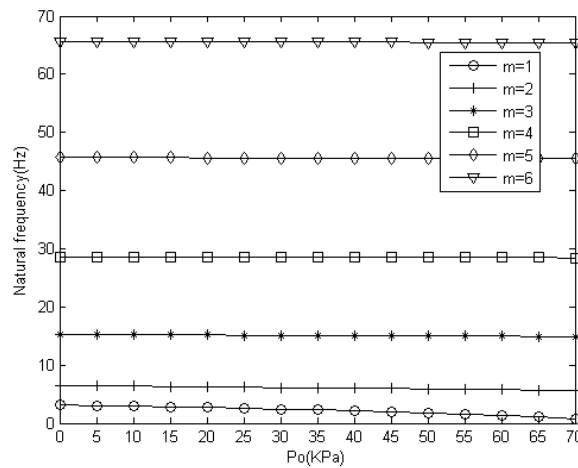


Fig.4. Variation of frequencies of submerged FG shells for some different axial half wave numbers.

5.2 Stability of FG cylindrical shell

As examples, based on the linear fitting method, critical pressures with different h/R , L/R , various boundary conditions, constituent materials and volume fractions are studied, see Fig.5 and Fig.6.

Fig.5 shows the curves of critical pressures of FG cylindrical shells for various values of power-law exponent. It is shown in the figure that the effects of power-law exponent on critical pressure are evident. The influences of power-law exponent on critical pressures are mainly reflected in the cases of small power-law exponent. With the increasing of power-law exponent, the functionally graded material is from a pure metal material to a pure ceramic material. This is due to the FG cylindrical shell is reduced to an isotropic cylindrical shell. Since critical pressure is material property dependent, use the FG cylindrical shell which composed of Stain steel and Zirconia as an example. Because of the critical pressure of pure Stain steel cylindrical shell is larger than pure Zirconia cylindrical shell, the critical pressure decreases with the increasing of power-law exponent.

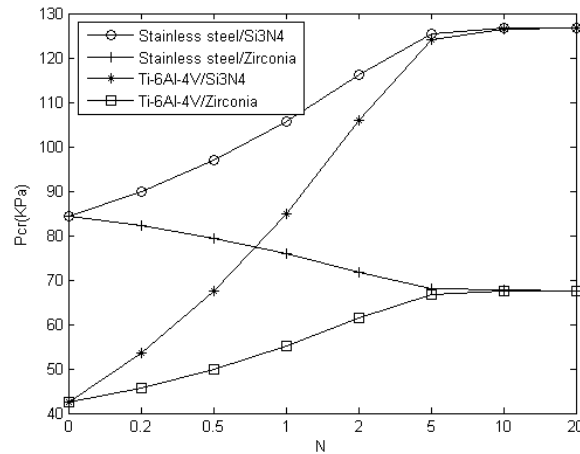


Fig.5. Variation of critical pressures of submerged shell for different values of power-law exponent.

The critical pressures of simply supported FG cylindrical shells for different h/R are shown in Fig.6. It is shown that with the increasing of h/R , the critical pressure increases rapidly. The influences of constituent material on critical pressure are mainly reflected in the cases of large h/R .

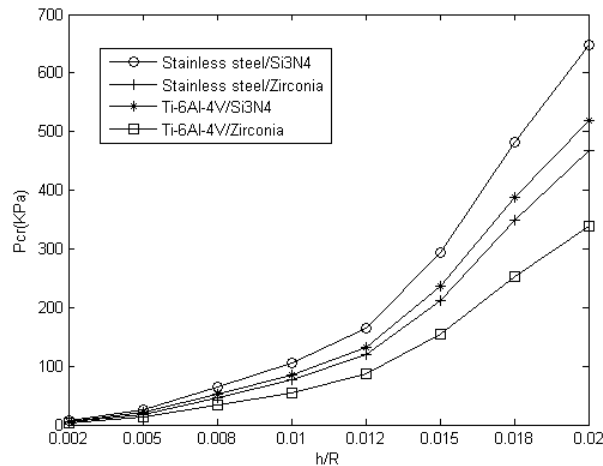


Fig.6. Variation of critical pressures of submerged cylindrical shell with different L/R ratios.

6 CONCLUSIONS

Based on the Flügge's shell theory, the natural frequencies and critical pressures of submerged FG cylindrical shells under hydrostatic pressure are studied. By means of conversion switch on axial wave number, the coupled frequency of submerged FG cylindrical shell with various boundary conditions is obtained, using wave propagation method and Newton method. Then the critical pressure of FG cylindrical shells is given by applying linear fitting method. The effects of the hydrostatic pressure, dimensions, constituent material, volume fraction and boundary condition on natural frequencies and critical pressure were investigated. Especially for the axial half wave number, the influence is obvious. In some cases, the change rules of natural frequency are similar to critical pressure. The characteristics of natural frequency and critical pressure will certainly provide guidance to the practical use and risk averse.

ACKNOWLEDGEMENTS

The authors wish to express their gratitude to the National Natural Science Foundation of China (No. 51105132) and Natural Science Foundation of Henan Province (No. 122300410112) that have supported this work..

7 REFERENCES

- [1] M.C.Junger, Vibrations of elastic shells in a fluid medium and the associated radiation of sound, J, Appl. Mech,19(3), 439-445,1952.
- [2] X.M. Zhang,. Frequency analysis of submerged cylindrical shells with the wave propagation approach. J. International Journal of Mechanical Sciences. 44 (7), 1259-1273, 2002.
- [3] G.G. Sheng, X.Wang, Thermomechanical vibration analysis of a functionally graded shell with flowing fluid , European Journal of Mechanics -A /Solids. 27(6), 1075-1087, 2008.
- [4] Z.Z. Liu, T.Y. Li, X. Zhu, J.J. Zhang, Effect of Hydrostatic Pressure on Input Power Flow in Submerged Ring-stiffened Cylindrical Shells, Journal of Ship Mechanics. 15 (3):301-312,2011.
- [5] R. Pinna, B.F. Ronalds, Hydrostatic buckling of shells with various boundary conditions, Constr. Stell. Res. 56 (1), 1–16, 2000.
- [6] W. Flügge, Stresses in Shells, Second edition, Springer-Verlag, New York, 1973.
- [7] Ю. А.Шиманский ,. Строительная Механика ПодводныхЛодок, Судпромгиз,1948.
- [8] H. Abramovich, J.Singer, T. Weller, Repeated buckling and its influence on the geometrical imperfections of stiffened cylindrical shells under combined loading. International Journal of Non-Linear Mechanics, 37(4-5), 577–588, 2002.
- [9] M. Shariyat, Dynamic buckling of suddenly loaded imperfect hybrid FGM cylindrical shells with temperature-dependent material properties under thermo-electro-mechanical loads, International Journal of Mechanical Sciences. 50(12), 1561-1571, 2008.
- [10] Y.W. Kim,. Temperature dependent vibration analysis of functionally graded rectangular plates, Journal of Sound and Vibration. 284(3-5), 531-549, 2005.
- [11] C.T Loy , K.Y. Lam, J.N. Reddy, Vibration of functionally graded cylindrical shells. J. International Journal of Mechanical Sciences. 41(3), 309-324, 1999.

EFFECTS OF RAINFALL INFILTRATION ON STABILITY OF GEOCELL REINFORCED SLOPE

Wang Guangyue^{1, a} and Zhang Janpeng^{1, b}

¹School of Civil Engineering, Shandong University, NO 17923 Jingshi Road, Jinan, China P R

^awgyue@sdu.edu.cn, ^b569031356@qq.com

Abstract. Geocell protection of slope was influenced by environment and climates largely. Many of them came to failure when subjected to rainfall infiltration. Aiming at the general shear failure mode of the geocell-protection-system (GPS), its stability analysis model during rainfall was established by the limit equilibrium method. A new approach of evaluating stability of the GPS was proposed.

Keywords: Geocell; Rainfall Infiltration; Stability; Moisture Content; Slope Angle

1 INTRODUCTION

Geocells are used to reinforce the superficial layer of bare slopes and then form a composite geocell-protection-system (GPS) with a certain thickness on slope surface. In this way, the anti-scouring ability of slope can be effectively improved and the purpose of slope protection and greening environment could be achieved. However, there is still no standard for this method. During the rainfall, the moisture content of the soil in geocells increases and the cohesion and internal friction angle would then decrease under the effect of rainfall infiltration and flow scouring, which could result in the decrease of stability and even general shear failure. Therefore, stability research on geocell protection of slope during rainfall has very important engineering significance, and it provides theoretical basis for geocell construction.

2 MECHANISM OF GEOCELL PROTECTION OF SLOPE

Geocells, with a structure of three-dimensional cells similar to the honeycomb, are made from high-density polyethylene (HDPE) strips through ultrasonic welding along their width. This structure is retractile, so it can be folded when being transported and be stretched into grid in construction, besides; it has many advantages of light material, abrasion resistance, ageing resistance, chemical corrosion resistance, high tensile strength and convenience in transport.

Geocells with vegetation protection of slope is to unfold geocells, link and fix them on the slope surface by rivets, then fill the cells with soil, sow seeds with hydro seeder and maintain, which is a hybrid technology of ecological slope protection. It's mechanism as follow: (1) soil is contained in the cells in order not to be washed away; (2) plants conserve soil and water, reduce rainfall scouring and penetration, and root system of plants also reinforces soil; (3) geocells dissipate the energy of slope surface runoff and reduce scour through confining and dispersing runoff and lengthening flow path; (4) flow could run out through holds in the side wall of cells and geotechnical drainage path, to avoid undercurrent and the potential erosion damage between slope surface and the GPS.

3 STABILITY ANALYSES OF THE GPS DURING RAINFALL

The stability of the GPS includes anti-scouring and anti-sliding capability. The reinforcement of the weak system of plant root is insidious early in the protection, so its stability depends on its anti-sliding. The influence of rainfall on the stability of the GPS mainly lies in the comprehensive softening effect of soil. In the process of rainfall, with rain infiltrating into the GPS, moisture content and weight density of the unsaturated soil increase gradually, while matric suction, cohesion and internal friction angle decrease, and the general shear strength of the soil also decreases accordingly. The mechanical state of the GPS will change, and then a new mechanical equilibrium may be established or general shear failure may be formed. The stability analysis model of the GPS is shown in Fig.1.

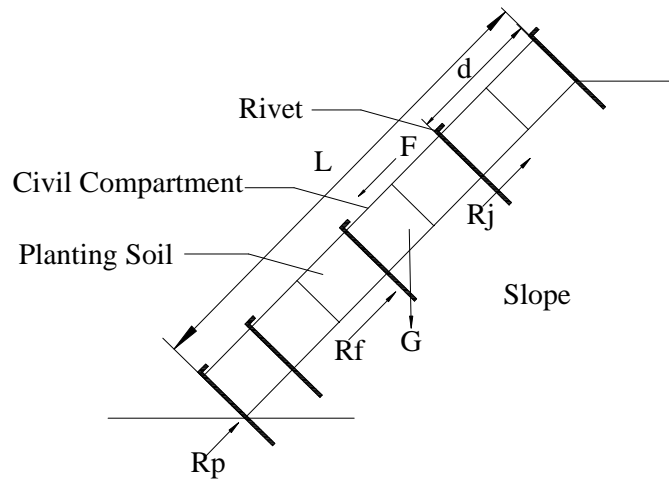


Fig.1. Stability analysis model of the GPS

Parameters of soil. The increase of gravity G caused by rainfall infiltration must be considered. The weight density γ of the soil affected by rainfall can be calculated as follow:

$$\gamma = \gamma_d + \theta \gamma_w \quad (1)$$

Where γ_d is the dry weight density of soil; θ the volume moisture content of soil and γ_w the weight density of water.

Generally speaking, the decrease of shear strength with the moisture content increasing is different for soils. According to the results Wang (2003) measured, this paper directly established the relationship between volume moisture θ and cohesion c or internal friction angle φ of the unsaturated soil by curve fitting method:

$$c = 4.905\theta^{-1.156} \quad (2)$$

$$\varphi = 24.0 - 8.262\theta \quad (3)$$

Stability calculation model of the GPS. In order to analyze the effect of rainfall infiltration on stability of the GPS quantitatively, we assume that the variation rules of the moisture content of soil at different height in the cells are the same in the process of rainfall; because the geocells are thin (its depth is usually between 50mm~200mm).

When it comes to instable, the GPS slides downward along a plane slip surface on the slope surface. Besides, the thickness of geocells is much less than its length. Therefore infinite slope method is appropriate. Considering the GPS as a rigid body, on the basis of force analysis of the GPS in limit equilibrium state by limit equilibrium method, the safety factor is defined as the ratio of the sliding resistance to the downslide strength on the entire slip surface:

$$K = \frac{R}{S} = \frac{R_f + R_j / K_j + R_p}{G \sin \alpha + F} \quad (4)$$

where R_f is the friction to which the GPS is subjected on the slip surface; R_j the additional resistance transferred by the rivets; K_j the safety factor for shelling resistance of geocells, usually is 1.5; R_p the passive earth pressure at slope toe; G the gravity of the GPS; F the shear force of the slope runoff; α the slope angle.

A unit width of the GPS was chosen as the research object, then

$$G \sin \alpha = \gamma L t \sin \alpha \quad (5)$$

$$F = \gamma_w L h \sin \alpha \quad (6)$$

$$R_f = G \cos \alpha \tan \varphi + c_f L = \gamma L t \cos \alpha \tan \varphi + c_f L \quad (7)$$

$$R_j = (t f_j L) / d^2 \quad (8)$$

in case of rigid support at slope toe,

$$R_p = \frac{1}{2} \gamma K_p t^2 + 2 c t \sqrt{K_p} = \frac{1}{2} \gamma t^2 \tan^2 (45^\circ + \frac{\varphi}{2}) + 2 c t \tan (45^\circ + \frac{\varphi}{2}) \quad (9)$$

in case of anti-press anchorage at slope toe,

$$R_p = \gamma t^2 N_\gamma + c N_c \quad (10)$$

$$N_\gamma = \frac{3 \sin(\frac{\pi}{4} + \frac{\varphi}{2})}{2(1 - \sin \varphi) \cos \varphi} \frac{\tan \varphi (e^{3\theta_0 \tan \varphi} - \cos \theta_0) + \sin \theta_0}{1 + 9 \tan^2 \varphi} \quad (11)$$

$$N_c = \frac{1 + \sin \varphi}{\cos \varphi} + \frac{3(e^{2\theta_0 \tan \varphi} - 1)}{4 \tan \varphi (1 - \sin \varphi)} \quad (12)$$

$$\theta_0 = \alpha + \pi/4 - \varphi/2 \quad (13)$$

where γ , c , φ are respectively the weight density, cohesion and internal friction angle of the soil in cells; γ_w , h respectively the weight density and depth of the slope surface flow; c_f the cohesion on the slip surface; L the length of geocells along vertical slope; t the depth of geocells; K_p the coefficient of passive earth pressure; f_j the peeling strength of the welding points of geocells in unit depth; d the rivet space (fixed with the same space in vertical and horizontal directions).

Insert the equations (5), (6), (7), (8), (9) or (10) into Eq. (4) to get the stability calculation model of the GPS, which can be used to evaluate the stability of the GPS and guide design and construction.

4 CASE STUDY

A bear rocky slope was formed because of mountain excavation in a highway construction project. The height H was 10m and slope angle α was 40° . Geocell protection of slope was adopted. Slope toe was rigidly supported. Rivet spacing d was 2.0m. Model of the geocells is TGG150 \times 400 \times 1.2–(4m \times 5m), and the parameters are shown in Table 1. Parameters of the planting soil were measured before filling as follows: dry weight density γ_d was 16.8kN, initial volume moisture content θ_0 was 0.12, and saturated volume moisture content θ_s was 0.43.

Table 1 Parameters of geocells

Material	Depth	Welding space	Thickness	Welding strength	Tensile strength	elongation
HDPE	150(mm)	400(mm)	1.2(mm)	10.6(kN/m)	23(MPa)	600%

We discuss the stability of the GPS for two cases respectively: one is the initial state, and the other is the saturated state because of rainfall infiltration. Cohesion between planting soil and rock on the slip surface is unstable, so c_f is assigned 0. L is calculated as follow: $L = H / \sin \alpha = 15.56m$.

Initial state. According to Eq. (1) (2) (3), parameters of the soil in geocells are calculated as follows:

$$\gamma_1 = \gamma_d + \theta_0 \gamma_w = 16.8 + 0.12 \times 10 = 18 \text{ kN/m}^3$$

$$c_1 = 4.905 \theta_0^{-1.156} = 56.90 \text{ kPa}$$

$$\varphi_1 = 24.0 - 8.262 \theta_0 = 23.01^\circ$$

Then the force situation of the GPS could be calculated according to Eq. (5) (7) (8) (9):

$$G \sin \alpha = 27.00kN$$

$$R_f = 13.67kN$$

$$R_j = 6.18kN$$

$$R_p = 26.25kN$$

The safety factor of the GPS:

$$K = \frac{R_f + R_j/K_j + R_p}{G \sin \alpha + F} = \frac{13.67 + 6.18/1.5 + 26.25}{27 + 0} = 1.63$$

Saturated state. The depth of geocells is small as mentioned above, so we assume the soil in geocells can reach the saturation state under usual rainfall intensity and duration.

Parameters of the saturated soil are calculated similarly as follows:

$$\gamma_2 = 21.1kN/m^3, c_2 = 13.01kPa, \varphi_2 = 20.45^\circ$$

Similarly, $G \sin \alpha = 31.66kN$

$$R_f = 14.07kN$$

$$R_j = 6.18kN$$

$$R_p = 6.11kN$$

Guan, X.J. (2009) carried out a series of laboratory experiments on slope erosion process of different soils. The results indicated that the runoff shear force on the slope surface increased with rainfall intensity increasing. But it became steady in 9 minutes in spite of rainfall intensity. Therefore we think the runoff shear force as constant for the same slope angle. Engineering practice shows that the slope runoff is always shallow flow and the depth can reach about 20mm under a rainstorm. We assume the depth of the slope runoff is the same everywhere and is valued 25mm on the safe side. Then the runoff force can be calculated:

$$F = \gamma_w Lh \sin \alpha = 10 \times 15.56 \times 25 \times 10^{-3} \times \sin 40^\circ = 2.5kN$$

And the safety factor:
$$K = \frac{R_f + R_j/K_j + R_p}{G \sin \alpha + F} = \frac{14.07 + 6.18/1.5 + 6.11}{31.66 + 2.5} = 0.71$$

It is now clear that effect of rainfall on the stability of geocells protection of slope is very great. The GPS will be unstable during rainfall if it is constructed according to the initial state.

5 CONCLUSIONS

Aiming at the general shear failure mode, the stability of the GPS during rainfall was studied, and the following conclusions were obtained:

The shear strength indexes (cohesion and inter friction angle) of soil in the geocells decrease with soil moisture content increasing during rainfall, which leads to large decrease of the anti-sliding strength of the GPS. Then the safety factor decreases accordingly and the general shear failure could be formed.

Considering the effect of rainfall infiltration and slope surface flow scouring, the stability calculation model of the GPS was established by the limit equilibrium method on the basis of anti-sliding stability analysis and it can be used to evaluate the stability of the GPS and guide design and construction.

ACKNOWLEDGEMENTS

This project was supported by the National Natural Science Foundation of China (Grant No.11072133).

6 REFERENCES

- [1] Li, L.J., 2009. Loess highway slope experimental study on flexible protection technology. Xi'an, China: Chang'an University.
- [2] Zeng, X.T., Yu Z.Q., 2001. Geocells and its application. China Haber Engineering (2), 33-37.
- [3] Chen, S.X., Chen, S.Y., 2001. Analysis of stability of unsaturated soil slope due to permeation of rainwater 22(4), 447-450.
- [4] Wang, X.F., 2003. Study of effects of rainfall infiltration on stability of unsaturated slopes. Xi'an, China: Xi'an University of Architecture and Technology.
- [5] Zhang, J.R., Zhu, R.G., Chen, X.Q., 2003. Stability analysis of geocells with vegetation used for controlling erosion of rocky slopes. Rock and Soil Mechanics 24(3), 359-362.
- [6] Guan, X.J., 2009. Study on experimental simulation and modeling of slope erosion process of different soils. Xi'an, China: Xi'an University of Tecnology.

PROPAGATION CHARACTERISTICS OF COUPLED WAVE THROUGH MICROPOLAR ELASTIC SOLID INTERLAYER IN MICROPOLAR FLUID

Xu Hongyu^{1, a}, Dang Songyang¹, Sun Qingyong¹ and Liang Bin¹

¹Department of Engineering Mechanics, Henan University of Science and Technology, Luoyang, 471023

^axuhongyu@haust.edu.cn

Abstract: Based on micropolar fluid theory and micropolar solid elasticity theory, reflection and transmission characteristics of longitudinal displacement wave and two coupled waves were studied when incident coupled wave propagated through micropolar elastic solid interlayer in micropolar fluid. Using numerical example, the rules of the amplitudes of reflection waves and refraction waves varying with incident angle are also discussed. Results show that there exist maximum values of reflection and transmission coefficient for coupled wave. There exist peak values of reflection and transmission coefficient for longitudinal displacement wave. When incidence angle is 45°, there exist zero values of reflection and transmission coefficient for longitudinal displacement wave.

Keywords: Micropolar Theory; Micropolar Elastic Wave; Reflection; Transmission; Amplitude Ratios

1 INTRODUCTION

Under continuum hypothesis of an elastic body, the classical theory of elasticity is based on linear stress-strain law (Hooke's law), in which the transmission of load across a surface element of an elastic body is described by a force stress and the motion is characterized by translational degrees of freedom only. For materials possessing granular structure, it is found that the classical theory of elasticity is inadequate to represent the complete deformation. Certain discrepancies are observed between the results obtained experimentally and theoretically, particularly, in dynamical problems of waves and vibrations involving high frequencies. Cosserat and Cosserat (1909) are the first who gave importance to the microstructure of a granular body and incorporated a local rotation of points, in addition to the translation assumed in classical theory of elasticity. This theory is known as 'Cosserat theory'. Mindlin (1964) presented a linear theory of a three-dimensional continuum having the properties of a crystal lattice, including the idea of unit cell[1]. Later, Eringen incorporated micro-inertia and renamed the 'Cosserat elasticity' as the 'Micropolar elasticity'. The linear theory of micropolar elasticity developed by Eringen(1966) is basically an extension of the classical theory of elasticity[2]. With rapid advance of the science and technology, the research in the space of the sandwich structure with the spread of the wave based on micropolar fluid theory has got more and more attention by scholars. The research of wave-absorbing materials is the most significant. Because the stealth and electromagnetic compatibility (EMC) technology become more and more important, the effect of electromagnetic wave absorption material is very outstanding and becomes a modern military in the magic weapon of the electronic counter and a "secret weapon". Many problems of reflection and refraction of micropolar elastic waves at a plane interface have been studied by several researchers in the past, including Tomar and his co-workers (1995,1999,2005,2008,2009), Song(2006), Hsia(2006)[3-9].

In this paper, we studied the propagation characteristics of couple wave in micropolar fluid with micropolar elastic plate.

2 EQUATIONS OF MOTION AND CONSTITUTIVE RELATIONS

In the absence of body force density and body couple density, for micropolar fluid medium and micropolar solid medium, the equations of motion are given as Eqs.(1) and (2), respectively.

$$\left. \begin{aligned} (c_{1f}^2 + c_{3f}^2) \nabla (\nabla \cdot \dot{\mathbf{u}}^f) - (c_{2f}^2 + c_{3f}^2) \nabla \times (\nabla \times \dot{\mathbf{u}}^f) + c_{3f}^2 \nabla \times \dot{\mathbf{\Phi}}^f &= \ddot{\mathbf{u}}^f \\ (c_{4f}^2 + c_{5f}^2) \nabla (\nabla \cdot \dot{\mathbf{\Phi}}^f) - c_{5f}^2 \nabla \times (\nabla \times \dot{\mathbf{\Phi}}^f) + c_{6f}^2 (\nabla \times \dot{\mathbf{u}}^f - 2\dot{\mathbf{\Phi}}^f) &= \ddot{\mathbf{\Phi}}^f \end{aligned} \right\} \quad (1)$$

$$\left. \begin{aligned} (c_{1s}^2 + c_{3s}^2) \nabla (\nabla \cdot \mathbf{u}^s) - (c_{2s}^2 + c_{3s}^2) \nabla \times (\nabla \times \mathbf{u}^s) + c_{3s}^2 \nabla \times \Phi^s &= \ddot{\mathbf{u}}^s \\ (c_{4s}^2 + c_{5s}^2) \nabla (\nabla \cdot \Phi^s) - c_{5s}^2 \nabla \times (\nabla \times \Phi^s) + c_{6s}^2 (\nabla \times \mathbf{u}^s - 2\Phi^s) &= \ddot{\Phi}^s \end{aligned} \right\} \quad (2)$$

where, $c_{1r}^2 = (\lambda^r + 2\mu^r)/\rho^r$, $c_{2r}^2 = \mu^r/\rho^r$, $c_{3r}^2 = K^r/\rho^r$, $c_{4r}^2 = (\alpha^r + \beta^r)/\rho^r j^r$, $c_{5r}^2 = \gamma^r/\rho^r j^r$, $c_{6r}^2 = c_{3r}^2/j^r$, ρ^r is the density of the medium, j^r is the micro-inertia and \mathbf{u}^r and Φ^r are, respectively, the displacement and microrotation vectors for the micropolar elastic half-spaces. Here, the quantity having superscript r corresponds to the fluid and solid medium when $r = f$ and $r = s$, respectively. λ^f , μ^f and K^f are the fluid viscosity coefficients and α^f , β^f and γ^f are the fluid viscosity coefficients responsible for gyrational dissipation of the micropolar fluid, λ^s , μ^s are Lamé's constant and K^s , α^s , β^s and γ^s are the micropolar elastic constants for the micropolar elastic solid.

For micropolar fluid medium and micropolar solid medium, the constitutive relations are given by Eqs.(3) and (4), respectively.

$$\tau_{kl}^f = \lambda^f \dot{u}_{r,r}^f \delta_{kl} + \mu^f (\dot{u}_{k,l}^f + \dot{u}_{l,k}^f) + K^f (\dot{u}_{l,k}^f - \varepsilon_{klp} \dot{\phi}_p^f), \quad m_{kl}^f = \alpha^f \dot{\phi}_{r,r}^f \delta_{kl} + \beta^f \dot{\phi}_{k,l}^f + \gamma^f \dot{\phi}_{l,k}^f \quad (3)$$

$$\tau_{kl}^s = \lambda^s \dot{u}_{r,r}^s \delta_{kl} + \mu^s (\dot{u}_{k,l}^s + \dot{u}_{l,k}^s) + K^s (\dot{u}_{l,k}^s - \varepsilon_{klp} \dot{\phi}_p^s), \quad m_{kl}^s = \alpha^s \dot{\phi}_{r,r}^s \delta_{kl} + \beta^s \dot{\phi}_{k,l}^s + \gamma^s \dot{\phi}_{l,k}^s \quad (4)$$

where τ_{kl}^r is the force stress tensor, m_{kl}^r is the couple stress tensor, the 'comma' in the subscript denotes the spatial derivative, δ_{kl} and ε_{klp} are Kronecker delta and the alternating tensors respectively. Other symbols have their usual meanings.

Using Helmholtz theorem, we can write

$$\begin{bmatrix} \mathbf{u}^r \\ \Phi^r \end{bmatrix} = \nabla \begin{bmatrix} A^r \\ C^r \end{bmatrix} + \nabla \times \begin{bmatrix} \mathbf{B}^r \\ \mathbf{D}^r \end{bmatrix}, \quad \nabla \cdot \begin{bmatrix} \mathbf{B}^r \\ \mathbf{D}^r \end{bmatrix} = 0 \quad (r = f, s) \quad (5)$$

where A^r and C^r are the scalar potentials, while \mathbf{B}^r and \mathbf{D}^r are the vector potentials. Plugging Eqs.(5) into Eqs.(1), we can obtain

$$\Pi_1 A^f = 0, \quad \Pi_2 C^f = 0 \quad (6)$$

$$(c_{2f}^2 + c_{3f}^2) \nabla^2 \dot{\mathbf{B}}^f + c_{3f}^2 \nabla \times \dot{\mathbf{D}}^f = \ddot{\mathbf{B}}^f, \quad c_{5f}^2 \nabla^2 \dot{\mathbf{D}}^f + c_{6f}^2 \nabla \times \dot{\mathbf{B}}^f - 2c_{6f}^2 \dot{\mathbf{D}}^f = \ddot{\mathbf{D}}^f \quad (7)$$

where $\Pi_1 = \left[(c_{1f}^2 + c_{3f}^2) \nabla^2 - \frac{\partial}{\partial t} \right] \frac{\partial}{\partial t}$ and $\Pi_2 = \left[(c_{4f}^2 + c_{5f}^2) \nabla^2 - 2c_{6f}^2 - \frac{\partial}{\partial t} \right] \frac{\partial}{\partial t}$.

It can be seen that equations in Eqs.(6) are un-coupled in scalar potentials A^r and C^r while Eqs.(7) are coupled in vector potentials \mathbf{B}^r and \mathbf{D}^r .

3 PLANE WAVE OF MICROPOLAR FLUID AND SOLID

Take the form of a plane wave propagating in the positive direction of a unit vector \mathbf{n} as

$$\{A^r, C^r, \mathbf{B}^r, \mathbf{D}^r\} = \{a^r, c^r, \mathbf{b}^r, \mathbf{d}^r\} \exp\{ik(\mathbf{n} \cdot \mathbf{r} - Vt)\} \quad (8)$$

where a^r , c^r , \mathbf{b}^r and \mathbf{d}^r are constants, $\mathbf{r} (= x\bar{i} + y\bar{j} + z\bar{k})$ is the position vector, V is the phase velocity in the direction of \mathbf{n} , $k (= \omega/V)$ is the wave number, ω is the angular frequency.

4 REFLECTION AND TRANSMISSION OF COUPLED WAVE

Introducing the Cartesian coordinates x , y and z , xy plane ($z = 0$) is the interface. Micropolar solid with the thickness of d is placed between micropolar fluid and the z -axis is taken perpendicular to the interface ($z=0$) and points downward into the medium M_2 . A two-dimensional problem in xz plane is taken into consideration, so that the followings are the displacement and microrotational vectors in micropolar elastic solid and in micropolar fluid:

$$\mathbf{u}^r = (u_1^r(x, z), 0, u_3^r(x, z)), \quad \Phi^r = (0, \Phi_2^r, 0) \quad (r = f, s) \quad (9)$$

The plan couple wave incident to the interface ($z=0$) with phase velocity V_{Π} and incident angle θ_0 in micropolar fluid. And then it goes through the micropolar solid medium M_2 . At last it entrances to micropolar fluid medium M_1 .

We take the following form of potentials: At interface $z=0$: when $z \leq 0$, in micropolar fluid medium M_1 ,

$$\{A^f, B_2^f, \phi_2^f\} = \left\{ A_0 \exp(\chi_0) + A_1' \exp(\chi_1'), \sum_{i=2}^3 A_i' \exp(\chi_i'), \sum_{i=2}^3 \eta_i' A_i' \exp(\chi_i') \right\} \quad (10)$$

And when $0 \leq z \leq d$, in micropolar solid medium M_2 ,

$$\{A^s, B_2^s, \phi_2^s\} = \left\{ A_1 \exp(\chi_1), \sum_{i=2}^3 A_i \exp(\chi_i), \sum_{i=2}^3 \eta_i A_i \exp(\chi_i) \right\} \quad (11)$$

where $\chi_0 = ik_1'(\sin \theta_0 x + \cos \theta_0 z) - i\omega t$, $\chi_i = ik_i(\sin \theta_i x + \cos \theta_i z) - i\omega t$, $\chi_i' = ik_i'(\sin \theta_i' x - \cos \theta_i' z) - i\omega t$, ($i=1,2,3$). A_0, A_1 and A_1' are the amplitude of the incident, reflected and refracted longitudinal displacement wave, respectively. A_2, A_3 and A_2', A_3' are the amplitude of the reflected and refracted couple wave with the reflected angle θ_2, θ_3 and refracted θ_2', θ_3' respectively.

When $d \leq z$, in micropolar fluid medium M_1 , for longitudinal displacement wave:

$$\begin{aligned} \{A^s, B_2^s, \phi_2^s\} &= \left\{ A_1 \exp(\chi_1) + B_1 \exp(\chi_1^0), \sum_{i=2}^3 B_i \exp(\chi_i^0), \sum_{i=2}^3 \eta_i B_i \exp(\chi_i^0) \right\} \\ \{A^f, B_2^f, \phi_2^f\} &= \left\{ B_1' \exp(\chi_1'), \sum_{i=2}^3 B_i' \exp(\chi_i'), \sum_{i=2}^3 \eta_i' B_i' \exp(\chi_i') \right\} \end{aligned} \quad (12)$$

For couple wave I,

$$\begin{aligned} \{A^s, B_2^s, \phi_2^s\} &= \left\{ B_4 \exp(\chi_4^0), A_2 \exp(\chi_2) + \sum_{i=5}^6 B_i \exp(\chi_i^0), \sum_{i=5}^6 \eta_i B_i \exp(\chi_i^0) (j=2,3) \right\} \\ \{A^f, B_2^f, \phi_2^f\} &= \left\{ B_4' \exp(\chi_4'), \sum_{i=5}^6 B_i' \exp(\chi_i'), \sum_{i=5}^6 \eta_i' B_i' \exp(\chi_i') (j=2,3) \right\} \end{aligned} \quad (13)$$

For couple wave II,

$$\begin{aligned} \{A^s, B_2^s, \phi_2^s\} &= \left\{ B_7 \exp(\chi_7^0), \sum_{i=8}^9 B_i \exp(\chi_i^0), A_3 \exp(\chi_3) + \sum_{i=8}^9 \eta_i B_i \exp(\chi_i^0) (j=2,3) \right\} \\ \{A^f, B_2^f, \phi_2^f\} &= \left\{ B_7' \exp(\chi_7'), \sum_{i=8}^9 B_i' \exp(\chi_i'), \sum_{i=8}^9 \eta_i' B_i' \exp(\chi_i') (j=2,3) \right\} \end{aligned} \quad (14)$$

where $\chi_i^0 = ik_i (\sin \varphi_i x - \cos \varphi_i z) - i\omega_i^0 t$, $\chi_i'' = ik_i' (\sin \varphi_i' x + \cos \varphi_i' z) - i\omega_i'' t$, ($i = 1, 2, \dots, 9$). B_i and B_i' are the amplitude of reflected and refracted longitudinal displacement wave or coupled wave, respectively. The coupling parameters $\eta_{2,3}$ and $\eta'_{2,3}$ are given by

$$\eta_{2,3} = -c_{6s}^2 \left[V_{s2,s3}^2 - 2 \frac{c_{6s}^2}{k_{2,3}^2} - c_{5s}^2 \right]^{-1}, \quad \eta'_{2,3} = ic_{6f}^2 \left[\frac{V_{f2,f3}}{k_{2,3}'} + 2 \frac{ic_{6f}^2}{k_{2,3}'^2} + ic_{5f}^2 \right]^{-1}.$$

Boundary conditions to be satisfied at the interface $z=0$ and $z=d$ are the continuity of force stress, couple stress, displacement and microrotation. Mathematically, these boundary conditions can be written as

$$\tau_{zz}^s = \tau_{zz}^f, \tau_{zy}^s = \tau_{zy}^f, m_{zy}^s = m_{zy}^f, u_1^s = u_1^f, u_3^s = u_3^f, \phi_2^s = \phi_2^f \quad (15)$$

Employing the Snell's law given by

$$\frac{\sin \theta_0}{V_{fl}} = \frac{\sin \theta_i}{V_{si}} = \frac{\sin \theta_i'}{V_{fi}} = \frac{\sin \varphi_i}{V_{si}} = \frac{\sin \varphi_{i+3}}{V_{si}} = \frac{\sin \varphi_{i+6}}{V_{si}} = \frac{\sin \varphi_i'}{V_{fi}} = \frac{\sin \varphi_{i+3}'}{V_{fi}} = \frac{\sin \varphi_{i+6}'}{V_{fi}}, \quad (i = 1, 2, 3),$$

and assuming that all frequencies are equal at the interface, 24 homogeneous equations can be obtained and written in a matrix form as

$$\mathbf{PZ} = \mathbf{Q} \quad (16)$$

where $\mathbf{P} = [a_{ij}]_{24 \times 24}$, $\mathbf{Z} = [z_k]^T$ ($k = 1, 2, \dots, 24$), $\mathbf{Q} = [110110000000000000000000]^T$.

5 NUMERICAL RESULTS AND DISCUSSIONS

For numerical computations, we take the values of the relevant parameters from Hsia(2006)[9]. And $\omega/\omega_0 = 100$ and thickness of the interlayer: $d=0.01\text{m}$. The system of equations given by Eqs.(16) is solved by Gauss elimination method. The values of the amplitude ratios are computed at different angles of incidence.

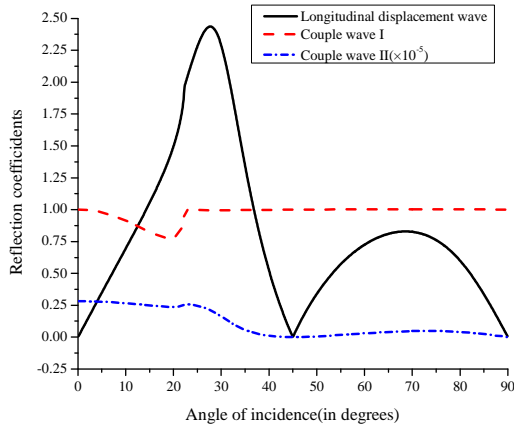


Fig.1. Reflection coefficient of longitudinal displacement wave, couple wave I and II

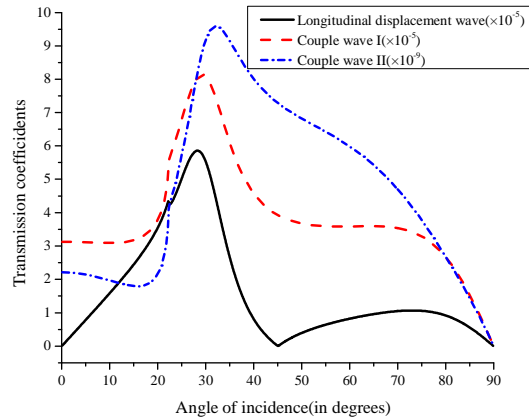


Fig.2. Transmission coefficient of longitudinal displacement wave, couple wave I and II

In Fig.1, when a plane couple wave propagating with phase velocity V_p is made incident from the micropolar fluid half-space, the variation of the amplitude ratios of reflected longitudinal displacement wave and the reflected couple waves with the incidence angle θ_0 . The amplitude ratio of longitudinal displacement wave amplitude ratio has two peak value when incidence angle θ_0 is 27.7° or 68.6° , respectively. And it is zero when $\theta_0 = 45^\circ$. The coefficients of amplitude ratios of coupled wave I is becoming decrease monotonically from the value 0 to the value 0.7784 at $\theta_0 = 19.1^\circ$ and then it increases rapidly. When $\theta_0 = 23^\circ$, there is a maximum value. And then, angle change has no effect on the amplitude ratio of coupled wave I. The variation of the amplitude ratios of coupled wave II decreased slowly at first, then get the valley value when θ_0 is about 20° , and suddenly reared up at the range of 5° . Then it declines sharply, the curve fluctuated when θ_0 is about 23° . When θ_0 is about 45° , it is zero.

Fig.2 shows the variation of the amplitude ratios of transmission longitudinal displacement wave and couple waves with the incidence angle θ_0 . The amplitude ratio of longitudinal displacement wave amplitude ratio has two peak value when incidence angle θ_0 is 28.3° or 73° , respectively. The curve fluctuated when θ_0 is about 23° and the amplitude ratio is zero when θ_0 is about 45° . The variation of the amplitude ratios of coupled wave I changed slowly at first, then get the peak value when θ_0 is about 30° , and suddenly reared up at the range of 10° , and then declines sharply. At last the curve is tending towards stability. And then decreaseing gradually when θ_0 is about 67° . The magnitude of transmission couple wave I transmission level is 10^{-9} , it is relatively small and has no effect on the amplitude ratio of coupled wave II.

From Fig.1 and Fig.2, it can be seen that at normal incidence the reflection and transmission of only reflected couple wave I take place and no other wave is found to reflect or transmit. At grazing incidence no reflection or transmission phenomena take place and the same wave propagates along the interface.

6 CONCLUSIONS

Based on micropolar fluid theory and micropolar solid elasticity theory, the reflection and transmission phenomena of an coupled wave propagating through the micropolar elastic solid infinite plate in micropolar fluid was discussed. For the specific medium material parameters, it can be concluded that:

- (1) At normal incidence, the reflection and transmission of only coupled waves take place and no longitudinal displacement wave is found to reflect or transmit. At grazing incidence, no reflection or transmission phenomena take place and the same wave propagates along the interface.
- (2) There have maximum values of reflection and transmission coefficient for coupled wave. There exist peak values of reflection and transmission coefficient for longitudinal displacement wave.
- (3) There have zero values of reflection and transmission coefficient for longitudinal displacement wave when incidence angle is 45° , at the same time, transmission coefficient presents wave phenomenon when incidence angle is 23° .

7 ACKNOWLEDGEMENTS

The authors acknowledge the financial support of National Natural Science Foundation of China (51075124).

8 REFERENCES

- [1] R.D. Mindlin: J. Arch. Ration. Mech. Anal.. 16 (1964), pp. 51-78.
- [2] A.C. Eringen: International Journal of Mathematics and Mechanics., 15 (1966), pp. 909-923.
- [3] V.R. Parfitt, A.C. Eringen: Journal of the Acoustical Society of America. 45 (1969), pp. 1258-1272.
- [4] S.K. Tomar, M.L. Gogna: Journal of the Acoustical Society of America. 97 (1995), pp. 822-830.
- [5] S.K. Tomar, R. Kumar: Journal of Sound and Vibration. 222(5) (1999), pp. 858-869.
- [6] S.K. Tamar, Monika Garg: International Journal of Engineering Science. 43 (2005), pp. 139-169.
- [7] Dilbag Singh, S.K. Tomar: International Journal of Solids and Structures. 45 (2008), pp. 225-244.
- [8] Yaqin Song, Hongyu Xu, Yuanchong Zhang: International Journal of Thermophysics. 27(3) (2006), pp. 970-993.
- [9] S.Y. Hsia, J.W. Cheng: Jpn. J. Appl. Phys.. 45 (3A) (2006), pp. 1743-1748.

GROWTH BEHAVIOR OF SMALL SURFACE-CRACKS OF ULTRAFINE GRAINED COPPER AT HIGH AND LOW CYCLIC-STRESSES

K. Yamauchi¹, M. Goto¹, SZ. Han², K. Euh² and T. Yakushiji³

¹Oita University, Oita, Japan

²Korea Institute of Materials Science, Changwon, Republic of Korea

³Oita National College of Technology, Oita, Japan

Abstract: The morphological feature of fatigue-induced surface damage and crack growth direction of ultrafine-grained copper depended on the magnitude of the applied stress amplitude. The growth direction occurred perpendicular to the loading axis at low stresses, and changed to 45° to the loading axis at high stress. To clarify the physical background of such different behaviors between the high- and low-stress amplitudes, two-step fatigue stress tests were conducted. The sizes and topographies of evolved microstructures, which have a great effect on the crack path formation, depended on stress histories. The formation mechanism of the crack paths under high- and low-stress amplitudes were discussed.

Keywords: Copper; Ultrafine-Grained Microstructure; Fatigue Crack; Shear Bands; Grain Coarsening

1 INTRODUCTION

Ultra fine grained (UFG) metals are becoming promising for engineering applications due to the recent progress in technology. Therefore, for envisaged structural applications of UFG metals, attention has been paid to fatigue performance, such as cyclic properties, S-N characteristics and the formation of shear bands (SBs) [1–4]. Fatigue crack propagation has recently attracted great interest. On the surface of cyclically deformed UFG metals, SBs extend over a much larger distance than the UFG grain size that is usually formed [2]. Meanwhile, for samples processed by equal channel angular pressing (ECAP), the YZ-, ZX-, and XY-planes are defined by three mutually orthogonal sectioning planes that are perpendicular to the longitudinal axis of the pressed sample, parallel to the sample side, and parallel to the sample top faces at the point of exit from the die, respectively. In strain-controlled low-cycle fatigue (LCF) tests, SBs in the ZX-plane were oriented at 45° to the loading axis parallel to the longitudinal axis of the pressed samples, while that in the XY-plane was nearly perpendicular to the loading axis. Fatigue cracks were initiated in and propagated along these SBs. No direct relationship was seen between SB formation and the oriented distribution of defects along the streamline plane due to shear direction in the ECAP. The SBs appear on a ZX-plane at 45° to the loading direction, mainly because it is the plane of maximum resolved shear stress.

In the high-cycle fatigue (HCF) regime, the growth behavior of millimeter-range cracks in UFG metals has been studied using compact tension (CT) [5–7] and single edge-notched specimens [8–10]. The crack growth direction of most of those specimens was nearly perpendicular to the loading axis; however, the positional relationship between the specimen faces and the YZ-, ZX- and XY-planes of the pressed samples was not clearly defined. Niendorf et al. [11] studied fatigue crack growth of UFG interstitial-free steel using CT specimens. To allow for investigation of the role of the ECAP-induced microstructure, the faces of the CT specimens were cut parallel to the YZ-, ZX- or XY-plane of the billets. They showed that both the ECAP processing route and the crack growth direction with respect to the extrusion direction dictate the crack growth behavior, and significant deviation from the expected crack growth normal direction to the loading axis was noted. This deviation was attributed to the presence of elongated structures that formed parallel to the material's plastic flow during ECAP processing. On the growth behavior of small cracks in the HCF regime, Goto et al. monitored the growth behavior of surface cracks in round-bar UFG copper specimens and discussed the effect of microstructural inhomogeneity on growth path formation [12] and a microstructure-related growth mechanism.

There are distinct differences in crack growth direction between LCF and HCF. However, little has been discussed about the physical background of different LCF and HCF growth behaviors. The objective of this

paper was to investigate the crack growth mechanism at high and low cyclic stresses corresponding to LCF and HCF, respectively.

2 FATIGUE EXPERIMENTS

2.1 Experimental procedures

The material used was pure oxygen-free copper (99.99 wt.% Cu). Before ECAP, the materials were annealed at 500 °C for 1 h (grain size, 100 μm). Fig. 1 shows a schematic of the ECAP die used in this investigation and the orientation of fatigue specimens relative to the final pressing direction. The die had a 90° angle between intersecting channels. The angles at the inner and outer corners of the channel intersection were 90° and 45°, respectively. Repetitive ECAP was accomplished according to the Bc route (after each pressing, the billet bar was rotated 90° around its longitudinal axis). Eight extrusion passages resulted in an equivalent strain of about 7.8. The pre-ECAP mechanical properties were 232 MPa tensile strength, 65% elongation and a Vickers hardness of 63 (load: 2.9 N). After eight ECAP passages, the properties changed to 438 MPa, 28% and 141%, respectively.

Fig. 2 shows details of fatigue specimens. Fatigue specimens (Fig. 2a) 5 mm diameters were machined from the processed bars. All specimens were electropolished to remove approximately 25 μm from the surface layer. Prior to testing, a small blind hole (diameter and depth were both 0.1 mm; Fig. 2b) was drilled as a crack starter on the middle surfaces of the specimens. Fig. 2c shows the location of the drilling hole. A hole was drilled on the surface (ZX-plane) where the intersection between the shear plane of the final pressing and specimen surface makes an angle of 45° with respect to the loading axis.

All tests were carried out at room temperature using a rotating bending fatigue machine operating at 50 Hz. Observations of fatigue damage on the specimen surface were performed using optical microscopy and scanning electron microscopy (SEM). The crack length, l , was measured along the circumferential surface direction.

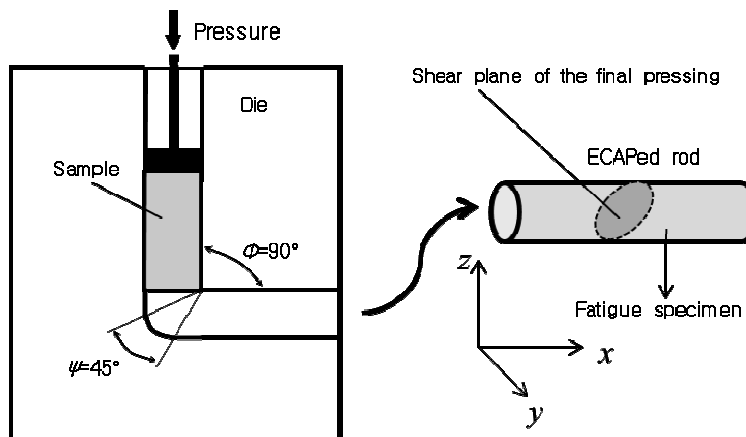


Fig. 1. Equal channel angular pressing process overview and the definition of orientation of fatigue specimens relative to the final pressing direction.

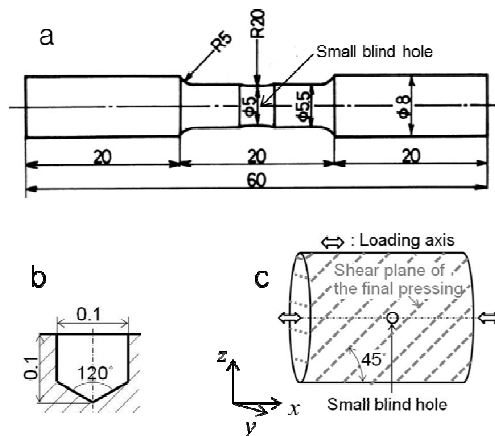


Fig. 2. Details of fatigue smooth specimens: (a) Shape of the fatigue specimen; (b) Shape of a small blind hole; (c) drilling location of a small blind hole with respect to shear plane of the final ECAP pressing.

2.2 Experimental results and discussion

In order to cover the wide high cycle fatigue regime, the specimens were stressed under two constant amplitudes: $\sigma_a = 240$ and 90 MPa. The fatigue lives were $N_f = 1.95 \times 10^5$ and 7.77×10^6 cycles, respectively. Fig. 3 shows the macroscopic morphological features in the surface observed at every 45° along the circumferential direction. Here, the location along the circumferential direction is expressed by θ measured in an anticlockwise direction from point A. A high population of damaged traces was observed over the surface fatigued at $\sigma_a = 240$ MPa. However, their orientations depend on the value of θ . Namely, the damage in the surface at $\theta = 0$ and 180° is oriented perpendicular to the loading axis. When $\theta = 45^\circ$ and 135° , the orientation of damage is about 55° with respect to the loading axis. However, at $\theta = 90^\circ$ it is about 45° . As shown in the illustration, points A and C of the fatigue specimen correspond to the upper and side surfaces of the ECAPed bar, and the shear plane of the last ECAP is given by the shaded lines. Thus, there is no doubt that the formation of damage is closely related to the shear plane of the last pressing. The morphology of damage is similar to the SBs observed by other researchers [5-7]. On the other hand, damaged traces at 90 MPa are randomly orientated, indicating no relationship between the formation of damage and the shear plane of the last pressing. In addition, damaged traces at 90 MPa had larger sizes and inferior uniformity of distribution density when compared to those at 240 MPa.

Fig. 4 shows the crack growth paths under constant stress amplitudes. At $\sigma_a = 240$ MPa (Fig. 4a), the crack that initiated from the hole created a 45° incline to the loading axis. The 45° inclined crack growth direction has been commonly observed in the ZX-plane of LCF UFG metals. Regarding the crack propagating under $\sigma_a = 90$ MPa (Fig. 4b), however, the macroscale growth direction was perpendicular to the loading axis. The crack propagated in a zigzag manner at the microscale. The degree of zigzag growth gradually increased with crack length.

To clarify the difference in crack growth mechanism between the high- and low-stress amplitudes, two-step fatigue stress tests were conducted, i.e. after the formation of a crack with an arbitrary length at the first stress amplitude (σ_{a1}), the crack continued to grow at the second stress amplitude (σ_{a2}). The two-step tests showed that, in low-to-high block (L-HB) stressing, the crack grew perpendicular to the loading axis under $\sigma_{a1} = 90$ MPa. Under the second stress ($\sigma_{a2} = 240$ MPa), although the crack paths on the macroscale were nearly perpendicular to the loading axis, the crack path had many branches and meanderings, and showed a very large zigzag pattern. In high-to-low block (H-LB) stressing, a crack with a growth path at a 45° incline to the loading axis was formed under $\sigma_{a1} = 240$ MPa. After a stress amplitude change to $\sigma_{a2} = 90$ MPa, the crack grew nearly perpendicular to the loading axis, leaving a linear crack path with very small deflections, while the crack path under the constant stress of $\sigma_a = 90$ MPa exhibited a comparatively large zigzag pattern.

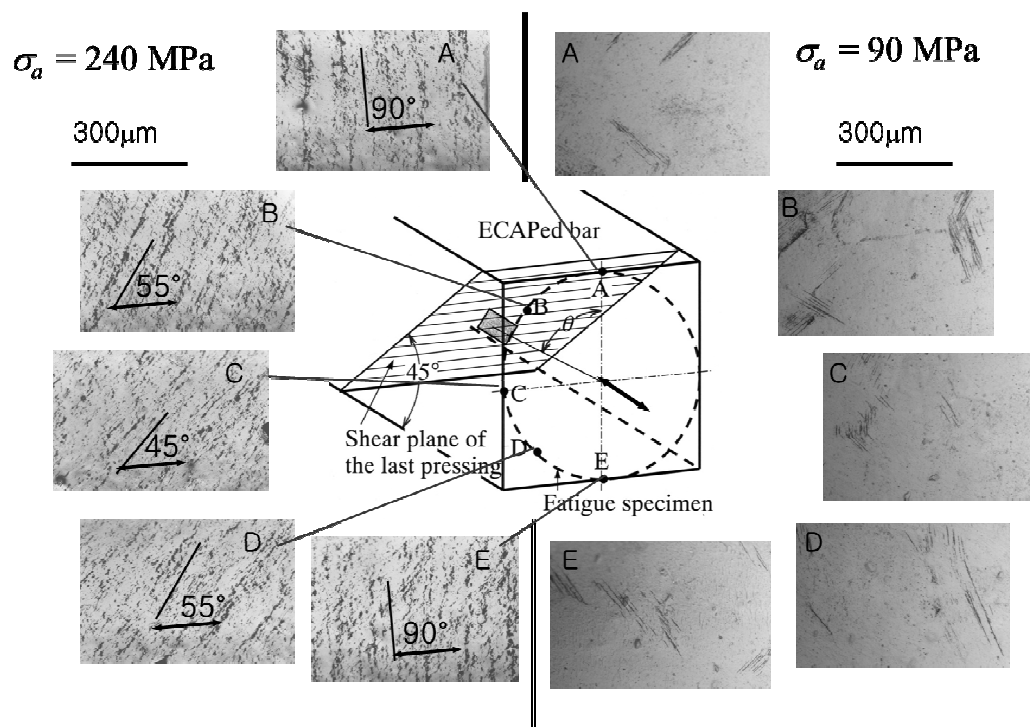


Fig. 3. Macroscopic features of the surface change along the circumferential direction.

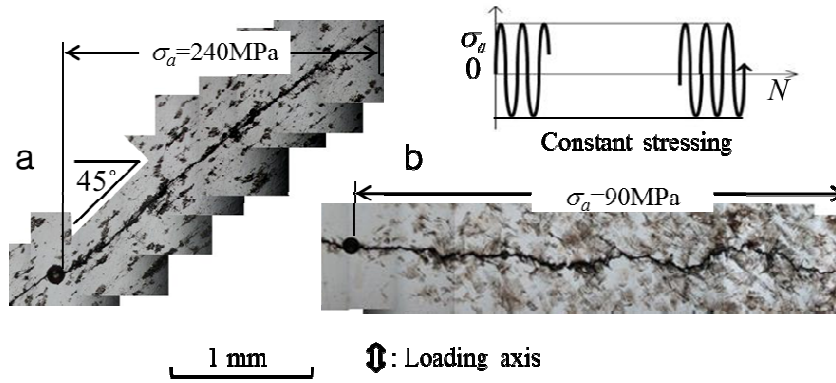


Fig. 4. Crack growth paths under the constant stress amplitudes: (a) 240 MPa; (b) 90 MPa.

Fig. 5 shows the surface states around the crack tips just before and after the stress change for L-HB stressing. Fig. 5a shows the surface damage just before the stress change, exhibiting a coarsened grain labeled “A” that formed under large repetitions of low-stress amplitude. The grain was accompanied by slip bands. After the stress change (Fig. 5b), a shear crack formed at the major crack tip and grew along the grain boundaries (GBs) of the coarsened grain A. The shear crack stopped propagating after it reached the coarse grain labeled “B”. This coarse grain might have formed under the large first low-stress repetitions, and it became visible because of the damaged traces formed under the second high-stress repetitions. After the stop propagation of the shear crack, the SBs, denoted by “C”, were initiated. At 6000 second-stress cycles, the SB growth ceased and the major crack changed its growth direction, followed by crack growth with continued SB formation and branching. Meanwhile, several studies on the GBs of UFG copper prepared by severe plastic deformation techniques have seemingly proven the existence of highly non-equilibrium GBs with high energy, excess volume and long-range stress fields [13–15]. Accordingly, diffusion is accelerated considerably in the GB regions, where GB sliding can easily occur. Thus, the crack may propagate with the assistance of sliding along the plane of maximum shear stress, showing a straight growth path along the shear direction. Unlike the shear crack growth under the constant stress of $\sigma_a = 240 \text{ MPa}$, the shear crack never continue to grow along its growth direction. This may be attributed to: (i) suppressed sliding, resulting from the lower non-equilibrium states related to the occurrence of patchy distribution of coarse grains over a few tens of micrometers; (ii) the arrest of shear crack growth upon reaching the coarsened grains; and (iii) a smaller driving force for the shear crack related to a mismatch in the crack face directions between the major crack and the shear crack (under constant stress, the directions of both faces were nearly the same, inclined 45° to the loading axis). Consequently, the very large zigzag paths were attributed to the crack-branching caused by SB formation, blocking growth at coarse grains and growth along the high-angle GBs (HAGBs) of the coarse grains.

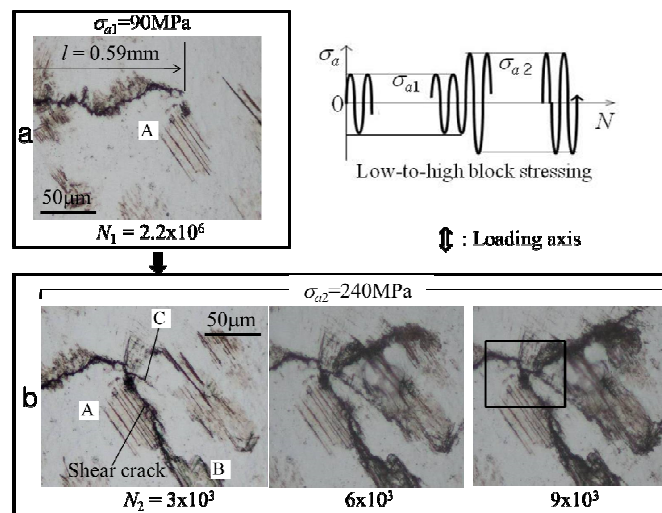


Fig. 5. Surface state changes around the crack tip just before and after the stress change for low-to-high block stressing.

Fig. 6 shows the change in surface state around the crack tips just before and after the stress change of the H-LB stressing. Fig. 6a shows the surface damage just before the stress change. The crack grew along the plane along an incline of about 45° to the loading axis and the crack path was accompanied by a narrow band composed of a large number of fine SBs. At 2×10^5 cycles of the second stress (Fig. 6b), no newly initiated SBs were observed at the region ahead of the crack tip just before the stress change, as highlighted by an open triangle. Heavily damaged zones were created at the crack tip instead of SBs. The crack grew nearly perpendicular to the loading axis, leaving damaged traces adjacent to the crack path.

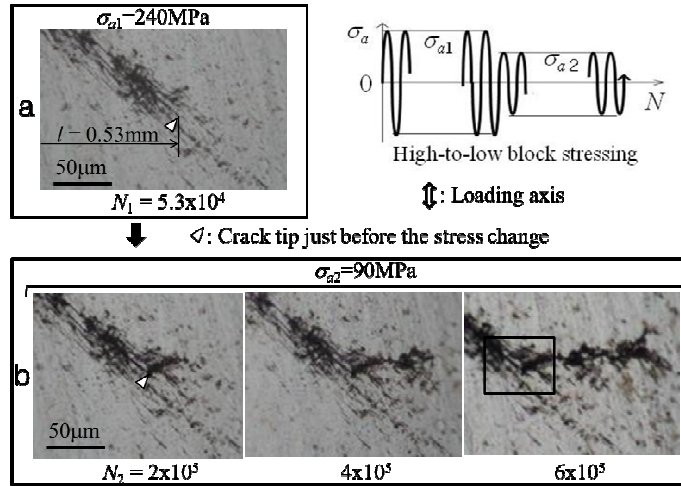


Fig. 6. Surface state changes around the crack tip just before and after the stress change for low-to-high block stressing.

Fig. 7 shows an SEM micrograph of the crack path at the point at which the stress changed. Fig. 7a is SEM micrograph in L-HB stressing. It shows shear crack and SBs are formed under second stress. In H-LB stressing (Fig. 7b), the surface at the crack edges that were formed under high stress was comparatively flat, whereas the surface that formed under low stress had traces of localized plastic deformations, suggesting change in the crack growth mechanism under high and low stresses. To summarize, a crack at high stress amplitudes grows at an incline of 45° to the loading axis because of the shear banding induced by the maximum shear stress and SB decohesion process. At low stress, the crack propagates via the striation formation mechanism, which is associated with crack tip retardation and blunting, because SB formation and decohesion are suppressed under low stress below a threshold value.

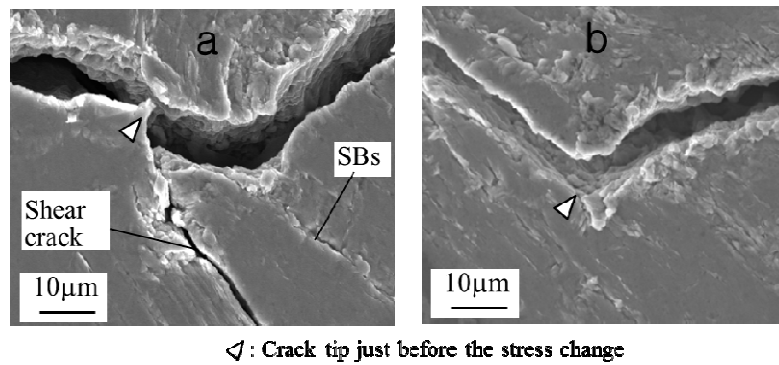


Fig. 7. SEM micrographs of the crack path at the point when the stress changed; (a) low-to-high block stressing, and (b) high-to-low block stressing.

3 CONCLUSIONS

The main findings of this study can be summarized as follows:

1. The crack at high-stress amplitudes grows along the direction at an incline of 45° to the loading axis because of the sliding induced by the maximum shear stress and the SB decohesion process.
2. At low stress, the crack propagates via the striation formation mechanism, which is associated with crack tip retardation and blunting, because SB formation and decohesion are suppressed under low stresses below a threshold value.
3. During L-HB stressing, the macroscopic direction of crack paths both before and after the stress change was nearly perpendicular to the loading axis. However, the crack path, which showed small zigzags during the low stress amplitude, developed a significantly large zigzag pattern under the subsequent high-stress loading. Coarse grains, which evolved during the first low-stress repetitions, gave rise to the significantly large zigzag paths under the second high-stress repetitions.
4. During H-LB stressing, a 45° inclined growth path under the first high stress amplitude turned into a path perpendicular to the loading axis after the stress change because SB formation and decohesion were suppressed at low stresses.

4 ACKNOWLEDGEMENTS

This study was supported by a Grant-in-Aid (23560093) for Scientific Research (C) from the Ministry of Education, Science and Culture of Japan, as well as the National Research Foundation of Korea (NRF) grant funded by the Korean government (MEST) (No. 2011-0030801), and by a grant from integrated Technology of Industrial Materials funded by the Ministry of Knowledge Economy, Korea.

5 REFERENCES

- [1] Agnew SR, Weertman JR. Cyclic softening of ultrafine grain copper, *Mater Sci Eng*, A244, 145-53, 1998.
- [2] Vinogradov A, Hashimoto S, Patlan V, Kitagawa K, Atomic force microscopic study on surface morphology of ultra-fine grained materials after tensile testing, *Mater Sci Eng*, A319, 862-66, 2001.
- [3] Höppel HW, Zhou ZM, Mughrabi H, Valiev RZ, Microstructural study of the parameters governing coarsening and cyclic softening in fatigued ultrafine-grained copper, *Philos Mag A*, 82, 1781-94, 2002.
- [4] Mughrabi H, Höppel HW, Kautz M, Fatigue and microstructure of ultrafine-grained metals produced by severe plastic deformation, *Scripta Mater*, 51, 807-12, 2004.
- [5] Vinogradov A, Nagasaki S, Patlan V, Kitagawa K, Kawazoe M, Fatigue properties of 5056 Al-Mg alloy produced by equal-channel angular pressing, *NanoStruct Mater*, 11, 925-34, 1999.
- [6] Chung CS, Kim JK, Kim HN, Kim WJ, Improvement of high-cycle fatigue life in a 6061 Al alloy produced by equal channel angular pressing, *Mater Sci Eng*, A337, 39-44, 2002.
- [7] Pao PS, Jones HN, Cheng SF, Feng CR, Fatigue crack propagation in ultrafine grained Al-Mg alloy, *Inter J Fatigue*, 27, 1164-9, 2005.
- [8] Kim HK, Choi M-I, Chung CS, Shin DH, Fatigue properties of ultrafine grained low carbon steel produced by equal channel angular pressing, *Mater Sci Eng*, A340, 243-50, 2003.
- [9] Hanlon T, Tabachnikova ED, Suresh S, Fatigue behavior of nanocrystalline metals and alloys, *Inter J Fatigue*, 27, 1147-58, 2005.
- [10] Meyer LW, Sommer K, Halle T, Hockauf M, Crack growth in ultrafine-grained AA6063 produced by equal-channel angular pressing, *J Mater Sci*, 43, 7426-31, 2008.
- [11] Niendorf T, Rubitschek F, Maier HJ, Canadinc D, Karaman I, On the fatigue crack growth-microstructure relationship in ultrafine-grained interstitial-free steel, *J Mat Sci*, 45, 4813-21, 2010.
- [12] Goto M, Ando Y, Han SZ, Kim SS, Kawagoishi N, Euh K, The effect of microstructural inhomogeneity on the growth paths of surface-cracks in copper processed by equal channel angular pressing, *Eng Fract Mech*, 77, 1914-25, 2010.
- [13] Valiev RZ, Kozlov EV, Ivanov Yu F, Lian J, Nazarov AA, Baudalet B, Deformation behaviour of ultrafine grained copper, *Acta Metall Mater*, 42, 2467-75, 1994.
- [14] Valiev RZ, Approach to nanostructured solids through the studies of submicron grained polycrystals, *NanoStructured Mater*, 6, 73-82, 1995.
- [15] Goto M, Han SZ, Kim SS, Kawagoishi N, Lim CY, Significance of non-equilibrium grain boundaries in surface damage formation of ultrafine-grained copper in high-cycle fatigue, *Scripta Mater*, 57, 293-96, 2007.

INVESTIGATION ON DYNAMICS AND FATIGUE PREVENTION OF STEEL CATENARY RISER

L. Guo, M.L. Duan, M. Ye and G.M. Cheng

Offshore Oil/Gas Research Center, College of Mechanical and Transportation Engineering,
China University of Petroleum-Beijing, China

Abstract: This paper mainly elaborates the dynamic characteristics of steel catenary riser (SCR) and a prevention method of fatigue failure about the hanging end of SCR. A support device is designed for the hanging end of SCR, which provides a connector support with multiple degrees of freedom for risers and platform. Calculation is done to compare the maximum stress and fatigue life between traditional hanging devices and newly designed hanging support for SCRs. Calculation results show that the maximum dynamic stress of hanging end with newly designed support is 13MPa less than that of using traditional support based on the same loads, but the fatigue life of the former is much longer than that of the latter.

Keywords: Riser Hanging End; Stress Concentration; Hanging Device; Mode Analysis; Fatigue Life

1 INTRODUCTION

Deep-water floating platforms are applied widely along with the development of exploiting deep-water oil & gas. Pipelines are always connected to floating platforms by various risers, among which, a steel catenary riser (SCR) is used universally because it is very simple and convenient. Generally conventional SCR is clamped on a riser support which is a supporting trestle with a socket. Riser's bottle-cork hanging end is seated in the socket of the support, and then the riser is fixed by its gravity. Hence the connecting method of riser and platform can be described simply as a clamped-end beam. A riser always bears many loads, for example, wind, wave, fluid and loads caused by platform moving because it extends from the seabed to water surface and then to the hanging support of the platform. Hence safety of structure need to be placed great emphasis as riser is one of the most important oil and gas transmitting structures. As a result, study of riser mechanical properties based on extreme loads, study of vibration and fatigue, study of damage and fracture, etc. are common research subjects.

Chatjigeorgiou [1] considered the complete 3D nonlinear dynamic problem of an extensible, submerged catenary pipe conveying fluid and followed the Newtonian derivation procedure for describing the dynamics of the system. The flow inside the pipe was considered inviscid, irrotational and incompressible with constant velocity along the complete length of the pipe. The hydrodynamic effects were taken into account through the nonlinear drag forces and the added inertia due to the hydrodynamic mass. Li and Low [2] studied fatigue design problem of a steel catenary riser (SCR) at the touchdown point and addressed riser-seabed contact uncertainties through a systematic reliability analysis. Soil model uncertainties were characterized by three variables representing stiffness, suction and trench. First-order reliability method (FORM) was used in conjunction with the response surface method to estimate the failure probability without considering soil uncertainties. An inverse-FORM (IFORM) analysis was performed to determine the alteration of the safety factor for the same level of reliability, when the soil variables were incorporated. Katifeoglou and Chatjigeorgiou [3] quantified the sea-bottom soil reaction effect on the dynamics of a steel catenary riser by incorporating the soil reaction forces into the theoretical model of the dynamic equilibrium system. Several tests cases of top end harmonic excitations were performed to investigate the effect of the TDP soil reaction on the various dynamic parameters. Souza and Goncalves [4] investigated non-linear dynamics and fatigue life of risers. They determined lateral movement of the vessel by frequency spectrum and wave propagation function. They also researched the rule about how lateral moving loads effect riser responses and fatigue characteristics. Vandiver [5] studied the interaction of fluid and risers, and elaborated a VIV suppression law. Martins et al [6] did some research about the fatigue characteristics of riser's hanging end. They used model simplifying, linear approximation and progressive representation method to obtain the solution in frequency range.

In this paper, a method about mitigating stress concentration and improving fatigue life is found based on studying vibration and fatigue characteristics of a 1000m riser model. At last, the superiority of the designed riser hanging support is proved by some calculations and comparisons.

2 NEW MITIGATION METHOD OF RISER VIBRATION AND FATIGUE

Riser fatigue is always induced by vibration, so slowing down riser vibration is the first work to improve riser fatigue life. Two methods can change riser's vibration property: The first method is to adjust the inherent properties of the structure itself, for example, increasing the effective mass and damping. So nature frequency can avoid the common external excitation frequency band. As a result, resonance is prevented. Another method is to change conditions of vortex occurring and interfere flow patterns. So vortex introduced force is weakened. For example, various spoiler devices can prevent vortex forming and discharging and suppress riser vibration by changing the location of flow separation point. But the second method is applied widely.

The hanging end mode of conventional SCR can be described as a clamped beam at the upper and lower ends. Here, imagine altering the natural vibration properties of the beam model by changing its boundary conditions. That is to relieve the rotation constraint of riser's hanging end. Taking floating production storage & offloading (FPSO) for example, a relative angular displacement appears between a riser and FPSO due to rolling, pitching and yawing of the FPSO when the riser is clamped on the hanging end. Bending stress concentration also occurs because the stiffness of the FPSO is much larger than that of the riser. In addition, the connection method can easily transfer the moving of FPSO to the riser and then cause vibration. Based on the above analysis, a new riser hanging device is designed (see fig. 1).

The device includes a degree of freedom release mechanism (DOFRM) and a locking mechanism. DOFRM is composed by a frame and three gyroscope rings. The frame and gyroscope rings are all hinged by six hinges and the angles between the hinge's axis are all 60° . Hence a riser can keep relatively stable by the DOFRM though the FPSO is swinging dramatically. Locking mechanism is constituted by four hydraulic cylinders, a pressing ring, eight springs and eight petal-shaped clamps. The working principle of the locking mechanism is as follows: when riser's cork-like hanging end is located in the groove formed by eight petal-shaped clamps, the clamps are closed by the press of riser's gravity and then a large fastening force is formed. The fastening force can lock the riser tightly.

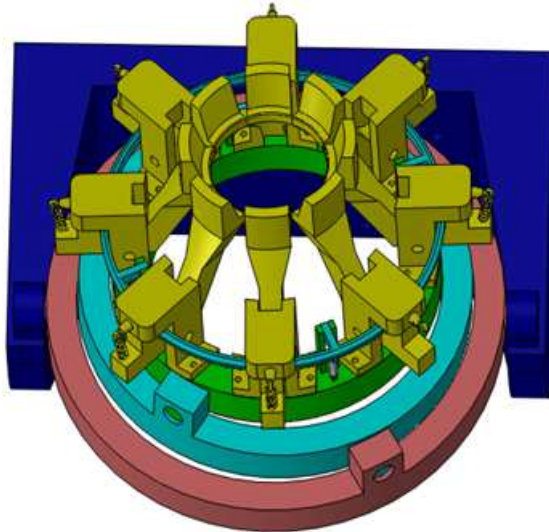


Fig. 1. Hinged riser hanging device.

3 VIBRATION CONTRAST BY USING AND NO USING HINGED HANGING DEVICE

This paper selects 1000m riser as a research target to investigate the mechanism properties of hanging end. Dimensions and material properties are as follows: outer diameter of 0.1778m, wall thickness of 0.025m, young's modulus of 2.1×10^5 MPa, Poisson's ratio of 0.3, density of 7850 kg/m³, strength limit of 439MPa. Table 1 shows the first 25 orders vibration frequencies and maximum amplitudes by using and no using hinged hanging device about 1000m riser.

After calculating, it can be obtained that the average frequency of the first 25 orders by using hinged hanging device is lowered down to 4.55% of that by using clamped hanging device. And the average amplitude reduces to 5.07% of the original value. The first order vibration frequency is 0.043054Hz and the corresponding vibration period is 23.23 s when the hanging end is clamped mode. The 25th order vibration frequency is 51.044 Hz and the corresponding period is 0.0196 s at the same mode. Generally the main energy concentrates in the waves with periods of 3 ~ 20 s, that is to say waves with the frequency of 0.05 ~ 0.33 Hz cause risers occurring heavy vibration. It can be seen from table 1 that the 3rd, 4th, 5th, and 6th order vibration frequencies are in the frequency range of 0.05 ~ 0.33 Hz whose corresponding amplitudes are 0.004817 m, 0.004824 m, 0.010060 m and 0.010065 m when hanging end is clamped mode. But the 13th to 24th order vibration frequencies are in the frequency band of 0.05Hz ~ 0.33 Hz when hanging end is hinged. The amplitude of 24th order is 0.00538 m which is higher than other orders.

Table 1. Comparison of vibration frequency and amplitude

Modal	Frequency (Hz)		Amplitude (m)	
	Clamped	Hinged	Clamped	Hinged
1	0.043054	0.001466	0.06901	0.00334
2	0.043275	0.001487	0.06902	0.00334
3	0.117020	0.004817	0.06564	0.00335
4	0.117120	0.004824	0.06563	0.00335
5	0.229040	0.010060	0.06574	0.00335
6	0.229100	0.010065	0.06573	0.00335
7	0.378470	0.017208	0.06573	0.00335
8	0.378510	0.017211	0.06572	0.00335
9	0.565300	0.026260	0.06572	0.00335
10	0.565320	0.026262	0.06572	0.00335
11	0.789510	0.037218	0.06572	0.00335
12	0.789520	0.037219	0.06572	0.00335
13	1.051100	0.050081	0.06572	0.00335
14	1.051120	0.050082	0.06572	0.00335
15	1.350000	0.064849	0.06572	0.00335
16	1.350100	0.064849	0.06572	0.00335
17	1.686400	0.081522	0.06572	0.00335
18	1.686410	0.081522	0.06572	0.00335
19	2.060000	0.100100	0.06572	0.00335
20	2.060100	0.100100	0.06572	0.00335
21	2.882000	0.140260	0.10126	0.00507
22	2.882100	0.140260	0.10126	0.00507
23	3.446300	0.168190	0.10567	0.00538
24	3.446310	0.168200	0.10567	0.00538
25	51.07400	2.603300	0.05950	0.00303

If waves with the period of 8 s act on two different kinds of risers with clamped and hinged hanging device separately, the riser with clamped hanging device presents the 4th order vibration and its amplitude is 0.06563 m. But the riser with hinged hanging device presents the 21st order vibration whose amplitude is 0.00507m. The amplitude of the former is 12.95 times that of the latter. It can be seen, different riser hanging mode may cause different vibration state largely when working condition is the same, and the designed hanging device can decrease riser's vibration to 10% at least of that when the device is not used. Hence relieving portion constraints and releasing portion freedoms of riser's hanging end can reduce the damaging effects from riser vibration significantly.

4 STRESS AND FATIGUE LIFE CONTRAST BY USING AND NO USING HINGED HANGING DEVICE

To contrast the stress distribution and fatigue life about using and no using hinged hanging device, a model the same as modal analysis in part 3 is applied. A 1000 m long riser is simulated by beam elements, and it is divided into 100000 elements. Node 1 is set to the origin coordinates which is on behalf of the riser length 0 m position. The top node number 100001 presents the riser length 1000 m position.

4.1 Contrast of stress distribution characteristics

Boundary conditions and loads are as follows when riser's hanging end is clamped: Both the top end and bottom end are clamped but a 5° rotation is added at the top end to simulate the angular displacement caused by waves between the riser model and platform. A force 30000 N is exerted at Node 99000 which stands for wave loads and the result is shown as fig. 2. Note that Node 99000 means 990m position.

Boundary conditions and loads of hinged hanging model are as follows: a whole constraint is used to simulate the connection of the riser and the pipeline, but translations are restricted while rotations are released at hanging end. A 30000 N concentrative force is also appended at the point Node 99000 (see fig. 3)

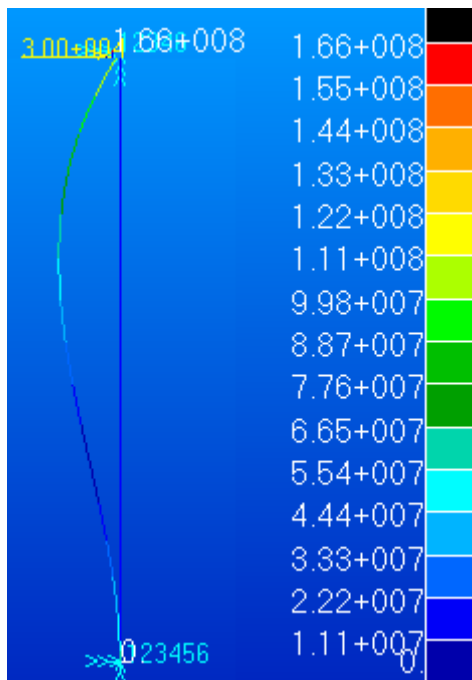


Fig. 2. Stress of clamped hanging model.

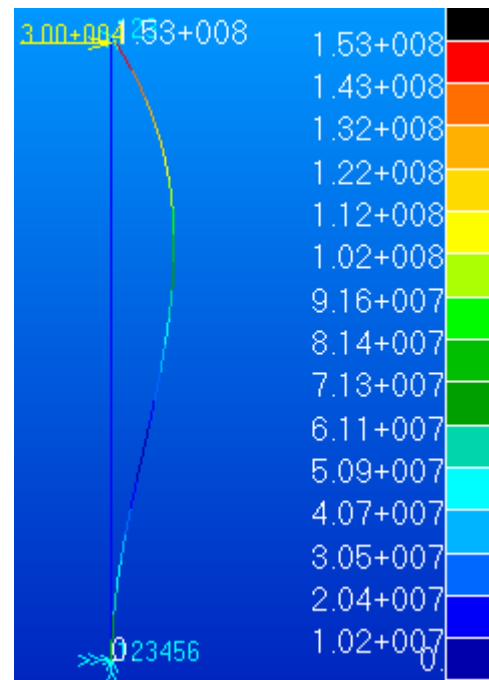


Fig. 3. Stress of hinged hanging model.

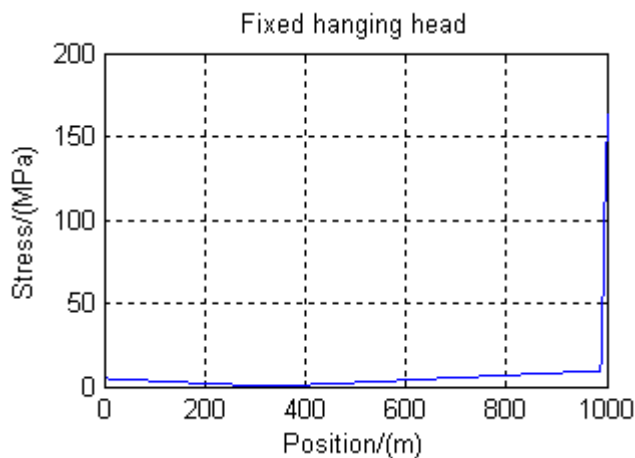


Fig. 4. Stress distribution of clamped hanging end.

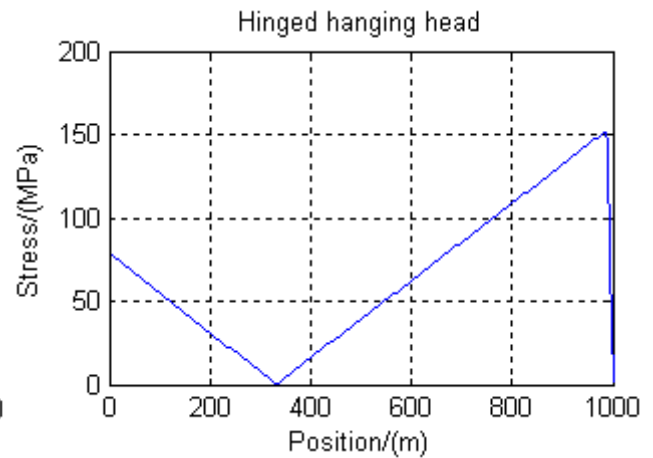


Fig. 5. Stress distribution of hinged hanging end.

When hanging end is clamped the maximum bending stress calculated is 166 MPa (see fig. 2), and the corresponding stress distribution along with riser length are shown as fig. 4. Inflexion points appear at the length position 330 m and 990 m separately. And the minimum stress which is 0.49 MPa is at the point of 330 m. Stress curve is divided into two obvious parts by the point of 990 m, of which the stresses are lower than 10 MPa at the length range of 0~990 m. But the stress jump to a peak value 166 MPa at the short length range from 990 m to 1000m. Stress curve inflexions also appear at the points of 330 m and 990 m position as shown in fig. 5. But the difference is that the stresses distributing at the length range 0~990 m are much larger than that of no using hinged hanging device. Some stresses are even larger than 50 MPa. The minimum stress is at the point of 330 m position which is 0.44 MPa and the maximum stress is at the point of 990m position which is 153MPa (see fig. 2 and 5). Stresses decline rapidly from the position of 990 m to 1000 m and it decrease to 0 MPa at the hanging end which is 1000 m position. A big difference of stress distribution is caused by different hanging devices though the load conditions are the same after comparing the two models. It can reduce stress concentration by using the designed hanging device and the maximum stress is reduced by 13 MPa while the minimum stress is also reduced by 0.44MPa. Because the former has a serious stress concentration and the latter has no stress concentration, the latter is better than the former though some stress value is larger. As the two maximum stress values are much lower than the ultimate strength of the material, both of them are within the safe strength range. But riser safety assessment also includes fatigue life assessment, so fatigue life need to be investigated. Please see the fatigue life calculation section at part 4 for detail.

4.2 Contrast of stress distribution characteristics

(1) S-N properties of selected material

Power function is always the common form to describe material's S-N curve as follows.

$$S^m N = C \quad (1)$$

C and m are parameters associated with material, stress ratio, loading etc. take the log of the above equation, then it turned into equation (2):

$$\lg S = A + B \lg N \quad (2)$$

Where, $A = \lg C / m$, $B = -1 / m$.

The material selected is Q235A, whose ultimate strength is 439 MPa. The corresponding B is 14.6843.

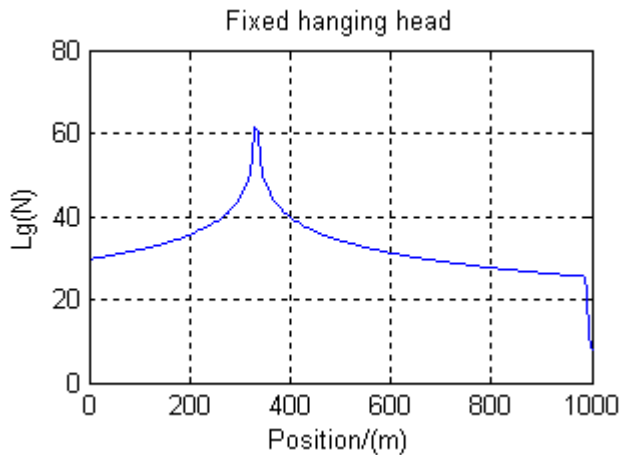


Fig. 6. Fatigue distribution of clamped hanging end.

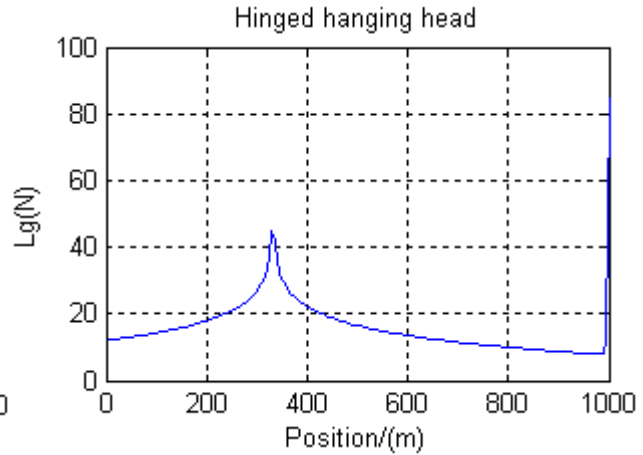


Fig. 7. Fatigue distribution of hinged hanging end.

(2) Loading form

A sinusoidal alternating load $F = 30000 \sin(2\pi t)$ which is equivalent to a wave load whose amplitude is 30000 N and period is 10 s. So calculated fatigue life can be described by number of circles, and a circle stands for 10 s which is the real time a riser working in the real working condition. Then fatigue life can be

described by years after turn the total circles into corresponding time year according to the transformation relationship of circle-time.

(3) Calculated fatigue result

When hanging end is clamped mode, calculated logarithmic circles are shown as fig. 6. Logarithmic circle curve is similar to the corresponding stress distribution curve that two inflexions also appear at the position 330 m and 990 m. The maximum value is 61.5281 corresponding to 3.3734×10^6 circles, and the minimum value is 7.3262 corresponding to 2.1192×10^7 circles. So the fatigue life is 6.72 years when the total minimum circles are turned into years.

Similarly, when hanging end is hinged mode, the distribution curve of logarithmic circles is shown as fig. 7. It also is divided into 3 parts by points of 330 m and 990 m and the value of logarithmic circle tends to infinity at the point of 1000 m. But the minimum value is 7.8577 (appear at the position of 990 m) corresponding to 7.2054×10^7 circles, which is 22.85 years when the minimum number of circle is turned into year.

It can be seen that both the two hanging modes are safe because their maximum stress values are much less than their material ultimate strength based on the same working conditions. But their fatigue lives are different largely. The fatigue life of the latter is 3.4 times that of the former. So the designed hanging device can increase the target riser's fatigue life from 6.72 years to 22.85 years.

5 CONCLUSIONS

The paper elaborates a method to release stress concentration of riser's hanging end and to improve riser's total fatigue life. The newly designed hanging device is much more excellent than the original hanging device. Its superiorities are mainly in the following aspects:

- (1) DOFRM of the newly designed hanging device is similar to the gimbal structure of a gyroscope. So a riser can do self-regulation by its gravity to be a balance state when it is put on the device. The structures of three hinged rings can prevent the transforming of movements from a FPSO. Hence a riser can keep a stationary state.
- (2) By contrasting modes of the first 25th orders, vibration frequencies and amplitudes are all decreased obviously after using the designed device. The amplitude is reduced 0.1 times that of no using hinged hanging device. Hence the device can slow down riser vibrating significantly and reduce the occurrence of vibration fatigue greatly.
- (3) Rotation freedoms between the riser and FPSO are increased by using newly designed hanging device. So a riser can rotate freely without bending force occurring in the connecting position. Hence the device can prevent the bending stress occurring though the FPSO is swinging heavily.
- (4) Rotation constraints between the riser and FPSO are relieved by using newly designed hanging device. It makes the stress curve much smoother as well as eliminates stress concentration. As a result, the maximum stress is reduced by 13 MPa and the maximum working life is increased to 3.4 times of the original life based on the same working conditions. -

6 ACKNOWLEDGEMENTS

The authors would like to acknowledge the support of Major Pproject for Science and Technology Development 'Deep underwater emergency repair equipment and technology' (2011ZX05027-005) as well as Major Project of Chinese National Programs for Fundamental Research and Development (973 Program) 'Extreme environmental effects of deep-water engineering structures and the whole life in service safety' (2011CB013702).

7 REFERENCES

- [1] IK. Chatjigeorgiou.(2010) Three dimensional nonlinear dynamics of submerged, extensible catenary pipes conveying fluid and subjected to end-imposed excitations. International Journal of Non-Linear Mechanics. 45(7): 667-680, 2010.
- [2] FZ. Li, YM. Low. Fatigue reliability analysis of a steel catenary riser at the touchdown point incorporating soil model uncertainties. Applied Ocean Research. 38: 100–110, 2012.

- [3] SA. Katifeoglou, IK. Chatjigeorgiou. Dynamic interaction of catenary risers with the seafloor. Applied Ocean Research. Applied Ocean Research 38: 1–15, 2012.
- [4] G.FM. Souza, E. Goncalves. Fatigue performance of deep water rigid marine risers. 7th International Offshore and Polar Engineering Conference, May 25-30, 1997, Honolulu, USA. pp. 144-151.
- [5] JK. Vandiver. Research challenges in the vortex induced vibration prediction of marine risers. Offshore Technology Conference. May 4 – 7, 1998, Houston, Texas. pp. 155-163.
- [6] CA. Martins, E Higashi, RMC. Silva. A parametric analysis of steel catenary risers: fatigue behavior near the top. Proc. of the 10th International Offshore and Polar Engineering Conference, May 28 - June 2, 2000, Seattle, Washington, USA. pp. 54-59.

NUMERICAL MODELING OF AXIALLY LOADED SUCTION PILE

G.M. Cheng¹, M.L. Duan¹, L. Guo¹ and F. Wang²

¹ China University of Petroleum, Beijing

² China Oilfield Services Limited, Tianjin

Abstract: The load bearing mechanism of soil is not completely understood, so the numerical method is widely used in geotechnical engineering. In this paper, the ABAQUS software is used to model the axial bearing capacity of suction piles in offshore application. The clay plasticity model is used for soil and elastic model for suction pile. The parameters and boundary conditions are set according to a experimental test by other researchers. The result shows that the numerical model works well. So the numerical analysis is an efficient and reliable method in geotechnical engineering.

Keywords: Suction pile; Bearing capacity; Numerical analysis;

1 INTRODUCTION

Suction piles have the advantages of precisely positioning, easy of recovery, reusable, less dependency on heavy installation equipments, capable of bearing significant lateral load and torque, short installation time[1], less sensitive to upper layer soil properties etc.. So suction piles is widely used for anchoring floating structures, foundations of subsea equipments in offshore oil and gas industry .

Scholars have done many work to understand the mechanism of load bearing of suction piles. P.G. Watson, M.F. Randolph, M.F. Bransby[2] conducted a four-year study of bearing capacity of caisson foundations by centrifuge models and numerical analysis. Knut H. Andersen, Hans Petter[3] researched the principles of suction foundations and anchors in clay. They also presented the procedures for penetration analyses and capacity calculation. H.A. Taiebat, J.P. Carter[4] worked on the interaction of forces on caisson in undrained soils by numerical method.

Because the suction pile is widely used for anchoring system, these researches are mainly on the pull-out capacity, lateral capacity and capacity under cyclic load. There are less work on the compression capacity. Scholars tend to recommend empirical formulas for compression capacity calculation in engineering. But as we know the subsea production system is used more and more, and suction pile is a kind of perfect foundations for these systems. So it is worthy of more intensive research on the mechanism of compression bearing of suction piles.

2 COMPRESSION BEARING CAPACITY OF SUCTION PILES IN CLAY

2.1 API method for compression bearing capacity of driven pile

Many scholars suggest that the method for calculating the compression bearing capacity of driven piles in API RP 2A-WSD should be used in engineering of suction pile. The method for calculating driven pile's bearing capacity in API RP 2A-WSD[5] standard is as following.

The ultimate bearing capacity

$$Q_d = Q_f + Q_p = fA_s + qA_p \quad (1)$$

Where, Q_d ——ultimate bearing capacity, kN; Q_f ——skin friction, kN; Q_p ——total ending bearing, kN; f ——unit friction capacity, kPa; A_s ——side surface area, m^2 ; q ——unit end bearing capacity, kPa; A_p ——end area of pile, m^2 .

In cohesive soil, such as clay discoursed here, the unit friction capacity f and unit end bearing capacity q are calculated as following.

Unit friction capacity

$$f = \alpha c \quad (2)$$

Where, α ——dimensionless factor, $\alpha \leq 1$. When $\psi \leq 1.0$, $\alpha = 0.5\psi^{-0.5}$; when $\psi \geq 1.0$, $\alpha = 0.5\psi^{-0.25}$.

$$\psi = c / p_o' \quad (3)$$

Where, p_o' ——effective overburden pressure, kPa; c ——undrained shear strength, kPa;

Unit end bearing capacity

$$q = 9c \quad (4)$$

Where, c ——undrained shear strength, kPa;

2.2 Model experiment on the bearing capacity of suction pile

Felipe A. Villalobos, Byron W. Byrne, Guy T. Houlsby [6] worked on the experiment of suction foundations under monotonic and cyclic vertical loading. They took the installation behaviour into consideration and got high quality experimental data. The caisson was of 150 mm diameter, 150 mm length and 1 mm wall thickness. The soil they used is overconsolidated Speswhite kaolin clay in 450 mm diameter and 900 mm height cylindrical tanks.

The result of the post-installation loading response experiments showed that the maximum load capacity of the suction pile is 1545N, and the corresponding vertical displacement is about 20 mm downward. The vertical displacement-load relationship is showed in fig. 1.

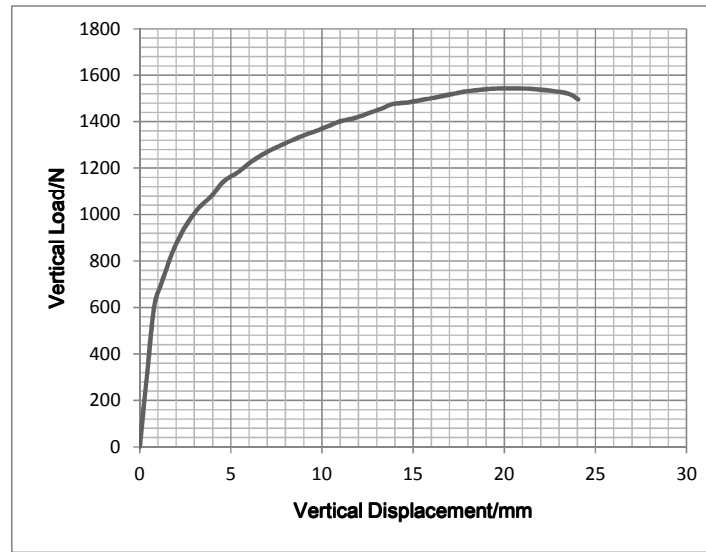


Fig.1. Vertical Displacement-load Relationship.

The numerical model will be constructed according to this experiment and the result of the simulation will be compared with the result of this test.

2.3 Finite Element Method(FEM)

FEM is useful in engineering. It's easy to use, and the results are reliable as showed by many applications.

We can use FEM to do design, to compare with calculations and experiments.

For FEM in geotechnical engineering, the constitutive relation of soil is the basic of numerical calculation.

The constitutive models of soil for numerous calculation have been developed significantly in the past four to five decades[7]. There are many types of constitutive models: elastic, simple elastic plastic, critical state, incrementally nonlinear, multiple surfaces, double hardening, bounding surface and single yield surface type. Each type has one or more models. The first three types is what we mostly used. The modified Cam Clay model belongs to the critical state type.

Cam clay and modified Cam clay models are the first critical state models developed by researchers at Cambridge University in 1968[8, 9]. In 1963, Roscoe[8] formulate a complete stress-strain model for normally consolidated or lightly over-consolidated clay as the Cam-clay model. And after that, the model was modified to three-dimensional stress state by Roscoe and Burland[9] in 1968.

The modified Cam-Clay use the means of hardening plasticity to model the non-linear behavior of soil. A plasticity model includes (1) a yield criterion that predicts whether the material should respond elastically or plastically due to a loading increment, (2) a strain hardening rule that controls the shape of the stress-strain

response during plastic straining, and (3) a plastic flow rule that determines the direction of the plastic strain increment caused by a stress increment.

The model used in Abaqus for modeling cohesionless materials is an extension of the “modified Cam-clay” theory. For extended Cam-clay theory, a strain rate decomposition, an elasticity theory, a yield surface, a flow rule, and a hardening rule are used. The main features of the model are the use of an elastic model which exhibits an increasing bulk elastic stiffness as the material be compressed, and for the inelastic part of the deformation a particular form of yield surface with associated flow and a hardening rule that allows the yield surface to grow or shrink.

3 FE MODELLING

The geometrical shape is axisymmetrical. So in order to save the calculation cost, the model is constructed as axisymmetrical parts. Because the time of the load applying is very short, the surrounding soil is modeled in an undrained manner. The downward axial loading is applied to the top of the pile using downward displacement. The soil inside the pile can be treated as part of the pile as rigid body, since that the problem is under undraind condition and there will be no volume or shape change of that part soil.

The model is axismmetical about the left edge. The dimensions are the same as the experiment equipments used in Felipe’s test mentioned above. The pile was of 150mm diameter and penetrate into the soil 150mm before load apply. The soil tested was in a tank with 450mm diameter inside and 900mm in length.

In geotechnical FE model, the mesh is critical for the convergence of the calculation. Too dense mesh will decrease the numerical efficiency, and too loose mesh will cause inaccuracy result. The mesh also matters about the time increment of the calculation. So dense mesh is used in the area near the pile that may experience large strain, and loose mesh is used in the area far from the pile to improve the calculation efficiency. The pile and the soil in it is constructed as on part and use 4-node bilinear axisymmetric quadrilateral element(CAX4). The soil around the pile is meshed with 4-node bilinear displacement and pore pressure element.

The pile is assumed to be linear elastic. The material properties of the pile is of 20GPa Young’s modulus and Poisson ratio of 0.2. The coefficient of friction is assumed to be 0.42. The soil is modeled with clay plastic. The parameters of the material properties used for soil are showed in the following table 2. The initial stress of the soil is assumed to vary with depth linearly.

Table 2. Soil material properties

Property	Value
Average effective unit weight, γ'	6.82 kN/m ²
Poisson ratio, ν	0.35
Logarithmic plastic bulk modulus, λ	0.20
Stress ratio at critical state, M	1.20
Log bulk modulus, κ	0.040
Intercept, e_1	2.0
Permeability, k	3×10^{-9} m/s

The specific weight of water is 10 kN/m³. The void ratio varies with depth according to the equation (5):

$$e_0 = e_1 - (\lambda - \kappa) \ln p'_c - \kappa \ln p'_0 \quad (5)$$

Surface to surface contacts are established at the soil-pile interface. The tangential behavior of the contact surface is penalty with a friction coefficient of 0.42. The “hard” contact option is used for normal behavior.

4 CONCLUSIONS

The result of the calculation is compared with the result of the experiment in fig. 2. The difference becomes larger after the axial displacement reaching 3.5mm and the load arriving at 1040N. This phenomenon may be caused by the plastic strain in the FE analysis being well distributed than in the experiment soil and the soil was not “set up” efficiently before being loaded. So more side friction is mobilized in FE model and as a result the vertical bearing capacity is bigger.

In the experiment, the downward load was converted to upward at the maximum load of 1545 N and the displacement reaches 20 mm when the bearing capacity no longer increase with the displacement. The change of the load direction caused a turn down at the end of the line. In the FE model, the bearing capacity is about 1610N at the displacement of 20 mm. The deviation from the experimental result is about 4.2%. After that the load continues to increase in the FE model with the increase in axial displacement. This may be caused by the FE soil model is continuous and no break is possible. This is not the reality in the experiment. But the increase after that is very slow. It is about 8N/mm in 20~25 mm displacement and 2 N/mm in 25~30 displacement. So the result of the FE analysis is of good agreement with that of the experiment.

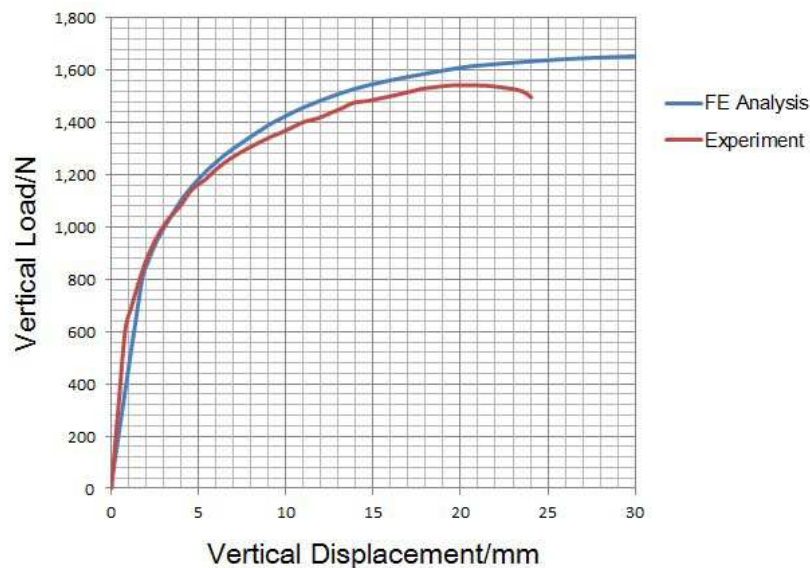


Fig.2. Comparison between FE Analysis and Experimental results.

5 REFERENCES

- [1] Li, Y. and J. Zhang. On the Suction Pile Relocation Distance. 2012: The International Society of Offshore and Polar Engineers.
- [2] Watson, P., M. Randolph and M. Bransby. Combined lateral and vertical loading of caisson foundations. 2000.
- [3] Andersen, K. and H. Jostad. Foundation design of skirted foundations and anchors in clay. 1999.
- [4] Taiebat, H.A. and J.P. Carter, Interaction of forces on caissons in undrained soils. PROCEEDINGS OF THE FIFTEENTH (2005) INTERNATIONAL OFFSHORE AND POLAR ENGINEERING CONFERENCE, VOL 2, 2005: p. 625-632.
- [5] Institute, A.P., Recommended Practice for Planning, Designing and Constructing Fixed Offshore Platforms—Working Stress Design, in RP 2A-WSD. 2000.
- [6] Villalobos, F.A., B.W. Byrne and G.T. Houlsby, Model testing of suction caissons in clay subjected to vertical loading. Applied Ocean Research, 2010. 32(4): p. 414-424.
- [7]. Lade, P.V. Overview of constitutive models for soils. 2005: ASCE.
- [8] Roscoe, K.H., A. Schofield and A. Thurairajah, Yielding of clays in states wetter than critical. Geotechnique, 1963. 13(3): p. 211-240.
- [9] Roscoe, K.H. and J.B. Burland, On the generalized stress-strain behaviour of wet clay. 1968.

SOLUTIONS FOR S-LAY VESSELS TO INSTALL SUBSEA PRODUCTION SYSTEMS

Mao Ye¹, Menglan Duan¹, Mingjie Li¹, Chenbo Zhao², Wei Li³, Guangluan Li⁴ and Zhenguo Hu⁵

¹ China University of Petroleum, offshore oil & gas research centre, Beijing, China

² Shandong Natural Gas Pipeline Co., Ltd, Qingdao, China

³ Tianjin Space Rocket, Tianjin, China

⁴ China ShengLi Oil Field Co Ltd, Dongying, China

⁵ China Offshore Oil Engineering Co Ltd (COOEC), Tianjin, China

Abstract: This paper presents a new engineered interdependency of pipe-laying vessels and related installation techniques when an S-lay vessel, HYSY201, comes into service and a J-lay vessel, 2*8000t, begins service on oil & gas pipelines under the South China Sea (SCS). The authors present new research-led advancements in these pipe-laying vessels which enable recovery and abandonment of pipelines while installing SPFs (Subsea production facilities). They present improved operation procedures for J-lay vessels and a new multi-functional SPF installation system, which is designed based on the concept of a J-lay model, which they developed at China University of Petroleum's Offshore Oil & Gas Research Center. This system enables the S-lay vessels to install SPFs and also expands the capability of J-lay vessels. This research combines safer, more efficient and more economical methods in these newly designed systems with corresponding instructions and guidance for SPFs' installation of pipelines in the SCS using both S-lay and J-lay vessels.

Keywords: S-Lay; J-Lay; Subsea Production Facilities Installation System; Abandon & Recovery of Pipeline

1 INTRODUCTION

Pipe-laying techniques and the installation of subsea production facilities (SPFs) are difficult, and they are the focus of this research. Because SPFs provide the link between subsea pipelines, wells and floating production platforms, SPFs are indispensable in deep water oil and gas exploitation. In a field development plan, SPFs are installed before or after pipe-laying using installation vessels. However, if extreme sea conditions are encountered, the pipelines need to be abandoned and then recovered.

For a J-lay system, except for the ability to lay pipelines; it has functions to install small-size PLETs, and can also be used to abandon or recover pipelines. However, functions of an S-lay system are limited as it has a stinger at the vessel's stern (Zhou 2008). As a result, other supporting vessels are needed to enable it to realize these functions (Perinet et al. 2007). Thus, it becomes very important to introduce the J-lay concept to the S-lay method in order to accomplish the whole process using one vessel (Jiang et al. 2009; Duan

2010 and Duan et al. 2010). By doing this, construction duration can be shortened and cost can be reduced (Hebret 2004 and Heerema 2005).

In order to ful-fill development needs in the south china sea (scs), the China National Offshore Oil Corp (CNOOC) built a 3000 m (Wang et al. 2010) water depth S-lay vessel (HYSY201), and is planning to build a semi-submersible J-lay vessel (2*8000t) (Chen et al. 2012). The author summarized the techniques of pipeline laying, abandonment & recovery and subsea production facility installation both at home and abroad, the purpose of which is to provide some references and guidance on S-lay and J-lay methods. As there is a shortage of deep water installation vessels, the concept of a multi-functional vessel is very important, so a multi-functional subsea facility installation system is illustrated in this paper and a new installation method is also presented.

2 FUNCTIONALITY OF J-LAY SYSTEM

The main functions of a J-lay system include three aspects: pipe-laying, abandonment and recovery of pipelines and subsea facility installation (Cavicchi et al. 2003 and Guan et al. 2011).

2.1 Procedures of pipe-laying

A pipe-laying process is comprised of the following steps: stalk upending/pipe loading, tower angle adjustment, pipe lowering, pipe line-up, welding, coating & testing (Hansan et al. 2001 and He et al. 2011).

- [1] Pipe loading: This step brings the pipe from the loader, which is horizontal, to the vertical J-Lay tower. The pipe can be loaded by winch clamp, chain, four-bar linkage structure or hydraulic four-bar linkage rotation arm (Baugh 2001a and Baugh 2001b).
- [2] Tower angle adjustment: The appropriate angle is determined by the laying pipe diameter and water depth. The use of a tower angle adjuster can adjust the angle and also provide support for the tower. Two types of angle adjusters are commonly used, hydraulic cylinder adjusters and pin-type adjusters (Moszkowski et al. 2004; Baugh2002a and Baugh 2002b).
- [3] Pipe lowering: The pipe will be lowered into water through the tower. There are mainly two methods, crane & collar (slip recess) lowering and tensioner lowering.
- [4] Pipe line-up: This is the process in which the laying pipe is lined up with the already laid pipe, and it is carried out by both internal and external centralizers.
- [5] Welding: The laying pipe and laid pipe are connected by welding, either manually or automatically.
- [6] Coating & testing: Flaw detection is carried out on the welded pipe in this step, followed by pipe coating.

2.2 Procedures of pipeline abandonment & recovery

Pipelines are always temporally abandoned when facing harsh weather conditions and the appropriate abandonment process for a J-lay system is summarized below (Andreuzzi et al. 1981, Frank et al. 2002, BP Trinidad et al. 2001, Heerema; Fan et al. 2013):

- [1] Lower the A&R Socket. Start the winch, lead the A&R line to the sheave block locating at the top of the tower, and then lower the A&R line.
- [2] Transfer the buoys and A&R tug head to the welding station.
- [3] Connect the A&R socket and hook. Hoist the hook and adjust its attitude using a small crane after the A&R wire has been landed to the targeting position. Connect the A&R socket and hook using pins under the support from working staff.
- [4] Connect the A&R hook and buoys. Lift the buoys up using the crane of the vessel until the steel cables at the bottom of the buoys are at the same height as the A&R hook and then fix the steel cables on the hook. Release the crane cable until the buoys are parallel to the deck and lift the hook by retrieving the A&R line. Disconnect the crane cable after all the weight of buoys has been transferred to the A&R line.
- [5] Connect the A&R line and the A&R tug head using riggings.
- [6] Connect the A&R tug head and the 2nd part of pipe section and then weld.
- [7] Tension Transferring. The A&R line is free of load when the friction clamp holds the pipe and sustains the tension of pipe. As the tension from the friction clamp decreases, the tension of the A&R line increases until all the tension is transferred to the A&R winch. At this point, open the traveling clamp and lower the pipe into water under constant tension. At the same time, the A&R line should be released slowly to avoid damage to the buoys. Activate the A&R line limiting device to prevent large movement when all the pipes and buoys have lowered into the water.
- [8] Continue the process. Lower the pipe section to the seabed, and disconnect the A&R hook and buoy by ROV when the abandoned buoys are 60 degrees to the vertical direction.

2.3 SPFs Installation Technique

PLET, WSA (Wye Sled Assembly) and ILS (in-line-sled) are three important types of connectors in the subsea system, whose function is to provide connection between pipelines and SPFs. The ability to install PLET (Forbord et al. 2007; Antani et al. 2008 and Wang et al. 2011), WSA (Dyson et al. 2004 and Wolbers et al. 2003) and ILS [Huang et al. 2009] is peculiar to the J-lay method. There are mainly two types of installation methods of PLET:

2.3.1 PLET 1st installation

- [1] Adjust PLET's attitude. Use the PLET operation system; make it vertical from horizontal.
- [2] Start pipe-laying procedures. Move the pipes to the work table of the tower; install buckle arrestor and anode block.
- [3] Connect PLET and pipe. Move PLET to a lower position of the pipe and line them up. Connect them by flange connection or welding.

- [4] Lower the whole structure. Lift PLET using an elevator or a tensioner and retract PLET operation system.
- [5] Continue the pipe-laying procedures. Continue the normal procedures until PLET is approaching the seabed.
- [6] Adjust PLET's attitude. Connect the auxiliary cable to PLET; then, pull it to make PLET horizontal and open the mud mats. Connect the free end of the inhibit line to the hook of ROV; land PLET to the target location after necessary measurements to ensure the location, orientation and inclination. Disconnect the auxiliary cable and prepare for subsequent work.
- [7] Continue the pipe-laying procedures until the pipe-laying process has been finished.

2.3.2 PLET 2st installation

- [1] Recover subsea pipelines. Use the J-lay system to recover subsea pipelines and hang the pipelines on the fixing device.
- [2] Move PLET into place. Lift PLET using the crane of the vessel and move it to the welding station.
- [3] Connect PLET with pipeline. Connect PLET base with the second end of pipeline by flanged connection or welding.
- [4] Lower PLET and pipeline. Connect A&R line with the first end of PLET; lift the whole structure by retrieving A&R line. Open fixing device, transfer tension from friction clamp to A&R line, and lower PLET and pipeline to sea surface.
- [5] Lower the whole structure to sea bed. During this process, open the limiting device of A&R wire to limit the oscillation of PLET. Vessel movement should be coordinated at the same time.

2.3.2 WSA(ISL) installation

- [1] Fix the pipeline. Fix the installed pipeline to hang-off table.
- [2] Put WSA (ILS) in place. Transfer WSA (ILS) to J-lay tower by crane.
- [3] Connect the facilities to pipeline. Connect the lower section of WSA (ILS) to the installed pipeline by flanged connection or welding.
- [4] Move the hang-off table by sliding. Move the whole structure outside of the welding station by hang-off table.
- [5] Lower the whole structure. Switch on the hang-off table, lower a certain distance of the whole structure by crane, providing enough space to make room for the pipe waiting for welding.
- [6] Move the hang-off table by sliding. Switch off the hang-off table; move it to the welding station.
- [7] Connect the facility to pipeline. Connect the upper section of WSA (ILS) to the laying pipe by flanged connection or welding.

- [8] Continue pipeline laying procedures until WSA (ILS) has been installed to the seabed. Vessel movement and adjustment of the J-lay tower should be coordinated at the same time.

As the above steps demonstrated, a J-lay system can efficiently take care of pipeline installation, pipeline abandonment & recovery and small dimension subsea facility installation. For large dimension subsea facilities, specially designed systems are needed.

3 FUNCTIONALITY OF S-LAY SYSTEM

The working flow line of an S-lay system (e.g., pipe transfer, welding, and coating) has a horizontal layout. All the operations are carried out on the deck of the vessel. The S-lay system has several welding stations, and many procedures can be done at one time, so it has a faster pipe laying speed than the J-lay system.

3.1 Procedures of pipeline abandonment and recovery

Before being abandoned, an A&R tug head will be welded to the second end of the pipe, and later, it will be connected to the A&R hook. As the vessel moves ahead, the A&R winch will provide the tension needed for the pipe instead of the tensioner. When the pipe has left the tensioner completely, connect the rope which has buoys to A&R tug head, and then release the rope. Make sure the pipe is under a constant tension when lowering. After the pipe has touched the seabed, disconnect the rope and A&R tug head to finish this pipe abandonment process. The rope will be floating in the sea because of the buoys.

3.2 Techniques for SPF installation

Because of the stinger, it is difficult for an S-lay vessel to install SPFs. In order to install the facilities, the structure of PLET or mud mat needs to be redesigned, or an installation vessel is needed.

During the pipe abandonment and recovery process, the buoys cannot go through the stinger; hence they can only be installed (or removed) after the pipe has left (or reached) the stinger. In addition, the S-lay system cannot install SPFs independently.

4 DESIGN OF THE MSPFIS (MULTI-FUNCTIONAL SUBSEA PRODUCTION FACILITY INSTALLATION SYSTEM)

A Multi-functional Subsea Production Facility Installation System (MSPFIS) is designed to deal with the disadvantages of both S-lay and J-lay systems, e.g., the S-lay system cannot install SPFs or abandonment and recovery pipeline conveniently and the J-lay system cannot install large SPFs independently and it also provides very limited operation space for pipeline abandonment and recovery.

This multi-functional system has nine parts, depicted by Fig. 1 as 1, top sheave; 2, upper operation platform;

3, tower structure; 4, lower operation platform; 5, SCR fixing device; 6, SCR limiting device; 7, fast connection joint; 8, A&R Wire limiting device; and 9, PLET positioning socket. Details of the configuration of the main parts are shown in Fig.2.

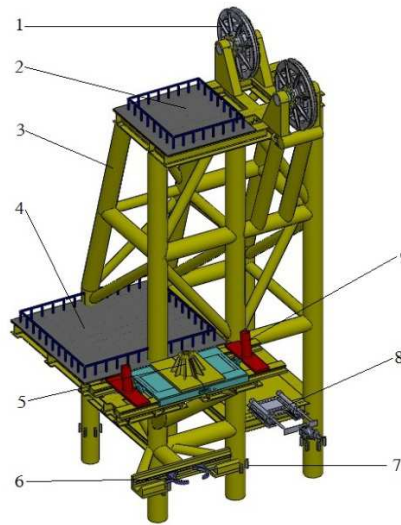


Fig. 1. Sketch of the MSPFIS.

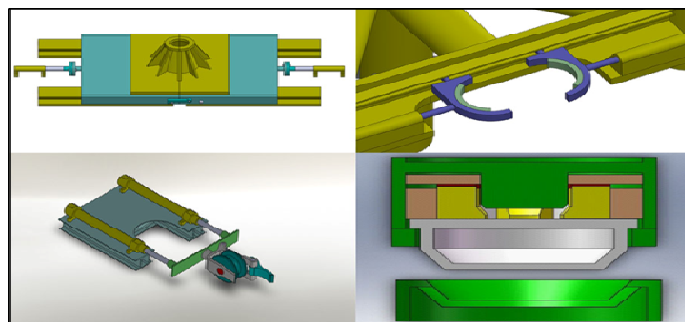


Fig. 2. Enlarged components of the MSPFIS.

The function of the top sheave is to lead the A&R line to the operation platform. The upper operation platform can assist the positioning of PLET during the PLET installation process, besides assisting some other operations. The truss type tower structure supports the whole system, and it is fixed to the deck by a cylindrical structure to decrease the deck area occupied by operation platform. The lower operation platform provides working space for the assisting operations, e.g., connection, buoys installation, and riggings installation. The SCR fixing device can fix the pipes with different diameters, which helps the connection between pipes and other facilities. The SCR limiting device can limit the range of motions of pipes when the vessel is under bad sea conditions, which assures the stability and accuracy of welding and other operations. The fast connection joint is able to connect or disconnect the tower structure and the deck very fast, which enables fast removal of the tower and provides more flexibility to the deck. In addition, the internal configuration of the fast connection joint can reduce the relative rotation between the tower and the deck.

The A&R Wire limiting device can inhibit large range oscillation of A&R line, thus assuring the accuracy of installation. The PLET positioning socket is designed to position the PLET during its installation process, so it is helpful for the connection of PLET and pipe.

This MSPFIS has a stable structure but requires a small deck area that is easy to be removed. More importantly, it can position PLET very accurately, inhibit large range movement of pipe and A&R wire, fix pipes with a wide range of diameters and provide a specialized working platform for assisting operations.

5 NEW INSTALLATION METHOD

The process for pipeline abandonment and recovery as well as SPF installation are described below after the employment of MSPFIS.

5.1 Procedures for pipeline abandonment and recovery

This is an example based on the pipeline abandonment process as pipeline recovering is the reverse process of pipeline abandonment, and the procedures are illustrated below:

- [1] Install A&R tug head at the second end of pipe and then install buckle arrestor and anode block, these steps are carried out on deck (S-lay) or tower (J-lay).
- [2] Lift the pipe to the fixing device by crane.
- [3] Activate the SCR fixing and limiting devices to prevent large pipeline movements.
- [4] Connect the SCR head and buoy by rigging, and connect rigging to the triangle plate.
- [5] Lift the SCR to certain height by crane.
- [6] Open the SCR fixing and limiting device and lower the pipe after finishing the connection.
- [7] After lowering to a certain depth, transfer pipeline to the bottom of the top sheave by crane, and connect A&R winch wire to the triangle plate; then increase the tension of A&R wire gradually.
- [8] Release the crane wire and activate the A&R wire limiting device when the A&R wire bears all the weight of the pipe.
- [9] Complete the abandonment process after the pipe is down to the seabed and then release A&R wire.

5.2 Procedures for PLET installation

- [1] S-lay first end installation: The mud mat of the PLET also need to be designed as a special structure in this process, and then the PLET will be lowered to seabed through stinger.
- [2] J-lay first end installation:
 - a) Lift the PLET and adjust its attitude; then, insert PLET Yoke into the positioning socket.
 - b) Connect the laying pipe and PLET; lower the whole structure and continue to connect more pipes

until PLET is close to the surface.

- c) Transfer the whole structure to J-Lay tower by crane.
- d) Fix the upper section of the pipe to the tensioner or fixing device.
- e) Continue pipe laying operation until PLET is lowered to the targeting area.

[3] Second end installation method (suitable for both S-lay and J-lay):

- a) Transfer the laid pipeline to SCR fixing device by crane; activate the SCR limiting device to prevent large movement of pipeline.
- b) Lift the PLET by crane, adjust its attitude, insert PLET Yoke into the positioning socket, and use the upper operation platform to assist positioning; then, complete the connection between PLET and pipe.
- c) After the connection, open the pipe fixing and limit device. Connect both the crane wire and A&R wire to the PLET by triangle plate and riggings, and lower the whole structure by crane.
- d) In the lowering process, increase the tension of the A&R wire, and transfer the tension of pipe from crane to the A&R wire gradually; activate the limiting device of the A&R wire to limit large movement of the PLET when all the weight is transferred to the A&R wire.
- e) Unfold the mud mat of the PLET. Connect the free end of inhibit line to the ROV hook.
- f) Land PLET to the targeting area and then carry out basic measurements to confirm its position, orientation and dip angle. Disconnect auxiliary cable and prepare for the follow-up work.

5.3 Procedures for SPF installation

- [1] Transfer the laid section to SCR fixing device by crane.
- [2] Open the SCR limiting device to limit the large swing of the pipeline.
- [3] Lift and adjust the attitude of WSA (ISL), welding the bottom part of WSA (ISL) and the pipe which fixed in the fixing device.
- [4] Open the fixing device and the limiting device, transfer the integral structure to J-lay tower or stinger by crane.
- [5] Continue pipe-laying operation until the WSA (ISL) is installed to the seabed.

6 ADVANTAGES OF NEW DEVICE AND CORRESPONDING METHODS

6.1 Abandonment & recovery of pipeline

S-lay: The installation of the buoy is transferred from underwater to deck, which makes the buoy installation and dismantling more convenient and reduces underwater operation thus ensuring operation stability. Horizontal operation is replaced by vertical operation, which reduces the suffered tension of A&R wire and makes the operation much safer.

J-lay: By moving the process of welding and installation of A&R tug head and buoy to the deck, more operation space is secured which ensures operation stability, and also buoy or structure damages caused by

collision between them are avoided. The multi-functional tower will bear all the tension of the pipe as operations are carried out on the deck, which ensures the safety of the J-lay system.

6.2 PLET installation

S-lay: The first end installation methods are all the same with the traditional installation method. PLET is not required to go through the stinger and the tensioner during the second end installation, so both the PLET and stinger are much safer. Horizontal operation is replaced by vertical operation, which reduces the tension of A&R wire and makes the operation more reliable.

J-lay: The complex multi-degree-freedom PLET operating system is no longer needed in the first end installation, making the operation much simpler. The size of PLET for installation is no longer limited by the dimension of the tower structures in the second end installation, which also avoids buoy or structure damage caused by collision between them. The multi-function tower bears the whole weight of the pipe when operations are carried out on the deck, and ensures the safety of the J-lay system.

6.3 SPF installation(WSA/ISL)

S-lay: The required deck area is reduced as horizontal operation is replaced by vertical operation for the slender structures, such as WSA (ISL). The tension provided by the tensioner or the A&R winch is no longer needed during the WSA (ISL) installation process.

J-lay: For the slender structures, inner-tower vertical operation is replaced by deck vertical operation, giving more space for WSA (ISL) installation. It solved the the space limitation problems of the J-lay tower which had made WSA(ISL) installation so inconvenient. Furthermore, the complex PLET operation handling system is no longer needed.

7 CONCLUSIONS

A multi-functional subsea production facility installation system-MSPFIS was designed in this paper to solve the problems encountered for both S-lay and J-lay systems. With the help of this system, an S-lay vessel can perform the pipeline abandonment and recovery process as well as the SPFs installation process very conveniently. Meanwhile, pipeline abandonment and recovery process for the J-lay system can also be done conveniently by equipping the syste enabling m the J-lay system to install SPFs with large dimension. To some degree, it expanded the functions of both S-lay and J-lay vessels. In addition, both working duration and cost is reduced by using this system because the abandonment and recovery processes or the SPFs installation process can now be done by the pipe-laying vessel, and supporting vessels are no longer needed. Furthermore, the A-frame, which was used to assist structures' lowering and installing is no longer

needed nor is the PLET operation handling system. All the operations are transferred from subsea to the deck, which improves worker safety and operational stability.

This paper also summarized the functions and working procedures of the J-lay and S-lay systems, which could provide some useful guidelines for the HYSY201 and 2*8000t vessels. The MSPFIS could be used in any J-lay and S-lay vessel to carry out the pipelines' abandonment and recovery operation as well as the SPFs' installation operation. Corresponding procedures for pipelines' A&R process and SPFs' installation procedures are proposed on the basis of the designed system. The authors hope their research on equipment and installation technique will lay a solid foundation for the HYSY201 and 2*8000t vessels seeking more economical, safer and more efficient installation of subsea pipelines.

8 ACKNOWLEDGEMENTS

The authors are grateful for the financial support from the China National Major Projects of Science and Technology (Grant No. 2011ZX05027-004-01), the National Basic Research Program of China (Grant No. 2011CB013702), and the National Natural Science Foundation of China (Grant No. 50979113).

9 REFERENCES

- Antani, J. K., Dick, W. T., Balch, D. and Leij, V. T. (2008). "Design, fabrication and installation of the Neptune Export Lateral PLETs[C]." *Proc., Offshore Technology Conf.*, ASCE, Reston, VA., pp..
- Andreuzzi, F. & Maier, G. (1981). "Simplified analysis and design of abandonment and recovery of offshore pipelines," *J., Ocean Management*, 7(1-4), pp. 211-230.
- Baugh, B.F.(2001a) Gimbal for J-Lay pipe Laying system. *United States Patent: US6213686 B1*, 2001.04.10.
- Baugh, B.F. (2001b). "Traveling table for J-lay pipe-laying system. *United States Patent: US6293732B1*, 2001.9.25.
- Baugh, B.F.(2002a). Jack mechanism for J-lay pipe-laying system. *United States Patent: US6364573B1*, 2002.04.02.
- Baugh, B.F. (2002b) Stinger for J-Lay pipe laying system. *United States Patent: US6334739 B1*, 2002.01.01.
- BP Trinidad and Tobago LLC; Shore Approach Pipeline Installation Specification; *BP Trinidad and Tobago LLC*; August 16, 2001.
- Cheng, F.; Research on pipelaying system of a 2x8,000 t semi-submerged crane pipelaying vessel[J]. *Ship & Boat*, 2012, Vol.23, No.1, pp71–75.

Cavicchi, M. & Ardavanis, K.; J-Lay Installations Lessons Learned[C]. *Offshore Technology Conference*, 5 May-8 May 2003, Houston, Texas, USA.

Dyson, K.C., McDonald, W.J., Olden, P. and Domingues F.; Design Features for Wye Sled Assemblies and Pipeline End Termination Structures to Facilitate Deepwater Installation by the J-Lay Method PLET[C]. *Offshore Technology Conference*, 3 May-6 May 2004, Houston, Texas. U.S.A.

Duan, M.L., A Lifting System For Installation Of Deep-Water Risers And Subsea Hardware[C]. *Presented at the 2010 SUT Technical Conference, Society for Underwater Technology*, Rio de Janeiro, Brazil, 23–24 March, 2010.

Duan, M.L., Wang, Y. , Estefen, S., He, N., Li, L. N. and Chen, B.M., An Installation system of Deep-water Risers by an S-Lay Vessel, *China Ocean Engineering*, Vol.24, No.4, 2010, pp.139-148.

Fan, D.Q., The Development Mode of Marginal Oilfield Based on Jack-Up Production Platform with Oil Cabins[J], *Journal of Convergence Information Technology*, Vol. 8, No. 1, pp. 382 ~ 387, 2013.

Forbord, P. K., Myklebost, L., Skeie, A., Bakken, B.O., Lund, G.M. and Grønvik, T.; The Challenges Associated With the Installation of Long-Distance Tiebacks[C]. *Offshore Technology Conference*, 30 April-3 May 2007, Houston, Texas, USA.

Guan, D.W., Duan, M.L., He, N., Yang, W.; Analysis of Deepwater Pipeline J-lay process. *China Petroleum Machinery*, 2011, Vol.39 , No.10, pp131–135.

Hebert, C.; West Seno Facilities and Pipelines, Using Conventional Vessels for Deepwater Installation[C]. *Offshore Technology Conference*, 3 May-6 May, 2004, Houston, Texas, U.S.A.

Heerema, E.P.; Recent Achievements And Present Trends In Deepwater Pipe-Lay Systems[C]. *Offshore Technology Conference*, 2 May-5 May 2005, Houston, Texas, U.S.A.

He, N., Xu, C. W., Duan, M.L., Ni, M.C.; Overview of J-lay Technology for Subsea Pipelines. *Oil Field Equipment*, 2011, Vol.40, No.(3), pp63-67.

HMC Deep-water Field Development experience; *Working With The Tools Of Today*. Frank Lange, DOT, 2002.

<http://hmc.heerema.com/About/Fleet/Balder/tabid/379/language/en-US/Default.aspx>.

Huang, K., Ji, A. and Uribe E.; Deepwater In-Line SLED Installation Methods and its Application to Frade Project[C]. *Offshore Technology Conference*, 4-7 May 2009, Houston, Texas, USA.

Jiang, X.Z., Li, Z.G., He, N., Wang, Y. and Duan M. L (2009). "A New Lifting System for Installation of Risers in Deeper Water," *Proc., ISOPE-IDOT 2009*, Beijing, China, Intl. Society of Offshore and Polar Engineers (ISOPE), Cupertino, CA, pp.36-42.

Moszkowski, M., Baugh, B.F.; Flex J-Lay tower. *United States Patent: US6776560 B2*, 2004.08.17.

Perinet, D. & Frazer I. (2007). "J-lay and steep S-lay: Complementary tools for ultradeep water," *Proc., The Offshore Technology Conference*. Curran Associates, Inc., Red Hook, NY, pp. 697-704.

Wang, S. & Gan, F.L. (2010). "First Chinese pipe-laying ship of 3000 meters left dock," *China Ship News*.

Wang, J., Hagen, R.K., Radan, E. and Bullock, J.; Technical Challenges and Success for rigid pipeline with PLET, Jumper and Flying Leads Installation in Conger 9 Field [C]. *Offshore Technology Conference*, 2-5 May 2011, Houston, Texas, USA.

Wolbers, D. & Hovinga, R.; Installation of deepwater pipelines with sled assemblies using the new J-Lay system of the DCV Balder[C]. *Offshore Technology Conference*, 5 May-8 May 2003, Houston, Texas, USA.

Zhou, J.; Investigation on Configuration and Construction Technics of S-lay for Deepwater Submarine Pipelines [D]. Hangzhou: Zhejiang University, 2008.

EFFECT OF INTDENTER SHAPE ON VICKERS HARDNESS BY FINITE ELEMENT ANALYSIS

K. Morita¹, K. Oda² and N. Tsutsumi²

¹ Graduate student, Oita University, Oita, Japan

² Mechanical and Energy Systems Engineering, Oita University, Oita, Japan

Abstract: In this study, the relation between indentation hardness H_{IT} obtained by using Berkovich triangular pyramid indenter and the Vickers hardness H_V obtained by using the quadrangular pyramid indenter is investigated by using elastic-plastic analysis. The effect of the difference of the indenter shape on the hardness value is considered. The calculation shows that H_{IT} can convert into H_V by using the proportional relationship.

Keywords: Vickers Hardness, Nano-Indentation, Elastic-Plastic Analysis, Hardness Test

1 INTRODUCTION

Indentation hardness tests have long been a standard method for material characterization. The Vickers hardness test is the most popular method for the investigation of hardness of materials. Recently, the ultra-low load hardness test has been considered as a useful tool for estimating the mechanical properties of a very small scale region or of a very thin layer. The nano-indentation, a type of low load hardness test, provides accurate measurements of hardness and elastic modulus with a high spatial resolution [1]. The mechanical properties of the materials are estimated from the relationship between load and penetration depth measured by the ultra-low load hardness tester in which a triangular pyramid diamond is used as the indenter. The advantage of using a triangular pyramid diamond is that it is easier to prepare the tip with a sharp point as compared with four-faced pyramidal indenters as illustrated schematically in Fig. 1. Although the vickers and nano-indentation tests are similar indentation test, the Vickers hardness H_V and the hardness, H_{IT} , obtained by nano-indentation test are not equivalent. Sawa [2] pointed out the problem that both values of hardness are treated as a completely equivalent value.

In this study, the relation between indentation hardness H_{IT} obtained by nano-indentation and the Vickers hardness H_V is investigated by using elastic-plastic analysis and the effect of the difference of the indenter shape on the hardness value is considered.

2 ANALYSIS METHOD

The commercial FEM code MARC is used for the numerical analysis of the indentation test [5]. Since the problem has to be analyzed within large strain formulation, the elastic-plastic analysis based on the strain incremental plastic theory of Prandtl-Reuss equation and the updated Lagrange approach are selected. The isotropic hardening rule and the Mises yield criterion are used in this FEM analysis [3-5].

The FEM models of indentation analysis are shown in Fig.2. An eight-node isoparametric hexahedral element is used. Four types of materials are treated as an indentation specimen, that is, 0.46% carbon steel (S45C), 70/30 brass, aluminium alloy (T6061) and austenitic stainless steel (SUS304). Stress-strain curves of 0.46% carbon steel and 70/30 brass in tensile tests are shown in Fig.3 [3]. True stress-logarithmic strain curves of other two materials are cited from Ref.[5]. All materials are assumed that the Poisson's ratio is 0.3. The indenter is assumed as a frictionless rigid body in this analysis.

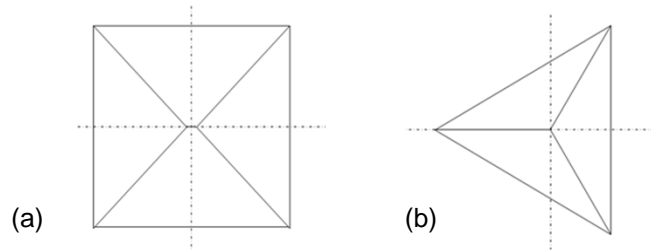


Fig.1. Shape of indenters, (a) Vickers quadrangular pyramid and (b) Berkovich triangular pyramid indenter.

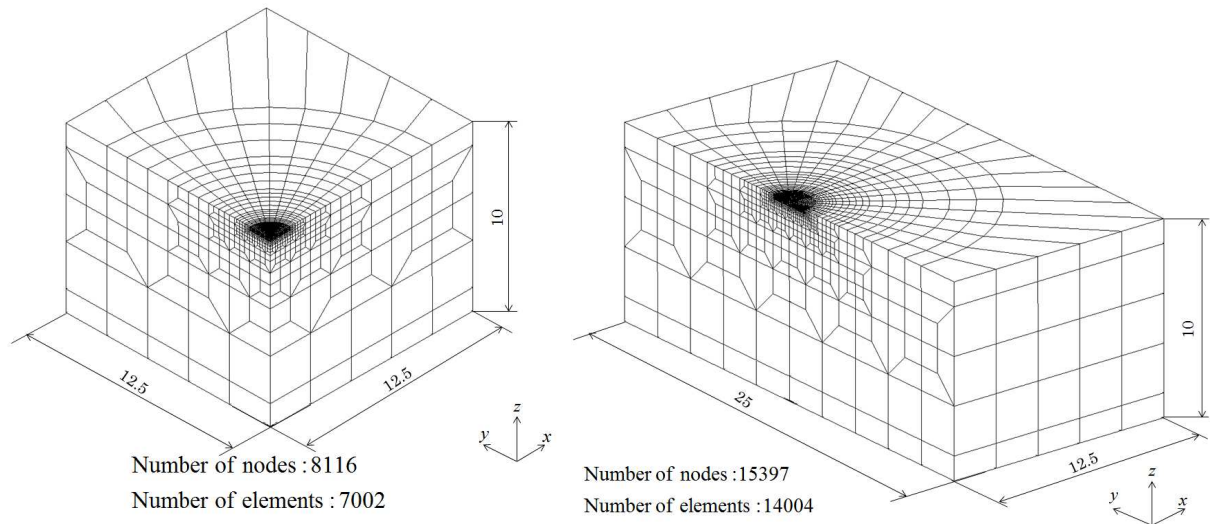


Fig. 2. FEM mesh of indentation specimens, (a) 1/4 model for Vickers indenter and (b) 1/2 model for Berkovich indenter.

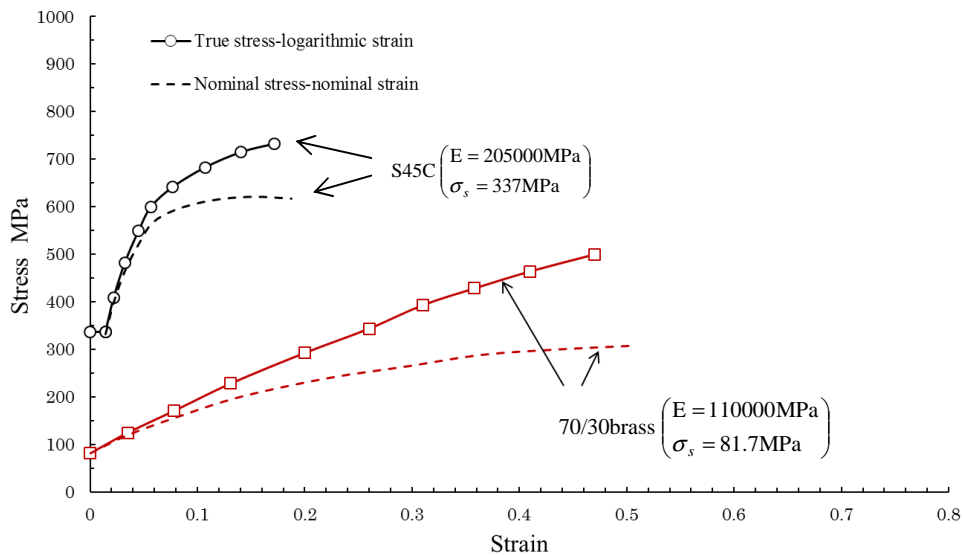


Fig. 3. Stress-strain curve used for elastic-plastic analysis [3].

3 RESULTS AND DISCUSSION

3.1 Evaluation method of hardness

The profile of the indentation on the z-axis for 0.46% carbon steel after removal of the load, $P=P_{\max}=600$ N, is shown in Fig. 4. The hardness with Vickers quadrangular pyramid indenter, H_V , is calculated by the diagonal dimension of the indentation, d .

$$H_V = \frac{2P}{d^2} \sin(\alpha/2) = 1.854 \frac{P}{d^2}. \quad (1)$$

On the other hand, the hardness with Berkovich triangular pyramid indenter, H_{IT} , is evaluated by the load-penetration depth curve (P-h curve) [1] as shown in Fig.5. The hardness H_{IT} is defined by

$$H_{IT} = \frac{P_{\max}}{A}, \quad A = 3\sqrt{3} \tan^2 65.03^\circ h_c^2 = 23.96 h_c^2, \quad h_c = h_{\max} - 0.75 \frac{P_{\max}}{S} \quad (2)$$

where A , h_{\max} and S stand for the projected contact area of the indentation at the contact depth h_c , the maximum penetration depth and the slope of tangent at unloading curve, respectively.

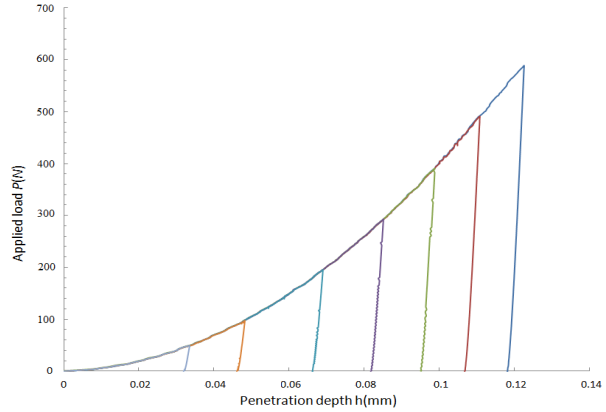
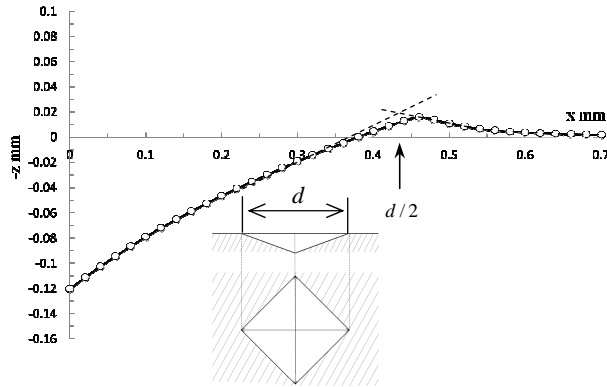


Fig. 4. Indentation shape of Vickers indenter after unloading (0.46% C steel, $P_{\max}=600$ N). **Fig. 5.** P-h curves used by Berkovich indenter for various applied loads (0.46% C steel).

3.2 Comparison of numerical and experimental results

Table 1 shows that the comparison of numerical and the experimental results for 0.46% carbon steel and 70/30 brass. The experimental results are cited from Ref.[3]. As shown in Table 1, the difference of the diagonal dimensions between numerical and experimental results is within about 6 % and the difference of hardness values is within about 12%. The diagonal size of indentation obtained from the analysis result depends on the mesh size of FEM model. Thus, the analytical method performed in this calculation may be considered accurate enough and useful for the analysis of indentation test.

Table 1. Comparison of numerical and experimental values for 0.46% carbon steel (S45C) and 70/30 brass.

Materials of specimen		Load P_{\max}	Diagonal of indentation d [mm]	Vickers hardness H_v
S45C	Experiment [3]	490N(50kgf)	0.737	171
	Calculation	490N(50kgf)	0.788	149
70/30 brass	Experiment [3]	490N(50kgf)	1.229	61.4
	Calculation	490N(50kgf)	1.299	54.9

3.3 Relation between H_{IT} and H_V

Figure 6 shows the relation between the numerical values H_{IT} and H_V for four kinds of materials. As shown in Fig.6, it is found that both values have a proportional relation, $H_{IT}=1.27H_V$. In Fig.6, H_{IT}^* is defined as the maximum load divided by the contact surface area as Vickers hardness. When the penetration depth is the same, the contact surface area for Berkovich triangular pyramid indenter is geometrically equal to that for Vickers quadrangular pyramid indenter. For the triangular pyramid indenter, the relationship between H_{IT} and H_{IT}^* is given by

$$H_{IT}^* = \frac{P_{\max}}{A^*} = 0.9065 H_{IT} . \quad (3)$$

Here, A^* is a contact surface area based on the indenter geometry. As illustrated in Fig. 6, the relationship between H_{IT}^* and H_V is obtained by the least square regression method as follows.

$$H_{IT}^* = 1.15 H_V . \quad (4)$$

From eq.(4), although H_{IT}^* and H_V have the same definition and physical meaning, both hardness values are not equivalent. However, the hardness values H_{IT} can convert into Vickers hardness H_V by using the proportional relationship in this study.

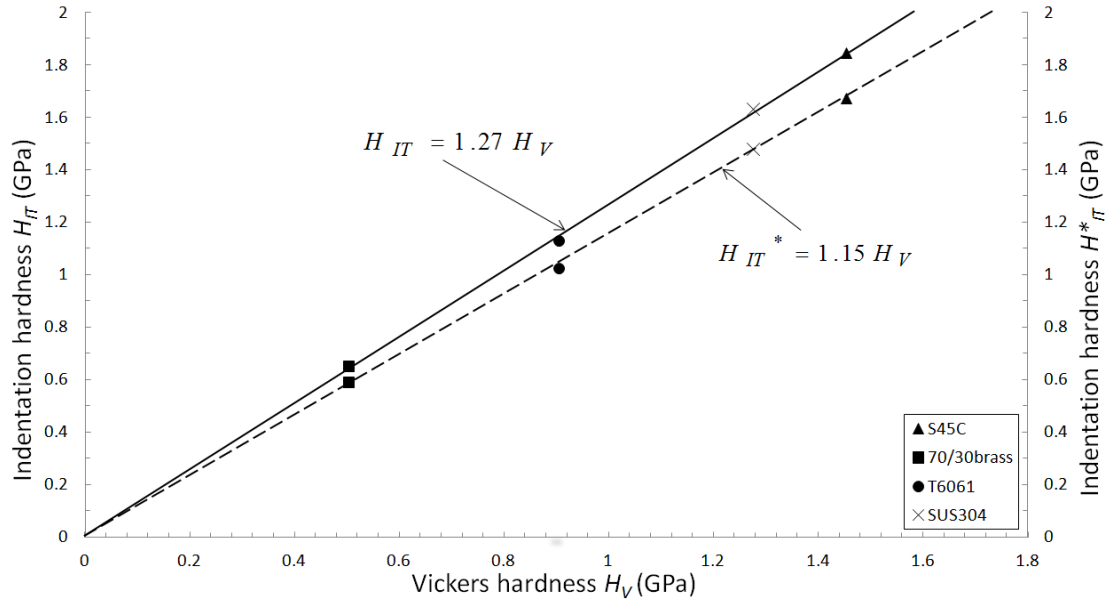


Fig. 6. Relation between H_{IT} and H_V for four materials obtained by the elastic-plastic analysis.

4 REFERENCES

- [1] W. C. Oliver, G. M. Pharr, An Improved Technique for Determining Hardness and Elastic Modulus Using Load and Displacement Sensing Indentation Experiments, J. Mater. Res., Vol.7, 1564-1583, 1992.
- [2] T. Sawa, The Problem of Correlation Value of Vickers Hardness Obtained by Nanoindentation and Suggesting New Analysis Method, Journal of Material Testing Research Association, 56(2), 94–98, 2011 (in Japanese).
- [3] Y. Murakami, K. Matsuda, Analysis of Vickers Hardness by the Finite-Element Method, Transactions of the Japan Society of Mechanical Engineers, 57A (539), 1665-1673, 1991 (in Japanese).
- [4] Y. Murakami, M. Itokazu, Elastic-Plastic Analysis of A Triangular Pyramidal Indentation, International Journal of Solids and Structures, 34 (30), 4005-4018, 1997.
- [5] N. Hamada, M. Sakane, M. Ohnami, FEM Analysis for Rockwell Hardness, Transactions of the Japan Society of Mechanical Engineers, 60A (579), 2645-2651, 1994 (in Japanese).

REVIEW OF THE DUAL BEM AND RECENT DEVELOPMENT OF NULL-FIELD INTEGRAL EQUATION APPROACH IN TAIWAN

J. T. Chen^{1, 2} and J. W. Lee¹

¹ National Taiwan Ocean University, Department of Harbor and River Engineering, Taiwan

² National Taiwan Ocean University, Department of Mechanical and Mechatronics Engineering, Taiwan

Abstract: In this talk, the development of dual BEM is reviewed since its appearance in 1986 by Hong and Chen. The academic activity of BEM community in Taiwan is also reported. Methods to deal with hypersingularity are also examined. Applications of the dual BEM to problems of civil and military engineering in Taiwan are reviewed. To avoid singular integrals, a null-field integral equation approach in companion with an addition theorem (or so called degenerate kernel or separable kernel) is proposed. Several gains, exponential convergence, free of singularity and boundary layer effect, are achieved. Applications to circular, elliptical (2D) and spherical boundaries (3D) with emphasis on harbor resonance and SH wave scattering of hill and canyon were done. Focusing effect in harbor engineering and earthquake engineering are also addressed.

Keywords: Dual BEM; Dual BIEM; Rank Deficiency; Null-Field BIEM; Degenerate Kernel

1 INTRODUCTION

The boundary element method (BEM) or so called boundary integral equation method (BIEM) have received much attention since Rizzo proposed a numerical treatment of the boundary integral equation for elastostatics. Most of the efforts have been focused on the singular boundary integral equation for primary fields, e.g. potential u or displacement. For most problems, the formulation of a singular boundary integral equation for the primary field provides sufficient conditions to ensure a unique solution. In some cases, e.g., those with Hermite polynomial elements, degenerate boundaries, corners, the construction of a symmetric matrix, the improvement of condition numbers, the construction of an image system, the tangent flux or hoop stress calculation on the boundary, an error indicator in the adaptive BEM, fictitious (irregular) frequencies in exterior acoustics, spurious eigenvalues, degenerate scale, the free surface seepage flow and the Tikhonov formulation for inverse problems, it is found that the integral representation for a primary field (Cauchy integral formula) can not provide sufficient constraints. In other words, the influence matrices are rank deficient. It is well known now that the hypersingular equation plays an important role in the aforementioned problems [1, 2]. Mathematicians and engineers have paid attention to the hypersingular equation from the viewpoint of mathematics and engineering, respectively. A review article by Chen and Hong on hypersingularity can be found. The hypersingular formulation provides the theoretical base of the dual BIE for degenerate-boundary problems. Totally speaking, four degenerate problems in BEM, degenerate scale, degenerate boundary, spurious eigenvalues and fictitious frequency, are encountered. The roles of hypersingularity in the dual BEM were examined by NTOU/MSV group in Taiwan. Engineering applications were also done. Later, the null-field BIEM was introduced [3-12]. Five goals: (1) free of calculating principal value, (2) exponential convergence, (3) well-posed algebraic system, (4) elimination of boundary-layer effect and (5) meshless, of the formulation can be achieved. In the following two sections, review of dual BEM in Taiwan and recent development of null-field BIEM will be addressed.

2 PROBLEM STATEMENT

In this talk, some engineering problems are considered and the governing equation is:

$$\mathcal{L}u(\mathbf{x}) = 0, \quad \mathbf{x} \in D, \quad (1)$$

where $u(\mathbf{x})$ is the potential function, \mathbf{x} is the field point, D is the domain of interest and \mathcal{L} denotes the operator which corresponds to problems as shown below

$$\mathcal{L}u(\mathbf{x}) = \begin{cases} \nabla^2 u(\mathbf{x}) & : \text{Laplace problem,} \\ (\nabla^2 + k^2)u(\mathbf{x}) & : \text{Helmholtz problem,} \end{cases} \quad (2)$$

where ∇^2 is the Laplacian operator and k is the wave number.

3 PRESENT APPROACHES

3.1 Dual boundary integral equations — the conventional version

Dual null-field boundary integral formulations — the present version

The dual boundary integral formulation [1,2] for the domain point for 2D Laplace and Helmholtz problems can be derived from Green's third identity

$$2\pi u(\mathbf{x}) = \int_B T(\mathbf{s}, \mathbf{x})u(\mathbf{s})dB(\mathbf{s}) - \int_B U(\mathbf{s}, \mathbf{x})t(\mathbf{s})dB(\mathbf{s}), \quad \mathbf{x} \in D, \quad (3)$$

$$2\pi t(\mathbf{x}) = \int_B M(\mathbf{s}, \mathbf{x})u(\mathbf{s})dB(\mathbf{s}) - \int_B L(\mathbf{s}, \mathbf{x})t(\mathbf{s})dB(\mathbf{s}), \quad \mathbf{x} \in D, \quad (4)$$

where \mathbf{s} is the source point, B is the boundary, and $t(\mathbf{x}) = \partial u(\mathbf{x})/\partial n_{\mathbf{x}}$ in which $n_{\mathbf{x}}$ denotes the unit outward normal vector at the field point \mathbf{x} . The kernel function, $U(\mathbf{s}, \mathbf{x})$, is the fundamental solution which satisfies

$$\mathcal{L}U(\mathbf{s}, \mathbf{x}) = 2\pi\delta(\mathbf{x} - \mathbf{s}) \Rightarrow \begin{cases} \nabla^2 U(\mathbf{s}, \mathbf{x}) = 2\pi\delta(\mathbf{x} - \mathbf{s}) & : \text{Laplace problem,} \\ (\nabla^2 + k^2)U(\mathbf{s}, \mathbf{x}) = 2\pi\delta(\mathbf{x} - \mathbf{s}) & : \text{Helmholtz problem,} \end{cases} \quad (5)$$

where $\delta(\mathbf{x} - \mathbf{s})$ denotes the Dirac-delta function. Then, we can obtain the fundamental solution as follows

$$U(\mathbf{s}, \mathbf{x}) = \begin{cases} \ln r & : \text{Laplace problem,} \\ -\frac{i\pi H_0^{(1)}(kr)}{2} & : \text{Helmholtz problem,} \end{cases} \quad (6)$$

where r is the distance between \mathbf{s} and \mathbf{x} ($r \equiv |\mathbf{x} - \mathbf{s}|$). The other kernel functions, $T(\mathbf{s}, \mathbf{x})$, $L(\mathbf{s}, \mathbf{x})$ and $M(\mathbf{s}, \mathbf{x})$, are defined by

$$T(\mathbf{s}, \mathbf{x}) = \frac{\mathbf{n}_s U(\mathbf{s}, \mathbf{x})}{\mathbf{n}_s}, \quad L(\mathbf{s}, \mathbf{x}) = \frac{\mathbf{n}_x U(\mathbf{s}, \mathbf{x})}{\mathbf{n}_x}, \quad M(\mathbf{s}, \mathbf{x}) = \frac{\mathbf{n}_s^2 U(\mathbf{s}, \mathbf{x})}{\mathbf{n}_s \mathbf{n}_x}, \quad (7)$$

where n_s denotes the unit outward normal vector at the source point \mathbf{s} . By moving the field point to boundary, Eqs. (3) and (4) becomes

$$\pi u(\mathbf{x}) = C.P.V. \int_B T(\mathbf{s}, \mathbf{x})u(\mathbf{s})dB(\mathbf{s}) - R.P.V. \int_B U(\mathbf{s}, \mathbf{x})t(\mathbf{s})dB(\mathbf{s}), \quad \mathbf{x} \in B, \quad (8)$$

$$\pi t(\mathbf{x}) = H.P.V. \int_B M(\mathbf{s}, \mathbf{x})u(\mathbf{s})dB(\mathbf{s}) - C.P.V. \int_B L(\mathbf{s}, \mathbf{x})t(\mathbf{s})dB(\mathbf{s}), \quad \mathbf{x} \in B, \quad (9)$$

where R.P.V., C.P.V. and H.P.V. denote the Riemann principal value, Cauchy principal value and Hadamard (or so-called Mangler) principal value, respectively. By collocating the field point \mathbf{x} on the complementary domain, we obtain the dual null-field boundary integral equations as shown below:

$$0 = \int_B T(\mathbf{s}, \mathbf{x})u(\mathbf{s})dB(\mathbf{s}) - \int_B U(\mathbf{s}, \mathbf{x})t(\mathbf{s})dB(\mathbf{s}), \quad \mathbf{x} \in D^c, \quad (10)$$

$$0 = \int_B M(\mathbf{s}, \mathbf{x})u(\mathbf{s})dB(\mathbf{s}) - \int_B L(\mathbf{s}, \mathbf{x})t(\mathbf{s})dB(\mathbf{s}), \quad \mathbf{x} \in D^c, \quad (11)$$

where D^c denote the complementary domain. After discretization by using constant element scheme, two linear algebraic equations can be obtained from Eqs. (8) and (9) as follows:

$$[\mathbf{U}]\{\mathbf{t}\} = [\mathbf{T}]\{\mathbf{u}\}, \quad (12)$$

$$[\mathbf{L}]\{\mathbf{t}\} = [\mathbf{M}]\{\mathbf{u}\}. \quad (13)$$

3.2 Dual null-field boundary integral formulations — the present version

By introducing the degenerate kernels, the collocation point in Eqs. (3), (4), (8) and (9) can be located on the real boundary free of calculating principal value. Therefore, the boundary integral equations can be rewritten in two parts as given in the following formulation of Eqs. (14)-(17), instead of three parts using Eqs. (3), (4) and (8)-(11) in the conventional dual BEM for 3D engineering problems,

$$4\pi u(\mathbf{x}) = \int_B T(\mathbf{s}, \mathbf{x})u(\mathbf{s})dB(\mathbf{s}) - \int_B U(\mathbf{s}, \mathbf{x})t(\mathbf{s})dB(\mathbf{s}), \quad \mathbf{x} \in D \cup B, \quad (14)$$

$$4\pi t(\mathbf{x}) = \int_B M(\mathbf{s}, \mathbf{x})u(\mathbf{s})dB(\mathbf{s}) - \int_B L(\mathbf{s}, \mathbf{x})t(\mathbf{s})dB(\mathbf{s}), \quad \mathbf{x} \in D \cup B, \quad (15)$$

and

$$0 = \int_B T(\mathbf{s}, \mathbf{x})u(\mathbf{s})dB(\mathbf{s}) - \int_B U(\mathbf{s}, \mathbf{x})t(\mathbf{s})dB(\mathbf{s}), \quad \mathbf{x} \in D^c \cup B, \quad (16)$$

$$0 = \int_B M(\mathbf{s}, \mathbf{x})u(\mathbf{s})dB(\mathbf{s}) - \int_B L(\mathbf{s}, \mathbf{x})t(\mathbf{s})dB(\mathbf{s}), \quad \mathbf{x} \in D^c \cup B. \quad (17)$$

It is found that Eqs. (14)-(17) can contain the boundary point (\mathbf{x} on B) since the kernel functions are expressed in terms of the degenerate kernel.

3.2.1 Expansions of fundamental solution and boundary density by using the spherical and the spheroidal coordinates

The closed-form fundamental solution for 3D Laplace and Helmholtz problems satisfy

$$\mathcal{L}U(\mathbf{s}, \mathbf{x}) = 4\pi\delta(\mathbf{x} - \mathbf{s}) \Rightarrow \begin{cases} \nabla^2 U(\mathbf{s}, \mathbf{x}) = 4\pi\delta(\mathbf{x} - \mathbf{s}), & \text{: Laplace problem,} \\ (\nabla^2 + k^2)U(\mathbf{s}, \mathbf{x}) = 4\pi\delta(\mathbf{x} - \mathbf{s}), & \text{: Helmholtz problem,} \end{cases} \quad (18)$$

where

$$U(\mathbf{s}, \mathbf{x}) = \begin{cases} -\frac{1}{r}, & \text{: Laplace problem,} \\ -\frac{e^{ikr}}{r} = -ikh_0^{(1)}(kr), & \text{: Helmholtz problem,} \end{cases} \quad (19)$$

where $r \equiv |\mathbf{x} - \mathbf{s}|$ is the distance between the field point and the source point and $h_0^{(1)}$ is the zeroth order spherical Hankel function of the first kind. To fully utilize the properties of spherical and spheroidal geometries, respectively, the degenerate (separable or finite-rank) kernel and the spherical harmonics or eigenfunction expansion are utilized for the analytical integration of boundary contour integrals. In the spherical and spheroidal coordinates, the field (source) point \mathbf{x} (\mathbf{s}) is expressed as $\mathbf{x} = (\rho_x, \theta_x, \phi_x)$ ($\mathbf{s} = (\rho_s, \theta_s, \phi_s)$) and $\mathbf{x} = (\xi_x, \eta_x, \phi_x)$, ($\mathbf{s} = (\xi_s, \eta_s, \phi_s)$), respectively. By employing the addition theorem [13] to separate the source point and field point in the kernel functions $U(\mathbf{s}, \mathbf{x})$ is expanded in terms of degenerate kernel as shown below:

$$U(\mathbf{s}, \mathbf{x}) = \begin{cases} U^E(\mathbf{s}, \mathbf{x}) = \lim_{N \rightarrow \infty} U_N^E(\mathbf{s}, \mathbf{x}) = \sum_{j=0}^N F_j(\mathbf{x})G_j(\mathbf{s}), \rho_x \geq \rho_s \text{ (spherical)}, \xi_x \geq \xi_s \text{ (spheroidal)}, \\ U^I(\mathbf{s}, \mathbf{x}) = \lim_{N \rightarrow \infty} U_N^I(\mathbf{s}, \mathbf{x}) = \sum_{j=0}^N F_j(\mathbf{s})G_j(\mathbf{x}), \rho_x < \rho_s \text{ (spherical)}, \xi_x < \xi_s \text{ (spheroidal)}, \end{cases} \quad (20)$$

where the superscripts “E” and “I” denote the exterior and interior cases, respectively. The other kernel functions in the boundary integral formulation can be derived by using operators in Eq. (7) with respect to the kernel function $U(\mathbf{s}, \mathbf{x})$. The degenerate kernels $U(\mathbf{s}, \mathbf{x})$, for 3D Laplace and Helmholtz problems can consult [13], respectively. For the unknown boundary densities, we apply the spherical harmonics or

eigenfunction expansions to approximate the boundary potential $u(s)$ and its normal derivative $t(s)$ along the spherical and spheroidal boundaries, respectively, as

$$u(s) = \sum_{v=0}^{\infty} \sum_{w=0}^v g_{vw} P_v^w(\cos(\theta_s)) \cos(w\phi_s) + \sum_{v=1}^{\infty} \sum_{w=1}^v h_{vw} P_v^w(\cos(\theta_s)) \sin(w\phi_s), \quad s \in B, \quad (21)$$

$$t(s) = \sum_{v=0}^{\infty} \sum_{w=0}^v p_{vw} P_v^w(\cos(\theta_s)) \cos(w\phi_s) + \sum_{v=1}^{\infty} \sum_{w=1}^v q_{vw} P_v^w(\cos(\theta_s)) \sin(w\phi_s), \quad s \in B, \quad (22)$$

and

$$u(s) = \sum_{v=0}^{\infty} \sum_{w=0}^v g_{vw} P_v^w(\eta_s) \cos(w\phi_s) + \sum_{v=1}^{\infty} \sum_{w=1}^v h_{vw} P_v^w(\eta_s) \sin(w\phi_s), \quad s \in B, \quad (23)$$

$$t(s) = \frac{1}{J_s} \left(\sum_{v=0}^{\infty} \sum_{w=0}^v p_{vw} P_v^w(\eta_s) \cos(w\phi_s) + \sum_{v=1}^{\infty} \sum_{w=1}^v q_{vw} P_v^w(\eta_s) \sin(w\phi_s) \right), \quad s \in B, \quad (24)$$

where g_{vw} , h_{vw} , p_{vw} and q_{vw} are the unknown coefficients of the boundary densities, P_v^w is the associated Legendre polynomial of the first kind and J_s is the Jacobian term. In the real computation, all boundary contour integrations can be easily determined by employing the orthogonal property of spherical harmonics or eigenfunction expansions. The null-field BIEM can be seen as one kind of semi-analytical method since errors only occur from the truncation of the number of terms after using spherical harmonics or eigenfunction expansions in the real implementation.

4 NUMERICAL EXAMPLES

4.1 Torsion problem containing a double-edge crack (degenerate boundary)

We consider the torsion problem of an elliptical bar containing a double-edge crack. The sketch of problem is shown in Fig. 1(a), where a is the length of semi-major axis, b is the length of semi-minor axis and the length of crack is extending to its foci $(\pm c, 0)$. By employing the singular value decomposition (SVD) to the four influence matrices in the dual BEM ([U], [T], [L] and [M]), the information of physics and mathematics can be found in the right and left unitary vectors. We plot the right and left unitary vectors of four influence matrices [U], [T], [L] and [M] corresponding to the zero singular value in a bar chart as shown in Fig. 2, where matrix [U] contains two zero singular values caused by degenerate boundary and matrix [T] contains three zero singular values that include two due to degenerate boundary and one due to rigid-body mode. After arranging it is found that the same fictitious information of mathematics comes from the degenerate boundary and the same true information of physics stems from the rigid body motion as shown in Fig. 3.

4.2 A circular harbor with 60° opening arc

In this case, we consider a circular harbor with a 60° opening arc subject to the incident wave of zero degree and the amplitude is $A = 0.5$ as shown in Fig. 1(b), where the incident wave can be represented by $0.5e^{ikx}$. The water depth in the harbor area and open sea is assumed to be a constant of 1. The radius of circular harbor is $a = 0.75$. The contour plot of the amplification factor is given in Fig. 4. It is worthy of noting that the focusing behavior appears and the position of the peak locates close to the origin of the harbor. The maximum value of the peak approaches 3.51 when ka is 3.95. This finding is similar to the problem of a hill scattering subject to a SH wave as shown in Fig. 5.

4.3 A prolate spheroidal resonator

In this example, we consider a prolate spheroidal resonator subject to the Dirichlet boundary condition as shown in Fig. 1(c). The lengths of semi-major and semi-minor axes are $a_0 = 1$ and $b_0 = 0.5$, respectively. The present results match well with those of Chang [14]. Table 1 shows the former four eigenmodes of Dirichlet boundary condition. It is found that the even mode is symmetric to the plane of $y = 0$ while the odd mode is antisymmetric to the plane of $y = 0$. It is found that the mode on some plane is a null field because those planes are nodal surface.

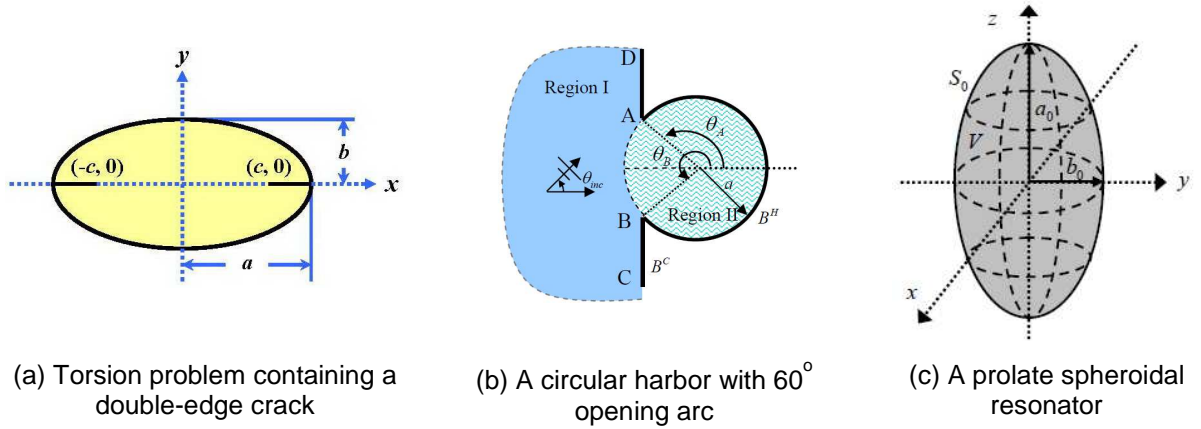


Fig. 1. Sketches of problems

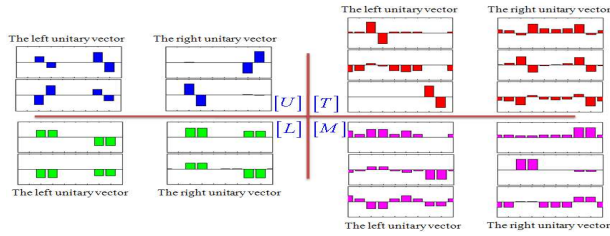


Fig. 2. Bar charts of the right and left unitary vectors of [U], [T], [L] and [M]

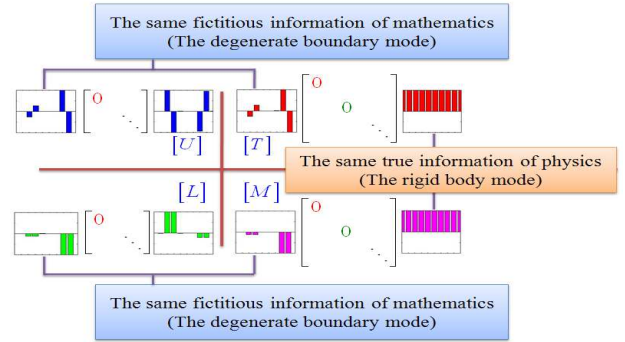


Fig. 3. Bar charts of the right and left unitary vectors (10 elements)

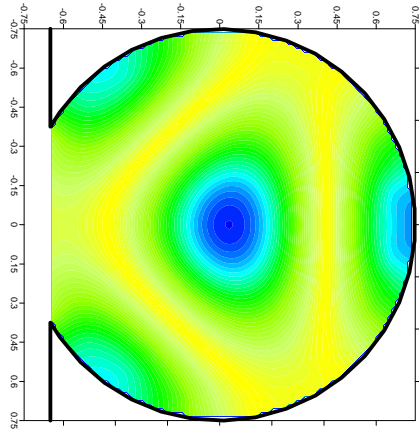


Fig. 4. Focusing effect in the contour plot of free-surface elevation for $ka=3.95$.

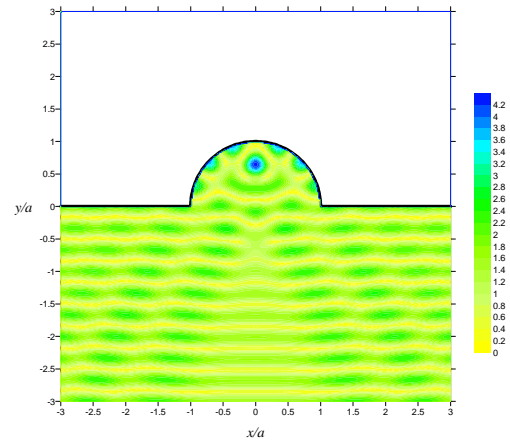
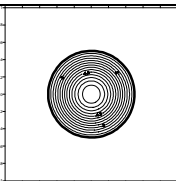
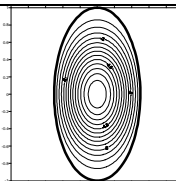
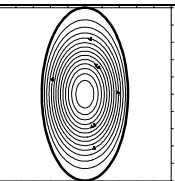
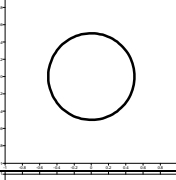
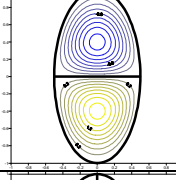
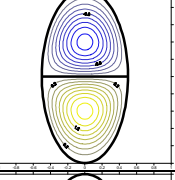
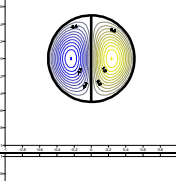
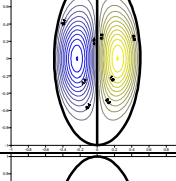
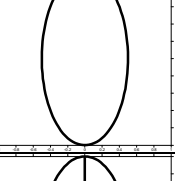
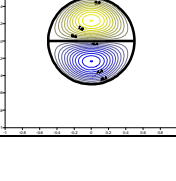
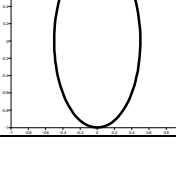
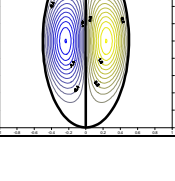


Fig. 5. Focusing effect in the contour plot of the SH-wave scattering

Table 1. The former four eigenmodes of the Dirichlet boundary conditions

	xy plane ($z = 0$)	xz plane ($y = 0$)	yz plane ($x = 0$)
$n = 0$ $m = 0$ $k = 5.398$ (5.39779) [14] Even mode			
$n = 1$ $m = 0$ $k = 6.560$ (6.55989) [14] Even mode			
$n = 1$ $m = 1$ $k = 8.221$ (8.22077) [14] Even mode			
$n = 1$ $m = 1$ $k = 8.221$ (8.22077) [14] Odd mode			

5 CONCLUSIONS

In this talk, not only the review of the dual BEM in Taiwan was done but also the recent development of null-field BIEM was addressed. For the degenerate problems (degenerate boundary), we have successfully employed the dual BEM in conjunction with the SVD technique to numerically discuss the SVD structure. Based on the SVD structure, it is found that information of physics is in the common right unitary (singular) vectors and information of mathematics exists in the left unitary (singular) vectors. The null-field BIEM in conjunction with the degenerate kernels and eigenfunction expansions is successfully applied to solve boundary value problems containing circular, elliptical, spherical or spheroidal boundaries. Based on the addition theorem, the closed-form fundamental solution is expanded into the degenerate kernel. Boundary densities are represented by using the eigenfunction expansions due to the orthogonal properties of eigenfunctions. By this way, the null-field BIEM is belonged to a semi-analytical and meshless approach. Five goals: (1) free of calculating principal value, (2) exponential convergence, (3) well-posed algebraic system, (4) elimination of boundary-layer effect and (5) meshless, of the null-field BIEM are achieved.

6 ACKNOWLEDGEMENTS

The financial support from the National Science Council under Grant No. NSC100-2221-E-019-040-MY3 and NSC100-2221-E-019-040-MY3 for the National Taiwan Ocean University is gratefully appreciated.

7 REFERENCES

- [1] H.-K. Hong, J. T. Chen, Derivations of integral equations of elasticity. Journal of Engineering Mechanics-ASCE, 114(6) 1028-1044. 1988.
- [2] J. T. Chen, H.-K. Hong, Review of dual boundary element methods with emphasis on hypersingular integrals and divergent series. Applied Mechanics Reviews-ASME, 52(1), 17-33, 1999.
- [3] J. T. Chen, A. C. Wu, Null-field integral equation approach for multi-inclusion problem under anti-plane shear, Journal of Applied Mechanics-ASME, 74, 469-487, 2007.

- [4] J. T. Chen, C. T. Chen, I. L. Chen, Null-field integral equation approach for eigenproblems with circular boundaries, *Journal of Computational Acoustics*, 15(4), 401-428, 2007.
- [5] J. T. Chen, Y. T. Lee, Y. J. Lin, Interaction of water waves with arbitrary vertical cylinders using null-field integral equations, *Applied Ocean Research*, 31, 101-110, 2009.
- [6] J. T. Chen, Y. T. Lee, J. W. Lee, Torsional rigidity of an elliptic bar with multiple elliptic inclusions using a null-field integral approach, *Computational Mechanics*, 46, 511-519, 2010.
- [7] J. T. Chen, Y. T. Lee, Y. J. Lin, Analysis of multiple-spheres radiation and scattering problems by using a null-field integral equation approach, *Applied Acoustics*, 71, 690-700, 2010.
- [8] J. T. Chen, J. W. Lee and C. F. Wu, I. L. Chen, SH-wave diffraction by a semi-circular hill revisited: A null-field boundary integral equation method using degenerate kernels, *Soil Dynamics and Earthquake Engineering*, 21, 729-736, 2011.
- [9] J. T. Chen, J. W. Lee, S. Y. Leu, Analytical investigation for spurious eigensolutions of multiply-connected membranes containing elliptical boundaries using the dual BIEM, *International Journal of Solids and Structures*, 48, 729-744, 2011.
- [10] J. T. Chen, J. W. Lee, Water wave problems using null-field boundary integral equations: Ill-posedness and remedies, *Applicable Analysis*, 91(4), 675-702, 2012.
- [11] J. W. Lee, J. T. Chen, A semi-analytical approach for a nonconfocal suspended strip in an elliptical waveguide, *IEEE Transactions on Microwave Theory and Techniques*, 60(12), 3642-3655, 2012.
- [12] J. T. Chen, J. W. Lee, C. F. Wu, Y. T. Lee, Study on the harbor resonance and focusing by using the null-field BIEM, *Engineering Analysis with Boundary Elements*, 37, 1107-1116, 2013.
- [13] P. Morse, H. Feshbach, *Method of Theoretical Physics*, McGraw-Hill, New York, 1953.
- [14] C. T. M. Chang, Natural resonant frequency of a prolate acoustical resonator, *Journal of the Acoustical Society of America*, 49(3), 611-614, 1971.

SIMULATION OF INTERFACE DELAMINATION GROWTH IN MICROELECTRONIC INTERCONNECT STRUCTURES

T.-C. Chiu, Y.-S. Lai and C.-H. Chen

National Cheng Kung University, Tainan, Taiwan

Abstract: The fatigue growth of a 3-D interfacial crack under temperature cycling (T/C) in microelectronic interconnect structure is investigated by using an incremental procedure. In this procedure the distribution of strain energy release rates and stress intensity factors along the curvilinear front of an interface defect is first estimated numerically by using the virtual crack closure technique. In the analysis the heterogeneous interconnect structures neighboring the cracked interface are approximated by homogenized layers with transversely isotropic elastic properties. The fracture mechanics parameters obtained from the numerical analysis are then substituted into a steady-state fatigue crack growth formula to predict the evolution of the interface defect.

Keywords: Fatigue; Debond; Anisotropic; Strain Energy Release Rate; Stress Intensity Factor

1 INTRODUCTION

Interconnect structure in state-of-the-art microelectronic component typically consists of multilayers of metal conductors and ceramic or polymer dielectrics, and is prone to interfacial delamination failure. Delamination typically occurs on interfaces such as molding compound-lead frame, underfill-silicon die, and silicon-level low-k dielectric-etch stop layer. Because of the low intrinsic adhesion between these dissimilar materials, initiations of interfacial defects are likely occurring on the stress concentration locations such as corners and edges. The defect may further propagate under subsequent T/C conditions, and would lead to eventual electrical failure when the front of the delamination defect reaches a critical circuit structure such as metal via or solder bump. Due to its critical role in the reliability of microelectronic devices, the problem of interfacial delamination and the associated design optimizations have been studied extensively in the past, e. g., Mercado et al. [1] investigated the effects of packaging process and T/C reliability test on Cu/low-k interconnect delamination, Zhai et al. [2] studied the underfill-silicon die delamination under T/C conditions. In these studies, two-dimensional (2-D) models were used for studying the influences of materials and dimensions on the fracture driving forces. The 2-D model, however, is not effective in predicting the delamination growth under fatigue loading because the propagation of interfacial defect in the heterogeneous interconnect structure is seldom in a 1-D fashion as considered in the 2-D model. Instead, a non-uniform driving force distribution and growth pattern is expected, and a 3-D model is required to consider the growth [3]. Another aspect of the IC interconnect that may complicate the delamination growth analysis is related to its heterogeneous nature. In a typical silicon-level interconnect stack, the effect of local inhomogeneity associated to metal conductor patterning can be approximated by an equivalent homogenous behavior of the whole structure because of the uniform metal density required by the fabrication processes. By using a representative volume element (RVE) homogenization approach, it was found that the BEOL interconnect structure can be modeled by a transversely isotropic elastic medium, with anisotropy in the out-of-plane direction of the thin film stack [4].

In this study a numerical procedure based on virtual crack closure technique is applied to study the fatigue growth of an interface defect in microelectronic components. In this procedure the distributions of fracture mechanics parameters along the curvilinear front of an interface defect are first estimated numerically, and then substituted into a steady-state fatigue crack growth formula to predict the evolution of the interface defect. The procedure is applied to investigate fatigue growths of interface cracks in Cu/low-k interconnect structure and in flip-chip package under T/C condition.

2.1 Fracture Mechanics Parameters

Consider an interface crack between two dissimilar anisotropic materials as shown in Fig. 1. A local coordinate system is defined such that the normal direction of the interface crack front is along the x_1 -axis.

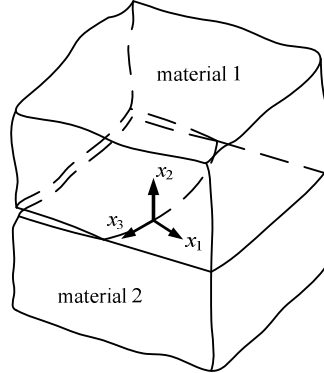


Fig. 1. A crack on the interface of two dissimilar materials.

A pseudo-3-D stress field around the crack tip is obtained by superpositioning the 2-D in-plane and anti-plane solutions. The strain energy release rate of the interface crack tip can be expressed as

$$G = G_I + G_{II} + G_{III}, \quad (1)$$

where G_I , G_{II} and G_{III} are the crack closure integrals corresponding to mode-I, -II and -III deformations, respectively, and are given by

$$G_I = \frac{1}{2\Delta} \int_0^\Delta \sigma_{22}(r) \delta_2(\Delta - r) dr, \quad G_{II} = \frac{1}{2\Delta} \int_0^\Delta \sigma_{12}(r) \delta_1(\Delta - r) dr, \quad G_{III} = \frac{1}{2\Delta} \int_0^\Delta \sigma_{23}(r) \delta_3(\Delta - r) dr. \quad (2)$$

In Eq. 2, Δ , σ and δ denote an infinitesimal crack extension, stress and crack opening displacement, respectively, along the x_1 -axis. In this study, the values of G_I , G_{II} and G_{III} are estimated by using a numerical finite element procedure incorporating collapsed quarter-point wedge crack-tip elements [5].

When the interface crack tip is under mode-I dominated loading conditions and the interface crack faces do not come into large scale contact around the crack tip, the stress intensity factors for the interface crack tip are given by [6]

$$\begin{Bmatrix} K_{II} \\ K_I \\ K_{III} \end{Bmatrix} = \lim_{r \rightarrow 0} \sqrt{2\pi r} \mathbf{A} \left\langle \left\langle \left(\frac{r}{\hat{r}} \right)^{-i\varepsilon_\alpha} \right\rangle \right\rangle \mathbf{A}^{-1} \begin{Bmatrix} \sigma_{12} \\ \sigma_{22} \\ \sigma_{23} \end{Bmatrix}, \quad (3)$$

where K_I , K_{II} and K_{III} are the mode-I, -II, and -III stress intensity factors, respectively, normalized by a characteristic length \hat{r} , the angular brackets $\langle \rangle$ denote a 3×3 diagonal matrix, ε_α , $\alpha = 1, 2, 3$, are the bimaterial constants, \mathbf{A} is a 3×3 bimaterial eigenvector matrix associated to the eigenvalue problem in the Stroh formalism, and the bimaterial constants are given by

$$\varepsilon_1 = \varepsilon = \frac{1}{2\pi} \ln \frac{1+\beta}{1-\beta}, \quad \varepsilon_2 = -\varepsilon, \quad \varepsilon_3 = 0, \quad \beta = \left\{ -\frac{1}{2} \text{tr} \left[(\mathbf{W}\mathbf{D}^{-1})^2 \right] \right\}^{1/2}. \quad (4)$$

For the problem of an interface crack between dissimilar transversely isotropic materials having isotropy in the plane normal to x_2 -axis, the bimaterial matrices \mathbf{W} and \mathbf{D} can be expressed as [5]

$$\mathbf{W} = \begin{bmatrix} 0 & -W_{21} & 0 \\ W_{21} & 0 & 0 \\ 0 & 0 & 0 \end{bmatrix}, \quad \mathbf{D} = \begin{bmatrix} D_{11} & 0 & 0 \\ 0 & D_{22} & 0 \\ 0 & 0 & D_{33} \end{bmatrix}. \quad (5)$$

The relationship between the crack closure integrals and the stress intensity factors can be obtained by substituting the near-tip asymptotic stress and crack opening displacement solutions into Eq. 2, and are given by

$$\begin{aligned}
G_I &= \frac{1}{8\pi \cosh(\pi\epsilon)} \left\{ \left[\frac{\pi}{\cosh(\pi\epsilon)} + \operatorname{Re}(A_I) \right] D_{22} K_I^2 + \left[\frac{\pi}{\cosh(\pi\epsilon)} - \operatorname{Re}(A_I) \right] D_{11} K_{II}^2 - 2 \frac{W_{21}}{|W_{21}|} \sqrt{D_{11} D_{22}} \operatorname{Im}(A_I) K_I K_{II} \right\}, \\
G_{II} &= \frac{1}{8\pi \cosh(\pi\epsilon)} \left\{ \left[\frac{\pi}{\cosh(\pi\epsilon)} - \operatorname{Re}(A_I) \right] D_{22} K_I^2 + \left[\frac{\pi}{\cosh(\pi\epsilon)} + \operatorname{Re}(A_I) \right] D_{11} K_{II}^2 + 2 \frac{W_{21}}{|W_{21}|} \sqrt{D_{11} D_{22}} \operatorname{Im}(A_I) K_I K_{II} \right\}, \\
G_{III} &= \frac{D_{33}}{4} K_{III}^2,
\end{aligned} \tag{6}$$

where

$$A_I = \frac{B(1/2 + i\epsilon, 1/2 + i\epsilon)}{1 + 2i\epsilon} \left(\frac{\Delta}{\hat{r}} \right)^{2i\epsilon}, \quad B(x, y) = \int_0^1 \tau^{x-1} (1-\tau)^{y-1} d\tau. \tag{7}$$

Table 1. Material constants for the homogenized BEOL interconnect structure [4].

	E_1 [GPa]	E_2 [GPa]	G_{12} [GPa]	ν_{13}	ν_{21}	α_1 [10 ⁻⁶ /°C]	α_2 [10 ⁻⁶ /°C]
interconnect 1	71.6	33.6	11.8	0.236	0.111	8.45	12.2
interconnect 2	83.7	86.2	34	0.218	0.222	5.22	5.79
silicon	150		64.1	0.17		2.9	

It can be seen from Eq. 6 that the crack closure integrals are quadratic functions of the stress intensity factors. Given the values of the crack closure integrals, the in-plane stress intensity factors may be obtained by using iterative approach. Alternatively, the in-plane stress intensity factors can be calculated by introducing an addition condition relating the coupled crack closure integral G_{II} and the in-plane stress intensity factors [5]. The phase angles corresponding to mode mixities are given by

$$\psi = \tan^{-1} \left(\frac{K_{II}}{K_I} \right), \quad \varphi = \tan^{-1} \left(\frac{K_{III}}{K_I} \right). \tag{8}$$

When large-scale contact occurs between crack faces, the crack opening displacement δ_2 is zero for the closed crack tip, and consequently, the crack closure integral G_I for the closed crack tip is zero. It can further be shown that [5]

$$G_{II} = \frac{1}{4} \left(D_{11} - \frac{W_{21}^2}{D_{22}} \right) K_{II}^2, \quad G_{III} = \frac{D_{33}}{4} K_{III}^2. \tag{9}$$

The absolute values of the mode-II and -III stress intensity factors for the closed crack tip can be calculated from Eq. 8, given that the values of G_{II} and G_{III} are first obtained. The signs of K_{II} and K_{III} may be determined from the values of the crack opening displacements and the crack tip stress fields.

Note that, when the parent materials of the interface are isotropic, expressions of the fracture mechanics parameters for the corresponding interface crack problem can also be obtained by assigning proper values to the bimaterial matrices \mathbf{W} and \mathbf{D} [5].

2.2 Incremental Fatigue Growth Model

A commonly used model for 1-D subcritical growth of interface crack under fatigue cyclic loading is given by

$$\frac{da}{dN} = B(\Delta G)^\alpha, \tag{10}$$

where a denotes the crack length, N denotes the number of fatigue cycles, ΔG is the applied range of strain energy release rate, B and α are parameters depending on the materials combination and the loading phase angles (ψ , φ). When considering the growth of an interface delamination with a curvilinear crack front, it is assumed that the extension of crack at a specific location on the crack front occurs along the normal direction of the crack front (the x_1 -direction in Fig. 1), and the amount of extension is governed by Eq. 10. Numerical estimation of the delamination growth can be achieved by using an incremental approach, in which the incremental crack extensions at various crack front locations are calculated from the incremental form of Eq. 10, given by:

$$\Delta a_i = B_i (\Delta G_i)^{\alpha_i} \cdot \Delta N, \quad (11)$$

where the subscript i denotes the i -th location on the crack front. By using the incremental extension of crack at the i -th location as a reference, the incremental crack extensions on the other crack front locations under the same incremental cycle numbers (ΔN) can be expressed as:

$$\Delta a = \frac{B(\Delta G)^{\alpha}}{B_i (\Delta G_i)^{\alpha_i}} \Delta a_i. \quad (12)$$

From Eq. 12 an updated crack front geometry can be obtained.

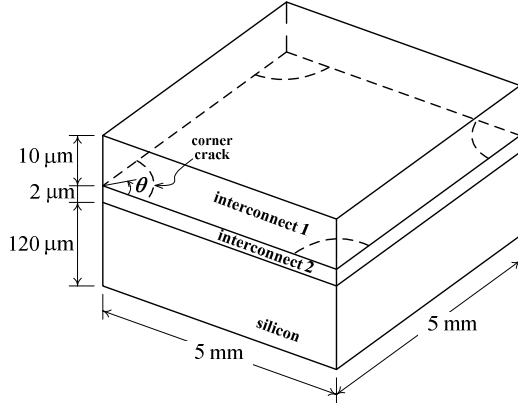


Fig. 2. Interface corner cracks in interconnect structure.

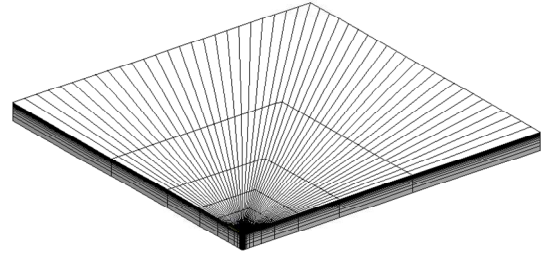


Fig. 3. Quarter finite element model for the interconnect stack containing corner cracks.

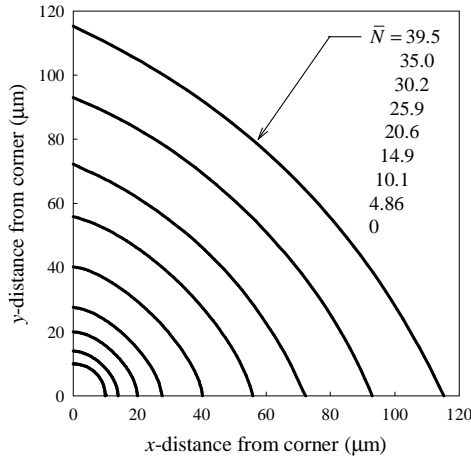


Fig. 4. Evolution of the crack front.

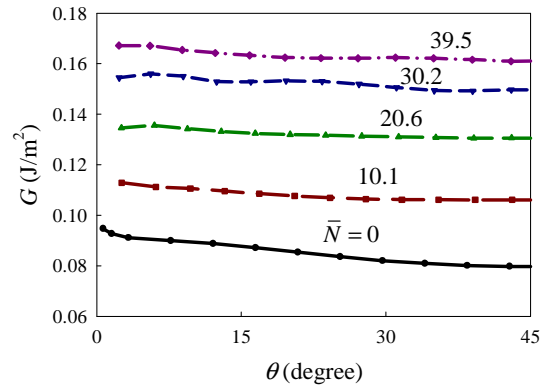


Fig. 5. Evolution of the strain energy release rate along the crack front.

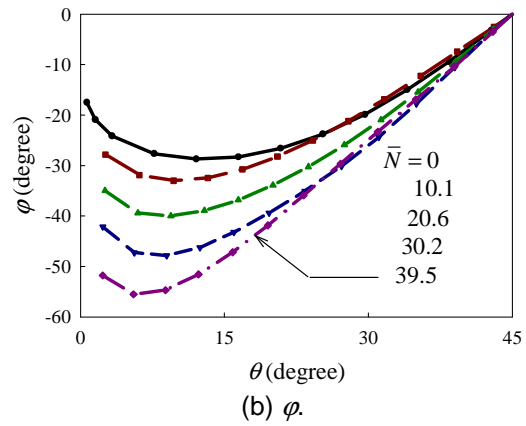
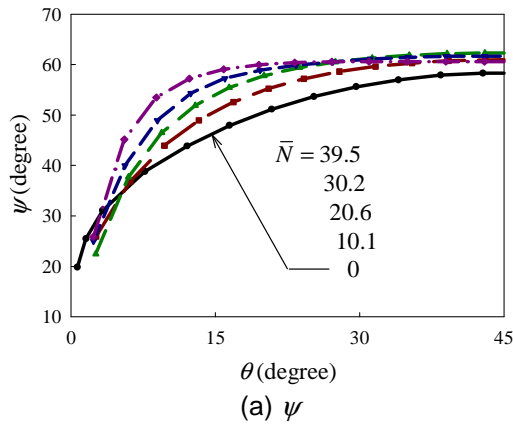


Fig. 6. Evolutions of the phase angles along the interface crack front.

3 RESULTS AND DISCUSSION

The fatigue growths of interface corner defects in microelectronic interconnect structures under a typical 0/100°C T/C are considered. In the analyses it is assumed that the structure is stress-free at 100°C and the thermal stress is most significant at 0°C. A silicon-level interconnect stack containing corner cracks as shown in Fig. 2 is first considered. It is assumed that quarter-circular defects of radius 10 μm are at the interface corners between low- k organosilicate glass dielectric and silicon carbide etch stop layers near the bottom of the interconnect stack. The heterogeneous structures above and beneath the interface defect are approximated by two dissimilar transversely isotropic layers, with equivalent thermomechanical properties given in Table 1. Shown in Fig. 3 is the quarter finite element model used for investigating the problem. From the numerical analysis it is observed that faces of the interface crack are open at 0 °C. Therefore, the oscillating field solutions are presented, and the bottom homogenized interconnect thickness is selected as the characteristic length, i.e., $\hat{r} = 2 \mu\text{m}$, for normalization. Because the experimental data on fatigue response of the interface considered is not available, it is assumed that the fatigue model parameters B and α are constants, and $\alpha = 3$. Advances of the corner delamination under T/C are shown in Fig. 4, in which the constants used for normalization are: $\bar{N} = N/N_0$, $N_0 = a_0/(BG_0^3)$, $a_0 = 1 \text{ mm}$, $G_0 = 1 \text{ J/m}^2$. It can be seen from Fig. 4 that the rate of crack front advancement increases gradually as the crack grows, and it slows down to a more steady level at a later stage. In addition, the growth rate of the crack front near the free surfaces is higher than that of the middle, and as a result, the quarter-circular crack evolves into a triangular crack as it grows. The corresponding fracture mechanics parameter evolutions over temperature cycles are shown in Figs. 5 and 6. Note that the results given in Figs. 5 and 6 are only for θ between 0 and 45°. Due to geometry symmetry with respect to the $\theta = 45^\circ$ plane, the fracture mechanics parameters along the interface front are either even functions of $(\theta - 45^\circ)$ (for G and ψ) or odd function of $(\theta - 45^\circ)$ (for ϕ).

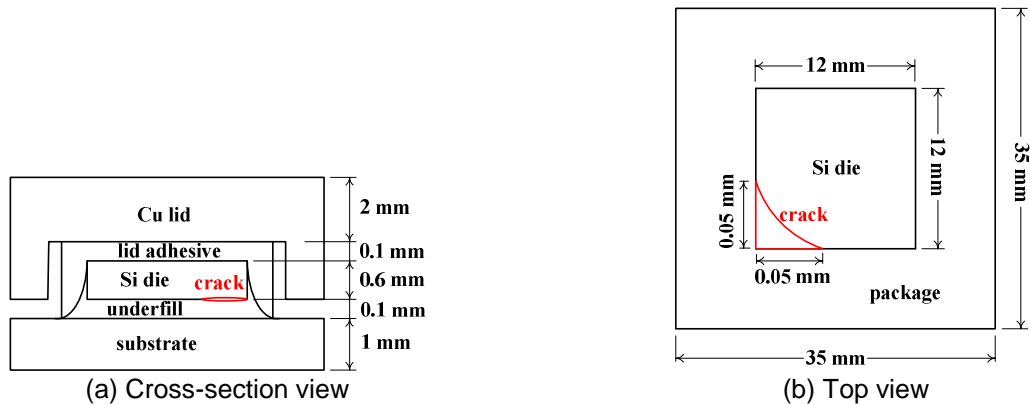


Fig. 7. Schematics of a flip-chip package containing an interface crack.

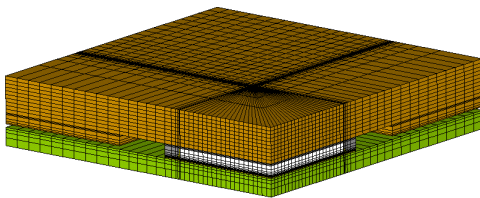


Fig. 8. Quarter finite element model for the flip-chip containing an interface crack.

Table 2. Thermomechanical constants for the flip-chip package.

	E [GPa]	ν	CTE [$10^{-6}/^\circ\text{C}$]
silicon die	150	0.17	2.9
underfill	5	0.35	35
substrate	16	0.35	18
lid adhesive	8	0.35	35
Cu lid	127	0.34	16.7

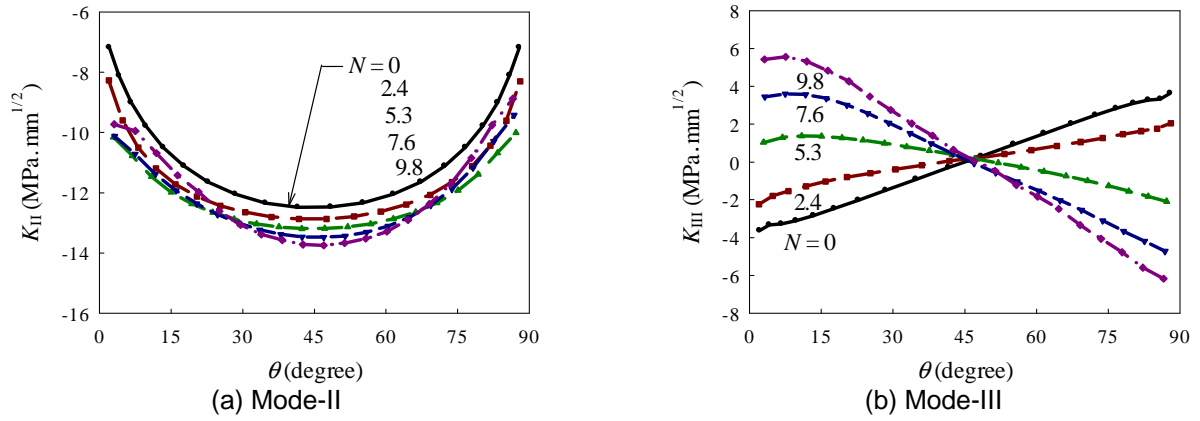


Fig. 9. Evolutions of the stress intensity factors along the crack front.

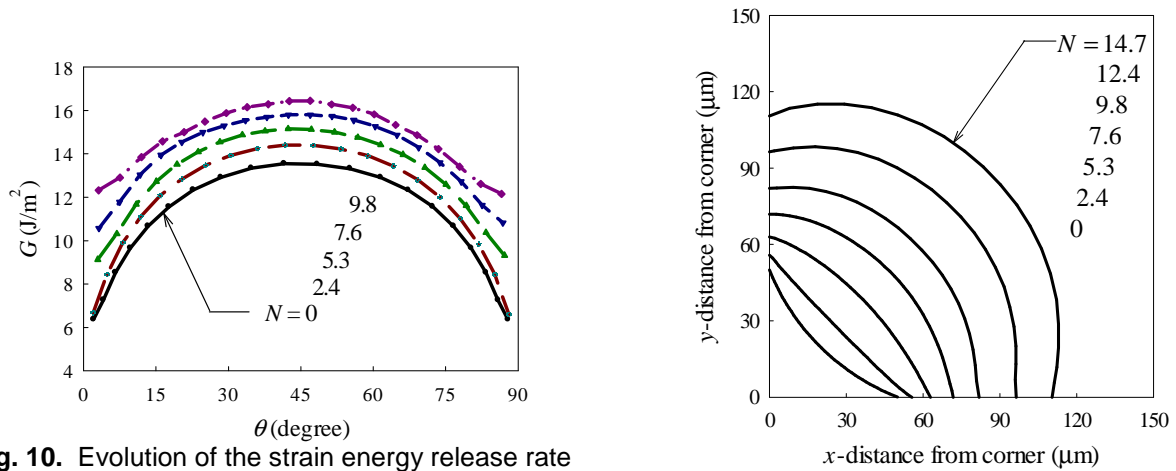


Fig. 10. Evolution of the strain energy release rate along the crack front.

Fig. 11. Evolution of the crack front.

The fatigue growth of an interface corner defect in a flip-chip package subjected to an accelerated 0/100°C T/C is also considered. Shown in Figs. 7 and 8 are the schematic of the package and the quarter finite element model used for the analysis, respectively. The package as shown in Fig. 7 contains corner defect embedded on the interface of Si die and underfill. It is assumed that the Si-underfill interface defect initially has a concave crack front. Material properties of the package are given in Table 2. Results of the incremental fatigue growth simulation are shown in Figs. 9-11. From the analysis it is observed that the faces of the corner delamination are in full contact at 0 °C. Consequently, K_I is zero along the curvilinear crack front. The stress intensity factors, K_{II} and K_{III} , along the crack front are shown in Fig. 9. It may be seen from Fig. 9 that the crack driving force is dominated by K_{II} except near die edges. In addition, K_{II} is highest around the middle of crack front. The strain energy release rate distribution along the crack front is shown in Fig. 10. By assuming that the fatigue subcritical growth behavior is independent of the ratio of K_{II} to K_{III} , the incremental growth of the crack front may be modeled with constant values of B and α . By assuming $\alpha = 3.19$ and $B = 0.001 \mu\text{m}/(\text{J/m}^2)^\alpha$ [7], advances of the corner delamination under T/C fatigue condition is estimated and shown in Fig. 11. It can be seen from Fig. 11 that the growth rates of the crack front near die edges are lower than that of the middle, and as a result, the concave crack front evolves into a quarter circular shape as it grows.

4 CONCLUSIONS

The fatigue subcritical growth of interface corner defect in interconnect structure under T/C is modeled by using an incremental procedure. From the analysis results it is shown that, depending on the location of the initial interface flow, the delamination could evolve into a quarter circular or concave crack front. It is therefore important to consider the more realistic 3-D crack growth to improve the accuracy of the corresponding reliability assessment.

5 ACKNOWLEDGEMENTS

This study was sponsored by the National Science Council of the R.O.C under the grant NSC 97-2218-E-006-048.

6 REFERENCES

- [1] L. L. Mercado, S. M. Kuo, C. Goldberg, D. Frear, Impact of flip-chip packaging on copper/low-k structures, *IEEE Trans. Adv. Packag.*, 26, 433-440, 2003.
- [2] C. J. Zhai, Sidharth, R. C. Blish II, R. N. Master, Investigation and minimization of underfill delamination in flip chip packages, *IEEE Trans. Device Mater. Reliab.*, 4, 86-91, 2004.
- [3] Z. Zhang, C. J. Zhai, R. N. Master, 3D fracture mechanics analysis of underfill delamination for flip chip packages, in *Proceedings of the 11th intersociety conference on thermal and thermomechanical phenomena in electronic systems*, pp. 751-755, 2008.
- [4] T.-C. Chiu, H. C. Lin, On the homogenization of multilayered interconnect for interfacial fracture analysis, *IEEE Trans. Compon. Packag. Technol.*, 31, 388-398, 2008.
- [5] T.-C. Chiu, C.-H. Chen, A numerical procedure for simulating delamination growth on interfaces of interconnect structures, *Microelectron. Reliab.*, 52, 1464-1474, 2012.
- [6] C. Hwu, Fracture parameters for the orthotropic bimaterial interface cracks, *Eng. Fract. Mech.*, 45, 89-97, 1993.
- [7] S. W. Zhu, C. P. Shih, T.-C. Chiu, G. S. Shen, Delamination fracture characteristics for polyimide-related interfaces under fatigue loadings, in *Proceedings of the 5th international microsystems, packaging, assembly and circuits technology conference*, TW076-1, 2010.

ACCURATE DETERMINATION OF STRESS INTENSITY FACTORS FOR INTERFACE CRACK PROBLEM UNDER THERMAL STRESS BY CRACK TIP STRESS METHOD

K. Oda¹, Y. Abe², T. Shinmoto¹ and N. Tsutsumi¹

¹ Mechanical and Energy Systems Engineering, Oita University, Oita, Japan

² Oita Canon Inc., Kunisaki, Oita, Japan

Abstract: This paper deals with the analysis of the stress intensity factor for interfacial crack in dissimilar materials under thermal stress by using the crack tip stress method. This method is based on the fact that the singular stress field near the interface crack tip is controlled by the stress values at the crack tip node calculated by the finite element method. The calculation shows that the present method has the sufficient accuracy in the interface crack problems under thermal stress.

Keywords: Interface Crack, Crack Tip Stress Method, Stress Intensity Factor, Thermal Stress

1 INTRODUCTION

The determination of stress intensity factor (SIF) for interface crack under thermal boundary conditions is a subject of practical importance [1-2]. Many methods have been developed to calculate the SIF of an interface crack by using the finite element method. However, it is still not necessarily easy to analyze SIF of interface crack under thermal stress by FEM because of the oscillatory stress singularity.

In this paper, interface crack problems subjected to uniform change of temperature are considered as shown in Fig.1. In Fig.1, E_j , ν_j , η_j ($j=1, 2$) and ΔT are Young's modulus, Poisson's ratio, linear coefficient of thermal expansion and temperature change, respectively. To determine the SIFs under thermal stress, the stresses at the interface crack tip calculated by FEM are used and are compared with the results of reference problem shown in Fig.2a under the same mesh pattern near the crack tip [3-7]. In this study, a central interface crack and a branched interface crack in a bonded rectangular plate will be examined with varying plate size and changing material combination. Then, the effect of material combination on the SIF for interface crack will be discussed.

2 CRACK TIP STRESS METHOD

Recently, the effective method was proposed for calculating the stress intensity factor by using FEM [5-7]. The method utilizes the stress values at the crack tip by FEM. From the stresses σ_y , τ_{xy} near the interface crack tip, stress intensity factors are defined as shown in Eq.1.

$$\sigma_y + i\tau_{xy} = \frac{K_1 + iK_2}{\sqrt{2\pi r}} \left(\frac{r}{2a} \right)^{i\varepsilon}, \quad \varepsilon = \frac{1}{2\pi} \ln \left[\left(\frac{\kappa_1 + 1}{G_1} + \frac{1}{G_2} \right) \right] / \left(\frac{\kappa_2 + 1}{G_2} + \frac{1}{G_1} \right) \quad (1)$$

In Eq.2, G_j is the shear modulus, $\kappa_j = 3 - 4\nu_j$ for plane strain, $\kappa_j = (3 - \nu_j)/(1 + \nu_j)$ for plane stress and ν_j is Poisson's ratio ($j=1, 2$). From Eq.1, SIFs may be separated as

$$K_1 = \lim_{r \rightarrow 0} \sqrt{2\pi r} \sigma_y \{ \cos Q + (\tau_{xy}/\sigma_y) \sin Q \}, \quad K_2 = \lim_{r \rightarrow 0} \sqrt{2\pi r} \tau_{xy} \{ \cos Q - (\sigma_y/\tau_{xy}) \sin Q \}, \quad (2)$$

$$Q = \varepsilon \ln \{ r/(2a) \}. \quad (3)$$

Here, r and Q can be chosen as constant values when the reference and unknown problems have the same crack length and the same material constants. If Eq.4 is satisfied, Eq.5 may be derived from Eqs.2.

$$\tau_{xy}^* / \sigma_y^* = \tau_{xy} / \sigma_y \quad (4)$$

$$K_1^* / \sigma_y^* = K_1 / \sigma_y, \quad K_2^* / \tau_{xy}^* = K_2 / \tau_{xy} \quad (5)$$

Here, σ_y^* , τ_{xy}^* are stresses of reference problem near the crack tip, and σ_y , τ_{xy} are stresses of unknown problem in Fig. 1. The asterisk means the value of reference problem. By using the stress values at the interface crack tip calculated by FEM, the SIFs of the unknown problem can be obtained by

$$K_1 = \frac{\sigma_{y0,FEM}}{\sigma_{y0,FEM}^*} K_1^*, \quad K_2 = \frac{\tau_{xy0,FEM}}{\tau_{xy0,FEM}^*} K_2^* \quad (6)$$

When the single interface crack in a dissimilar bonded infinite plane subjected to the loads T and S shown in Fig. 2a is selected as the reference problem, the SIFs of the reference problem are evaluated by

$$K_1^* + iK_2^* = (T + iS)\sqrt{\pi a}(1 + 2i\varepsilon) \quad (7)$$

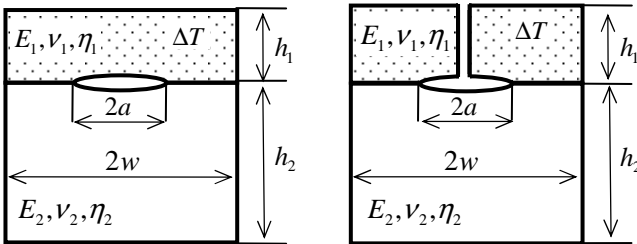
In order to determine the applied loads T and S in Eq.7, the reference problem is expressed by superposing the tension and shear problems [5, 6]. The stresses at the interface crack tip of the reference problem are expressed by

$$\sigma_{y0,FEM}^* = T \cdot \sigma_{y0,FEM}^{T=1} + S \cdot \sigma_{y0,FEM}^{S=1}, \quad \tau_{xy0,FEM}^* = T \cdot \tau_{xy0,FEM}^{T=1} + S \cdot \tau_{xy0,FEM}^{S=1} \quad (8)$$

where $\sigma_{y0,FEM}^{T=1}$ stands for the stress σ_y at the crack-tip node calculated by FEM in the condition of T=1 and S=0. From the condition that the crack-tip-stresses between the unknown and the reference problems are the same, we obtain the applied loads T and S as follows,

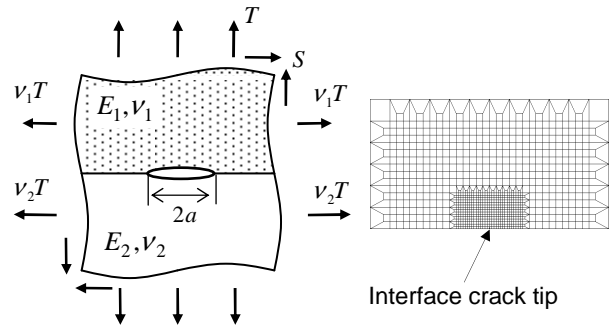
$$T = \frac{\sigma_{y0,FEM} \cdot \tau_{xy0,FEM}^{S=1} - \sigma_{y0,FEM}^{S=1} \cdot \tau_{xy0,FEM}}{\sigma_{y0,FEM}^{T=1} \cdot \tau_{xy0,FEM}^{S=1} - \sigma_{y0,FEM}^{S=1} \cdot \tau_{xy0,FEM}^{T=1}}, \quad S = \frac{\sigma_{y0,FEM}^{T=1} \cdot \tau_{xy0,FEM} - \sigma_{y0,FEM} \cdot \tau_{xy0,FEM}^{T=1}}{\sigma_{y0,FEM}^{T=1} \cdot \tau_{xy0,FEM}^{S=1} - \sigma_{y0,FEM}^{S=1} \cdot \tau_{xy0,FEM}^{T=1}} \quad (9)$$

Since the applied loads T and S determined by Eq.9 satisfy the condition that $\sigma_{y0,FEM}^* = \sigma_{y0,FEM}$ and $\tau_{xy0,FEM}^* = \tau_{xy0,FEM}$, the SIFs of unknown problem are equivalent to that of reference problem. Therefore, we can obtain the SIFs of unknown problem from Eqs.7 and 9 by using the crack tip stress values calculated by FEM under the same mesh pattern.



(a) Centre interface crack (b) Branched interface crack

Fig. 1. Two types of thermal crack problems subjected to uniform temperature change



(a) Reference problem (b) FEM mesh near the crack

Fig. 2. Reference problem and FEM mesh pattern

3 NUMERICAL RESULTS AND DISCUSSION

In this analysis, four-node-quadrilateral element is used and the FEM mesh near the crack tip is made fine systematically as illustrated in Fig. 2b [3-6]. It should be noted that the same mesh patterns near the crack tip have to be used in the calculation of stress values for the unknown and reference problems.

3.1 Stress distribution near the crack tip

The stress distributions near the interface crack tip are indicated in Fig. 3 to confirm the effectiveness of the proposed method. The open marks indicate the stress distributions of the thermal problem shown in Fig.1a and the solid marks are that of the reference problem. As shown in Fig.3, it is found that the stress distributions are in good agreement with each other and the singular stress field is controlled by the crack tip stress values obtained by FEM under the same mesh pattern near the crack tip.

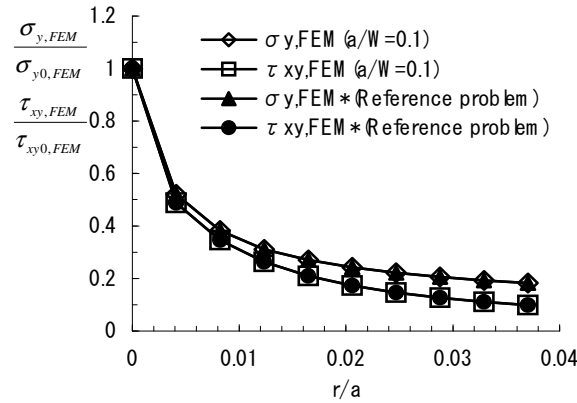


Fig. 3. Relative stress distributions near the interface crack tip under the same mesh pattern.

3.2 Effect of material combination

In order to examine the effect of material constants on the SIFs, four kinds of bonded rectangular specimens with a center interface crack, which have the equal Dundurs' parameters, are selected as shown in Table 1. The Dundurs' parameters α and β are defined by

$$\alpha = \frac{G_1(\kappa_2 + 1) - G_2(\kappa_1 + 1)}{G_1(\kappa_2 + 1) + G_2(\kappa_1 + 1)}, \quad \beta = \frac{G_1(\kappa_2 - 1) + G_2(\kappa_1 - 1)}{G_1(\kappa_2 + 1) + G_2(\kappa_1 + 1)} \quad (10)$$

Table 2 shows the normalized SIFs computed by using four material combinations (a-d) in Table 1. The SIFs in this thermal stress problem can be expressed by the following normalized values,

$$F_1 = \frac{K_1}{E_1^* \Delta \eta^* \Delta T \sqrt{\pi a}}, \quad F_2 = \frac{K_2}{E_1^* \Delta \eta^* \Delta T \sqrt{\pi a}} \quad (11)$$

$$E_1^* = \begin{cases} E_1 & : \text{Plane stress} \\ E_1 / (1 - \nu_1^2) & : \text{Plane strain} \end{cases}, \quad \Delta \eta^* = \begin{cases} \eta_1 - \eta_2 & : \text{Plane stress} \\ (1 + \nu_1) \eta_1 - (1 + \nu_2) \eta_2 & : \text{Plane strain} \end{cases} \quad (12)$$

As shown in Table 2, the values of F_1 and F_2 for the material combinations (a-d) are almost the same. Therefore, the normalized SIFs in this thermal problem are determined by the Dundurs' parameter.

Table 1. Material constants for four kinds of bonded dissimilar plates with the equal Dundurs' parameters ($\alpha=0.3$, $\beta=0.1$) as shown in Fig.1a.

Material combination	Plane strain		Plane stress	
	(a)	(b)	(c)	(d)
E_1	210	180	210	180
E_2	114.672	95.901	113.076	96.923
ν_1	0.3	0.2	0.3	0.2
ν_2	0.27778	0.22388	0.31538	0.26154
$\alpha_1 [\times 10^{-6}]$	2.0	3.0	2.0	3.0
$\alpha_2 [\times 10^{-6}]$	1.0	1.5	1.0	1.5

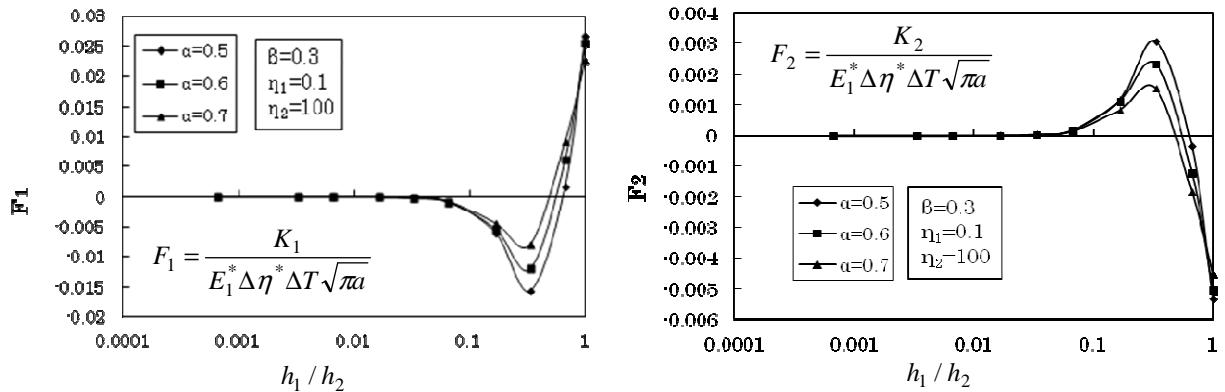
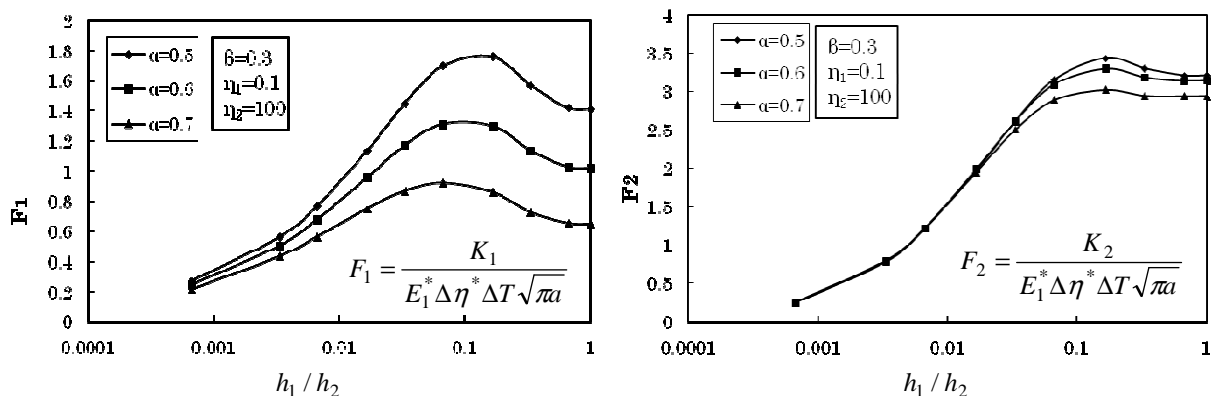
Table 2. Normalized SIFs for four kinds of material combinations shown in Table 1.

a/w	Material combination		F ₁	F ₂
0.1	Plane strain	(a)	-0.017193	0.006316
		(b)	-0.017191	0.006312
	Plane stress	(c)	-0.017192	0.006313
		(d)	-0.017191	0.006311

3.3 Comparison between centre interface crack and branched interface crack

Two interface crack problems under uniform temperature change are analyzed as illustrated in Fig.1. In this analysis, the half crack length $a=10\text{mm}$, the width of plate $w/a=1500$ and Dundurs' parameter $\beta=0.3$ are assumed. The ratio h_1/h_2 of plate height and Dundurs' parameter α are changed to consider the free boundary effect.

The effect of the ratio h_1/h_2 on the normalized SIFs is illustrated in Figs.4 and 5. Fig.4 is the normalized SIFs of the center interface crack problem, and Fig.5 is that of the branched interface crack problem. As shown in these figures, The normalized SIFs, F_1 and F_2 , for both problems represent the extreme value when $h_1/h_2 > 0.1$ and the normalized values decrease with decreasing the ratio h_1/h_2 when $h_1/h_2 < 0.1$. In the branched interface crack problem, it is found that F_1 and F_2 are always positive.

**Fig. 4.** Relation between normalized SIFs and h_1/h_2 for the center interface crack problem (Fig.1a).**Fig. 5.** Relation between normalized SIFs and h_1/h_2 for the branched interface crack problem (Fig.1b).

4 CONCLUSIONS

The stress intensity factor for two kinds of interfacial crack in dissimilar materials under thermal stress were analyzed by using the crack tip stress method. In this present method, the accurate stress intensity factor is easily determined only by calculating the stress values at the crack tip node. The normalized SIFs defined by Eq.11 in the thermal problem are determined by the Dundurs' parameters α and β . The calculation showed that the normalized SIFs, F_1 and F_2 , for both problems represent the extreme value when the ratio of plate height $h_1/h_2 > 0.1$ irrespective of the material combination.

5 REFERENCES

- [1] F. Erdogan, Stress Distribution in Bonded Dissimilar Materials with Cracks, *Journal of Applied Mechanics*, Vol.32, pp.403–410, 1965.
- [2] T. Ikeda, T. Sun, Stress Intensity Factor Analysis for an Interface Crack between Dissimilar Isotropic Materials under Thermal Stress, *International Journal of Fracture*, Vol. 111, pp.229-249, 2001.
- [3] H. Nisitani, T. Kawamura, W. Fujisaki, T. Fukuda, Determination of Highly Accurate Values of Stress Intensity Factor or Stress Concentration Factor of Plate Specimen by FEM, *Transactions of the Japan Society of Mechanical Engineering (JSME)*, Vol. 65A, No. 629, pp. 26-31, 1999 (in Japanese).
- [4] H. Nisitani, T. Teranishi, K. Fukuyama, Stress Intensity Factor Analysis of a Bimaterial Plate Based on the Crack Tip Stress Method, *Transactions of the JSME*, Vol. 69A, No. 684, pp. 1203-1208, 2003 (in Japanese).
- [5] K. Oda, N.-A. Noda, S.N. Atluri, Accurate Determination of Stress Intensity Factor for Interface Crack by Finite Element Method, *Key Engineering Materials*, Vols. 353-358, pp.3124-3127, 2007.
- [6] K. Oda, K. Kamisugi, N.-A. Noda, Stress Intensity Factor Analysis of Interface Crack by Proportional Method, *Transactions of the JSME*, Vol. 75A, No. 752, pp. 476-482, 2009 (in Japanese).
- [7] N.-A. Noda, Y. Zhang, X. Lan, Y. Takase, K. Oda, Stress Intensity Factor of an Interface Crack in a Bonded Plate under Uni-Axial Tension, *Journal of Solid Mechanics and Materials Engineering*, Vol. 4, No. 7, pp.974-987, 2010.

TOPOLOGICAL OPTIMIZATION FOR MACHINE STRUCTURE DESIGN

Tae-Jin Chung, Henry Panganiban and Won-cheol Kim

School of Mechanical and Automotive Engineering, Kunsan National University, Korea

Abstract: Optimal design of base structure for a telescopic boom lift is obtained using topology optimization method. The classical topology optimization formulation is implemented with consideration on various load cases encompassing actual operation conditions. Reaction forces due to various load cases are used for analysis and optimization of the isolated base structure of the boom. This method greatly reduces model size and consequently computation time allowing more opportunities to explore possible design configurations. The topology or material layout of the base structure at the converged iteration is translated into manufacturable final design. Structural performance of the proposed base structure design is verified against various load cases using FE analysis. Maximum stresses are relatively low for all load cases. Subsequent size and/or shape optimization can be performed for significant weight reduction without degradation of structural performance.

Keywords: Optimal Design, Topology Optimization, Telescopic Boom Lift, Base Structure Design

1 INTRODUCTION

The design of a long-range telescopic aerial boom lift (Fig. 1) used for lifting and positioning work platforms at elevated locations requires serious consideration of structural integrity for safe and reliable operation of the system. The various structural components within the whole mechanical system must be designed within acceptable safety factor. To quickly come-up with a solution for component design problem, the use of computer-aided engineering (CAE) tools is a practical approach for a designer or engineer. CAE tools have been proven effective and economical for product development over a wide variety of industries [1-4].

Topology optimization is a kind of CAE tool or more specifically a finite element (FE) – based structural optimization technique that enables a fast conceptualization of structural designs [5]. The basic principle of topology optimization method is that it finds the best layout of a limited amount of material over the given design space for a particular support and load conditions. In this paper, the use of topology optimization method for the design of base support structure for a long-range telescopic boom lift is presented. With various load cases corresponding to actual operation conditions, topology optimization can be carried out in order to obtain the optimal structural layout of the stiffest base structure of the boom. The optimal topology result can be interpreted to conceptualize structural layout design and further post-processed to enhance the desired structural performance and weight reduction [6]. This optimization approach can be readily carried out using Altair HyperWorks analysis and optimization tools.

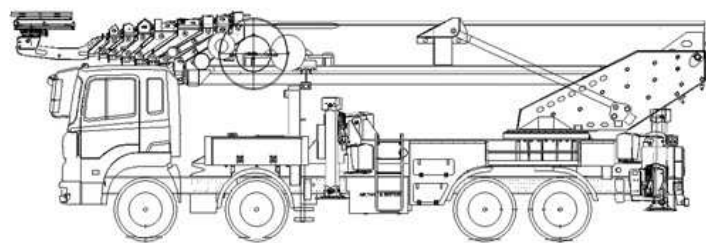


Fig. 1. Profile of a telescopic aerial boom lift [7].

2 BOOM SUPPORT STRUCTURE LOADS

Fig. 2 shows the fully-extended 9-segment telescopic boom lift. By design, full extension of the boom is permitted only when the boom is tilted starting from 64° to 85° angle with the horizontal. The boom is pinned-jointed with the support structure at the base of the boom and its hydraulic cylinder brackets as illustrated in Fig. 2(a). The work platform (not shown) attached at the tip of the boom including the maximum payload weigh 700 kg while the total weight of the 9-segment boom is 8,935 kg acting at the center of gravity. To enable the optimal design of boom support structure, the reaction forces acting at the pins resulting from the application of the maximum operating load and self-weight or gravity load of the massive boom are calculated using fundamental static engineering mechanics approach. The static loads are represented by the corresponding forces acting at known points i.e. at the boom tip and center of gravity for a given working length. The coordinates of the load points for a given length and boom orientation are obtained using a CAD tool.

Fig. 2(a) illustrates the schematic diagram of point loads acting on the boom. The corresponding rectangular components of the reaction forces with assumed directions at the support structure are shown in Fig. 2(b). Using equilibrium equations, R on points A and B can be expressed as

$$R_{Ax} = \frac{[W(x_D - x_B) + P(x_E - x_B)]}{\sin \beta (x_C - x_B) - \cos \beta (y_C - y_B)} \cos \beta$$

$$R_{Ay} = \frac{[W(x_D - x_B) + P(x_E - x_B)]}{\sin \beta (x_C - x_B) - \cos \beta (y_C - y_B)} \sin \beta \quad (1)$$

$$R_{Bx} = -R_{Ax}$$

$$R_{By} = W + P - R_{Ay}$$

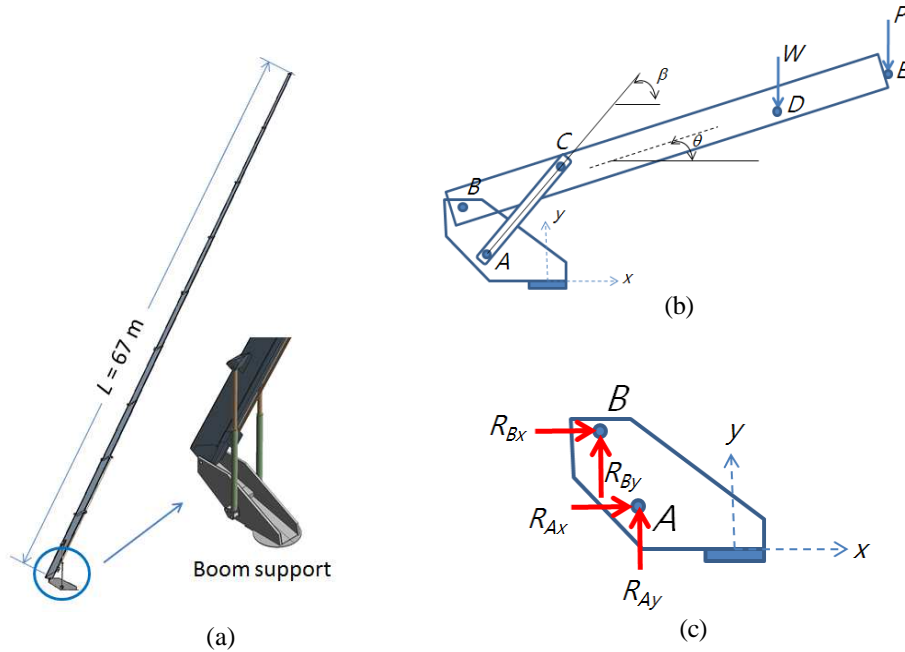


Fig. 2. (a) Boom base support structure (b) static loads on the boom (b) forces acting (reaction forces) on the base support structure.

3 BASE STRUCTURE TOPOLOGY OPTIMIZATION

The design domain defined for the topology optimization of the boom base structure defined for this study is shown in Fig. 3. Note that the imposed loads are obtained using Eq. (1) with an addition of wind load which is acting in transverse direction relative to the plane of the boom. Five load cases

representing essential actual scenarios are considered: boom tilt angles at -13° , 0° , 64° , and 85° and a conservative wind load. The topology optimization problem is formulated as shown in Eq. (2). In Eq. (2) $f(x)$ is the objective function, $g(x)$ is the constraint function, \mathbf{x} is the design variable vector, \mathbf{v} is the element volume vector, \mathbf{u} is the displacement vector, \mathbf{K} is the stiffness matrix, m^* is the specified mass limit of the base structure, w_i is the weighting factor for load case i ($i=1,2,\dots,5$), and C_i is the compliance for load case i . The design variables represent the relative density of each finite element in the design space.

$$\begin{aligned}
 &\text{minimize} \quad f(\mathbf{x}) = \sum_{i=1}^5 w_i C_i = \sum_{i=1}^5 w_i \mathbf{u}^T \mathbf{K} \mathbf{u} \\
 &\text{subject to} \quad g(\mathbf{x}) = \mathbf{x}^T \mathbf{v} \leq m^* \quad (2) \\
 &\quad \mathbf{K}(\mathbf{x}) \mathbf{u} = \mathbf{f}; E_e = x_e^p E; p = 3 \\
 &\quad 0.01 = x_e^L \leq x_e \leq x_e^U = 1.0 \\
 &\quad \mathbf{x} = \{x_1, x_2, x_3, \dots, x_N\}^T
 \end{aligned}$$

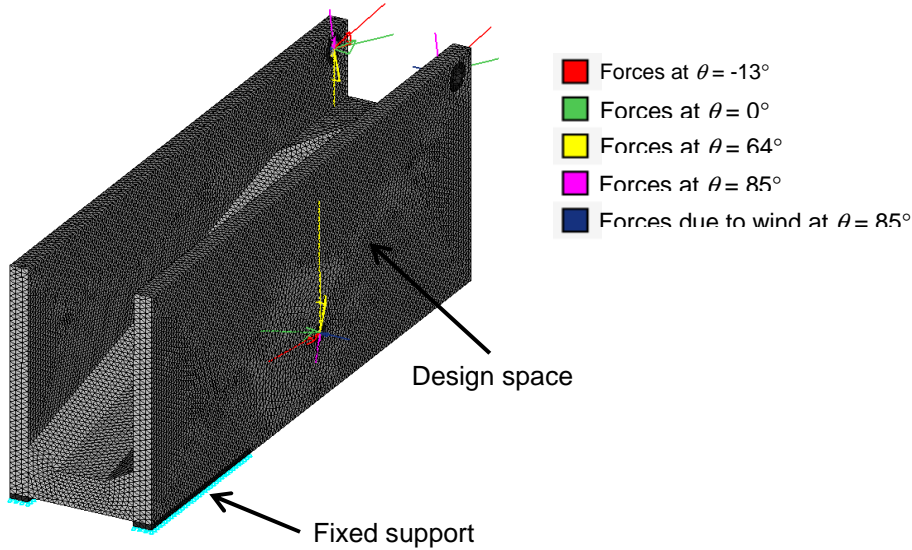


Fig. 3. Design space and load definition for the base structure topology optimization.

4 RESULTS

Assuming 20% of the initial structure (at iteration 0) as the mass constraint and equal weights ($w_i = 1.0$; $i = 1, 2, \dots, 5$) for the five load cases, the optimal layout of the base structure shown in Fig. 4 was found after 25 iterations. Fig. 5 shows the element density contour plot with threshold value for the relative densities or design variables set to 0.70. Thicker members forming a frame enclosure to the structure are noticeable. This appears to provide support to vertical bending loads. The cross members that serve as stiffeners against the transverse load are also obvious. An interpretation of the optimal topology of the boom base structure as obtained from the optimization solution is shown in Fig. 6. Structural analysis of the proposed design of the base structure was carried out to check the performance when subjected to the assumed load cases. Table 1 shows the summary of structural performance of the proposed design of the boom base structure. Stress contour plot for the boom post when the telescopic boom is at maximum length of 67 m and tilted at 85° is shown in Fig. 6(b). The maximum stresses for all load cases are observed

to be low. Thus, subsequent optimization steps with the objective of reducing mass while maintaining the structural performance can be carried out in future study.

Table 1. Maximum stresses in the proposed design of the boom base structure for the five load cases (LC).

	LC1: $\theta = -13^\circ$	LC2: $\theta = 0^\circ$	LC3: $\theta = 64^\circ$	LC4: $\theta = 85^\circ$	LC5: Wind load
Max. VM stress [MPa]	31.1	61.6	75.1	56.3	137.7

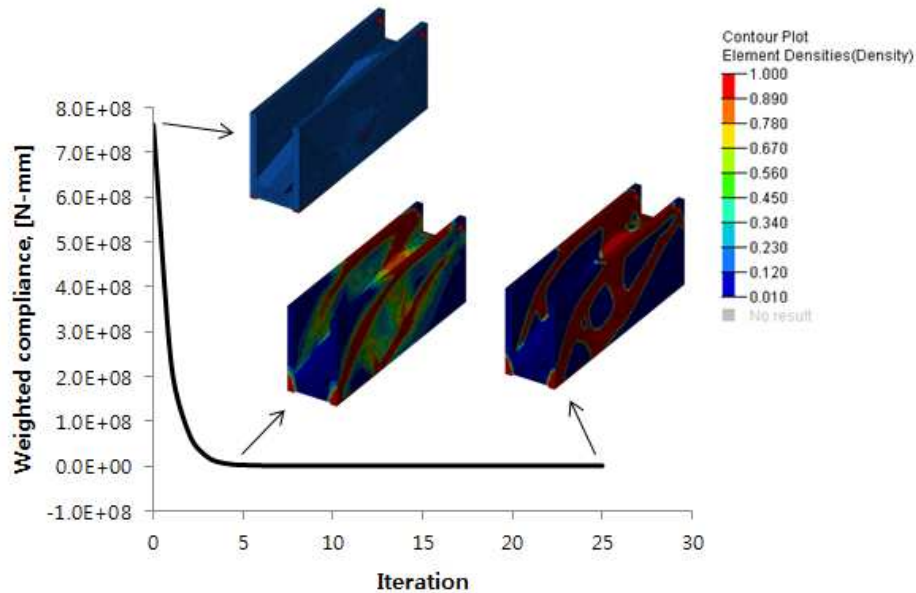


Fig. 4. Optimal base structure topology under weighted compliance minimization with 20% mass constraint.

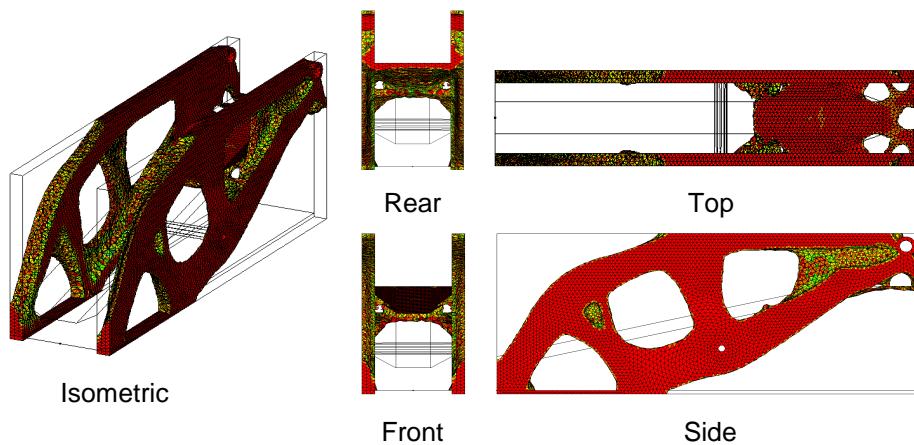


Fig. 5. Optimal base structure topology with element densities or design variables threshold set to 0.70.

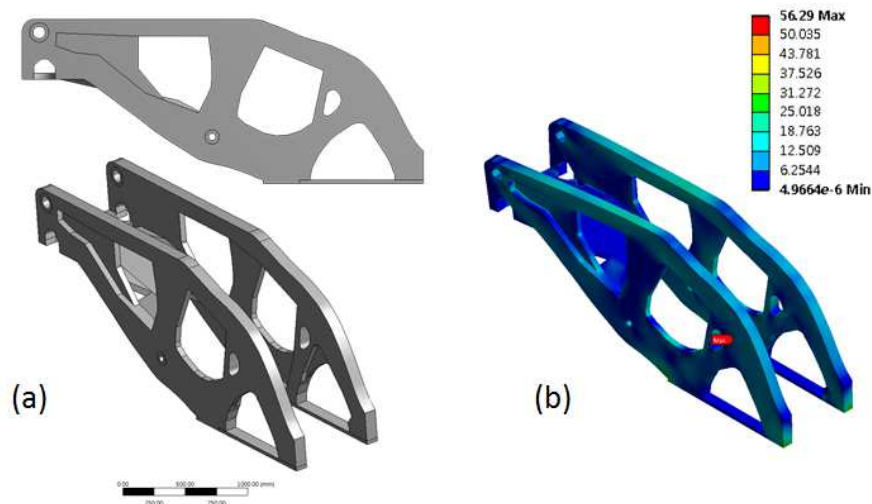


Fig. 6. Interpretation of the boom post topology optimization result (a) and the equivalent VM stress contour plot for 85° boom tilt scenario (b).

5 CONCLUSIONS

Design concept of the boom base structure was quickly generated using topology optimization technique. Post-processed design interpreted out of the topology optimization solution is proposed as the optimal design for the prescribed loading conditions. The maximum stresses in the proposed optimal design for all load cases are observed to be low. Thus, subsequent size and/or shape optimization steps with the objective of reducing mass while maintaining the structural performance can be carried out in future study.

ACKNOWLEDGMENT

This research was supported by Basic Science Research Program through the National Research Foundation of Korea (NRF) funded by the Ministry of Education, Science and Technology (2011-0023016).

REFERENCES

- [1] H.-S. Park and X.-P. Dang, "Structural optimization based on CAD–CAE integration and metamodeling techniques," *Computer-Aided Design*, vol. 42, pp. 889-902, 2010.
- [2] H. Panganiban, I. G. Ahn, and T. J. Chung, "Multi-phase Design Optimization of a Long Range Aerial Lift Boom Structure," in *World Congress on Engineering 2012*, London, U.K., 2012, pp. 1697-1700.
- [3] Y. M. Deng, Y. C. Lam, S. B. Tor, and G. A. Britton, "A CAD-CAE Integrated Injection Molding Design System," *Engineering with Computers*, vol. 18, pp. 80-92, 2002.
- [4] Y. Kang, Y. P. Chang, J. W. Tsai, S. C. Chen, and L. K. Yang, "Integrated "CAE" strategies for the design of machine tool spindle-bearing systems," *Finite Elements in Analysis and Design*, vol. 37, pp. 485-511, 2001.
- [5] H. Panganiban, G. W. Jang, and M. S. Yoon, "Optimal Design Of Lightweight Flatbed Trailer Frame Using The Ground-Structure Method," in *9th World Congress on Structural and Multidisciplinary Optimization*, Shizuoka, Japan, 2011.
- [6] G. W. Jang, M. S. Yoon, and J. H. Park, "Lightweight flatbed trailer design by using topology and thickness optimization," *Struct Multidisc Optim*, vol. 41, pp. 295-307, 2010.
- [7] Horyong. Available: http://www.horyong.co.kr/sub3/menu3_05.php

ESTIMATION OF THE KNEE JOINT FORCE DURING DEEP KNEE FLEXION

M. Fukunaga¹, K. Koguchi¹ and S. Hirokawa²

¹ Ariake National College of Technology, Omuta, Japan

² Research Center for Advanced Biomechanics, Kyushu University, Fukuoka, Japan

Abstract: The objective of our study is to estimate the knee joint force during deep knee flexion. When a knee flex deeply, contact force works on thigh and calf. We measured the contact force by pressure sensor sheet, and took it into consideration calculating the knee joint force. The objective motion was standing up from squatting position. As a result, the thigh-calf contact force was about 0.8[BM] at maximum flexion and it decreased zero when the knee extended about 20°. Knee joint force was reduced 20-30% at maximum flexion, considering the thigh-calf contact force.

Keywords: Biomechanics; Knee Joint Force; Deep Knee Flexion; Thigh-Calf Contact; Model Analysis

1 INTRODUCTION

Recently, artificial knee joints have obtained their higher performance and longer product-life by improving their geometrical design and materials. And today, the artificial knee joint which is capable of deep knee flexion motion with over 130° of knee flexion angle, have been developed.

Dynamic model analysis is used for design evaluation of the artificial knee joint. Knee joint force and muscle forces around the knee are required for using as an input data of such analysis. However, most of previous studies have targeted level walking, and studies of targeting deep knee flexion are extremely few. The model calculating the knee joint forces during level walking might not be acceptable for estimating the knee joint forces during deep flexion. We must construct the dynamic model which can consider the phenomena which do not occur during level walking. Thigh- calf contact is one of the typical phenomena occurring during deep knee flexion.

The purpose of this study is to determine the effect of the thigh calf contact force to the knee joint force during deep knee flexion.

2 MATERIALS AND METHODS

2.1 Musculo-skeletal model of a lower limb

Model analysis was performed using the two-dimensional model of a lower limbs. The model was constructed referring some previous studies targeting level walking[1,2]. And the thigh-calf contact force, P in Fig.1, was taken into consideration as an external force.

Muscle force was calculated by using the moment equilibrium conditions around each joint and some assumptions about the ratio of the forces of synergist muscles[3,4]. Knee joint force was estimated from the muscle forces. Equations (1)-(3) show the moment equilibrium conditions around hip, knee and ankle joint respectively. Z and X stand for floor reacting forces, $W1$, $W2$, $W3$ for gravity forces, GAS , S , H , R , GM , Q' for muscle forces, and a , b , c with additional character for the moment arm length around each joint, as shown in Fig.1.

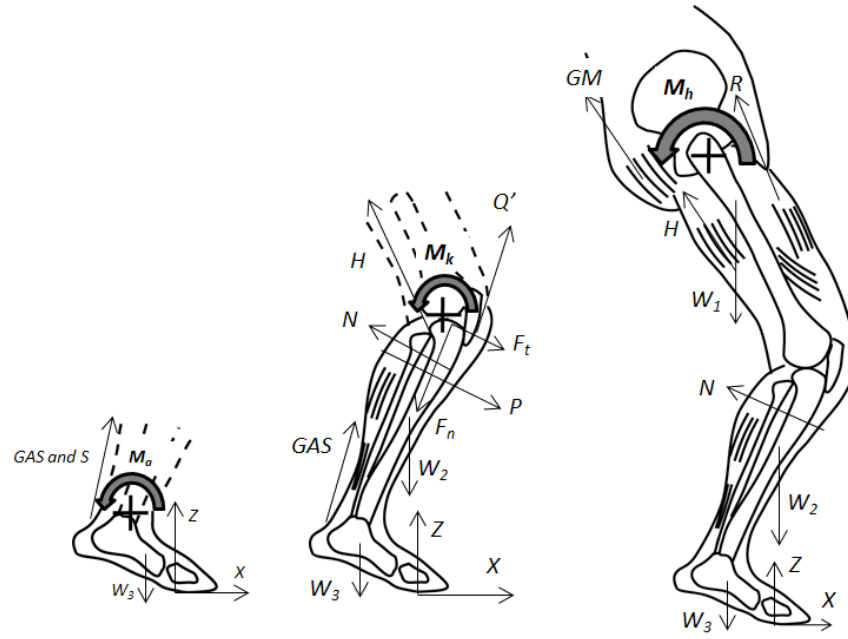


Fig.1. Forces to calculate the moment equilibrium condition around each joint.

$$Z_{cZ} + X_{cX} - W_3 a_{W3} - (GAS + S) c_{GAS} = 0 \quad (1)$$

$$-Zb_Z + Xb_X + W_2 b_{W2} + W_3 b_{W3} - GAS b_{GAS} + Q' b_{Q'} - H b_H + P b_P = 0 \quad (2)$$

$$Za_Z + Xa_X - W_1 a_{W1} - W_2 a_{W2} - W_3 a_{W3} - GM a_{GM} - Ha_H + Ra_R = 0 \quad (3)$$

2.2 Measurement of the thigh-calf contact force

Test subjects were four healthy male. Average age was 20, height was 1.68[m] and weight was 65[kg]. The motion to be subjected was a rising from a squatting posture to a standing posture. The squatting posture was without heel-ground contact. Thigh-calf contact force were measured by pressure distribution sensor, CONFORMat (Nitta Co., Japan). We introduced the thigh-calf contact force and its acting position from the measured data of pressure between thigh and calf. CONFORMat was inserted between the thigh and calf of both legs of the subjects. Pressure was measured during the motion. Knee joint angle was measured (Fig.2). Therefore we put the measured data into the model, and calculated knee joint force.

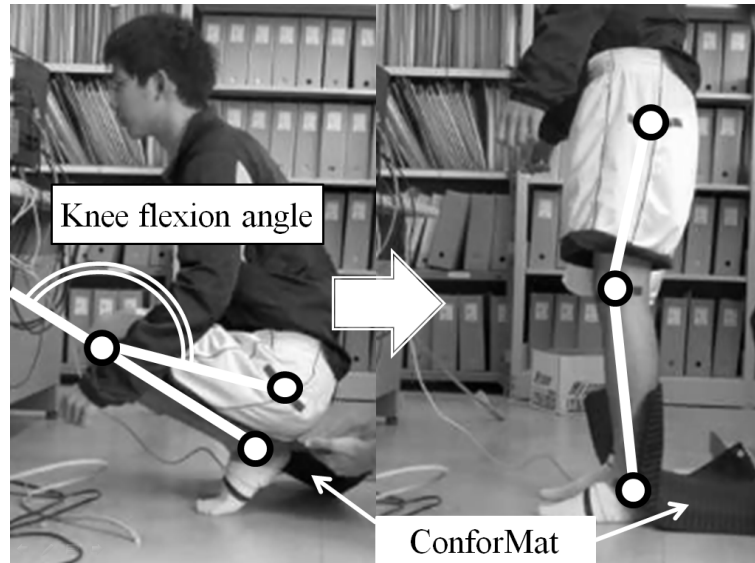


Fig. 2. Measurement of a thigh-calf contact force during objective motion.

3 RESULTS AND DISCUSSIONS

As a result, thigh-calf contact forces among four subjects varied very much when organized by knee flexion angle[5], however, the variation reduced by organizing them by the knee extension angle from the squatting position. Fig.3 shows the thigh-calf contact forces organized by the knee extension angle. It was about 0.85[BW] maximum at the squatting position, and decreased rapidly. It did not act when the knee extend over 20°.

Fig.4 shows the acting positions of the thigh-calf contact force. It was shown as the moment arm length around a knee joint, as a ratio between the lengths and lengths of their calf. It showed maximum value at the squatting position and decreased rapidly, as similar to the contact force.

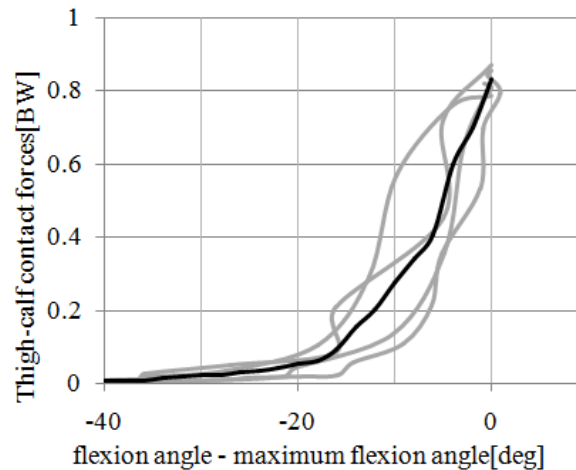


Fig. 3. Thigh-calf contact forces.

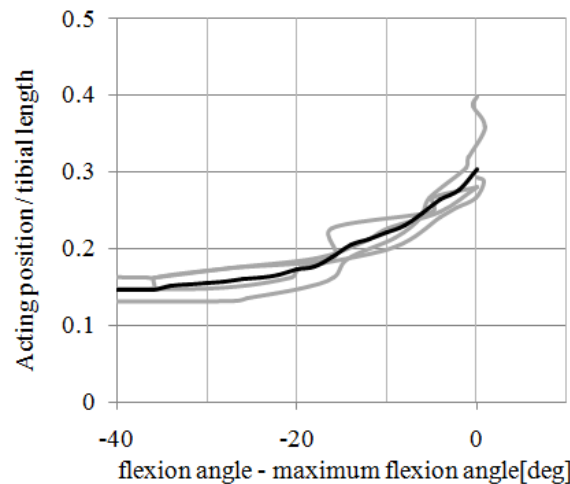


Fig. 4. Action position of contact forces.

Therefore, we estimated the knee joint force by taking the result above into the model analysis.

Fig.5 shows the knee joint forces, without considering the contact force and considering it. The character F_n stands for the tibial axial component of the knee joint forces and F_t for the anterior-posterior component respectively. Knee joint force was reduced slightly in both the axial component and anterior-posterior component. It reduced about 30% maximum at the squatting position. The maximum knee joint force also reduced about 20%. It might be a reasonable result, because, at squatting position, the knee joint moment by the floor reacting force was reduced by the thigh-calf contact force. The thigh-calf contact force was about 80% of the floor reacting forces, because the floor reacting force might be equal to the body weight during quasi-static motion. And the moment arm length of the thigh-calf contact forces were 30% of that of

floor reacting forces. We could simply estimate how much the knee joint force reduced by multiplying 80% and 30%.

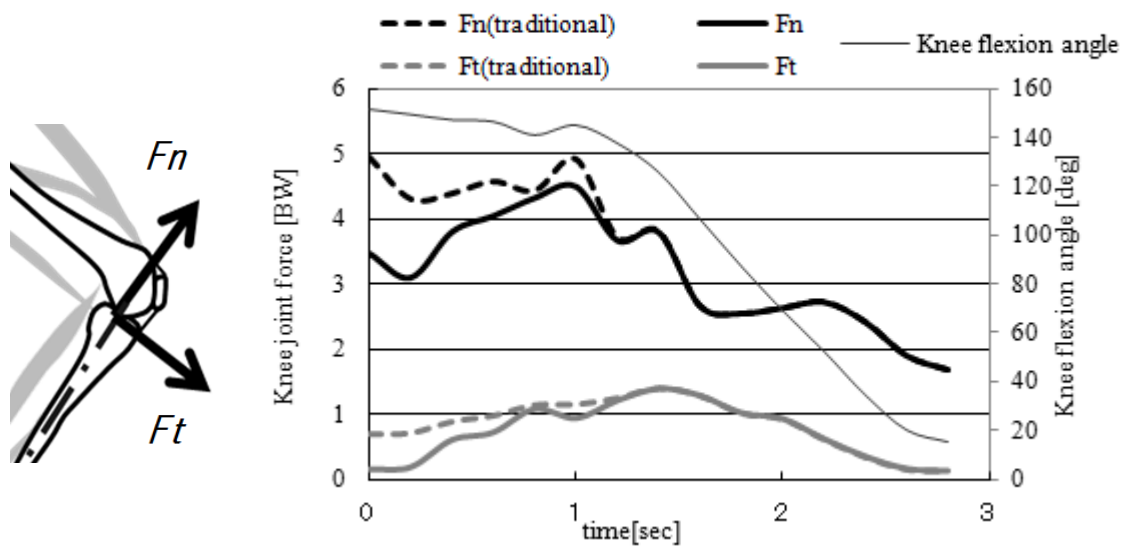


Fig. 5. Knee joint forces.

Thus, knee joint force reduced much during deep knee flexion, considering the thigh-calf contact force. It might be mentioned that a thigh-calf contact might be taken into consideration when discussing the dynamics around a knee or a lower limb.

4 CONCLUSION

In this study, we measured a thigh-calf contact force during rising from squatting position, and calculated a knee joint force using the measured value. As a result, a thigh-calf contact force was about 0.8[BW] at squatting position, and it reduced rapidly as a knee extend. Knee joint force decreased about 20% at a squatting position considering the force.

5 ACKNOWLEDGEMENTS

This work was supported by JSPS KAKENHI Grant Number 24700577.

6 REFERENCES

- [1] M. Fukunaga, S. Hirokawa, The Model Analysis of Lower Limb at Ascending from Deep Knee Flexion, *Memoirs of the Faculty of Engineering, Kyushu University*, 69(4), 139–148, 2009.
- [2] N. J. Dahkvist, P. Mayo, B. B. Seedhom, Forces during Squatting and Rising from a Deep Squat, *Engineering in Medicine*, 11(2), 69–76, 1982.
- [3] M. Fukunaga, S. Hirokawa, Effect of the Tensile Force Ratio of Gluteus Maximus and Hamstrings on the Knee Joint Force, *Transactions of the Japan Society of Mechanical Engineers*, 78(788), 1192–1201, 2012 [in Japanese].
- [4] M. Fukunaga, T. Katsuhara, S. Hirokawa, M. Mawatari, T. Hotokebuchi, A 2D Model Analysis of Artificial Knee Joint during Deep Squatting, *Journal of Biomechanical Science and Engineering*, 4(2), 298–305, 2009.
- [5] J. Zelle, M. Barink, R. Loeffen, M. De Waal Malefijt, N. Verdonschot, Thigh-calf contact force measurements in deep knee flexion, *Clinical Biomechanics*, 22(7), 821–826, 2007.

DEBONDING CRITERION BASED ON THE INTENSITY OF SINGULAR STRESS

Tatsujiro MIYAZAKI¹, Nao-Aki NODA², Long LI³,

Takumi UCHIKOBA³ and Yoshikazu SANNO²

¹ University of the Ryukyus, Okinawa, Japan

² Kyushu Institute of Technology, Fukuoka, Japan

³ Graduate School of Engineering, Kyushu Institute of Technology, Fukuoka, Japan

Abstract: In the previous study, the authors discussed a debonding fracture criterion for single lap joints (SLJs) with varying the adhesive thickness and overlap length in terms of the critical intensity of a singular stress field. Here it is simply assumed that the identical singular stress fields are formed at the edge corner of the SLJ for different geometries. In this paper, by applying the reciprocal work contour integral method (RWCIM) it is shown that the two distinct intensities of the singular stress fields are determined accurately when the orders of stress singularity are two different real numbers. It is found that the ratio of the intensities of two types of the singular stress fields is almost the same for the wide range of the adhesive thickness and the overlap length. Then, it is found that the debonding fracture criterion is represented in terms of the intensity of the singular stress field with the strong stress singularity when aluminum alloy is bonded by epoxy resin.

Keywords: Intensity Of Singular Stress Field, Adhesion, Interface, Single Lap Joint, Reciprocal Work Contour Integral Method, Finite Element Method.

1 INTRODUCTION

The testing method for the tensile lap-shear strength of the single lap joint (SLJ) is standardized by Japanese Industrial Standards (JIS) [1]. In this standard, the fracture tensile load is measured as the tensile lap-shear strength. Therefore, when the overlap length and adhesive thickness are different, the tensile lap-shear strength is also changed even if the same adherend and adhesive are used. The mechanical parameter, which is suitable for the design, should be chosen as the tensile lap-shear strength from the viewpoint of the fracture phenomenon.

Recently, Mintzas – Nowell [2] reported that the debonding fracture criterion for the adhesively bonded joints can be expressed with the critical value of the generalised stress intensity factor, H_{cr} [2-4]. The authors also confirmed that the debonding fracture criterion for the butt joints with the various adhesive thicknesses can be expressed with the critical intensity of the singular stress field at the fracture [5]. The singular stress field of the butt joints is expressed with only one singular stress term with order $\lambda - 1$. However, generally, the singular stress field which is formed near an arbitrary interface corner edge is expressed with several singular stress terms with the orders $\lambda_1 - 1$, $\lambda_2 - 1$, \dots . Because the intensities of the singular stress field the number of which equals that of the orders exit, it is difficult to evaluate the debonding fracture criterion base on the intensity of the singular stress field. The authors clarified that the singular stress fields of the SLJs with various overlap lengths and adhesive thicknesses are almost similar by FEM analyses based on the crack tip stress method [6, 7] when the singular stress field of the SLJ is often expressed with two singular stress terms with the real orders $\lambda_1 - 1$ and $\lambda_2 - 1$ ($\lambda_1 < \lambda_2$). From the analysis results, the debonding fracture criterion of the SLJs can be expressed with the critical intensity of the singular stress field at the fracture. However, the intensities of the singular stress field were not calculated in the earlier study [6, 7]. The similarity of the singular stress field needs to be examined from the intensities of the singular stress field in detail.

In this study, the intensities of the singular stress field of the SLJ with two real orders $\lambda_1 - 1$ and $\lambda_2 - 1$ ($\lambda_1 < \lambda_2$) are calculated by the reciprocal work contour integral method (RWCIM) [8] exactly. The similarity

of the singular stress field is examined from the intensities of the singular stress field. The validity that the debonding fracture criterion of the SLJs can be expressed with $K_{\sigma c} = \text{constant}$ is discussed, where $K_{\sigma c}$ is the critical intensity of the singular stress field at the fracture.

2 EXPERIMENTAL DATA

The tensile shear-lap strength as obtained from experiments performed by Park et al [9] is used. Figure 1 shows the schematic illustration of the specimens. In the experiment, the adherend and adhesive are aluminum alloy 6061-T6 (Young's modulus $E_1 = 68.9$ GPa, Poisson's ratio $\nu_1 = 0.3$) and epoxy resin ($E_2 = 4.2$ GPa, $\nu_2 = 0.45$), respectively. The total length of the specimen is 225 mm; the adhesive thickness is varied from 0.15 mm to 0.9 mm; the overlap length is varied from 15 mm to 50 mm.

Table 1 shows the tensile lap-shear strength P_{af} . In the experiment, the linear relation between the load and displacement was obtained except for the specimen A10. The results suggest that the fracture was caused by the debonding crack which was initiated from the corner edge of the interface between the adhesive and the adherend. Then, the experimental result gives the validity that the critical intensity of the singular stress field at the fracture is used as the debonding fracture criterion.

Figure 2 shows the tensile lap-shear strength P_{af} under t_2 constant condition. The P_{af} tends to increase with increasing the l_2 . Figure 3 shows the average shear stress at the fracture, $\tau_c = P_{af} / (l_2 W)$. When the l_2 is smaller than 15 mm, the τ_c becomes constant at about 28.7 MPa. However, When the l_2 is larger than 15 mm, the τ_c tends to decrease. Nono and Nagahiro [10] reported that the fracture is caused by the general yielding of the adhesive layer and the τ_c becomes constant when the overlap length is short. In this study, it is supposed that debonding fracture occurs when $l_2 > 15$ mm.

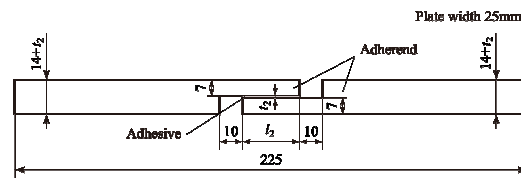


Fig. 1. Specimen configurations [9].

Table 1. Experimental results [9].

(a) t_2 constant condition				(b) l_2 constant condition			
Specimen	l_2 [mm]	t_2 [mm]	P_{af} [kN]	Specimen	l_2 [mm]	t_2 [mm]	P_{af} [kN]
A10	10	0.15	6.87	A25	25	0.15	14.17
A15	15	0.15	10.57	A25-30	25	0.30	14.32
A20	20	0.15	12.41	A25-45	25	0.45	14.26
A25	25	0.15	14.17	A25-90	25	0.90	14.19
A30	30	0.15	14.56	A30	30	0.15	14.56
A35	35	0.15	16.41	A30-30	30	0.30	16.91
A40	40	0.15	18.09	A30-45	30	0.45	16.12
A50	50	0.15	18.22	A30-90	30	0.90	15.37

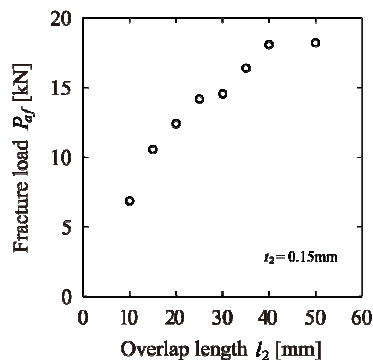


Fig. 2. Adhesive tensile strength of specimens with $t_2 = 0.15$ mm [9].

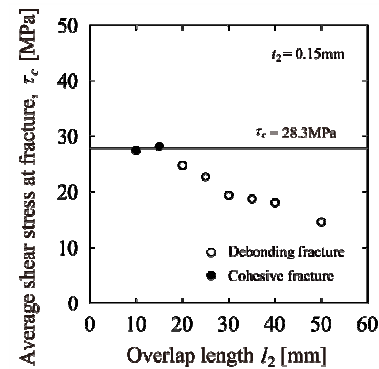


Fig. 3. Average shear stress at fracture of specimens with $t_2 = 0.15$ mm [9].

3.1 Characteristics of the singular stress field

Figure 4 shows the schematic illustration of the analysis model and boundary condition. l_1 and t_1 are adherend length and adherend thickness, respectively; l_2 and t_2 are overlap length and adhesive thickness, respectively; E is Young's modulus, ν is Poisson's ratio, and subscripts 1 and 2 refer to the adherend and the adhesive, respectively.

The singular stress field is formed at the corner edge of the interface between the adherend and the adhesive. The singular stress field is governed by the order of stress singularity, $\lambda - 1$. The eigenvalue λ can be obtained by solving the eigenequation which was derived by Bogy [11]. In the case of the corner edge as shown in Fig. 4, the eigenequation is given by the following equation [6, 7, 11].

$$4\sin^2(\pi\lambda)\left\{\sin^2\left(\frac{\pi\lambda}{2}\right)-\lambda^2\right\}\beta^2+4\lambda^2\sin^2(\pi\lambda)\alpha\beta+\left\{\sin^2\left(\frac{\pi\lambda}{2}\right)-\lambda^2\right\}\alpha^2-4\lambda^2\sin^2(\pi\lambda)\beta-2\left\{\lambda^2\cos(2\pi\lambda)+\sin^2\left(\frac{\pi\lambda}{2}\right)\cos(\pi\lambda)+\frac{1}{2}\sin^2(\pi\lambda)\right\}\alpha+\sin^2\left(\frac{3\pi}{2}\lambda\right)-\lambda^2=0 \quad (1)$$

Here, α and β are Dundurs' parameter [12] and defined as follows

$$\alpha = \frac{G_2(\kappa_1+1)-G_1(\kappa_2+1)}{G_2(\kappa_1+1)+G_1(\kappa_2+1)}, \quad \beta = \frac{G_2(\kappa_1-1)-G_1(\kappa_2-1)}{G_2(\kappa_1+1)+G_1(\kappa_2+1)}, \quad \kappa_m = \frac{3-\nu_m}{1+\nu_m} \text{ (plain stress)}, 3-4\nu_m \text{ (plain strain)} \quad (2)$$

Here, G_m ($m=1, 2$) is the shear modulus of elasticity.

The root of the eigenequation (1), λ , depends on the α and the β . In the case of the material combination in Section 2, $\lambda_1=0.6062$ and $\lambda_2=0.9989$ are obtained from $\alpha=-0.8699$ and $\beta=-0.006642$. The stresses at a radial distance r from the point O on the interface, σ_θ and $\tau_{r\theta}$, are expressed as follows.

$$\sigma_\theta = \frac{K_1}{r^{1-\lambda_1}} f_{\theta\theta}(0, \lambda_1) + \frac{K_2}{r^{1-\lambda_2}} f_{\theta\theta}(0, \lambda_2) = \frac{K_{\sigma, \lambda_1}}{r^{1-\lambda_1}} + \frac{K_{\sigma, \lambda_2}}{r^{1-\lambda_2}}, \quad \tau_{r\theta} = \frac{K_1}{r^{1-\lambda_1}} f_{r\theta}(0, \lambda_1) + \frac{K_2}{r^{1-\lambda_2}} f_{r\theta}(0, \lambda_2) = \frac{K_{\tau, \lambda_1}}{r^{1-\lambda_1}} + \frac{K_{\tau, \lambda_2}}{r^{1-\lambda_2}} \quad (3)$$

Here, K_1 and K_2 are real numbers, $f_{\theta\theta}(\theta, \lambda_k)$ and $f_{r\theta}(\theta, \lambda_k)$ are non-dimensional functions of the angle θ , the λ_k , the α and the β , K_{σ, λ_k} and K_{τ, λ_k} are the intensities of the singular stress field. Because four intensities of the singular stress field, K_{σ, λ_1} , K_{σ, λ_2} , K_{τ, λ_1} and K_{τ, λ_2} are determined by two real numbers K_1 and K_2 , the singular stress field in the vicinity of the corner edge is also determined by them.

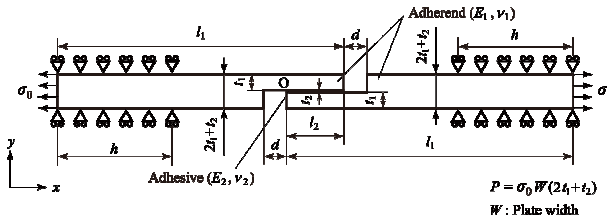


Fig. 4. Analysis model and boundary condition.

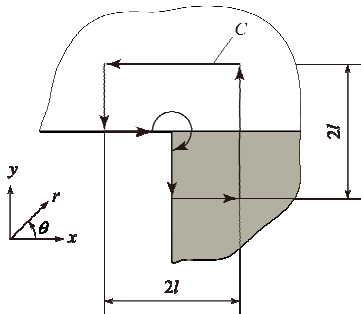


Fig. 5. Contour integral path for RWCIM.

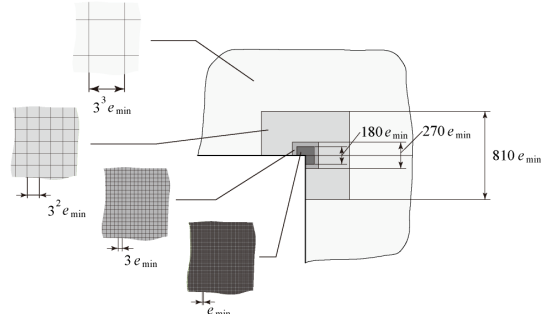


Fig. 6. Mesh pattern near the interface edge corner.

3.2 Analysis method

The intensities of the singular stress field, K_{σ, λ_k} and K_{τ, λ_k} , were calculated by RWCIM. Figure 5 shows the integral path C . The linear elastic analyses were performed under the plane strain condition using the commercial FEM code MSC Marc 2008 R1. Figure 6 shows the schematic illustration of the mesh pattern in the vicinity of the interface corner edge. In the region which contains the corner edge and the integral path, 8-Node quadratic isoparametric element was used; in the other region, 4-Node quadratic isoparametric element was used.

3.3 Analysis results and discussion

The analysis result of the specimen A25 is mentioned. The contour integral path C in Fig. 5 and the mesh pattern in Fig. 6 were used in order to calculate the intensities of the singular stress field. The intensities of the singular stress field under $\sigma_0 = 1$ MPa were calculated changing the e_{\min} and the l/e_{\min} variously. Table 2 shows the intensities of the singular stress field. The K_{σ, λ_1} value converges at 0.1010 when $l/e_{\min} \geq 10$. On the other hand, the K_{σ, λ_2} value tends to converge at -0.5485 with increasing the l/e_{\min} . When $\sigma_0 = 1$ MPa, $K_{\sigma, \lambda_1} = 0.1010$ MPa \cdot m $^{1-\lambda_1}$, $K_{\tau, \lambda_1} = -0.04723$ MPa \cdot m $^{1-\lambda_1}$, $K_{\sigma, \lambda_2} = -0.5485$ MPa \cdot m $^{1-\lambda_2}$ and $K_{\tau, \lambda_2} = -0.01168$ MPa \cdot m $^{1-\lambda_2}$ were obtained in this analysis. Figure 7 shows the stress distributions on the interface. The solid line is the stresses σ_θ and $\tau_{r\theta}$ which are obtained by substituting these intensities of the singular stress field into Eq. 3. Then, the circle and triangle marks are the stresses σ_θ and $\tau_{r\theta}$ by FEM, respectively. When $r \leq 0.01$ mm, the marks are good agreement with the solid curves.

Table 3 shows the intensities of the singular stress field of all specimens. Because the K_{σ, λ_1} and the K_{τ, λ_1} are determined by the K_1 as shown in Eq. 3, the $K_{\tau, \lambda_1}/K_{\sigma, \lambda_1}$ becomes constant independent of the l_2 and the t_2 . In the present SLJ models, $K_{\tau, \lambda_1}/K_{\sigma, \lambda_1} = -0.4678$ and $K_{\tau, \lambda_2}/K_{\sigma, \lambda_2} = 0.02130$ were obtained. Then, the $K_{\sigma, \lambda_2}/K_{\sigma, \lambda_1}$ values and the $K_{\tau, \lambda_2}/K_{\tau, \lambda_1}$ values of all the models except for the models A10 and A15 range from -5.574 to -4.827 and from 0.2198 to 0.2538, respectively. Figure 8 shows the relation between $\sigma_\theta/(K_{\sigma, \lambda_1}/r^{1-\lambda_1})$, $\tau_{r\theta}/(K_{\tau, \lambda_1}/r^{1-\lambda_1})$ and r . The dashed lines are the $\sigma_\theta/(K_{\sigma, \lambda_1}/r^{1-\lambda_1})$ and the $\tau_{r\theta}/(K_{\tau, \lambda_1}/r^{1-\lambda_1})$ of the model A50 the $K_{\sigma, \lambda_2}/K_{\sigma, \lambda_1}$ and the $K_{\tau, \lambda_2}/K_{\tau, \lambda_1}$ of which are minimum; the chain lines are the $\sigma_\theta/(K_{\sigma, \lambda_1}/r^{1-\lambda_1})$ and the $\tau_{r\theta}/(K_{\tau, \lambda_1}/r^{1-\lambda_1})$ of the model A25-90 the $K_{\sigma, \lambda_2}/K_{\sigma, \lambda_1}$ and the $K_{\tau, \lambda_2}/K_{\tau, \lambda_1}$ of which are maximum. There are a few differences between the dashed line and the chain line. From the analysis results, it can be found that the singular stress fields of all the models except for the models A10 and A15 are similar. Then, the σ_θ and the $\tau_{r\theta}$ are approximately expressed with the following equation.

$$\sigma_\theta \cong \frac{K_{\sigma, \lambda_1}}{r^{1-\lambda_1}}(1 + C_\sigma r^{\lambda_2 - \lambda_1}), \quad \tau_{r\theta} \cong \frac{K_{\tau, \lambda_1}}{r^{1-\lambda_1}}(1 + C_\tau r^{\lambda_2 - \lambda_1}) \quad (4)$$

Here, C_σ and C_τ are constant.

Because the K_{σ, λ_1} and the K_{τ, λ_1} are determined by the K_1 as shown in Eq. 3, the intensities of the singular stress field can be represented with the K_{σ, λ_1} . Therefore, the condition that the debonding fracture of the SLJ does not occur can be expressed with the following equation.

$$K_{\sigma, \lambda_1} \leq K_{\sigma c} \quad (5)$$

Here, $K_{\sigma c}$ is the critical intensity of the singular stress field at the fracture.

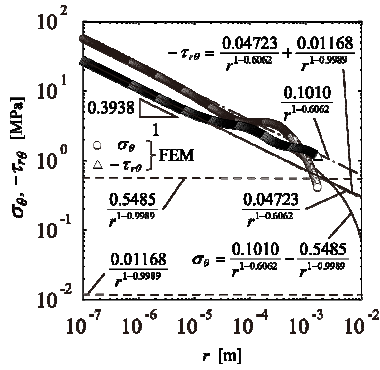
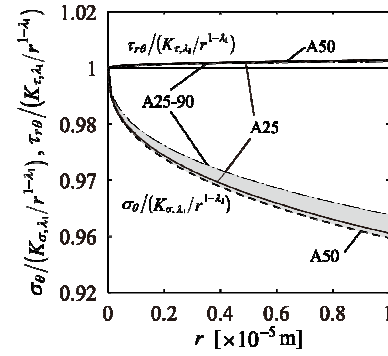
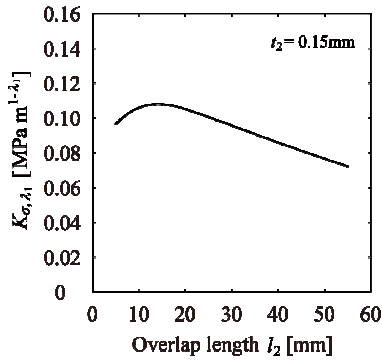
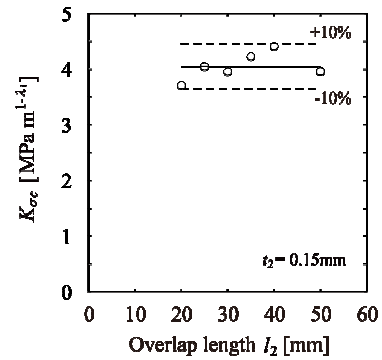
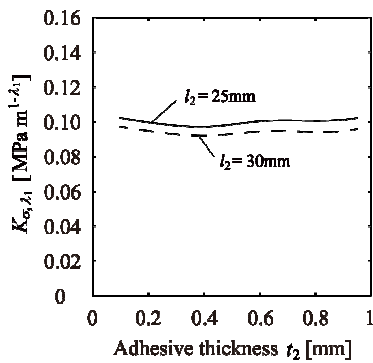
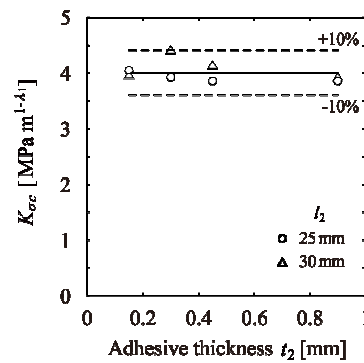
Table 2. K_{σ, λ_1} and K_{σ, λ_2} of specimen A25 under $\sigma_0 = 1$ MPa.

l/e_{\min}	$e_{\min} = 3^{-11}$ mm		$e_{\min} = 3^{-9}$ mm	
	K_{σ, λ_1}	K_{σ, λ_2}	K_{σ, λ_1}	K_{σ, λ_2}
5	0.1011	-0.5553	0.1011	-0.5510
10	0.1010	-0.5500	0.1010	-0.5491
20	0.1010	-0.5492	0.1010	-0.5486
40	0.1010	-0.5484	0.1010	-0.5486
80	0.1010	-0.5485	0.1010	-0.5484

$K_{\sigma, \lambda_1} : \text{MPa} \cdot \text{m}^{1-\lambda_1}, \quad K_{\sigma, \lambda_2} : \text{MPa} \cdot \text{m}^{1-\lambda_2}$

Table 3. Intensities of singular stress field under $\sigma_0 = 1$ MPa.

(a) t_2 constant condition					(b) l_2 constant condition				
Specimen	K_{σ, λ_1}	K_{σ, λ_2}	K_{τ, λ_1}	K_{τ, λ_2}	Specimen	K_{σ, λ_1}	K_{σ, λ_2}	K_{τ, λ_1}	K_{τ, λ_2}
A10	0.1065	-0.6469	-0.04981	-0.01378	A25	0.1010	-0.5485	-0.04723	-0.01168
A15	0.1083	-0.6021	-0.05068	-0.01282	A25-30	0.09796	-0.5022	-0.04583	-0.01070
A20	0.1056	-0.5735	-0.04940	-0.01222	A25-45	0.09777	-0.4884	-0.04574	-0.01040
A25	0.1010	-0.5485	-0.04723	-0.01168	A25-90	0.1013	-0.4888	-0.04738	-0.01041
A30	0.09606	-0.5237	-0.04494	-0.01116	A30	0.09606	-0.5237	-0.04494	-0.01116
A35	0.09107	-0.4985	-0.04261	-0.01062	A30-30	0.09294	-0.4785	-0.04348	-0.01019
A40	0.08618	-0.4741	-0.04032	-0.01010	A30-45	0.09246	-0.4644	-0.04325	-0.009893
A50	0.07680	-0.4280	-0.03593	-0.009118	A30-90	0.09482	-0.4631	-0.04436	-0.009865

 $K_{\sigma, \lambda_1}, K_{\tau, \lambda_1} : \text{MPa} \cdot \text{m}^{1-\lambda_1}, K_{\sigma, \lambda_2}, K_{\tau, \lambda_2} : \text{MPa} \cdot \text{m}^{1-\lambda_2}$

Fig. 7. Comparison between stress distribution of Specimen A 25 by Eq. 3 and FEM.

Fig. 8. Relationship between $\sigma_\theta / (K_{\sigma, \lambda_1} / r^{1-\lambda_1})$, $\tau_{r\theta} / (K_{\tau, \lambda_1} / r^{1-\lambda_1})$ and r .

Fig. 9. Relationship between K_{σ, λ_1} and l_2 .

Fig. 10. Relationship between K_{σ, λ_1} and l_2 .

Fig. 11. Relationship between K_{σ, λ_1} and t_2 .

Fig. 12. Relationship between K_{σ, λ_1} and t_2 .

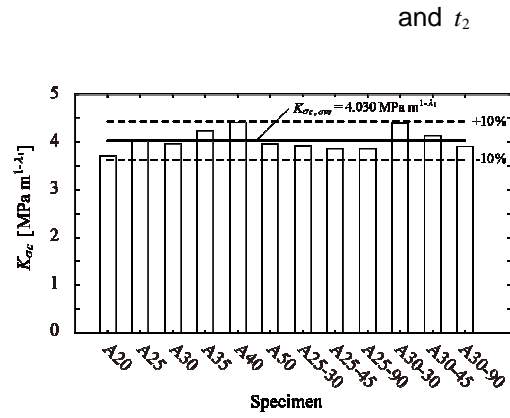


Fig. 13. Debonding fracture criterion $K_{\sigma c}$.

4 DEBONDING FRACTURE CRITERION

As mentioned in Section 3, the intensities of the singular stress field can be represented with the K_{σ, λ_1} from the similarity of the singular stress field. Figure 9 shows the K_{σ, λ_1} values of the specimens with $t_2 = 0.15$ mm under $\sigma_0 = 1$ MPa. When $l_2 \geq 15$ mm, the K_{σ, λ_1} tends to decrease with increasing the l_2 . Figure 10 shows the critical intensities of the singular stress field of specimen with $t_2 = 0.15$ mm, where $K_{\sigma, \lambda_1} |_{P=P_{af}}$ is the intensity of the singular stress field under $P = P_{af}$, $K_{\sigma c} = K_{\sigma, \lambda_1} |_{P=P_{af}}$. The $K_{\sigma c}$ values become constant independent of the l_2 .

Figure 11 shows the K_{σ, λ_1} values of the specimens with $l_2 = 25, 30$ mm under $\sigma_0 = 1$ MPa. Figure 12 shows the critical intensities of the singular stress field of the specimen with $l_2 = 25, 30$ mm. The $K_{\sigma c}$ values become constant independent of the t_2 .

Figure 13 shows the $K_{\sigma c}$ values of all specimens in Figs. 10 and 12. The solid line is the average of the $K_{\sigma c}$ values, $K_{\sigma c, ave}$. In this study, the $K_{\sigma c, ave}$ was $4.030 \text{ MPa} \cdot \text{m}^{1/2}$. The $K_{\sigma c}$ values were within the range of 10 % difference. From the result, it can be confirmed that the $K_{\sigma c}$ becomes constant independent of the l_2 and the t_2 .

5 CONCLUSION

In this study, four intensities of the singular stress field of the SLJ with the different real orders $\lambda_1 - 1$ and $\lambda_2 - 1$, K_{σ, λ_1} , K_{σ, λ_2} , K_{τ, λ_1} and K_{τ, λ_2} , were calculated by RWCIM exactly. Then, the similarity of the singular stress field and the debonding fracture criterion based on the intensity of the singular stress field were examined.

- (1) The debonding fracture criterion was expressed with the critical intensity of the singular stress field at the fracture except that the overlap length is short significantly.
- (2) The $K_{\sigma, \lambda_2} / K_{\sigma, \lambda_1}$ and $K_{\tau, \lambda_2} / K_{\tau, \lambda_1}$ are nearly equal independent of the overlap length l_2 and the adhesive thickness t_2 . From the analysis results, it was found that the similar singular stress fields are formed even if the l_2 and the t_2 are different.
- (3) Four intensities of the singular stress field can be represented with the K_{σ, λ_1} based on the similarity of the singular stress field. Therefore, the debonding fracture criterion $K_{\sigma c}$ was expressed with the critical intensity of the singular stress field at the fracture, $K_{\sigma, \lambda_1} |_{P=P_{af}}$, within the range of 10% error.

REFERENCES

- [1] JIS K6850, Adhesives-Determination of tensile lap-shear strength or rigid-to-rigid bonding assemblies.
- [2] A. Mintzas & D. Nowell, Engineering Fracture Mechanics, 80 (2012), 13 - 27.
- [3] Z. Qian & A. R. Akisanya, Acta Materialia, 46 - 14(1998), 4895 - 4904.
- [4] A. R. Akisanya & C. S. Meng, Journal of the Mechanics and Physics of Solids, 51 (2003), 27 - 46.

- [5] N. -A. Noda et al., Proc. 3rd ACMFMS, (2012), 813-816.
- [6] N. -A. Noda et al., Trans. JSME, A78 – 789 (2012), 651 – 655.
- [7] T. Miyazaki et al., Trans. JIEP, 16 – 2 (2012), 813 – 316.
- [8] W. C. Carpenter & C. Byers : International Journal of Fracture, **35**, (1987), pp. 245-268.
- [9] J. -H. Park, J. -H. Choi, J. -H. Kweon : Composite Structures, **92** (2010), 2226-2235.
- [10] K. Nono & T. Nagahiro, Trans. JSME, A52 – 479 (1986), 1698 – 1707.
- [11] D. B. Bogy : Transaction of the ASME, Journal of Applied Mechanics, **35**, (1968), 460-466.
- [12] J. Dundurs : Journal of Applied Mechanics, **36**, (1969), 650-652.

STABILITY OF FLEXURAL MEMBERS ON BI-MODULI ELASTIC FOUNDATION

L. Wang¹ and Z.H. Lui¹

¹ Shandong University, Jinan, China

Abstract: Typical flexural members are beams and plates. This paper focuses on beams as the representative of flexural members to analyze their stability on bi-moduli elastic foundation, and adopts the newly structured δ function and displacement function, and uses two adjacent transition points as two interval terminals while beams buckle makes the interval $[x_{i-1}, x_i]$. According to the buckling theory of flexural members on the Winkler's elastic foundation, we present the energy solutions of beams and the exact solutions of buckling load of simple supported beams on bi-moduli elastic foundation. Finally, the authors show the part of the research results on the stability of simple supported rectangular plates on bi-moduli elastic foundation.

Keywords: Stability; Flexural Members; Bi-Moduli; Elastic Foundation

1 INTRODUCTION

The bi-moduli elastic foundation model assumes that when the foundation is compressed or tensioned, the reaction that the foundation gives its above construction is expressed by:

$$P(x, y) = \begin{cases} K_1 W(x, y), & W \geq 0 \\ K_2 W(x, y), & W < 0 \end{cases}$$

Where k_1 and k_2 are the non-negative reaction coefficients. When k_1 equals to k_2 , the bi-moduli elastic foundation model becomes the Winkler elastic foundation model. Because the variation of the tension and pressure reaction of the foundation leads to the non-linear of governing equation, the mechanical problems of structures on bi-moduli elastic foundation becomes more complicated. Even if relatively simple conditions, it is very difficult to get the solutions of the non-linear differential equations. In 1967, Tsai and Westmann first made the analysis of bending of beams on tensionless foundation (k_1 or k_2 is zero) [1]. Since that, many scholars have always studied the bending of beams on tensionless foundation [2-6]. In 1985, Adin first made the analysis of bending of beams on relatively common bi-moduli elastic foundation [7]. At present, the stability analysis of the flexural members on bi-moduli elastic foundation is also rarely presented. In this paper, authors present the exact solutions of buckling load of simple supported beams on bi-moduli elastic foundation and the part of the research results on the stability of simple supported rectangular plates on bi-moduli elastic foundation.

2 THE SOLUTION OF THE STABILITY OF FLEXURAL MEMBERS ON BI-MODULI ELASTIC FOUNDATION

Typical flexural members are beams and plates. This paper focuses on beams as the representative of flexural members to analyze their stability on bi-moduli elastic foundation. Finally the part of the research results on the stability of simple supported rectangular plates on bi-moduli elastic foundation is showed.

2.1 The solution of the stability of beams on bi-moduli elastic foundation

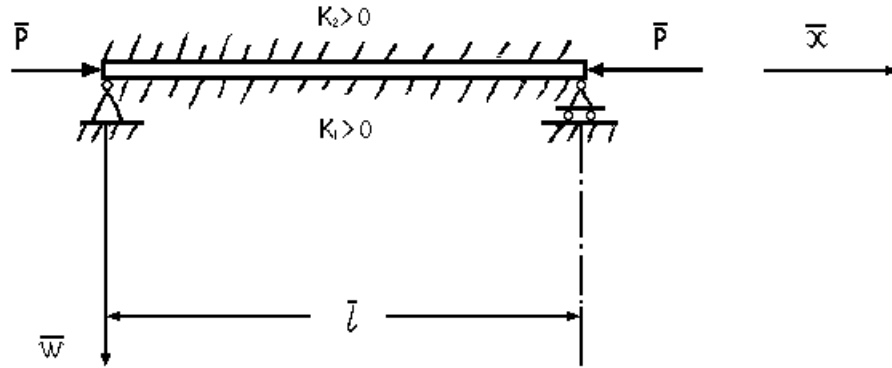


Fig. 1. A simply supported beam.

For the simply supported beam shown in Figure 1, if $k_1=k$ and $\alpha=k_2/k$, then the potential energy of beams is:

$$\bar{\Pi} = \frac{1}{2} \int_0^l [EI(\bar{W}'')^2 - \bar{P}(\bar{W}')^2 + \frac{1+\alpha}{2} K\bar{W}^2 + \frac{1-\alpha}{2} K\bar{W}|\bar{W}|] d\bar{x} \quad (1)$$

Induct the following changes into Eq.1:

$$\begin{aligned} x &= \bar{x}/\bar{l}, W = \bar{W}/\bar{l}, \lambda = \bar{l}^4 \sqrt{K/EI}, \\ P &= \bar{P}/\sqrt{EIK}, \Pi = \bar{\Pi} \bar{l} / \sqrt{EIK} \end{aligned} \quad (2)$$

Then

$$\Pi = \frac{1}{2} \int_0^1 \left[\frac{1}{\lambda^2} (W'')^2 - P(W')^2 + \frac{1+\alpha}{2} \lambda^2 W^2 + \frac{1-\alpha}{2} \lambda^2 W|W| \right] dx \quad (3)$$

The interval $[0,1]$ is divided into n small intervals: $[x_0, x_1], [x_1, x_2], \dots, [x_{n-1}, x_n]$. The displacement function made in the interval $[x_{i-1}, x_i]$ is:

$$W_i(x) = A_i \sin \frac{x - x_{i-1}}{x_i - x_{i-1}} \pi \quad i = 1, 2, \dots, n \quad (4)$$

$$W'_i(x) = \frac{\pi}{\Delta x_i} A_i \cos \frac{x - x_{i-1}}{\Delta x_i} \quad i = 1, 2, \dots, n \quad (5)$$

Eq.4 should be subjected to the following conditions:

$$W'_{i+1}(x_i) = W'_i(x_i) \quad i = 1, 2, \dots, n-1 \quad (6)$$

From Eq.5 and Eq.6, the following expression is obtained:

$$-\frac{A_i}{\Delta x_i} = \frac{A_{i+1}}{\Delta x_{i+1}} \quad i = 1, 2, \dots, n \quad (7)$$

Then

$$\frac{A_1}{\Delta x_1} = \frac{(-1)^{2-1} A_2}{\Delta x_2} = \frac{(-1)^{3-1} A_3}{\Delta x_3} = \dots = \frac{(-1)^{n-1} A_n}{\Delta x_n} \quad (8)$$

$$\frac{A_1 + (-1)^{2-1} A_2 + \dots + (-1)^{n-1} A_n}{\Delta x_1 + \Delta x_2 + \dots + \Delta x_n} = \frac{(-1)^{i-1} A_i}{\Delta x_i} \quad (9)$$

Thus

$$\Delta x_i = \frac{(-1)^{i-1} A_i}{\sum_{j=1}^n (-1)^{j-1} A_j} \quad i = 1, 2, \dots, n \quad (10)$$

Eq.10 yields:

$$(-1)^{i-1} A_i = A \Delta x_i \quad i = 1, 2, \dots, n \quad (11)$$

Then

$$A_i^2 = A^2 (\Delta x_i)^2 \quad i = 1, 2, \dots, n \quad (12)$$

in which

$$\Delta x_i = x_i - x_{i-1} \quad i = 1, 2, \dots, n$$

$$A = A_1 - A_2 + A_3 - A_4 + \dots + (-1)^{n-1} A_n$$

From Eq.12, the following three integral solutions are obtained:

$$\begin{cases} \int_{x_{i-1}}^{x_i} (W_i'')^2 dx = \frac{1}{2} \pi^4 A^2 (\Delta x_i)^{-1} \\ \int_{x_{i-1}}^{x_i} (W_i')^2 dx = \frac{1}{2} \pi^2 A^2 \Delta x_i \\ \int_{x_{i-1}}^{x_i} W_i^2 dx = \frac{1}{2} A^2 (\Delta x_i)^3 \end{cases} \quad i = 1, 2, \dots, n \quad (13)$$

In the interval $[x_{i-1}, x_i]$, Π is signed as Π_i ,

$$\Pi_i = \frac{1}{2} \int_{x_{i-1}}^{x_i} \left[\frac{1}{\lambda^2} (W_i'')^2 - P (W_i')^2 + \lambda^2 \delta_i^4 W_i^2 \right] dx \quad i = 1, 2, \dots, n \quad (14)$$

Using Eq.13, Eq.14 and Eq.16, yields:

$$\text{where } \delta_i = \frac{1+(-1)^i}{2} \quad i = 1, 2, \dots, n \quad (15)$$

$$4\Pi = A^2 \left[\frac{\pi^2}{2} \sum_{i=1}^n (\Delta x_i)^{-1} - \pi^2 P \sum_{i=1}^n \Delta x_i + \lambda^2 \sum_{i=1}^n \delta_i^4 (\Delta x_i)^3 \right] \quad (17)$$

$$\Pi = \sum_{i=1}^n \Pi_i \quad i = 1, 2, \dots, n \quad (16)$$

For $\frac{\partial \Pi}{\partial A_j} = 0$ $j = 1, 2, \dots, n$, and $\sum_{i=1}^n \Delta x_i = 1$, thus

$$P = \frac{\pi^2}{\lambda^2} \sum_{i=1}^n (\Delta x_i)^{-1} + \frac{\lambda^2}{\pi^2} \sum_{i=1}^n [\delta_i^4 (\Delta x_i)^3] \quad (18)$$

$$\frac{\partial P}{\partial \Delta x_i} = -\frac{\pi^2}{\lambda^2} (\Delta x_i)^{-2} + 3 \frac{\lambda^2}{\pi^2} \delta_i^4 (\Delta x_i)^2 \quad i = 1, 2, \dots, n \quad (19)$$

To find the minimum of P , solve the equation $\frac{\partial P}{\partial \Delta x_i} = 0$, thus

$$\Delta x_i = \frac{\pi}{\sqrt[4]{3\lambda}\delta_i} \quad i = 1, 2, \dots, n \quad (20)$$

$$\Delta x_i / \Delta x_1 = \delta_i^{-1} \quad i = 1, 2, \dots, n \quad (21)$$

$$\text{For } \sum_{i=1}^n \Delta x_i = \sum_{i=1}^n [\Delta x_1 \delta_i^{-1}] = \Delta x_1 \sum_{i=1}^n \delta_i^{-1} = 1, \text{ thus}$$

$$\Delta x_1 = \frac{1}{\sum_{i=1}^n \delta_i^{-1}} \quad (22)$$

$$\Delta x_i = [\delta_i \sum_{j=1}^n \delta_j^{-1}]^{-1} \quad (23)$$

Substituting Eq.23 into Eq.18, gives:

$$P = \frac{\pi^2}{\lambda^2} \left(\sum_{i=1}^n \delta_i \right) \left(\sum_{j=1}^n \delta_j^{-1} \right) + \frac{\lambda^2}{\pi^2} \left(\sum_{i=1}^n \delta_i \right) \left(\sum_{j=1}^n \delta_j^{-1} \right)^{-3} \quad (24)$$

If n is an even number, then

$$P = \frac{n^2 \pi^2}{\lambda^2} \frac{(1 + \alpha^{\frac{1}{4}})(1 + \alpha^{-\frac{1}{4}})}{4} + \frac{\lambda^2}{n^2 \pi^2} \frac{4(1 + \alpha^{\frac{1}{4}})}{(1 + \alpha^{-\frac{1}{4}})^3} \quad (25)$$

$$\text{for } \frac{\partial P}{\partial \lambda} = 0, \text{ thus}$$

$$\lambda = \frac{1}{2} (1 + \alpha^{-\frac{1}{4}}) n \pi \quad (26)$$

$$P_{\min} = 2\alpha^{\frac{1}{4}} \quad (27)$$

If n is an odd number, then

$$P = \frac{n^2 \pi^2}{4\lambda^2} \left[(1 + \alpha^{\frac{1}{4}}) + \frac{1}{n} (1 - \alpha^{\frac{1}{4}}) \right] \cdot \left[(1 + \alpha^{-\frac{1}{4}}) + \frac{1}{n} (1 - \alpha^{-\frac{1}{4}}) \right] + \frac{\lambda^2}{n^2 \pi^2} \left[(1 + \alpha^{\frac{1}{4}}) + \frac{1}{n} (1 - \alpha^{\frac{1}{4}}) \right] \cdot \left[(1 + \alpha^{-\frac{1}{4}}) + \frac{1}{n} (1 - \alpha^{-\frac{1}{4}}) \right]^{-3} \quad (28)$$

$$\text{for } \frac{\partial P}{\partial \lambda} = 0, \text{ thus}$$

$$\lambda = \frac{1}{2} \left[(1 + \alpha^{-\frac{1}{4}}) + \frac{1}{n} (1 - \alpha^{-\frac{1}{4}}) \right] n \pi \quad (29)$$

$$P_{\min} = 2 \left[(1 + \alpha^{\frac{1}{4}}) + \frac{1}{n} (1 - \alpha^{\frac{1}{4}}) \right] \left[(1 + \alpha^{-\frac{1}{4}}) + \frac{1}{n} (1 - \alpha^{-\frac{1}{4}}) \right]^{-1} \quad (30)$$

According to Eqs. (25) (26) (27) or (28) (29) (30), the following curves are plotted. In Fig. 2 and Fig. 3, the curves p-λ are shown for α=1 and 5, when the half-wave number n is 4. The solid line represents the real curves p-λ. When λ exceeds the critical λ corresponding to the point of intersection of two adjacent curves, the half-wave number will be increased.

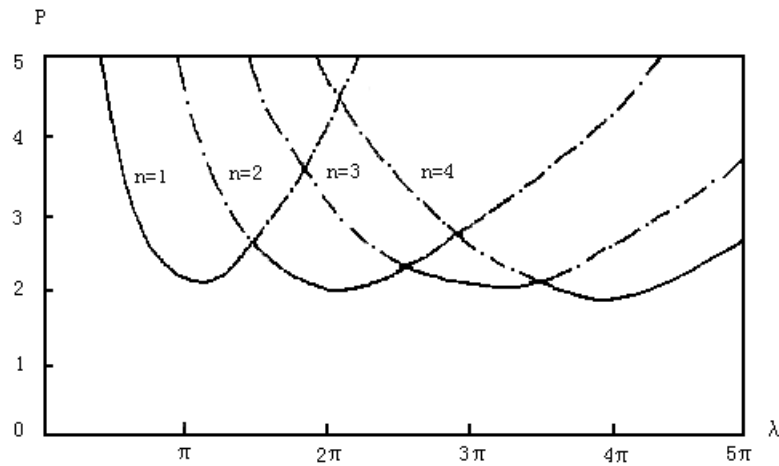


Fig. 2. curves p - λ for $\alpha=1$ and $n=4$.

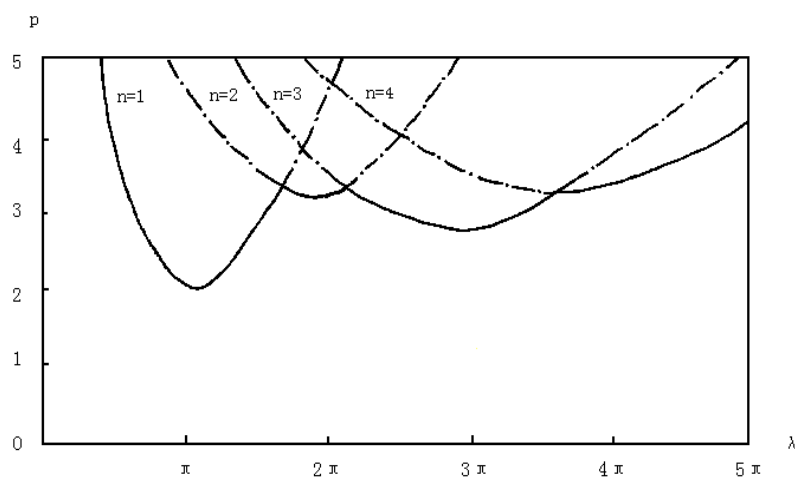


Fig. 3. curves p - λ for $\alpha=5$ and $n=4$.

2.2 The solution of the stability of simple supported rectangular plates on bi-moduli elastic foundation

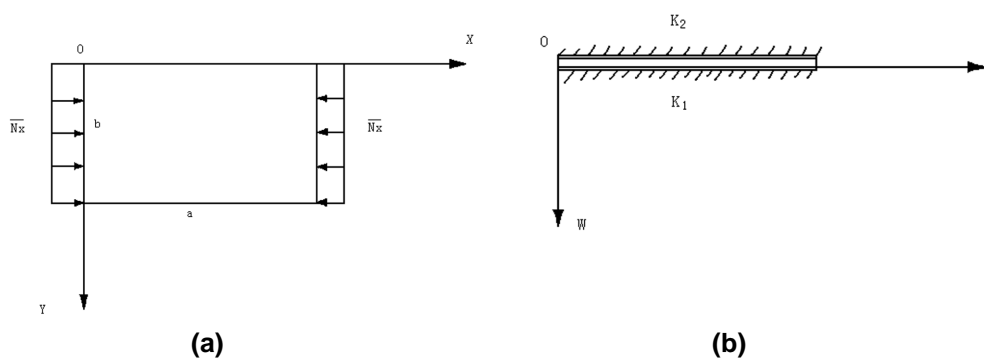


Fig. 4. A simply supported plate.

A simply supported plate is shown in Fig. 4, where k_1 and k_2 are the tension and compress reaction coefficients, respectively.

The authors adopt the newly structured δ_{ij} function, $\delta_i(\lambda)$ function and displacement function, and continues to use the buckling theory of rectangular plates on the Winkler's elastic foundation, then obtains the exact solution of buckling load of simple supported rectangular plates on bi-moduli elastic foundation by using the

energy method. The following figure presents the curves p - a/b of simple supported rectangular plates on bi-moduli elastic foundation when there are one half-wave along the direction y and $m=4$ half-waves along x . The curves p - a/b are shown in Fig. 5 when $\lambda=0.8$.

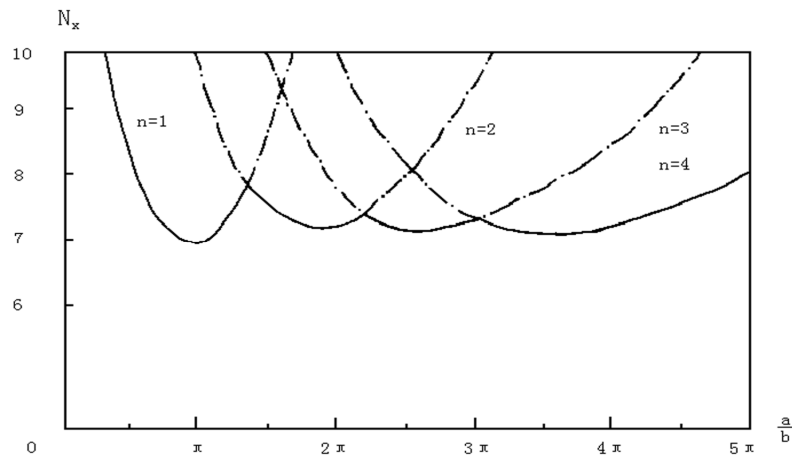


Fig. 5. Curves p - a/b of simple supported rectangular plates.

3 CONCLUSIONS

The stability analysis of the flexural members on bi-moduli elastic foundation is also rarely presented. In this paper, authors present the exact solutions of buckling load of simple supported beams on bi-moduli elastic foundation and the part of the research results on the stability of simple supported rectangular plates on bi-moduli elastic foundation. As for under the other boundary conditions, the stability of beams and rectangular plates on bi-moduli elastic foundation needs to make further researches.

4 ACKNOWLEDGEMENTS

The authors would like to acknowledge the support of the Department of Civil Engineering, Shandong University.

5 REFERENCES

- [1] Tsai, N. C. and Westmann, R. A., 1967, Beams on tensionless foundation, J. Engineering Mech., ASCE Vol.93, EM5, 1-12.
- [2] Selvadurai, A.P.S., 1979, Elastic analysis of soil-foundation interaction, Elsevier Scientific Publishing Company, Amsterdam.
- [3] Hu, H. C., 1981, The variational principle and application of elasticity, Science press, Beijing.
- [4] Zekai. Celep, and Dogan Turhan, 1990, Axisymmetric Vibrations of Circular Plates on Tensionless Elastic Foundations, ASME J. Appl. Mech., 57, 667-681.
- [5] Zhou, C. C., 1981, The theory of the elastic stabilization, Sichuan People Press, Chongqing.
- [6] Liu Z. H., Wang L. and Pan L. Z., 2001, Stability of beams on bi-moduli elastic foundation, ASME J. Appl. Mech., 68, pp. 668-670.
- [7] Adin, M. A., Yankelevsky, D. Z., and Eisenberger, M., 1985, Analysis of beams on bi-moduli elastic foundation, Comput. Methods in Appl. Mech. and Eng., Vol. 49, 319-330.

EFFECT OF HYDROGEN ON TENSILE PROPERTIES OF CARBON STEELS

N. Tsutsumi¹ and K. Oda¹

¹ Department of Mechanical and Energy Systems Engineering, Oita University, Oita, Japan

Abstract: Tensile tests were conducted on hydrogen charged and uncharged specimens of carbon steels (0.09 mass%C, 0.27 mass%C and 0.46 mass%C). In order to investigate the influences of hydrogen content on tensile properties, pre-strained specimens (0%, 5% and 10%) were used. Tensile strength and yield stress of hydrogen charged specimens was almost the same as those of uncharged. However, the reduction of area decreased with increasing hydrogen content. Fracture surface and longitudinal section through specimen was observed to reveal fracture mechanism. It was observed that voids of uncharged specimens were nucleated at pearlite or inclusions, and grew in axial direction. On the other hand, voids of hydrogen charged specimens grew in a direction perpendicular to axis.

Keywords: Hydrogen; Tensile Property; Carbon Steel

1 INTRODUCTION

Hydrogen energy recently attracts attention as one of the clean and renewable energy source for the next generation. Fuel cell vehicles (FCVs) and stationary fuel cell systems have been developed. However, hydrogen penetrates into materials and it leads to a reduction of ductility. The phenomenon is known as hydrogen embrittlement (HE). For the mechanism of HE, some researchers suggested some theories. For example, Troiano suggested the lattice decohesion model [1, 2], Beachem suggested the hydrogen enhanced localized plasticity model [3].

In this study, the effects of hydrogen on the tensile strength properties of carbon steels with different carbon content were investigated. And the effects of hydrogen on fracture surface were observed.

2 MATERIALS AND EXPERIMENTAL PROCEDURE

Low carbon steels (JIS SS400 (0.09 %C), JIS S25C (0.27 %C), JIS S45C (0.46 %C)) were used for tensile tests. Table 1 shows chemical compositions of low carbon steels. Figure 1 shows the shape and dimensions of tensile specimens. Specimen surface was polished by emery paper # 800.

W. Y. CHOO et al. [4] reported that hydrogen content in pure iron increased in increasing pre-strain. In this study, pre-strain specimens (pre-strain: 0, 5, 10 %) were used in order to investigate the relationship between hydrogen content and tensile properties. Pre-strain was introduced by tensile tests under crosshead speed 1 mm/min. Then, the specimens were charged hydrogen by immersing in 20 mass% NH₄SCN solution at 313 K for 48 hours. Tensile tests were carried out at room temperature in air under crosshead speed 1 mm/min.

Table 1. Chemical compositions of JIS SS400, S25C and S45C.

	C	Si	Mn	P	S	Cu	Ni	Cr	NC
SS400	0.09	0.14	0.5	0.03	0.043	–	–	–	–
S25C	0.27	0.2	0.4	0.024	0.017	0.01	0.03	0.05	0.08
S45C	0.46	0.27	0.73	0.012	0.024	0.01	0.03	0.1	0.13

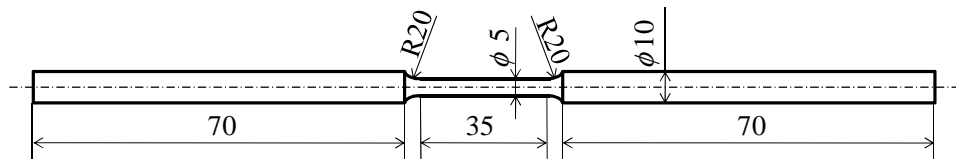


Fig. 1. Shape and dimensions of tensile specimens (mm).

3 RESULTS AND DISCUSSIONS

3.1 Hydrogen content

Figure 2 shows the relationship between pre-strain and hydrogen content for hydrogen charged specimens. Hydrogen content in specimens was measured by Thermal Desorption Analysis (TDA) with heating rate 0.028 K/s. Hydrogen content of all uncharged specimens was 0.0 wppm. From Fig. 2, it is found that hydrogen content of hydrogen charged specimens increase in increasing pre-strain. The hydrogen content of JIS SS400 specimens was the highest and that of JIS S25C was the lowest in the three kinds of carbon steels.

3.2 Tensile properties

Figure 3 and 4 shows the tensile strength σ_B and the reduction of area ϕ . The tensile strength σ_B of hydrogen charged specimens was almost the same as uncharged. However, the reduction of area ϕ of hydrogen charged specimens was obviously smaller than uncharged. The reduction of area ϕ of JIS S25C and JIS S45C hydrogen charged specimens decrease in increasing pre-strain. Thus, the reduction of area ϕ tends to decrease in increasing hydrogen content of specimens.

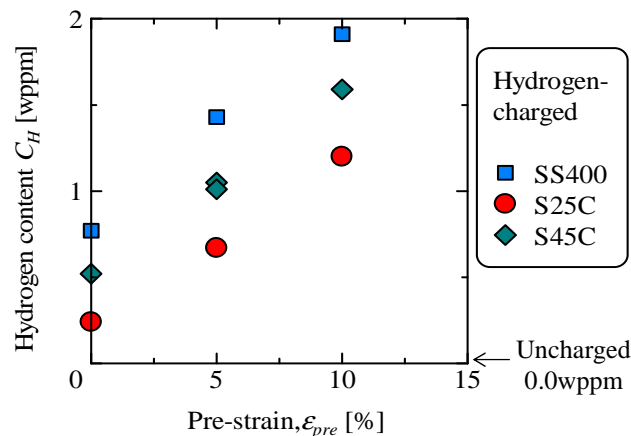


Fig. 2. Relationship between pre-strain and hydrogen content.

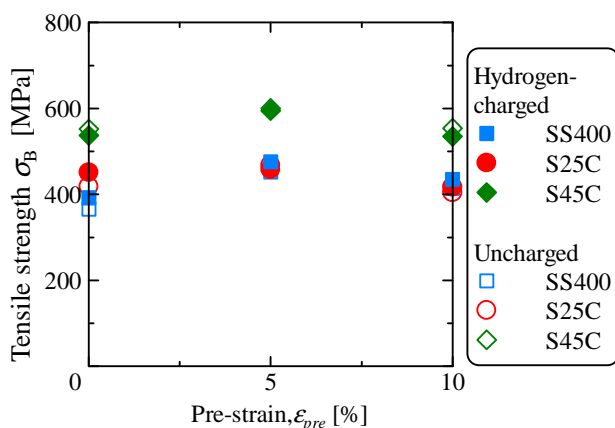


Fig. 3. Tensile strength σ_B .

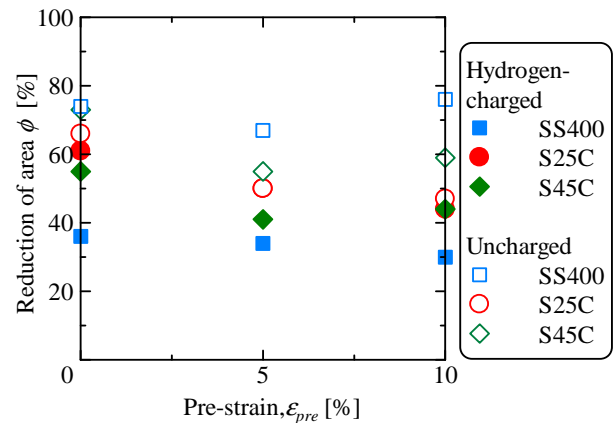


Fig. 4. Reduction of area ϕ .

3.3 Fracture surface

Figure 5 (a)-(c) shows the fracture surface of JIS SS400. Typical dimples were observed on fracture surface of a 0% pre-strained uncharged specimen (Fig. 5 (a)). Similar dimples were also observed in 5% and 10% pre-strained uncharged specimens. On the other hand, it was observed that dimples of a 0% pre-strained hydrogen charged specimen were slightly larger than uncharged (Fig. 5 (b)). Flat fracture surface was often observed in 5% and 10% pre-strained hydrogen charged specimens (Fig. 5 (c)).

Figure 5 (d)-(f) shows the fracture surface of JIS S25C. Typical dimples were observed on fracture surface of 0%, 5% and 10% pre-strained uncharged specimens (Fig. 5 (d)). On the other hand, in hydrogen charged specimens, dimples (Fig. 5 (e)), flat fracture and pearlite cracking (Fig. 5 (f)) were observed.

Figure 5 (g)-(i) shows the fracture surface of JIS S45C. Compared with fracture surface of JIS SS400 and JIS S25C, smaller dimples were observed in a 0% pre-strained uncharged specimen of JIS S45C (Fig. 5 (g)). On the fracture of 5% and 10% pre-strained uncharged specimens, lots of pearlite cracking was observed. On the other hand, the dimples of 0% pre-strained hydrogen charged specimen were slightly larger than uncharged and pearlite cracking was observed (Fig. 5 (h)). The number of pearlite cracking (Fig. 5 (i)) increased in increasing pre-strain.

3.4 Longitudinal section near fracture surface

In order to reveal the mechanism of fracture surface formation, the longitudinal section near fracture surface was observed. The longitudinal section was polished by buffing and etched with nital solution.

Figure 6 shows the longitudinal section near fracture surface of JIS SS400, JIS S25C and JIS S45C. Almost all voids of hydrogen charged and uncharged specimens were initiated from pearlite structure. In uncharged specimens of JIS SS400, it was observed that the voids were formed along axial direction (Fig. 6 (a)). On the other hand, it was observed that the voids of JIS SS400 hydrogen charged specimens were formed perpendicular to axial direction (Fig. 6 (b)). The voids of hydrogen charged specimen was initiated from pearlite structure and grew through ferrite structure. Considering the fracture surface of uncharged specimen (Fig. 5 (a)) and hydrogen charged (Fig. 5 (b)), the voids of hydrogen charged was larger than uncharged, therefore the shape of voids of longitudinal section correspond to that on fracture surface. The voids formed along axial direction were observed in JIS S25C uncharged specimens (Fig. 6 (c)) and those perpendicular to axial direction were observed in the hydrogen charged specimens (Fig. 6 (d)). However, the voids formed along axial direction and perpendicular to axial direction were observed in JIS S45C uncharged (Fig. 6 (e)) and hydrogen charged specimens (Fig. 6 (f)). This is because that JIS S45C steel has more pearlite structure from which voids might be initiated and voids can not be grow perpendicular to axial direction substantially.

4 CONCLUSIONS

The effects of hydrogen on tensile properties of carbon steels were investigated with observation of fracture surface and longitudinal section. The conclusions can be summarized as follows.

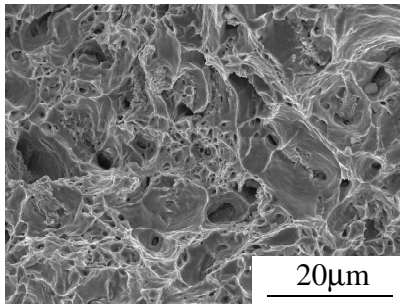
- (1) The tensile strength of hydrogen charged specimens was almost the same as that of uncharged. However, the reduction of area of hydrogen charged specimens was obviously smaller than uncharged. The reduction of area tends to decrease in increasing hydrogen content.
- (2) Flat fracture surface was often observed in JIS SS400 hydrogen charged specimens. On the other hand, in JIS S45C hydrogen charged specimens pearlite cracking was often observed. This is because that JIS S45C steel has more pearlite structure from which voids might be initiated.
- (3) All most voids of hydrogen charged and uncharged specimens were initiated from pearlite structure. In uncharged specimens of JIS SS400 and JIS S25C, it was observed that the voids were formed along axial direction. On the other hand, it was observed that the voids were formed perpendicular to axial direction. This observation might be corresponding to that fracture surface of hydrogen charged specimens has more larger dimples than uncharged.

5 ACKNOWLEDGEMENTS

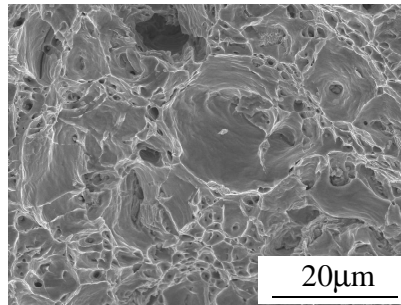
This research has been supported by the NEDO Fundamental Research Project on Advanced Hydrogen Science (2006 to 2012).

6 REFERENCES

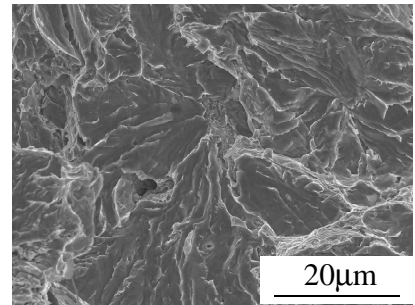
- [1] A.R. Troiano, Trans. of the ASM, 52 ,54-81, 1960.
- [2] H.H. Johnson, et al., Trans. of the Metallurgical Society of AIME, 212, 528-536, 1958.
- [3] C. D. Beachem, Metallur. Trans., 3, 1065-1074, 1972.
- [4] W. Y. Choo, et al., Metallur. Trans., A13, pp. 135-140, 1982.



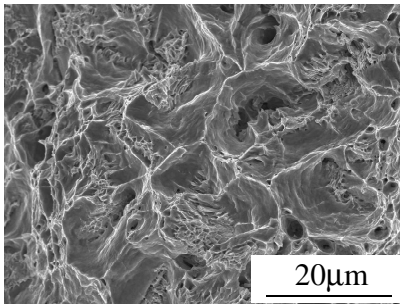
(a) SS400, $\epsilon_{pre}=0\%$, uncharged



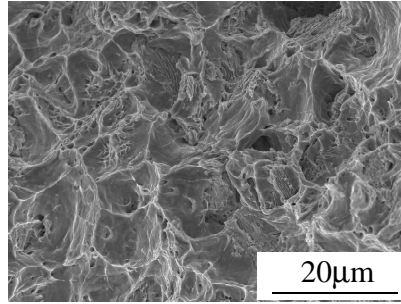
(b) SS400, $\epsilon_{pre}=0\%$, H-charged



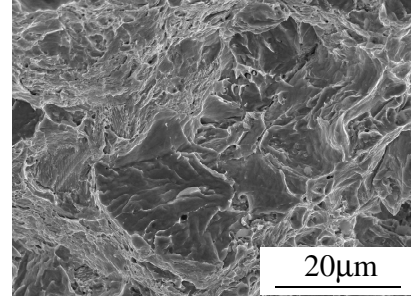
(c) SS400, $\epsilon_{pre}=10\%$, H-charged



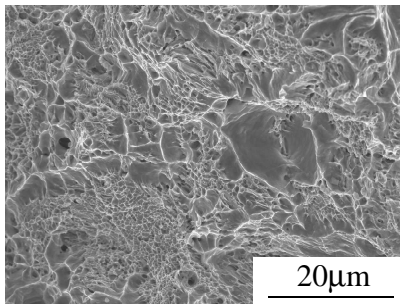
(d) S25C, $\epsilon_{pre}=0\%$, uncharged



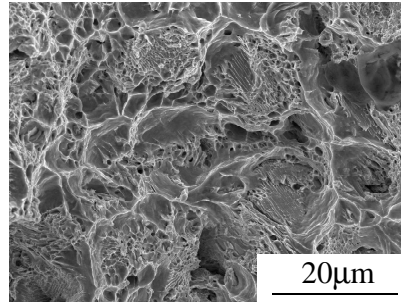
(e) S25C, $\epsilon_{pre}=0\%$, H-charged



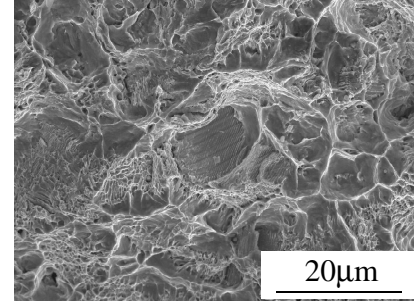
(f) S25C, $\epsilon_{pre}=10\%$, H-charged



(g) S45C, $\epsilon_{pre}=0\%$, uncharged



(h) S45C, $\epsilon_{pre}=0\%$, H-charged



(i) S45C, $\epsilon_{pre}=10\%$, H-charged

Fig. 5. Fracture surface.

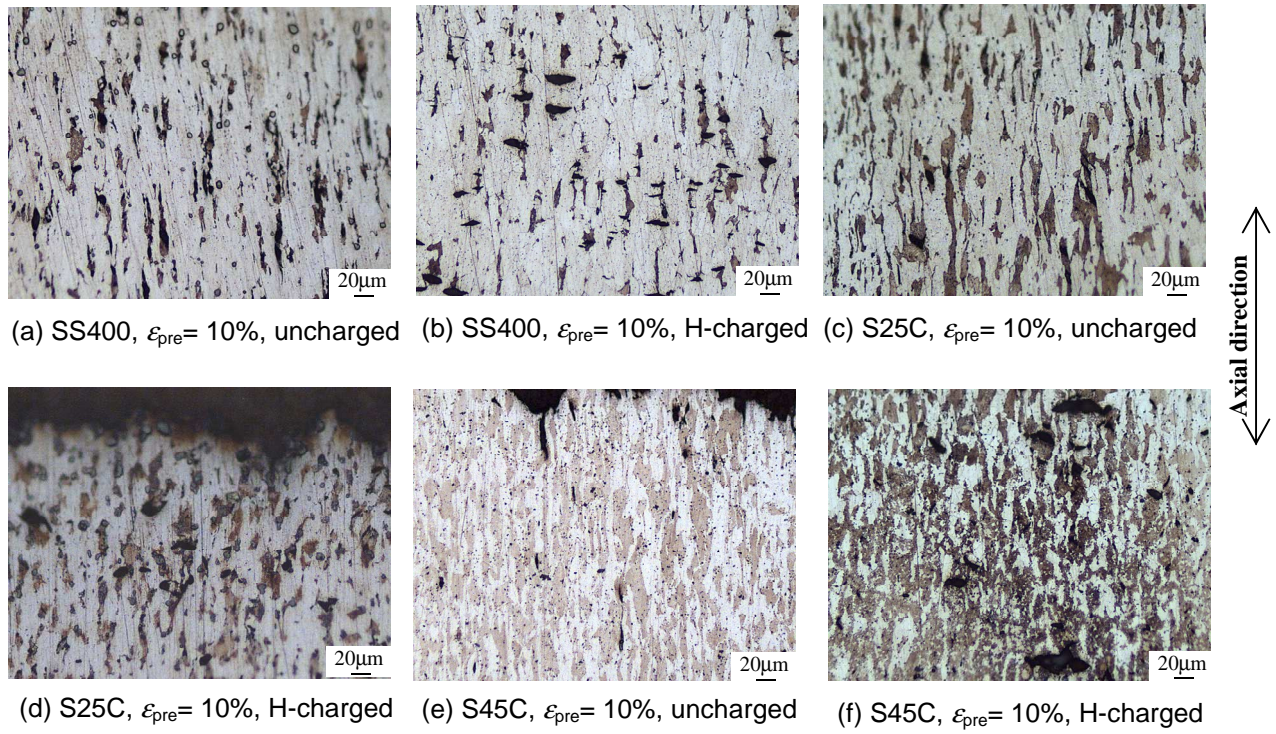


Fig. 6. Longitudinal section near fracture surface.

Proposal of Practicing Education for Engineering Ethics using a Safety Activity

Genji Hotta ¹

¹ Ariake National College of Technology University, Omuta, Japan

Abstract: Engineering ethics is a response to the public's opinions, and "Awareness", "Autonomy", and "Practice" are its basic elements. In Japan, Engineering ethics education is offered at a lot of schools, but actually many of these studies are provided by the lecture method. By using this teaching approach, it is difficult for the students to acquire the three basic elements of engineering ethics. Even if the student understands the content, he feels that he obtained knowledge only, and thus may forget the content of study by the time he/she graduates. Moreover, the time when engineering ethics is really needed is when the student finds employment in an enterprise. Until that time, the engineer should experience continuous motivation toward ethical actions, similar to the soldier in the Trojan horse. We propose adding a fieldwork component with the theme of safety to the engineering ethics education class. To address the problem concerning safety, the students should fulfill this responsibility by communicating and acting in regards to their surroundings. The students' independent behavior in the fieldwork experience should help them acquire the necessary and practice for the basic elements of engineering ethics.

Keywords: Engineering Ethics, Awareness, Autonomy, Safety Activity

1 INTRODUCTION

Life esteem and environmental preservation are common problems throughout the world, as well as basic demands of the public. The engineer's role and responsibility to solve these problems are demanding. Recently, engineering ethics education has been offered at many colleges and universities, and the approach of the scientist and the engineer in regards to the public's ethical demands has become more active. Australia's Commonwealth Scientific and Industrial Research Organization (CSIRO) are planning to execute the scientific study on the influence that genetically engineered organisms (The plant, the animal, and the microorganism are included) exert on the environment [1]. This is a good example of scientists and engineers trying to provide answers to the uneasiness surrounding genetically engineered organisms. Japan is a member of APEC (Asia-Pacific Economic Cooperation) with Australia, engineering qualifications that are valid throughout in the APEC region can be acquired in Japan. It is thus vital that the engineering trainees in Japan understand engineering ethics from a global perspective. The Japanese people strongly desire and expect peaceful use of science and technology, after an atomic bomb was dropped on Japan in World War II. In Japan, the JABEE (Japan Accreditation Board for Engineering Education) was recently established based on ABET (Accreditation Board for Engineering and Technology and Inc.) of the United States, and engineering ethics education is delivered to students who study science as part of their engineering education program. However, there are various problems with current engineering ethics education in Japan.

2 WHAT ARE ENGINEERING ETHICS

Engineering ethics are a response to the public's opinions [2]. The Public demands that the engineer will prevent disaster or damage, and announce danger. This will promote the engineer's trust by the public. The engineer should notice the danger in his work, plan to prevent danger, and talk about danger and its measures sufficiently with the public to answer these demands. Even if it might be difficult, the engineer should put plans into action, obtain results, and achieve public safety. It is necessary to receive evaluation of the results from the public. Engineering ethics thus covers a series of actions. A feature of engineering ethics is that the engineer actually rushes into action, to obtain a concrete result, rather than simply making

value judgments. "Awareness"[3], "Autonomy"[4], and "Practice" are necessary elements of the engineering ethics. "Awareness" is to identify problems of danger and scandals, etc. at work or at organizations to which they belong. "Autonomy" means not submitting unconditionally to the opinions and the policy of the group, but to act based on their own sense of values. "Practice" is to have not only an ethical desire but also to negotiate on danger with others, and to act toward the achievement of safety measures. Thus, it is important in that engineering ethics education pass on "Awareness", "Autonomy", and "Practice" in the form of skills and information to be acquired by the students. However, there are some problems with current engineering ethics education. I will address this problem in the next chapter.

3 PROBLEMS OF ENGINEERING ETHICS EDUCATION

3.1 Difficulty of continuing education and training for a long term necessary for training "Awareness"

"Awareness" in engineering ethics is characterized by the ability to divide an ethical element into various ethical issues, and it is very effective in the prevention of the accidents or scandals. However, since this ability is not necessarily natural, education and training are necessary. Moreover, it is difficult to acquire this ability in the short term even with intensive training. Young students should have educational training for "Awareness" over a relatively long period. (entrance ~ graduation ~ finding employment ~ career formation). As a result of such continuous education, when an event happens, the engineer should be able to identify the ethics problem and to act practically. For this purpose, in engineering ethics education, programs should be targeted not only at the student but also at members of society. For educational content, schools and enterprises should have the shared understanding and recognition. However, it is difficult to maintain education of engineering ethics with the same conceptual consistency after schooling, on to achieve united agreement about the concept of ethics on both the management side and technological side.

3.2 The engineer is in a workplace environment that is not "Autonomy" friendly

In the evaluation of values regarding an event to which engineer ethics are applied, the judgment is different in the case of the individual and the organization. This value gap is caused by the difference in perception of the public, the enterprise considers the public as a market while the engineer considers the public as a civilian. It is normal for an engineer to do business such as designing and manufacturing as an employee in an enterprise etc. In the office, first of all, the engineer should act as an individual when ethics are involved. However, the sense of belonging to one's enterprise is especially strong in Japan, and engineers are consider themselves to be not engineers but employees in their office. So, even when their sense of values differs from that of the company, their stated opinion often follows that of the group.

3.3 Formalization of engineer ethics to make practice desire lost

Lecture on engineering ethics might touch on various events by mentioning cases and examples, but the student doesn't has no experience as a member of society and it is thus difficult for them to understand the social issues behind the event. There is also a concern that engineering ethics are misunderstood as a formal liberal arts subject by them. After the student graduates and enters an enterprise, they feel that they should actually follow to the culture of the office, and follow the customs and standards of the office. Before long, they come to embrace the standpoint of the organization and the office, and engineer ethics that were understood and acquired in the school days cannot be applied to the business; a "polite fiction" theory of ethics is feared. The ethics education that they receive in the enterprise mostly concerns compliance. The engineer experiences conflicts with the public regarding complaints, and before long they will come to recognize that "The public is defended from the activity of the organization" and "The organization is defended from the public's activity". This is similar to the conflicted feeling when entering an enterprise after the product liability (PL: Product Liability) method as public protection is learnt and product liability prevention (PLP) and product liability defense (PLD) are learnt as corporate risk management.

4 MEASURES TO IMPROVE ENGINEERING ETHICS EDUCATION

4.1 Necessity of object lessons

There is a limit to the acquisition of Awareness, Autonomy and Practice taught by lecture study in the classroom. Combined coordinated education of knowledge and the body and mind is necessary in engineering ethics education. Moreover, it is also necessary that education continues even after starting

one's adult life. It seems that a program that combines fieldwork with classroom study is ideal. However, one problem here is how to choose the theme. It is difficult to plan a concrete action policy even if engineer ethics are chosen as the theme of the fieldwork. When thinking about the features of engineer ethics, a serious problem and matter that relates directly to the individual and a problem that can be addressed continuously in the future is necessary as the theme of the fieldwork. Judging from the above, a safety issue is appropriate as the theme.

4.2 Safety as a common view that exceeds standpoints

A safety problem is adopted as the training theme in engineer ethics. The sense of values differs according to the person and the standpoint but the safety problem allows problem recognition by everyone. There is no enterprise that does not offer safety education and training and measures for safety. So, by using a safety problem as a center theme of the engineering ethics training, common recognition that exceeds standpoints and time is obtained by all participants. An ethical element is inherent in a safety problem, so safety can be addressed up as an ethical issue. And, goal of devising a method for the public to be defended from harm can be clearly displayed, so the student can understand the purpose of the subject as a common view of society. Moreover, it is easy to image the situation when he behaves as a subject.

5 CONCRETE METHOD

It is difficult to acquire Awareness, Autonomy and Practice for the student that has not worked in an office where risk is present and who has not witnessed an actual industrial injury. We have thus devised an achievement method involving motivation of another type that even the student can have understand. For "Awareness" we train the discipline by exercises in class. For "Autonomy" we encourage students to show a positive approach in developing a sense of responsibility, and for "Practice" we enhance the student's motivation with a numeric target. In this way, we convert motivation concerning Awareness, Autonomy, and Practice into activity for Discipline, Responsibility, and Evaluation. In doing so, the student becomes able to behave independently, voluntarily, and ethically. Cooperation of the student who receives the education and the staff of the school is vital, and it is indispensable to offer an appropriate orientation to the activity by a safety specialist and make the activity part of the management cycle to achieve an educational effect.

5.1 Discipline

To identify an ethics problem is to find a problem in or our job, as stated above, and it is important in the ethics activity to make this a custom. The custom in this case is to have a habit of "Noticing" the risk. To nip danger in the bud, it is necessary to be able to discover the bud, and at the same time it is important to make a habit of not forgetting to find the bud. "Awareness" is supported by developing customs (=discipline) through repetition of the maneuvers and training. For an example of training, the author asks students to find danger existing in the campus at Kyushu Institute of Technology. Each student fills out a form "Dangerous place for us and dangerous states" like Figure 1. This questionnaire is completed at the end of the class and modify the perspective of the hazard in every case to "Danger of school" and "Danger of experiment or practice" and "Danger of machines and electric equipment".

Subject
Student number
Name
Describe danger in school that you found.

Fig.1. Questionnaire concerning hazard ^[5]

To respond to the questionnaire, the student should actively search out danger. This becomes training to discover danger. They will have to guess at first. At the start, they might recall their own experiences, and answer creatively. But, as time goes on, they come to consider danger in all their areas of activity to respond to questionnaire. Before long, students are made to be able to do training for discovering danger outside the classroom (for instance, workshop etc.). This becomes training in the discipline of discovering danger whatever the situation, and before long, it is connected with acquiring the custom of being aware of ethical issues.

5.2 Responsibility

Autonomy is the freedom of an individual to act or make decisions independently from others. One of the causes of difficulty in solving safety problems is the idea that accident prevention is the responsibility of others. In disaster prevention, it is important for us not to blindly follow this general idea but to have a sense of responsibility for society, so that we may help prevent or become involved in disaster aid. Then, we replace autonomy, one of the attainments of engineer ethics, with a responsibility concerning safety and training. For that, we give the student a role concerning safety, and give them a student "Sense of responsibility" concerning the safety activity, so we promote basic attainments that will develop into "Autonomy" in the future. We give students roles concerning safety activities using names such as "Safety committee" and "Safety team", and allot roles of experiment officer, practice officer, the subject officer, and the school year officer, etc, in addition, we divide the allotment of work such as report member, investigator, total members, and preparation member for each group. When necessary, we introduce a duty system such that responsibility falls to all members in turn as much as possible. As points of concern in this case, we are clarifying the content of work performed by each role, and "evaluation of surroundings" is transmitted to the student in drafting announcements by the school to the public, or transcripts, or the activity reports filed in this personal histories. And it is also important that we have the next generation continue this system.

5.3 Practice

For safe action in the factory, as the next step towards realizing one's responsibility we practice disaster prevention as "Our responsibility" for safety activity and safety measures execution, and the organization makes the result a safety result and it is evaluated. In other words, it is practice = evaluation, and the result of practice not seen actualized as an evaluation numerical value. Thus, we replace "practice" in engineering ethics education with "evaluation", and we make the system such that the student cannot help out behave. And, we have the student actually experience the difficulty and the feeling of moving the body and physically practicing a safety plan. Thus, the student can obtain the practical ability that will be needed in the future. "Evaluation" concerning safety as the fieldwork is concretely done by grading the student's activity. That is, we have the student count the number of dangers that he encounters, and students applies higher points to greater dangers.

	The first week	The second week	The third week	The fourth week	Total during month
Experiment	H	H	S	S	
Practice	S	S	2 H	S	
Campus	S	H	S	S	
Class	K	S	S	S	
Another	S	S	S	S	
Total of S	3	3	4	5	15
Total of H&K	-3	-2	-2	0	-7
Total	0	1	2	5	8

S: No danger(=1), H: dangerous(=-1), K: injured(=-2).

Fig. 2. Risk discovery card ⁽⁵⁾

Thus, students confirm their safety every day. When the student does an excellent safety activity hard, a low number will be counted, and the school gives good grades to students with low counted numbers. Thus, the student's safety activity is evaluated as a fixed quantity. Through this action, the student comes to recognize that he should voluntarily move his body and act forward safety achievement, while a third party evaluates the result. The purpose to put the safety result is his risk situation is always understood by confirming my safety point every day, and It has recognition of "My safety is defended for myself". With this method the daily approach and the evaluation by the third party are important. Students should always carry a safety card etc. It is good for the third party such as staff of the school to check it every day. An example safety grading card is shown in Figure 2 .

6 CONCRETE ACTIVITY AND RESULTS

Actualizing the content of this proposal will be attempted in the future. However, the author has already verified the effects of some basic elements in this proposal in safety education and training in an auto components supplier and the University. The following results were obtained regarding responsibility. In the new style of training in the auto components supplier where the author was working, roles and the responsibility actions by the committees were considerably effective. And so it is recognized that this is an effective method for Vocational Training. Moreover, in Department of Engineering at Kyushu Institute of Technology, the author recognizes safety ethics as a subject of engineering ethics and plans to improve the student's desire to learn and goal setting by using safety as a teaching material for engineer ethics education. Concretely, we are giving the students the following objectives at all times.

- 1) Enumerate dangerous locations in the school.
- 2) Think about measures for safety at the dangerous locations.
- 3) Your responsibility and role in the measures for safety
- 4) Action agenda and trouble for measures for safety
- 5) Forecast of results of your behavior and evaluation

By maneuvering like this, we think that students can become conscious of ethics problems by recognizing that risk is a familiar problem, noticing the ethical problem, being conscious of his responsibility and role, taking the trouble to address it, and thinking about the measures according to the progress of the lecture. As shown in Figure 3, we are finding that students consider the practical policy, and can experience the necessity of a social evaluation of results from finding an ethics problem to extrapolating the results.

7 FUTURE TASKS

In Japan, the employment situation has recently picked up with the economic recovery of manufacturing. However, the occurrence of industrial injuries has not increased, and expansion of licensing of technology to and from foreign countries may lead to a stagnation of the safety technology.

In this economic ambience, students graduating from science courses will not feel so much economical unease, and may not appreciate the necessity of engineering ethics.

To raise engineers of global caliber, we should improve the engineer's concept of responsibility in his school days. I think that it preferable that engineering ethics education begins with young people before the university.

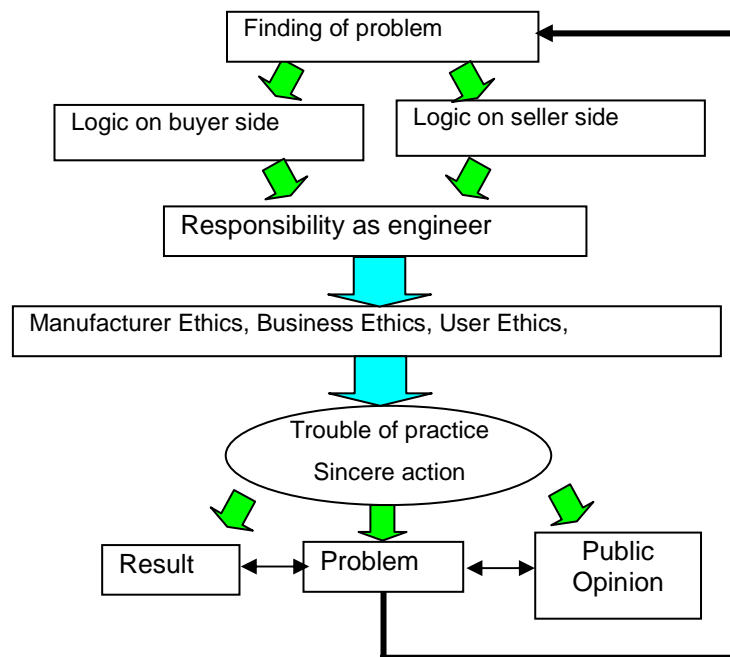


Fig.3. Practice system of engineering ethics ^[6]

REFERENCES

- [1] Information on <http://wiredvision.jp/archives/200008/2000083107.html>
- [2] G.Hotta, Engineering ethics of the present time, JIPM Solution, Tokyo, 2003, pp18-32.
- [3] T.Yamada, Education for promoting people's companion mind, Human Meeting, 11(4), 228-231, 2004.
- [4] C.B.Fleddermann, Engineering Ethics, third ed., Macmillan, Pearson Prentice Hall, New Mexico, 2008.
- [5] G.Hotta, Education for safety and sense of security that stares at disaster-prevention, Lecture thesis collection of Educational symposium of Osaka University, 2007.
- [6] G. Hotta, Engineer ethics education that treated safety problem to promote development of general human competence and independent engineer, Engineering education, 565(1), 16-21, 2008.

THE STRUCTURE AND MECHANICAL PROPERTY OF TURTLE SHELL

C. W. Wu¹, W. Zhang¹, C. Z. Zhang and Z. Chen^{1,2}

¹State Key Laboratory of Structural Analysis for Industrial Equipment
Faculty of Vehicle Engineering and Mechanics, Dalian University of Technology
Dalian, 116024, China

²Department of Civil and Environmental Engineering, University of Missouri
Columbia, MO 65211-2200, USA

Abstract: The turtle shell is an amazing structure optimized through the long-term evolution by nature. This paper reports the experimental study and numerical analysis on the mechanical property and the microstructure of the shell of *Trachemys scripta* (Red-ear turtle) living in South China. The inside surface of the shell, especially the bottom plate, is covered with a biofiber-reinforced thin film with a thickness of ~28 microns. This layer of thin film material gives the highest strength in the turtle shell, reaching ~100MPa. Especially, the reinforced biofibers first go down from the four rib surfaces and then spread into the inside surface of the bottom plate. It is found that such a distribution of the biofibers follows the stress direction on the inside surface of the bottom plate to resist the evolution of shell cracking.

Keywords: Turtle Shell, Microstructure, Mechanical Property

1 INTRODUCTION

Turtle is among the oldest animals that still exist in the world, which is believed to have evolved since 220 millions years ago [1]. The turtle shell, as the protective armor, plays an important role in helping the animal survive and evolve. The delicacy and optimal design of the turtle shell yields not only strong defense ability, but also an anchoring site for the muscles and the major mineral reservoir of the body [2]. The vaulting shell of the turtle not only provides the animal with the optimal load-bearing capacity, but also results in the maximum space for the animal storing and protecting its internal organs [3]. Rhee et al. [4] found that the turtle shell consists mainly of three layers of materials, namely, the interior and exterior layers consisting of cortical bone, and the middle layer consisting of cancellous bone. Although the turtle shell is quite stiff at the surface, the shell can still yield a small amount of deformation during the turtle movement so as to help it keep the efficiency of both respiration and locomotion. This is because the shell consists of many small plates connected with the soft sutures that give rise to a small elastic deformation of the shell under a small load but become considerably stiff under a large load. Krauss et al.[5] have given a detailed description of the microstructure and mechanical property of the sutures of turtle shell. Until now, most of the reported studies on turtle shell are focused on the genetic, molecular and cellular aspects of its embryonic development. However, little is known on the detailed mechanical property of the turtle shell at different levels and positions. The present study is therefore focused on the microstructure and mechanical property of the turtle shell.

2 OBSERVATION OF MICROSTRUCTURE

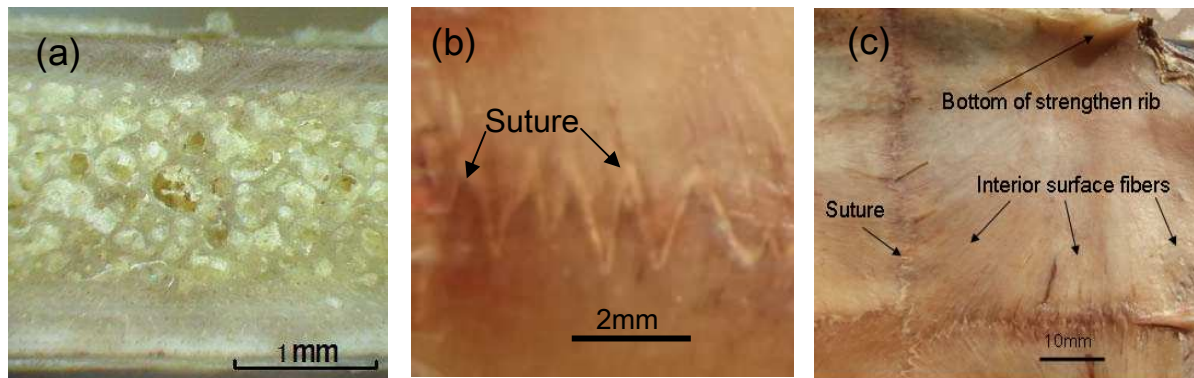


Fig.1. Microstructure of the turtle shell of *Trachemys scripta*: (a) photo image of the cross section of the bottom shell; (b) photo image of the suture at interior surface showing the suture structure; (c) inside surface image of the bottom plate.

The turtle shell studied here was *Trachemys scripta* (Red-ear turtle) living in South China. Its microstructure is shown in Fig. 1, which is almost the same as *Terrapene carolina* carapace studied by Rhee et al. [4]. On each side of the shell, there are two strengthening ribs covered with biofibers extending to the bottom plate surface. They give rise to the highest strength in the turtle shell. The mass densities of the shell at the interior, exterior and middle layers are respectively 1.52, 1.47 and 1.03 g/cm³.

3 MEASUREMENT OF MECHANICAL PROPERTY

To measure the mechanical property at different levels and positions, the turtle shell (length ~220 mm, width ~145 mm) was arranged between two parallel steel surfaces and was pressed with a materials testing system using a compression speed of 2mm/min. The compression failure load for this shell is around 3330 N corresponding to the maximum displacement (top board center) of 10.8mm. During the compression experiment, it was found that the rear part of the top board gave the maximum compression displacement, while the front part of the top board almost did not produce the normal displacement. Therefore, the rear part of the top board started to fail first. At the beginning of the failure process, some cracking sounds could be heard from the rear part, and finally a few visible cracks occurred.

The tensile modulus and strength of the turtle shell materials at different locations are given in Tables 1 and 2. The strength and modulus at the strengthening rib are obviously larger than those at other locations. The initial modulus is defined as the modulus at the small strain less than 0.001 and the final modulus is defined as the ratio of the fracture stress and the fracture strain. The later is similar to the average tensile modulus. As mentioned above, the inside surface of the shell, especially the bottom plate, is covered with a biofiber-reinforced thin film with a thickness of ~28 microns. This special composite film yields the highest strength reaching over 100 MPa, about 2.5 times the strength of the interior layer material.

Table 1. The tensile modulus and strength of the turtle shell materials

location	Interior	Exterior	Middle	Rib Interior	Rib Middle
Initial Modulus (MPa)	985	530	315	1190	700
Final Modulus (MPa)	500	256	230	511	382
Tensile Strength (MPa)	40	28	19	51.8	34.5

4 DISCUSSIONS AND CONCLUSIONS

The turtle shell is an amazing structure optimized through the long-term evolution by nature. Both its material and structure realize a cooperative optimization design to yield an optimal load-bearing capacity. This paper reports the tensile mechanical properties at different levels and locations, and the microstructure of *Trachemys scripta* (Red-ear turtle) living in South China.

The shell can be divided into three layers according to their strength: interior layer, exterior layer and middle layer. Their average tensile moduli are respectively 500MPa, 256MPa and 230MPa, and their tensile strengths are respectively 40MPa, 28MPa and 19MPa. The inside surface of the shell, especially the bottom plate, is covered with a biofiber-reinforced thin film with a thickness of ~28 microns. This layer of thin film material gives the highest strength in the turtle shell, reaching 98MPa. The turtle shell as a whole will be subjected to bending load so that the inside surface is under tension while the outmost surface is under compression. Thus, the inside surface of the shell is covered with the biofiber-reinforced composite film with a strength of about 100 MPa. Especially, the reinforced biofibers first go down from the rib surface and then spread into the inside surface of the bottom plate. It is found that such a distribution of the biofibers follows the stress direction on the inside surface of the bottom plate to resist the evolution of cracking. An integrated analytical, computational and experimental effort is being made to further explore this interesting issue.

ACKNOWLEDGMENTS

This work was supported by the National Natural Science Foundation of China (10972050, 90816025).

REFERENCES

- [1] O. Rieppel, R. R. Reisz. The origin and early evolution of turtles. *Annual Review of Ecology and Systematics*, 30, 1-22 (1999).
- [2] D. C. Jackson. How a turtle's shell helps it survive prolonged anoxic acidosis. *News in Phys. Sci.*, 15, 181-185 (2000).
- [3] Y. J. Zhou, W. Z. Zhang, Y. P. Yuan, et al. Load bearing behavior of turtle shell structure and its applications, *Machine Design (in Chinese)*, 23(3), 37-40 (2006).
- [4] H. Rhee, M. F. Horstemeyer, Y. Hwang, et al. A study on the structure and mechanical behavior of the *Terrapene carolina* carapace: A pathway to design bio-inspired synthetic composites. *Materials Science and Engineering C*, 29, 2333-2339 (2009).
- [5] S. Krauss, E. Monson-Orran, E. Zelzer, et al. Mechanical function of a complex three-dimensional suture joining the bony elements in the shell of the red-eared slider turtle. *Advanced Materials*, 21, 407-412 (2009).

FINITE ELEMENT ANALYSIS OF FRETTING FATIGUE

M. Abdel Wahab and R. Hojjati-Talemi

Department of Mechanical Construction and Production, Faculty of Engineering, Ghent University, B-9000
Ghent, Belgium

Abstract: Fretting fatigue is an important phenomenon in applied mechanics because it may lead to fretting damage, fatigue failure and reduction in the service life of mechanical components. This phenomenon takes place when bodies are in contact with one another and undergo small oscillatory relative motion due to cyclic loading. The damage introduced in the components is due to the high stresses generated at the contact surface between the two bodies. In order to calculate the contact stresses, numerical techniques, such as Finite Element Analysis (FEA), are very useful. FEA is frequently used to understand the fretting fatigue phenomenon and to investigate techniques that may reduce its effect on fatigue lifetime. In this paper, FEA of a fretting fatigue laboratory test specimen is carried out in order to study the stress distribution, crack initiation location and crack propagation.

Keywords: Finite Element Analysis, Fretting Fatigue, Crack Propagation

1 INTRODUCTION

The phenomenon of fretting takes place when two bodies in contact slide on one another at micrometer level over a large number of cycles. It may lead to fretting fatigue that reduces the fatigue lifetime of mechanical components. Fretting fatigue behaviour of a component depends on the contact stresses and the amount of micro-slip oscillatory motion between the two bodies. Due to these contact stresses and the micro-slips, micro cracks are nucleated and initiated. These micro-cracks will start to propagate under fretting fatigue loading conditions. Fretting fatigue appeared in many mechanical applications, such as bolted or riveted joints [1], shrink-fitted shafts [2] and blade dovetail of turbo machinery [3]. Although fretting fatigue has been experimentally studied in the literature [4], very few numerical models have been proposed [5]. This is due to the difficulties associated with modelling of fretting fatigue, which requires the application of several theories including contact mechanics, stress analysis, damage mechanics and fracture mechanics. In this paper, FEA of a fretting fatigue test specimen is carried out in order to analyze the stresses in the specimen and determine the expected position of crack initiation. Furthermore, fretting fatigue crack propagation is studied using the finite element code FRANC2D/L [6].

2 TEST SPECIMEN

Figure 1 shows the experimental set-up and the specimen's configuration. The specimen is made of Aluminium alloy 7075-T6 having an ultimate strength of 590 MPa and a yield stress of 503 MPa. Whereas, the two pads are made of stainless steel 410 having an ultimate strength of 700 MPa and a yield stress of

420 MPa. Each pad has two bases, as shown in Fig. 1, through which the contact force, F , is applied. A cyclic axial stress, σ_{Axial} , which varies as a function of time, t , from a maximum stress, σ_{max} , to a minimum stress, σ_{min} , is applied to the specimen. The fatigue ratio R is defined as $\sigma_{min} / \sigma_{max}$. The cyclic oscillatory elongation of the specimen at the contact surface between specimen and pads lead to fretting fatigue phenomenon.

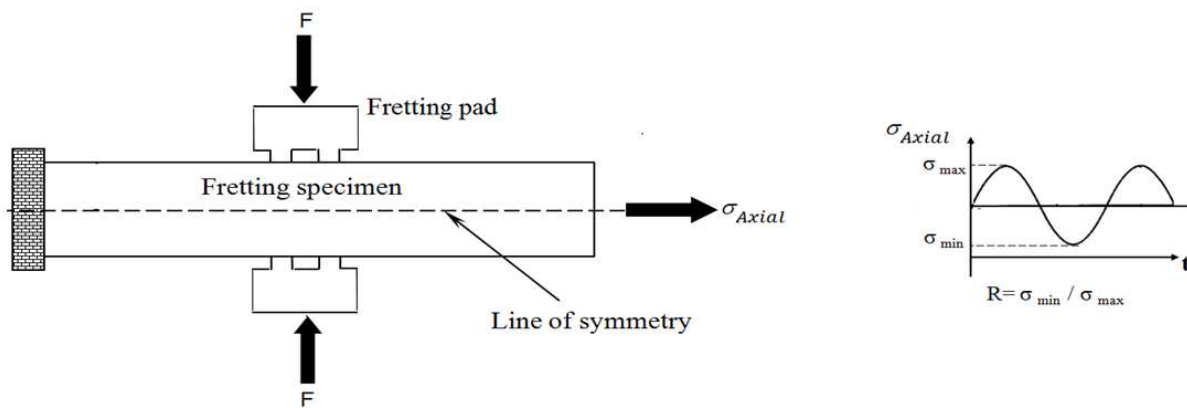


Fig. 1. Fretting fatigue test specimen.

3 STRESS ANALYSIS

The numerical simulations presented in this paper are for calculating the stress distribution, estimating the location of initial crack, modelling of crack propagation and estimating fretting fatigue lifetime. The FEA commercial package ANSYS is used to analyze the un-cracked specimen. The FE model of the fretting fatigue test specimen, shown in Fig. 2, is constructed using the geometry illustrated in Fig. 1 and assuming flat pads. Four-noded plane strain solid elements (PLAN82) were used to model the specimen and pads, whereas contact pairs, CONTA172 and TARGE169 elements, were used to model the interface surface between pads and specimen. The nonlinear contact problem is solved in ANSYS using the Augmented Lagrange method and a coefficient of friction of 0.5 is assumed. Due to symmetry, only one quarter of the specimen is modelled with appropriate boundary conditions as shown in Fig.2. The pad is further constrained in the in the X direction and one half of the normal $P/2$ is applied at the middle of the top side of the pad, followed by an axial stress, σ_{Axial} . The FE mesh was refined in the contact region, where high stress gradient is expected. From a convergence study, it was found that an element size of at least $9 \mu\text{m} \times 9 \mu\text{m}$ in the refined contact zone provided acceptable results.

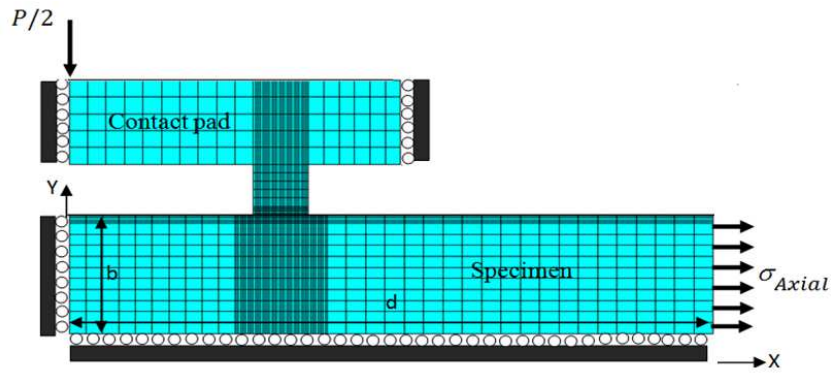


Fig. 2. FE model for fretting fatigue test specimen.

The contour plot of von-Mises stress distribution is shown in Fig. 3, where it can be seen that the maximum stress takes place near the trailing edge where crack initiation is expected. This is in agreement with experiments observations and test results [7].

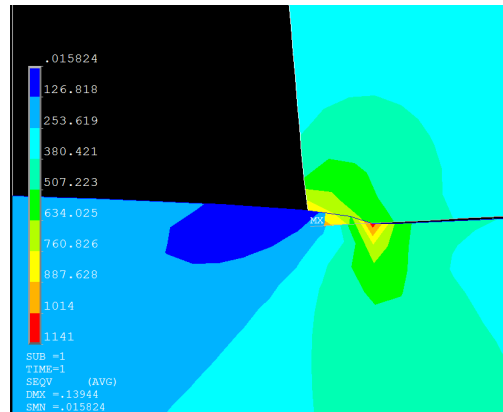


Fig. 3. von-Mises stress distribution.

4 CRACK PROPAGATION

After identifying the position of crack initiation from the stress analysis in the previous section, a crack propagation analysis is carried out for the fretting fatigue specimen using the FE code, FRANC2D/L [6]. The crack propagation analysis is performed in two steps. In the first step, the ANSYS FE model in Fig. 2 is used to calculate the contact stresses between specimen and pad. While in the second step an edge crack is inserted and the crack propagation analysis is carried out in FRANC2D/L code. In order to validate the FRANC2D/L model and the proposed mesh size, the stresses are compared to those obtained using ANSYS model and a difference of less than 1% was observed. In FRANC2D/L, the contact between specimen and pad is modelled using a gap element. After each crack increment, the stress intensity factors are calculated and used to compute the incremental number of cycles [8]. The orientation of the initial crack is assumed to be 45° , as observed from previous experimental results reported in the literature [9]. An initial crack length of 0.01 mm is assumed at the position predicted by the stress analysis presented in the previous section. After each crack increment, the FE mesh is modified using the maximum hoop stress criterion [10] to determine

the direction of crack propagation:

$$\theta_i = \theta_{i-1} + 2 \tan^{-1} \left[\frac{K_{I\max i} - \sqrt{K_{I\max i}^2 + 8K_{II\max i}^2}}{4K_{II\max i}} \right] \quad (1)$$

Where $K_{I\max i}$ and $K_{II\max i}$ are the stress intensity factors at the i th step for modes I and II at the maximum load and 'i' is the crack increment number. It was assumed that the final failure would occur if the stress intensity factor, K_I reaches its critical value, K_{IC} . The Forman NASGRO material model [11], is used to extract the stress intensity factor as a function of crack length and integrates the crack growth rate da/dN :

$$\frac{da}{dN} = C \left[\left(\frac{1-f}{1-R} \right) \Delta K \right]^n \frac{\left(1 - \frac{\Delta K_{th}}{\Delta K} \right)^p}{\left(1 - \frac{K_{max}}{K_{crit}} \right)^q} \quad (2)$$

Where C , n , p and q are empirical constants, which are obtained by curve fitting the fatigue experimental data and f is the ratio between mode I stress intensity factor and the maximum stress intensity factor. The threshold stress intensity range ΔK_{th} includes the effect of short crack by involving an intrinsic crack length and the parameter f . The empirical constants were $C=6 \times 10^{-10}$ and $n=2.51$. Figure 4 shows an example of a crack propagation analysis of a fretting fatigue test specimen.

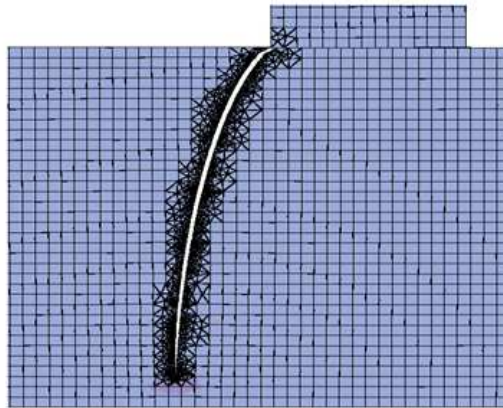


Fig. 4. Crack propagation analysis of fretting fatigue test specimen.

The FE results were validated using experiment data that were carried out for $R=0.1$, at a frequency of 20 Hz, a normal force of 1200 N, and maximum fatigue stresses of 130, 145 and 180 MPa. The tests was conducted for both pure fatigue and fretting fatigue. The fretting fatigue lifetime was lower than that of pure fatigue with a higher effect for high cycle fatigue. The lifetime obtained from FEA simulations are compared to those obtained from experimental tests in Fig. 5. It can be seen from Fig.5 that a maximum difference of about 24% can be observed between simulations and experiments. This could be explained by the effects of many factors that were not considered in this study and affected fretting fatigue crack propagation lifetime either directly or indirectly, such as crack initiation lifetime, wear, environmental conditions, the change in coefficient of friction due to debris at contact interface, etc.

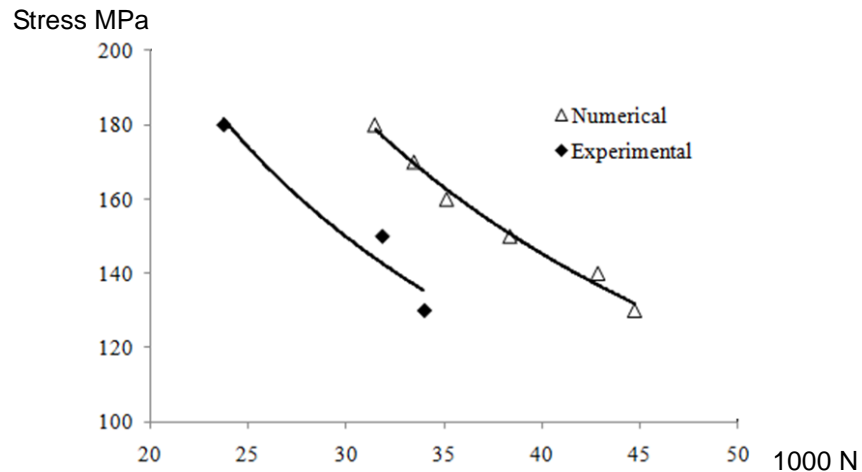


Fig. 5. FEA versus experiments fretting fatigue crack propagation.

5 CONCLUSIONS

Stress analysis and crack propagation analysis of fretting fatigue test specimen was carried out using FEA. From the stress analysis, it was possible to identify the position of crack initiation, which was found near the trailing edge. At this position, a crack of initial length of 0.1 mm orientated at a direction of 45° was used as an initial crack for the crack propagation analysis, which was carried out using the FE code, FRANC2D/L. The lifetimes obtained using simulations were compared to those obtained using experimental data and good agreement was observed. The differences between both results were attributed to many factors that have not been considered in the analysis.

ACKNOWLEDGEMENTS

The authors wish to thank the Ghent University for the financial support received by the Special Funding of Ghent University (Bijzonder Onderzoeksfonds), in the framework of BOF project BOF 01N02410.

REFERENCES

- [1] A. Buch, Fatigue and fretting of pin-lug joints with and without interference fit, *Wear* (1977); 43:9.
- [2] T. Hattori, S. Kawai, N. Okamoto and T. Sonobe, Torsional fatigue strength of a shrink-fitted shaft. *Bull JSME* (1981); 24(197):1893.
- [3] R.L. Johnson and R.C. Bill, Fretting in aircraft turbine engines, NASA TM X-71606 (1974).
- [4] P. Golden and M. Shepard, Life prediction of fretting fatigue with advanced surface treatments, *Materials Science and Engineering A* (2007); 468-470; 15-22.
- [5] H.A. Fadag, S. Mall and V.K. Jain, A finite element analysis of fretting fatigue crack growth behaviour in Ti-6Al-4V, *Engineering Fracture Mechanics* (2008);75(6):1384-1399.
- [6] FRANC2D/L, A crack propagation simulator for plane layered structures, Ithaca, New York: Cornell University, (1998).

- [7] R. Hojjati Talemi, M.M. Abdel Wahab and P. De Baets, Numerical modeling of fretting fatigue, 9th International Conference on Damage Assessment of Structures, DAMAS, Oxford, UK, 11-13 July (2011).
- [8] P.J. Golden and A.GF. Grandt, Fracture mechanics based fretting fatigue life predictions in Ti–6Al–4V, Engineering Fracture Mechanics (2004); 71: 2229-2243.
- [9] G.H. Majzoobi, J. Nemat, A.J.N. Rooz and G.H. Farrahi, Modification of fretting fatigue behaviour of AL7075–T6 alloy by the application of titanium coating using IBED technique and shot peening, Tribology International (2009), 42: 121-129.
- [10] F. Erdogan, G. Sih, On the crack extension in plates under plane loading and transverse shear, Journal of Basic Engineering, Trans. ASME (1963), 85: 519-527.
- [11] R.G. Forman, S. R. Mettu, Fracture Mechanics 22nd Symposium (1992), Vol. 1, Philadelphia: ASTM.